



8-1991

Atmospheric pressure and elevated pressure crystallization of isotactic polypropylene

Richard A. Campbell

Follow this and additional works at: https://trace.tennessee.edu/utk_gradthes

Recommended Citation

Campbell, Richard A., "Atmospheric pressure and elevated pressure crystallization of isotactic polypropylene. " Master's Thesis, University of Tennessee, 1991.
https://trace.tennessee.edu/utk_gradthes/12363

This Thesis is brought to you for free and open access by the Graduate School at TRACE: Tennessee Research and Creative Exchange. It has been accepted for inclusion in Masters Theses by an authorized administrator of TRACE: Tennessee Research and Creative Exchange. For more information, please contact trace@utk.edu.

To the Graduate Council:

I am submitting herewith a thesis written by Richard A. Campbell entitled "Atmospheric pressure and elevated pressure crystallization of isotactic polypropylene." I have examined the final electronic copy of this thesis for form and content and recommend that it be accepted in partial fulfillment of the requirements for the degree of Master of Science, with a major in Polymer Engineering.

Paul J. Phillips, Major Professor

We have read this thesis and recommend its acceptance:

Joe E. Spruiell, Roberto S. Benson

Accepted for the Council:

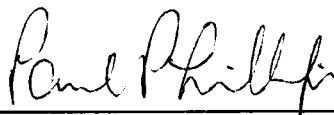
Carolyn R. Hodges

Vice Provost and Dean of the Graduate School

(Original signatures are on file with official student records.)

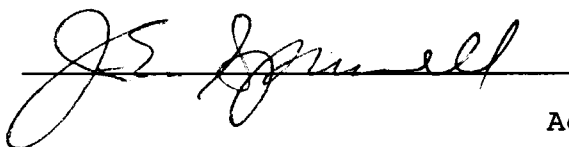
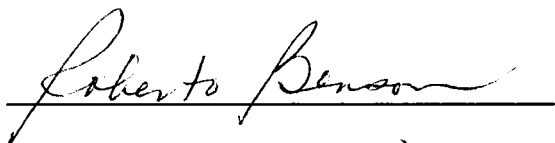
To the Graduate Council:

I am submitting herewith a thesis written by Richard A. Campbell entitled "Atmospheric Pressure and Elevated Pressure Crystallization of Isotactic Polypropylene." I have examined the final copy of this thesis for form and content and recommend that it be accepted in partial fulfillment of the requirements for the degree of Master of Science, with a major of Polymer Engineering.



Paul J. Phillips, Major Professor

We have read this thesis
and recommend its acceptance:



Accepted for the Council:



Vice Provost
and Dean of The Graduate School

STATEMENT OF PERMISSION TO USE

In presenting this thesis in partial fulfillment of the requirements for a Master's degree at The University of Tennessee, Knoxville, I agree that the Library shall make it available to borrowers under rules of the Library. Brief quotations from this thesis are allowable without special permission, provided that accurate acknowledgement of the source is made.

Permission for extensive quotation from or reproduction of this thesis may be granted by my major professor, or in his absence, by the Head of Interlibrary Services when, in the opinion of either, the proposed use of the material is for scholarly purposes. Any copying or use of the material in this thesis for financial gain shall not be allowed without my written permission

Signature

Richard A. Campbell

Date

April 29, 1991

Atmospheric Pressure and Elevated Pressure Crystallization of
Isotactic Polypropylene

A Thesis

Presented for the

Master of Science

Degree

The University of Tennessee, Knoxville

Richard A. Campbell

August 1991

ACKNOWLEDGEMENTS

The author would like to express his most sincere thanks to his advisor, Professor Paul J. Phillips, for his support and guidance.

Sincere thanks are extended to the author's committee, professors Joe E. Spruiell and Roberto S. Benson, for their efforts in making this work possible.

The author appreciates the discussions with his fellow students, the work performed by the undergraduate technicians, and the support provided by the Materials Science office personnel and the electronics and machine shops.

The deepest appreciation is extended to my wife Sandra for her unfailing support, patience, and encouragement. Truly, this work would not have been accomplished without her help.

ABSTRACT

The crystallization of isotactic polypropylene was studied at atmospheric pressure and elevated pressures up to 200 MPa (2 kbar). At atmospheric pressure, two homopolymers and an 0.5% ethylene copolymer were studied. The investigation included studies of crystallization rates under quiescent isothermal conditions. The morphology and thermal behavior were also studied. The Avrami model of crystallization behavior was applied to the bulk crystallization data. Secondary nucleation theory was also applied to the crystallization data.

At atmospheric pressure the bulk crystallization kinetics exhibited similar Avrami exponents for the three polypropylene samples. However, the results of the secondary nucleation analysis using reciprocal crystallization halftimes showed a Regime II - Regime III transition only for the low molecular weight homopolymer. The elevated pressure kinetics studies showed differences in bulk crystallization kinetics and secondary nucleation kinetics analysis as a function of pressure.

The morphology at atmospheric pressure for the homopolymers exhibited similar behavior as a function of crystallization temperature, but the copolymer exhibited distinct differences from the homopolymers. The elevated

pressure crystallization samples exhibited spherulitic morphology at all observed pressures and crystallization temperatures.

The thermal behavior of the atmospheric pressure crystallized samples exhibited the complex behavior common to isotactic polypropylene. The low molecular weight homopolymer showed somewhat different behavior from the high molecular weight homopolymer and the copolymer.

Table of Contents

Chapter	Page
1. Introduction	1
2. Review of Theoretical Background and Literature	4
2.1 Polymer Crystallization and Morphology	4
2.1.1 Single Crystals	4
2.1.2 Spherulites	7
2.1.3 Axialites	13
2.2 Polymer Fold Surface	13
2.2.1 Fold Surface Nature	13
2.2.2 Summary Arguments on Fold Surface Structure	18
2.3 Crystallization Theory	20
2.3.1 Background	20
2.3.2 Model	20
2.3.3 Total Flux	24
2.3.4 Initial Lamellar Thickness	26
2.3.5 Retardation Factor	28
2.3.6 Free Energy of Fusion	29
2.3.7 Growth Rates: Regimes I, II, and III ...	30
2.3.7.1 Regime I Growth	31
2.3.7.2 Regime II Growth	33
2.3.7.3 Regime III Growth	34
2.3.8 Regime Test	35
2.3.9 Limitations of Secondary Nucleation Theory	36
2.3.9.1 Adjacent Re-Entry	36
2.3.9.2 Constant Fold Period	37
2.4 Melting of Polymer Crystals	38
2.4.1 Thermodynamic Considerations	38
2.4.2 Kinetic Considerations	39
2.5 The Effects of Pressure	41
2.5.1 Morphology	41
2.5.2 Crystallization Kinetics	43
2.5.3 Melting Response	44
2.5.4 Glass Transition Temperature	45
2.6 Molecular Weight Effects	47
2.7 Polymerization	49
2.8 Polymer Molecular Weights	50
2.9 Tacticity Analysis	52

2.9.1	Tacticity from IR Spectroscopy	53
2.9.2	Tacticity from NMR Spectroscopy	53
3.	Experimental and Analytical Techniques	56
3.1	Materials	56
3.2	Bulk Crystallization	56
3.3	Melting	67
3.4	Morphology	70
4.	Results	73
4.1	Crystallization	73
4.1.1	Atmospheric Pressure Bulk Data	73
4.1.2	Elevated Pressure Bulk Data	80
4.2	Thermal Analysis Results	94
4.2.1	Differential Scanning Calorimetry	95
4.2.2	Depolarized Light Intensity	107
4.3	Morphology	122
4.3.1	Atmospheric Pressure	122
4.3.1	Elevated Pressure	135
5.	Discussion	144
5.1	Thermal Analysis	144
5.1.1	Equilibrium Melting Temperature	144
5.1.2	Comparison of DSC and DLI	156
5.2	Kinetics Analysis	157
5.2.1	Avrami Analysis	157
5.2.2	Half-time Analysis	172
6.	Conclusions	191
6.1	Morphology	191
6.2	Thermal Behavior	192
6.3	Crystallization Behavior	192
7.	Recommendations for Further Work	194
7.1	Linear Growth Rate Kinetics	194
7.2	Stereoregularity	194
7.3	Copolymers	194
7.4	Additional Morphological Studies	195
References		196
VITA		

List of Tables

Table	Page
2.1 Keith-Padden Classification of Polypropylene Spherulites	
2.2 Avrami Coefficients and Interpretation	12
3.1 Characteristics of Polypropylene Materials	57
5.1 Values of the Equilibrium Melting Temperature, T_m^0 , and the Thickening Factor, γ , for isotactic polypropylenes crystallized at atmospheric pressure.	148
5.2 Values of the Equilibrium melting temperature, T_m^0 , and the Thickening factor, γ , for isotactic polypropylene crystallized at elevated pressure.	153
5.3 Change in Melting Temperature with Pressure for isotactic polypropylene and other polymers.	155
5.4 Values for DSC and DLI melting analysis for isotactic polypropylenes crystallized at atmospheric pressure.	159
5.5 Avrami Coefficients as a function of crystallization temperatures for isotactic polypropylene at atmospheric pressure (DLI).	164
5.6 Avrami Coefficients as a function of supercooling for iPP $M_w = 83,000$ at elevated pressures (DLI)	171
5.7 Results of Half-time Kinetics Analysis of iPP at Atmospheric pressure.	180
5.8 Results of Half-Time Kinetics Analysis of iPP at Various Pressures.	189

List of Figures

Figure	Page
2.1 Schematic of a polymer single crystal.	6
2.2 Schematic of a polymer spherulite	8
2.3 Possible polymer growth paths	9
2.4 Polymer chain folding models	14
2.5 Fringed micelle model	16
2.6 Polymer lamellar crystal idealized schematic	21
2.7 Free energy of formation of chain folded surface nucleus	23
2.8 Lauritzen-Hoffman crystallization regimes schematic ..	32
2.9 Infrared spectra of stereoregular forms of polypropylene	54
3.1 Elevated pressure system schematic and photograph ...	59
3.2 Elevated pressure cell schematic and photograph	61
3.3 Elevated pressure system heat exchanger schematic ...	62
4.1 Schematic of intensity versus time relation typical of isothermal crystallization of polymers. Labeled points are defined in text.	74
4.2 Light intensity versus time curves at various temperatures for isotactic polypropylene homopolymer $M_w = 151,000$	76
4.3 Light intensity versus time curves at various temperatures for isotactic polypropylene homopolymer $M_w = 83,000$	77
4.4 Light intensity versus time curves at various temperatures for isotactic polypropylene copolymer (0.5% ethylene) $M_w = 151,000$	78

4.5	Comparison of the overall transformation kinetics at $T_c = 130^\circ\text{C}$ ($\Delta T = 57^\circ$) for isotactic polypropylene.	79
4.6	Reciprocal of crystallization half-times for isotactic polypropylenes as a function of crystallization temperature.	81
4.7	Light intensity versus time curves at various temperatures for isotactic polypropylene homopolymer $M_w = 83,000$. Crystallization pressure 25 MPa.	84
4.8	Light intensity versus time curves at various temperatures for isotactic polypropylene homopolymer $M_w = 83,000$. Crystallization pressure 50 MPa.	85
4.9	Light intensity versus time curves at various temperatures for isotactic polypropylene homopolymer $M_w = 83,000$. Crystallization pressure 75 MPa.	86
4.10	Light intensity versus time curves at various temperatures for isotactic polypropylene homopolymer $M_w = 83,000$. Crystallization pressure 100 MPa.	87
4.11	Light intensity versus time curves at $\Delta T = 50^\circ$ for isotactic polypropylene homopolymer $M_w = 83,000$ at several crystallization pressures.	88
4.12	Reciprocal of crystallization half-times for isotactic polypropylene homopolymer $M_w = 83,000$ as a function of crystallization temperature. Crystallization pressure 25 MPa.	89
4.13	Reciprocal of crystallization half-times for isotactic polypropylene homopolymer $M_w = 83,000$ as a function of crystallization temperature. Crystallization pressure 50 MPa.	90
4.14	Reciprocal of crystallization half-times for isotactic polypropylene homopolymer $M_w = 83,000$ as a function of crystallization temperature. Crystallization pressure 75 MPa.	91
4.15	Reciprocal of crystallization half-times for isotactic polypropylene homopolymer $M_w = 83,000$ as	

	a function of crystallization temperature. Crystallization pressure 100 MPa.	92
4.16	Comparison of reciprocal crystallization half-times for isotactic polypropylene homopolymer $M_w = 83,000$ at several crystallization pressures.	93
4.17	DSC melting behavior of isotactic polypropylene homopolymer $M_w = 83,000$ at various isothermal crystallization temperatures. Heating Rate = $10^\circ\text{C}/\text{min}$	96
4.18	DSC melting behavior of isotactic polypropylene homopolymer $M_w = 151,000$ at various isothermal crystallization temperatures. Heating Rate = $10^\circ\text{C}/\text{min}$	98
4.19	DSC melting behavior of isotactic polypropylene copolymer $M_w = 151,000$ at various isothermal crystallization temperatures. Heating Rate = $10^\circ\text{C}/\text{min}$	99
4.20	Comparison of DSC melting behavior at $10^\circ\text{C}/\text{min}$ heating rate for isotactic polypropylenes isothermally crystallized at $T_c = 130^\circ\text{C}$	100
4.21	Comparison of DSC melting behavior at $10^\circ\text{C}/\text{min}$ heating rate for isotactic polypropylenes isothermally crystallized at $T_c = 146^\circ\text{C}$	101
4.22	Heating rate effect on DSC melting behavior for isotactic polypropylene homopolymer $M_w = 83,000$ isothermally crystallized at $T_c = 130^\circ\text{C}$	103
4.23	DSC melting behavior of isotactic polypropylene homopolymer $M_w = 83,000$ crystallized at fixed supercooling $\Delta T = 50^\circ$ at several crystallization pressures. Heating Rate = $10^\circ\text{C}/\text{min}$	105
4.24	DSC melting behavior of isotactic polypropylene homopolymer $M_w = 83,000$ crystallized at fixed supercooling $\Delta T = 50^\circ$ at several crystallization pressures. Heating Rate = $40^\circ\text{C}/\text{min}$	106
4.25	DLI melting behavior of isotactic polypropylene homopolymer $M_w = 83,000$ isothermally crystallized at various temperatures. Heating Rate = $10^\circ\text{C}/\text{min}$	108

4.26	DLI melting behavior as a function of heating rate for isotactic polypropylene homopolymer $M_w = 83,000$ isothermally crystallized at $T_c = 130^\circ\text{C}$	110
4.27	DLI melting behavior for isotactic polypropylenes isothermally crystallized at $T_c = 130^\circ\text{C}$. Heating Rate $10^\circ\text{C}/\text{min}$	111
4.28	DLI melting behavior of isotactic polypropylene crystallized at fixed supercooling $\Delta T = 50^\circ$ at several crystallization pressures. Heating Rate = $10^\circ\text{C}/\text{min}$. Melting performed at atmospheric pressure.	113
4.29	DLI melting behavior of isotactic polypropylene crystallized at fixed supercooling $\Delta T = 50^\circ$ at 200 MPa. Heating rate = $10^\circ\text{C}/\text{min}$. Melting performed at atmospheric pressure.	115
4.30	Optical morphology of A. 200 MPa crystallized sample ($\Delta T = 50^\circ$); B. recrystallization of (A.) at atmospheric pressure, ($\Delta T = 50^\circ$); C atmospheric pressure crystallized ($\Delta T = 50^\circ$)	116
4.31	DLI melting behavior of isotactic polypropylene homopolymer $M_w = 83,000$ isothermally crystallized at 25 MPa crystallization pressure; various temperatures. Heating rate $3^\circ\text{C}/\text{min}$. Melted at 25 MPa.	118
4.32	DLI melting behavior of isotactic polypropylene homopolymer $M_w = 83,000$ isothermally crystallized at 50 MPa crystallization pressure; various temperatures. Heating rate $3^\circ\text{C}/\text{min}$. Melted at 50 MPa.	119
4.33	DLI melting behavior of isotactic polypropylene homopolymer $M_w = 83,000$ isothermally crystallized at 75 MPa crystallization pressure; various temperatures. Heating rate $3^\circ\text{C}/\text{min}$. Melted at 75 MPa.	120
4.34	DLI melting behavior of isotactic polypropylene homopolymer $M_w = 83,000$ isothermally crystallized at 100 MPa crystallization pressure; various temperatures. Heating rate $3^\circ\text{C}/\text{min}$. Melted at 100 MPa.	121
4.35	Optical micrographs of isotactic polypropylene homopolymer $M_w = 151,000$ isothermally crystallized	

	at $T_c = 130^\circ\text{C}$ ($\Delta T = 57$): A. Crossed polars, B. Crossed polars, full wave plate.	124
4.36	Optical micrographs of isotactic polypropylene homopolymer $M_w = 151,000$ isothermally crystallized at $T_c = 138^\circ\text{C}$ ($\Delta T = 49^\circ$): A. Crossed polars, B. Crossed polars, full wave plate.	125
4.37	Optical micrographs of isotactic polypropylene homopolymer $M_w = 151,000$ isothermally crystallized at $T_c = 146^\circ\text{C}$ ($\Delta T = 41^\circ$): A. Crossed polars, B. Crossed polars, full wave plate.	126
4.38	Optical micrographs of isotactic polypropylene homopolymer $M_w = 83,000$ as a function of crystallization temperature. A. $T_c = 130^\circ\text{C}$, B. $T_c = 138^\circ\text{C}$, C. $T_c = 146^\circ\text{C}$	127
4.39	Optical micrographs of isotactic polypropylene copolymer $M_w = 151,000$ as a function of crystallization temperature A. $T_c = 130^\circ\text{C}$, B. $T_c = 138^\circ\text{C}$, C. $T_c = 146^\circ\text{C}$	129
4.40	Optical micrographs of isotactic polypropylene homopolymer $M_w = 83,000$ as a function of crystallization time at $T_c = 130^\circ\text{C}$. A. $t_c = 0.8$ min., B. $t_c = 2.4$ min., C. $t_c = 4.5$ min.	130
4.41	Optical micrographs of isotactic polypropylene homopolymer $M_w = 83,000$ morphology observed on heating from $T_c = 130^\circ\text{C}$ at $10^\circ\text{C}/\text{min}$. A. 130°C , B. 152°C , C. 159°C	133
4.42	Optical micrographs of isotactic polypropylene homopolymer $M_w = 83,000$ at fixed supercooling $\Delta T = 50^\circ\text{C}$. A. atmospheric pressure crystallized, B. 25 MPa crystallized.	136
4.43	Optical micrographs of isotactic polypropylene homopolymer $M_w = 83,000$ at fixed supercooling $\Delta T = 50^\circ\text{C}$. A. 50 MPa crystallized, B. 75 MPa crystallized.	138
4.44	Optical micrographs of isotactic polypropylene homopolymer $M_w = 83,000$ at fixed supercooling $\Delta T = 50^\circ\text{C}$. A. 100 MPa crystallized, B. 200 MPa crystallized.	139
4.45	Optical micrographs of isotactic polypropylene homopolymer $M_w = 83,000$ isothermally crystallized at $P_c = 50$ MPa. A. 152°C , B. 154°C , C. 156°C	140

4.46	Optical micrographs of isotactic polypropylene homopolymer $M_w = 83,000$ isothermally crystallized. A. $P_c = 75$ MPa, $T_c = 156^\circ\text{C}$, B. $P_c = 100$ MPa, $T_c = 166^\circ\text{C}$	142
4.47	Optical morphology of isotactic polypropylene $M_w = 83,000$ isothermally crystallized at atmospheric pressure and $T_c = 156^\circ\text{C}$	143
5.1	Melting temperature versus crystallization temperature for isotactic polypropylenes. DSC heating rate $10^\circ\text{C}/\text{min}$. Modified return-to-baseline melting definition.	147
5.2	Melting temperature versus crystallization temperature for isotactic polypropylene crystallized at elevated pressure DLI heating rate $3^\circ\text{C}/\text{min}$. Modified return-to-baseline melting definition.	151
5.3	Change in equilibrium melting temperature T_m° with crystallization pressure P_c	154
5.4	Comparison of DSC and DLI melting behavior for isotactic polypropylene homopolymer $M_w = 83,000$ isothermally crystallized at atmospheric pressure, $T_c = 130^\circ\text{C}$. Heating rate $10^\circ\text{C}/\text{min}$	158
5.5	Avrami plots for isotactic polypropylene homopolymer $M_w = 151,000$ at various crystallization temperatures and atmospheric pressure.	161
5.6	Avrami plots for isotactic polypropylene homopolymer $M_w = 83,000$ at various crystallization temperatures and atmospheric pressure.	162
5.7	Avrami plots for isotactic polypropylene copolymer $M_w = 151,000$ at various crystallization temperatures and atmospheric pressure.	163
5.8	Comparison of experimental and theoretical I versus t data for isotactic polypropylene $M_w = 151,000$. . .	166
5.9	Avrami plots for isotactic polypropylene homopolymer $M_w = 83,000$ crystallized at 25 MPa pressure, various temperatures.	167

5.10	Avrami plots for isotactic polypropylene homopolymer $M_w = 83,000$ crystallized at 50 MPa pressure, various temperatures.	168
5.11	Avrami plots for isotactic polypropylene homopolymer $M_w = 83,000$ crystallized at 75 MPa pressure, various temperatures.	169
5.12	Avrami plots for isotactic polypropylene homopolymer $M_w = 83,000$ crystallized at 100 MPa pressure, various temperatures.	170
5.13	Homogeneous nucleation analysis for isotactic polypropylene $M_w = 83,000$ crystallized at atmospheric pressure.	174
5.14	Kinetics analysis plot for isotactic polypropylene homopolymer $M_w = 83,000$ using reciprocal half-time data.	175
5.15	Kinetics analysis plot for isotactic polypropylene homopolymer $M_w = 151,000$ using reciprocal half-time data.	176
5.16	Kinetics analysis plot for isotactic polypropylene copolymer $M_w = 151,000$ using reciprocal half-time data.	177
5.17	Kinetics analysis comparison using reciprocal half-time data for isotactic polypropylenes.	178
5.18	Homogeneous nucleation analysis for isotactic polypropylene $M_w = 83,000$ crystallized at elevated pressure.	182
5.19	Reciprocal half-time kinetics analysis plot for isotactic polypropylene $M_w = 83,000$ crystallized at 25 MPa pressure.	183
5.20	Reciprocal half-time kinetics analysis plot for isotactic polypropylene $M_w = 83,000$ crystallized at 50 MPa pressure.	184
5.21	Reciprocal half-time kinetics analysis plot for isotactic polypropylene $M_w = 83,000$ crystallized at 75 MPa pressure.	185
5.22	Reciprocal half-time kinetics analysis plot for isotactic polypropylene $M_w = 83,000$ crystallized at 100 MPa pressure.	186

- 5.23 Reciprocal half-time kinetics analysis plot for isotactic polypropylene $M_w = 83,000$ crystallized at elevated pressure. 187
- 5.24 Regime transition temperature for isotactic polypropylene $M_w = 83,000$ as a function of crystallization pressure. 190

List of Tables

2.1	Keith-Padden Classification of Polypropylene Spherulites	
2.2	Avrami Coefficients and Interpretation	12
3.1	Characteristics of Polypropylene Materials	57
5.1	Values of the Equilibrium Melting Temperature, T_m^0 , and the Thickening Factor, γ , for isotactic polypropylenes crystallized at atmospheric pressure.	148
5.2	Values of the Equilibrium melting temperature, T_m^0 , and the Thickening factor, γ , for isotactic polypropylene crystallized at elevated pressure.	153
5.3	Change in Melting Temperature with Pressure for isotactic polypropylene and other polymers.	155
5.4	Values for DSC and DLI melting analysis for isotactic polypropylenes crystallized at atmospheric pressure.	159
5.5	Avrami Coefficients as a function of crystallization temperatures for isotactic polypropylene at atmospheric pressure (DLI).	164
5.6	Avrami Coefficients as a function of supercooling for iPP $M_w = 83,000$ at elevated pressures (DLI) ...	171
5.7	Results of Half-time Kinetics Analysis of iPP at Atmospheric pressure.	180
5.8	Results of Half-Time Kinetics Analysis of iPP at Various Pressures.	189

Chapter 1

Introduction

Morphological structure is known to be an important determinant of polymer physical properties. The relationship between structural and processing variables must be understood in order to optimize polymer properties. The basic processing variables which control polymer crystallization are temperature and pressure. The effects of temperature on polymer crystallization have been studied extensively for several polymer systems. However, the effects of pressure on polymer crystallization have not been thoroughly studied. Crystallization at elevated pressures can be significantly different from that at atmospheric pressure. In some polymers, an extended-chain morphology, rather than folded-chain morphology, can be produced with high pressure-high temperature conditions. In some polymers, different crystal forms can be developed.

Considering the sensitivity of isotactic polypropylene crystal structure to both crystallization conditions (temperature and pressure) and stereospecificity, the commercial importance of iPP, and the available literature on iPP, isotactic polypropylene was chosen for this study. Isotactic polypropylene is known to exist in three polymorphic crystalline forms. Several investigators have

studied the effects of pressure on iPP. The bulk crystallization of iPP [1], the structure [2], and the melting behavior have been studied [3]. However no in-depth studies of the crystallization process and especially the linear growth rates at elevated pressures have been reported.

In order to understand the crystal growth process and to obtain some of the important kinetic parameters at elevated pressures, the measurement of linear growth rates is essential. It is necessary to identify the regime under which crystallization is occurring since this affects the evaluation of kinetic data. Some researchers have reported the presence of all three regimes in iPP for a low molecular weight fraction, making it a potentially very useful system for exploring the effect of pressure on regime transitions. The proposed experimental research includes the measurement of linear growth rates of bulk isotactic polypropylene of several molecular weights at atmospheric pressure. Linear growth rates of isotactic polypropylene at elevated pressure will also be measured. The linear growth rates of narrow molecular weight distribution fractions of iPP will also be measured. The morphology of isothermally crystallized samples will be studied by optical microscopy, electron microscopy, wide-angle X-ray diffraction, and small-angle X-ray scattering. The thermal behavior of isothermally crystallized samples will be studied by means of differential

scanning calorimetry, depolarized light intensity, and transmitted light intensity.

Lauritzen-Hoffman secondary nucleation theory is chosen for initial analysis of the crystallization kinetics because of its simplicity and its wide applicability. It has been shown to compare well with experimental data for several polymers at atmospheric pressure [4] and also at elevated pressure [5,6]. Not only will further understanding of the relation between observed changes and polymer composition and structure be obtained, but also important information on the nature of regime transitions. The effect of pressure on the regime transition temperatures is important to the understanding of the nature of the transition. If the change of the transition temperature with pressure follows the change of the glass transition temperature with pressure, a diffusion controlled mechanism can be concluded. If the transition temperature changes with pressure as melting temperature, then the transition is thermodynamic and controlled by the nucleation process.

Chapter 2

Review of Theoretical Background and Literature

2.1 Polymer Crystallization and Morphology

When polymer molecules can crystallize, the extent of crystallization is affected by such factors as structural regularity, chain substituents, and branching. Crystalline polymers are distinguished from other crystalline materials in that they are only semicrystalline. The density of a crystalline polymer is found to be between that of a fully crystalline polymer and that of fully a amorphous polymer. The x-ray diffraction pattern, while indicating the existence of long-range order, is usually in the form of rings superimposed on a diffuse background.

Polymers capable of crystallizing can form ordered structures from the melt or from dilute solution. These ordered structures contain the polymer molecules folded back and forth on themselves to some degree. The crystallization process involves the transformation of the disordered amorphous state to the ordered crystalline state. These crystals form in platelets or ribbons, usually referred to as lamellae.

2.1.1 Single Crystals

Single crystals of a polymer can be formed by cooling a dilute polymer solution, Keller [7] having grown polyethylene

single crystals by this method. These crystals are lamellar in habit and are approximately 100 angstroms thick (Figure 1). Electron diffraction indicates that the polymer molecules are normal to the relatively large upper and lower surfaces of the crystal. Keller thus concluded that the polymer molecules are folded back and forth on themselves within the crystals. Similar observations by Fischer [8] and Till [9] supported this conclusion. Thus the upper and lower crystal surfaces must consist of molecular folds of one form or other (Figure 2.1). Factors controlling the size and shape of single crystals include solvent, concentration, and temperature. The thickness of lamellae is affected by the crystallization temperature and by any further annealing treatments.

From a nucleus, the lamella grows along its lateral edges, with the molecules folding back and forth along these edges. Sectors of growth are distinguished by the plane of folding, thus the single crystal can be subdivided into sectors of growth. Single crystals usually form a nonflat hollow pyramid-like morphology, the different sectors forming the pyramid's panels (Figure 2.1). The pyramids often collapse and flatten during normal sample collection resulting in crystals with corrugations.

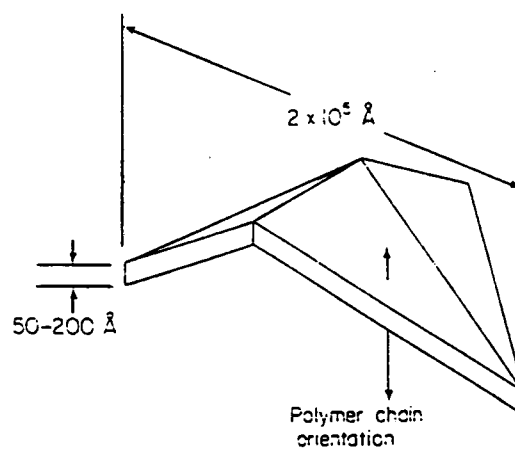


Figure 2.1 Schematic of a polymer single crystal.

2.1.2 Spherulites

Spherulitic aggregates of a crystallizable polymer can be formed by cooling a quiescent polymer melt. Spherulites consist of chain folded lamellae radiating outward from a central nucleus (Figure 2.2). The radial dimension of the spherulite increases linearly with time until the spherulite impinges on other growing spherulites. The fibrillar lamellae that compose the spherulite are on the order of 100 Å thick and may be several hundred or even thousands of angstroms in width. Although exact details of its composition are unknown, the nucleus is considered to be a single crystal or fibril, a stack of single crystals or fibrils, or an inhomogeneity such as a dust particle. The spherulite develops from the nucleus through the growth path shown in Figure 2.3. In primary crystallization, the growing entity evolves from the nucleus through sheaf-like structures into the growing spherulite. Growth continues until the spherulite impinges with other growing spherulites, becoming a polyhedron. Secondary crystallization occurs within the spherulite, transforming a portion of the interlamellar material into crystalline material. The fine structure of the spherulite will depend on the nature of branching of the growing radial lamellae and on the form of the crystals between branches. Spherulites have generally been described as radially growing lamellae branching at small angles.

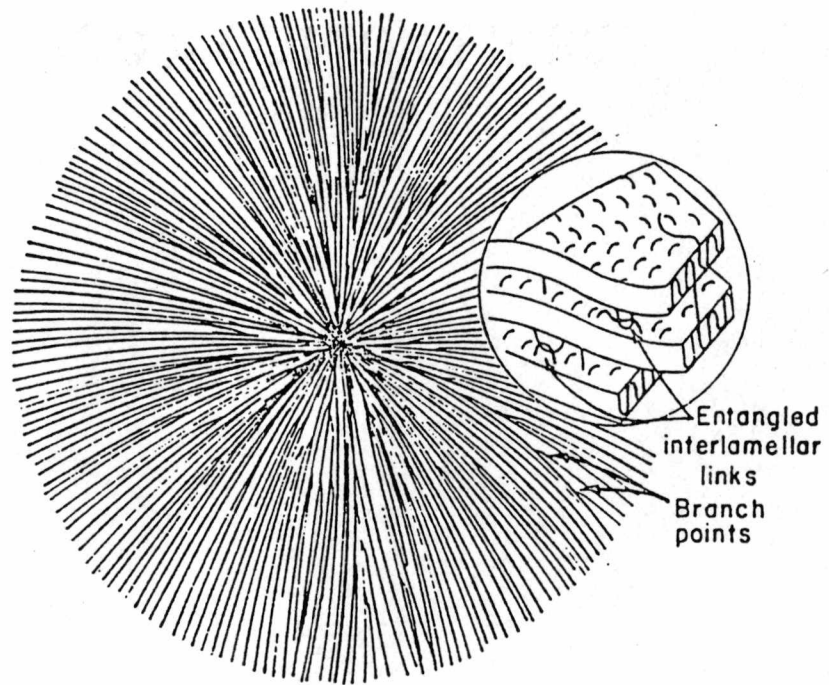


Figure 2.2 Schematic of a polymer spherulite.

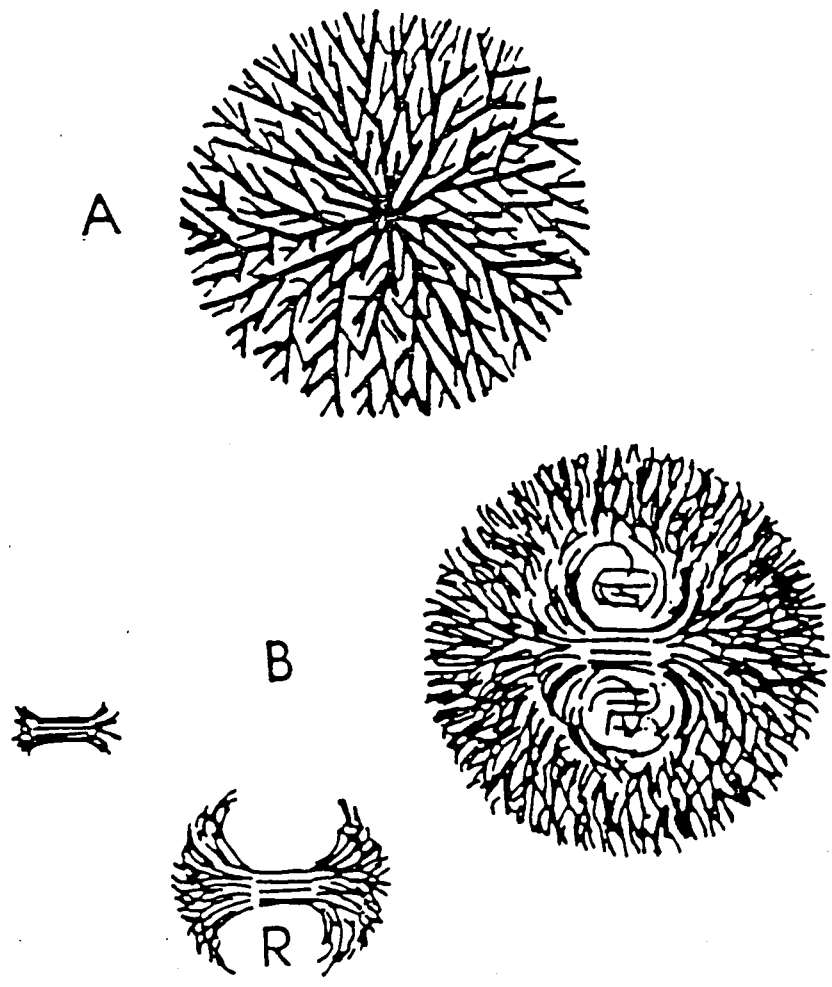


Figure 2.3 Possible polymer growth paths.

Isotactic polypropylene (i-PP) can exhibit at least four distinct crystal structures: the α -form, which is monoclinic and generally predominant; the β -form which is hexagonal; the γ -form which is triclinic; and a "smectic" form believed to be associated with the amorphous phase. The morphology observed in melt crystallized i-PP spherulites was first reported by Padden and Keith [10] who classified the spherulites depending on crystallization temperature, T_c , and the observed birefringence and growth rates. For T_c less than 132°C , i-PP spherulites are of α_I form and exhibit a positive birefringence. For T_c greater than approximately 138°C , the spherulites are of α_{II} -form and exhibit a negative birefringence. However for T_c less than 140°C , the largest number of observed spherulites are 'mixed' in that they possess no distinct Maltese cross and are revealed as radiating arrays of intermingled areas of positive and negative birefringence. The birefringence change of α -form spherulites has been related to a variation of the relative amounts of radial and tangential lamellae inside the spherulites [11]. Thus the low T_c spherulites have high tangential lamella content. At high T_c (145°C) lamellae are nearly all radial and straight for long distances, sometimes the length of a radius. However cross-hatching has been observed as high as 155°C . Radial lamellae are thicker than tangential lamellae.[12] If positive α -form spherulites are

taken near T_m , they turn negative, suggesting that the tangential lamellae melt leaving only the radial lamellae. These phenomena tend to indicate that tangential lamellae crystallize subsequently, possibly due to a segregation effect due to molecular weight or tacticity. The β -form spherulites occur infrequently below $T_c = 132^\circ\text{C}$. The β -form nucleates at a much lower rate than α -form, but grows 20 to 70 percent faster [13]. Table 2.1 lists spherulite types according to Keith and Padden's classification. It has been shown that certain nucleating agents favor β -form crystallization. Quenching of the melt also produces large amounts of β -form [14]. The β -form consists of broad, locally parallel stacked lamellae just as in spherulites of other polymers. The lamellae are extended sheet structures in all dimensions rather than lath-like entities of the α -form spherulites. The γ -form appears in samples crystallized from low molecular weight fractions or crystallized at pressure [15]. The temperature ranges of the spherulite types should not be regarded as rigid values but rather representing trends. The ranges of formation and specific details are influenced by several factors, including molecular weight, molecular weight distribution, and stereoregularity.

Table 2.1. Keith-Padden Classification of Polypropylene Spherulites

Spherulite Type	I	Mixed	II	III	IV
Crystal Structure	α	α	α	β	β
Sign of Birefringence	$+v_e$	$+v_e$	$-v_e$	$-v_e$	$-v_e$
Magnitude of Birefringence	≈ 0.003	≈ 0.002	≈ 0.002	0.007	0.007
Crystallization Temperature	$<134^\circ\text{C}$	134- 138 $^\circ\text{C}$	$>138^\circ\text{C}$	$<122^\circ\text{C}$	126- 132 $^\circ\text{C}$

2.1.3 Axialites

Axialitic crystals can be formed from a polymer melt under certain conditions. High crystallization temperatures favor formation of axialites in certain polymers. Axialites are crystal lamellae grouped so that they resemble two slightly open books placed back to back. Axialites then can exhibit the optical properties of spherulites or single crystals depending on the viewing angle. Tie molecules or crystalline areas between lamellae have been suggested as limiting the splaying of the lamellae [16], but the phenomenon is not really understood.

2.2 Polymer Fold Surface

2.2.1 Fold Surface Nature

The nature of the fold surface of chain-folded polymer crystals is much debated. Various models describing the possible structure of the fold surface have been proposed. The adjacent re-entry model (AR) and the switchboard model (SB) are limiting extremes, represented schematically in Figure 2.4a and 2.4b. The AR model, proposed by Keller [17], involves regular folding with short, uniform folds. The SB model, proposed by Flory [18] has irregular re-entry of the folded chains resulting in random, loose folds.

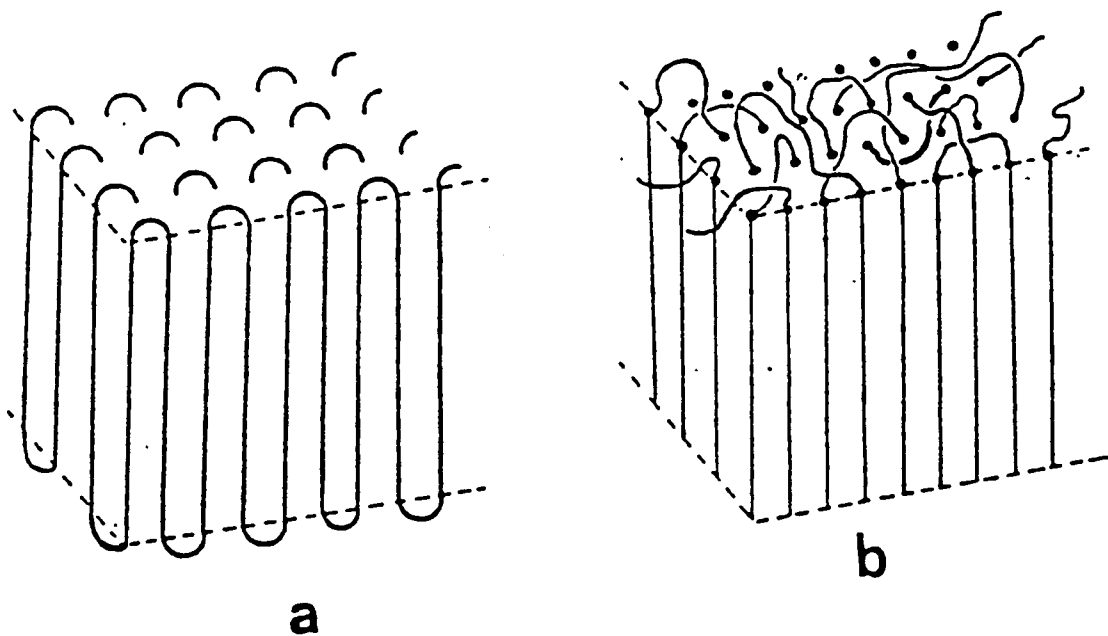


Figure 2.4 Polymer chain folding models: A. adjacent re-entry, B. switchboard.

The fringed-micelle model proposed by Hermann et al. [19] was the first to address polymer crystallization. This model consists of long molecules traversing regions of order (crystalline) and disorder (amorphous). Figure 2.5 is a schematic of the fringed-micelle model. The limited information from x-ray line broadening suggested a small crystal size. The necessity of polymer chains folding on crystallization was identified by Keller [7], Till [20], and Fisher [21]. The experimental evidence from electron microscopy and x-ray diffraction on polyethylene single crystals indicated that the polyethylene molecules lay in the crystals with the chain direction normal to the crystal surface.

In the adjacent re-entry model, the nature of the folds results in a regularly folded surface. The only possible defects are the ends of the molecules which could either form as short length flexible rods above the surface (cilia) or else fold back into the crystal so that a "hole" is created within the crystal. A detailed analysis of infrared spectra of mixtures of deuterated and nondeuterated polyethylenes led Bank and Krimm [22] to conclude that the predominant type of folding involves adjacent re-entry. However the known existence of intercrystalline and interlamellar links show that non-adjacent re-entry must occur to some extent. The probability of adjacent re-entry being less than unity is

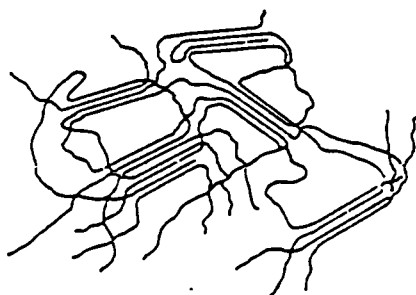


Figure 2.5 Fringed micelle model.

accepted by most researchers that support the adjacent re-entry model. The probability of adjacent re-entry (P_{ar}) = 0.6 to 0.8 is typically claimed, and Hoffman [23] suggested $P_{ar} = 0.3$ to 0.5 is possible under conditions of high molecular weight and large supercoolings.

Various modifications of the adjacent re-entry model exist which include $P_{ar} < 1$. A model based on the "Gambler's Ruin" problem of mathematical statistics [24] predicts the minimum fraction of stems tightly folded in a semicrystalline polymer to be 2/3 for a simple cubic lattice with the stems normal to the surface. Hoffman [4] introduced a "variable cluster model" for crystallization at moderately large supercoolings.

The switchboard model is postulated primarily on the basis of space limitations at the crystal-liquid interface and the density defect nature of single crystals. In this model, while folding of the molecules exists, the molecules re-enter the crystal predominantly in a non-adjacent manner. The resulting fold surface is somewhat irregular with loops of various lengths due to random re-entry, entanglements, etc. Fischer [25] and Mandelkern [26] have proposed similar models. Mandelkern's interzonal model layers an interzonal region between the outermost amorphous region and the innermost crystalline region.

Different crystallization conditions lead to somewhat different macroscopic morphologies, observed directly using optical or electron microscopy. It is reasonable to assume that polymer molecules could have different fold structures dependent on the crystallization conditions. It is then difficult to apply either extreme model to describe the crystal structure as a function of various crystallization conditions. However, in order to obtain a reasonably simple treatment, the assumption of AR is used in most kinetic theories of polymer crystal growth. The various kinetic theories assuming adjacent re-entry or predominant adjacent re-entry have achieved some success in explaining several experimental observations. The theories adequately predict growth rate and lamellar thickness for crystallization both from the melt at low supercoolings and from dilute solution.

2.2.2 Summary Arguments on Fold Surface Structure

Results from density and neutron scattering experiments and arguments based on the mobility of the crystallizing melt question the validity of the models of the polymer fold surface.

Density: The densities measured for polymer single crystals are less than the densities determined from the unit cell dimensions of the polymer. The SB model and the AR model account for the discrepancy in densities with the fold surfaces. The non-adjacent re-entry of the SB model creates

a largely amorphous fold surface. The adjacent re-entry folds in the AR model also create a fold surface with a density lower than the crystal's interior, reducing the overall density of the crystal.

Neutron Scattering: Small angle neutron scattering can be used to determine dimensions and trajectories of isotopically labeled molecules in a host matrix. At very small angles, the radius of gyration of the labeled molecules can be determined in the host. Results on melt grown crystals show that the radius of gyration of the labeled molecules is only slightly smaller after crystallization than it was in the melt. Flory and Yoon [27] claim this small reduction in radius of gyration supports the SB model, arguing that adjacent re-entry would have a larger effect on the radius of gyration. Hoffman [23] states that tie molecules and multiple nucleations on the same molecule result in the observed liquid-like radius of gyration. Hoffman [28] suggests that the radius of gyration is the limiting interlamellar spacing.

Mobility: Yoon and Flory [29] suggest that the rates of molecular disentanglements are sufficiently low to preclude AR folding. DiMarzio et al. [29] contend that reptation of the polymer molecule increases the expected rate of rearrangement such that sequences of AR folds are possible.

2.3 Crystallization Theory

Kinetic theories for polymer crystallization are based mostly on a modification of surface nucleation theory [30,31,32] but other theories exist that are not nucleation controlled [33]. The theory of Hoffman et al. will be reviewed extensively.

2.3.1 Background

Secondary nucleation theory predicts the growth rate and fold period of single crystals from solution and lamellae from the melt as a function of supercooling ΔT . The extent of supercooling determines the kinetic crystallization procedure of the polymer. Lauritzen and Hoffman [34] have developed a kinetic theory for low and moderate supercooling. Regime I (single nucleation) kinetics describe crystallization at low supercoolings while Regime II (multiple nucleation) kinetics describe crystallization at moderate supercoolings. For large supercoolings, a more recent complementary kinetic theory [23,35] added another possible kinetic procedure. Regime III predicts narrowly spaced niches on the growth front.

2.3.2 Model

The idealized schematic model, shown in Figure 2.6, describes polymer lamellar crystal growth. The width, thickness, and height of the surface nucleus are represented

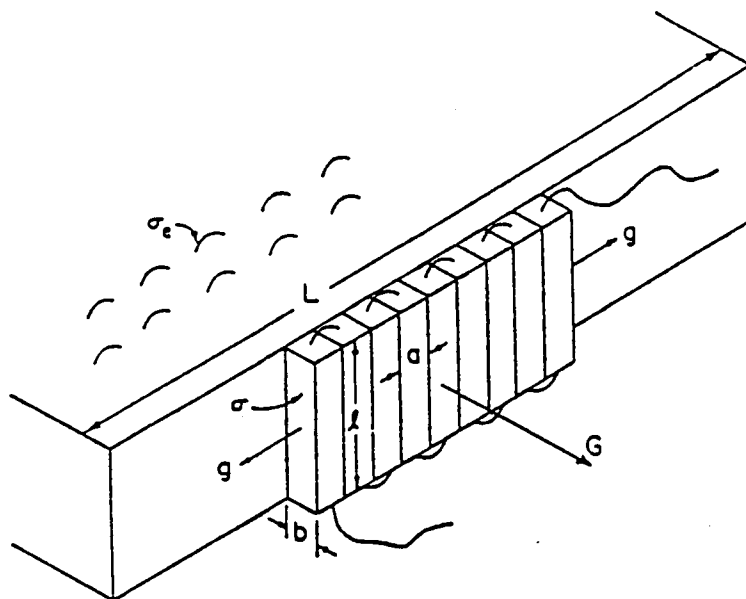


Figure 2.6 Polymer lamellar crystal idealized schematic.

by a , b , and l , respectively. The surface nucleus grows in the g direction, but the measured growth is in the G direction. The surface nucleus is considered to be started by a polymer segment or segments from the supercooled melt attaching to the lamellar surface. The first stem is formed at a cost of $2bl\sigma$. The molecule then folds back on itself in a position adjacent to the first stem. The adjacent position is the most probable position for re-entry after folding since attachment on a nonadjacent position would cost $2ab\sigma_e$ rather than $2bl\sigma$. The surface nucleus, through repeated folding, will approach stability as it grows in the g direction. When v stems and $v_f = v - 1$ folds have been formed, the free energy of formation is (ignoring negligible chain end effects):

$$\phi_v = 2bl\sigma + 2v_f ab\sigma_e - vabl\Delta f \quad (2.1)$$

For large v , the equation becomes:

$$\phi_v = 2bl\sigma + vab(2\sigma_e - l\Delta f) \quad (2.2)$$

The free energy of formation of the surface nucleus goes through a maximum at or near the first stem ($v = 1$) and approaches stability as the surface nucleus increases in size (Figure 2.7). A set of connected rate processes for the

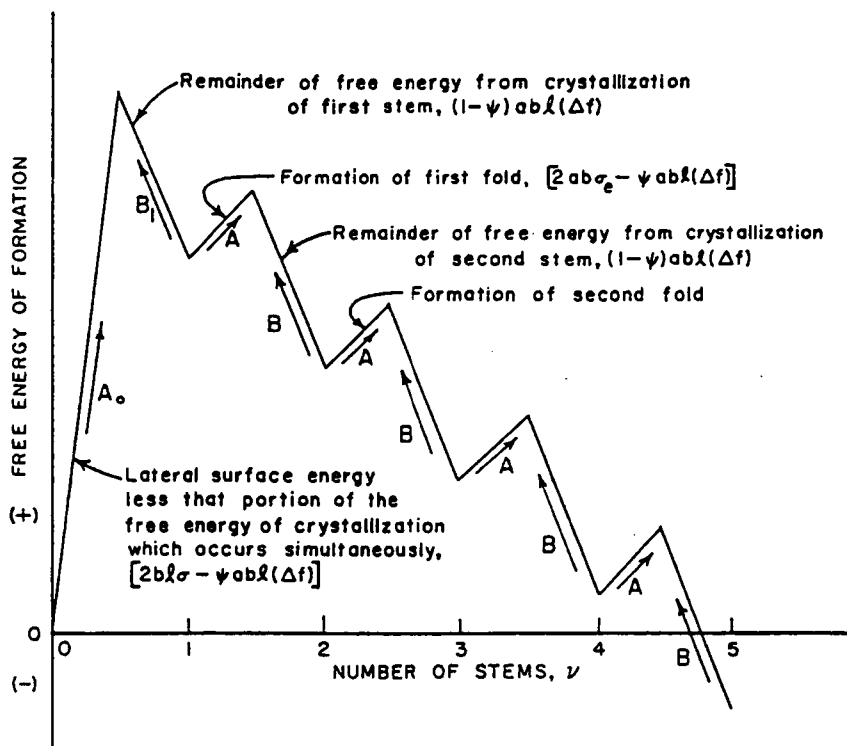


Figure 2.7 Free energy of formation of chain folded surface nucleus.

forward and backward reactions corresponds in general to a nucleation controlled process. In the nucleation controlled process, a large barrier resulting from the creation of new surfaces must be overcome to initiate the nucleus.

2.3.3 Total Flux

The flux S represents the net flow of polymer from sites in the liquid to the first stem of polymer in the nucleus. The first step in the surface nucleation problem is to find the general steady-state expression for S in terms of the rate constants for the forward and reverse reactions and the occupation numbers. In terms of these rate constants and occupation numbers we have

$$S = N_0 A_0 - N_1 B_1 \quad (2.3)$$

where A_0 and B_1 are the rate constants for the forward and reverse reactions and N_0 and N_1 are the occupation numbers for the states $v=0$ and $v=1$.

The rate constants can be expressed as

$$A_0 = \beta \exp\{-(2bl\sigma/kT_c) + [\phi abl(\Delta f)/kT_c]\} \quad (2.4)$$

$$B_1 = \beta \exp\{-(1-\phi)abl(\Delta f)/kT_c\} \quad (2.5)$$

where β is a factor which accounts for retardations to molecular motion for the transport of polymer molecules or

segments to the site of crystallization; ϕ is the fraction of the free energy of fusion to the activation energy of the forward reaction. This apportioning of the free energy attempts to account for the complex intermediate steps by which a segment attaches to the substrate. The value of ϕ may be related to whether or not the segment is physically adsorbed on the substrate surface prior to actual crystallographic attachment. The net rate of formation of nuclei of length l is given by

$$S(l) = bN_0 \exp \{[-2bl\sigma + \phi abl(\Delta f)/kT]\} \quad (2.6)$$

$$\times [1 - \exp\{[-abl(\Delta f) - 2ab\sigma_e]/kT\}]$$

The total flux, S_T , is found by integrating equation (2.6) over all possible values of l , the lower limit of l being set by $2\sigma_e/\Delta f$ and the upper limit infinity.

$$S_T = \frac{1}{l_n} \int_{\frac{2\sigma_e}{\Delta f}}^{\infty} S(l) dl \quad (2.7)$$

$$= N_0 (b/l_n) P \exp(2ab\sigma_e\phi/kT) \exp[-4b\sigma\sigma_e/(\Delta f)kT]$$

where

$$P = \frac{kT}{2b\sigma - ab\Delta f} - \frac{kT}{2b\sigma + (1-\psi)ab\Delta f} \quad (2.8)$$

At low supercoolings the factor $\exp[-4b\sigma\sigma_e/(\Delta f)kT]$ controls S_T . Thus the overall growth rate G will be proportional to this factor at low supercoolings for growth processes that are proportional to the first power of the nucleation rate.

2.3.4 Initial Lamellar Thickness

The initial lamellar thickness l_g^* of a chain-folded lamella, which is kinetically determined, is of the form

$$l_g^* = (2\sigma_e/\Delta f) + \gamma l \quad (2.9)$$

The average value of the lamellar thickness, $\langle l \rangle_{av}$, which can be identified with l_g^* , is calculated from the flux by

$$l_g^* = (1/l_n) \int_{2\sigma_e/\Delta f}^{\infty} l S(l) dl / (1/l_n) \int_{2\sigma_e/\Delta f}^{\infty} S(l) dl \quad (2.10)$$

and this can be expressed as

$$l_g^* = \frac{2\sigma_e}{\Delta f} + \frac{kT}{2b\sigma} \times \frac{[2 + (1-2\psi)a\Delta f]/2\sigma}{(1-a\Delta f\psi/2\sigma)[1+a\Delta f(1-\psi)/2\sigma]} \quad (2.11)$$

The last term is the γl of Equation (2.9), and is a strong function of ϕ .

The behavior of γl at various values of ϕ is interesting. By setting $\phi = 1$,

$$\delta l = \frac{kT}{2b\sigma} \times \frac{(4\sigma/a) - \Delta f}{(2\sigma/a) - \Delta f} \quad (2.12)$$

It can be shown that δl becomes infinite at the critical supercooling ΔT_c given by

$$\Delta T_c = 2\sigma T_m^0 / (\Delta h_f) a \quad (2.13)$$

This is the " δl catastrophe." However, no sharp upswing in l_g^* corresponding to the δl catastrophe is found experimentally.

At $\phi = 0$,

$$\delta l = \frac{kT}{2b\sigma} \times \frac{(4\sigma/a) + \Delta f}{(2\sigma/a) - \Delta f} \quad (2.14)$$

Here there is no " δl catastrophe" and l_g^* decreases continuously with decreasing temperature.

As ϕ is decreased, the value of T_c corresponding to the " δl catastrophe" is lowered. The term $(2\sigma_e/\Delta f)$ is the main contribution to l_g^* near the melting point. As the supercooling is increased, the contribution from $(2\sigma_e/\Delta f)$ decreases and that from δl increases.

In some systems the lamellae can undergo isothermal thickening. This slow and spontaneous increase occurs naturally when the molecular mobility exists in the chain-folded crystal, because a thick crystal is more stable from a thermodynamic viewpoint. The crystal increases its stability by decreasing the area of its high-energy surface by reducing the number of chain folds. This thickening is more rapid near the melting point. At sufficiently low crystallization

temperatures, the lamellae do not thicken appreciably and the expressions for l_g^* may be applied.

2.3.5 Retardation Factor, β

Since the overall growth rate G is a function of the total flux S_T for all regimes and S_T according to equation (2.7) contains the retardation factor, it is necessary to comment on the nature of β . Polymers at high supercoolings become extremely viscous so that the retardations represented by β are the controlling feature of the flux. Thus it is necessary to establish the functional form for β in order to understand growth rate experiments.

For bulk polymeric systems at high supercoolings, the jump rate for local motions can be used for β . This is expressed as

$$\beta = (kT/h)J_1 \exp[-U^*/R(T_c - T_\infty)] \quad (2.15)$$

The factor $\exp[-U^*/R(T_c - T_\infty)]$ represents the temperature dependence of the segmental jump rate in polymers. The factors U^* and T_∞ are derived from bulk viscosity experiments. The activation energy U^* for the transport of segments to the site of crystallization is generally within 10 - 15% of 4100 cal/mole [36]. The temperature T_∞ is a hypothetical temperature where all motion associated with viscous flow ceases and is related to the glass transition

temperature T_g of the polymer. The temperature T_∞ is usually within about 5 - 10 K of being 50 K below T_g . At moderate to high molecular weights where T_g does not vary significantly, neither U^* nor T_g is a strong function of molecular weight. The values of U^* and T_∞ that apply to the crystallization process need not be exactly the same as those that apply to bulk fluidity, because crystallization may occur from an adsorbed layer rather than directly from the bulk amorphous melt ($\phi < 1$). A procedure that assumes an initial set of values of U^* and T_∞ and then linearly fits $\ln G + U^*/R(T_c - T_\infty)$ to $1/T(\Delta T)$ has resulted in a better linear fit for the kinetics data of some polymers. The values U^* and T_∞ are varied separately to maximize the linear fit. This method is similar to that suggested by Suzuki and Kovacs [37] in which the transport parameters are analyzed on the basis of the Williams-Landel-Ferry (WLF) equation.

The J_1 term allows for any barriers not accounted for by the exponential term. Compared to the temperature dependence of the exponential term, that of J_1 is small, so J_1 generally will act as a pre-exponential factor that reduces β .

2.3.6 Free Energy of Fusion

The bulk free energy of fusion, Δf , is the driving force for crystallization in the expression for total flux. The free energy of fusion can be approximated near the melting

point by assuming that Δh_f is independent of temperature so that

$$\Delta f = \Delta h_f - T\Delta S_f = \frac{\Delta h_f - T(\Delta h_f)}{T_m^\circ} \quad (2.16)$$

where Δh_f is the heat of fusion per unit volume of crystal at the equilibrium melting temperature T_m° and ΔT is the supercooling $T_m^\circ - T_c$. Hoffman and Weeks [38] introduced a correction factor f to compensate for any error in the assumption of the temperature independence of Δf . This factor is of the form

$$f = 2T_c / (T_m^\circ + T_c) \quad (2.17)$$

This modifies the Δf Equation (2.16) to give

$$\Delta f = f(\Delta h_f \Delta T / T_m^\circ) \quad (2.18)$$

The factor f is approximately unity at low supercoolings but decreases Δf considerably at high supercoolings to account for the decrease in Δh_f at high supercoolings.

2.3.7 Growth Rates: Regimes I, II, and III

In the three growth regimes the overall growth rate G is a function of the product of the layer thickness and the net nucleation rate $i = S_T / aN_a$ where N_a is Avogadro's number.

The difference in the surface nucleation process at different ranges of supercoolings gives rise to the three different regimes of crystal growth, Regime I, II, and III. The model for each regime is shown schematically in Figure (2.8).

2.3.7.1 Regime I Growth

In the idealized case for Regime I growth, a nucleus is formed on the growing lamellar surface followed by lateral growth on the surface, forming a new layer of thickness b . Thus each surface nucleation act results in the addition of a new surface layer before a second nucleation occurs. In this regime the rate of lateral growth g is much greater than the rate of surface nucleation and the overall growth rate is nucleation controlled. The overall growth rate is given by [39]:

$$G_I = biL = bLS_T/aN_a \quad (2.19)$$

Inserting the net flux, equation (2.6) into equation (2.19) gives

$$G_I = G_{O,I} \exp[-U^*/R(T_c - T_\infty)] \exp[-4b\sigma\sigma_e/(\Delta f)kT] \quad (2.20)$$

where $G_{O,I}$ includes factors not strongly dependent on temperature gathered into pre-exponential form. Then $G_{O,I}$ is given by

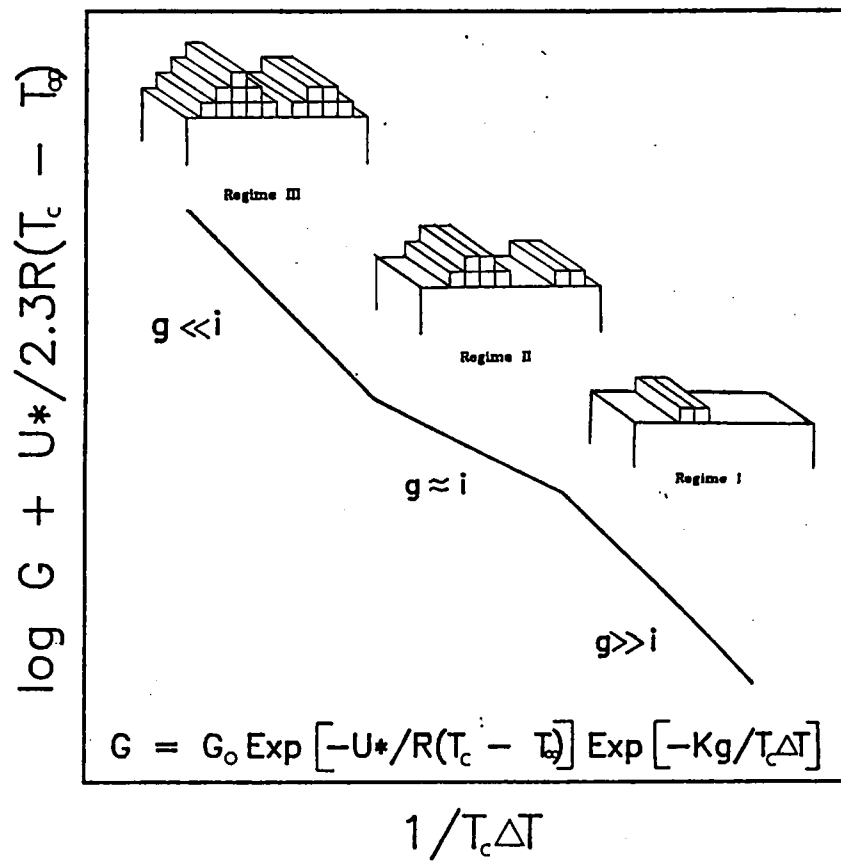


Figure 2.8 Lauritzen-Hoffman crystallization regimes schematic.

$$G_{O,I} = b(kT/h)n_s J_1 \exp(2ab\sigma_e \phi/kT) \quad (2.21)$$

where n_s is the number of sites or steps corresponding to the length of the surface, i.e. L/a .

2.3.7.2 Regime II Growth

In Regime II growth, many new surface nuclei form before the previous layer is complete. Sanchez and Dimarzio [40] indicated that the overall growth rate is proportional to the square root of the surface nucleation rate. The overall growth rate is then

$$G_{II} = b(ig)^{1/2} = b(S_T g/aN_a)^{1/2} \quad (2.22)$$

Inserting the net flux into equation (2.22) gives

$$G_{II} = G_{O,II} \exp[-U^*/R(T_c - T_\infty)] \exp[-2b\sigma\sigma_e/(\Delta f)kT] \quad (2.23)$$

where

$$G_{O,II} = b(kT/h)J_1 \exp[ab\sigma_e(2\phi - 1)/kT] \quad (2.24)$$

The ratio of the G_O values for Regimes I and II is

$$G_{O,I}/G_{O,II} = n_s \exp(ab\sigma_e/kT) \quad (2.25)$$

It is clear that $G_{O,I} \gg G_{O,II}$ for a given polymer. Regime II crystallization leads to a rough growth front on a molecular scale.

2.3.7.3 Regime III Growth

In Regime III, the rate of surface nucleation is much greater than the rate of substrate completion and nuclei form on partially grown strips. The effective substrate length is restricted by the abundance of niches so that the crystallization is accomplished by nucleation of stems on the surface [3] as is Regime I. The overall growth rate is then expected to be proportional to the nucleation rate and is given by

$$G_{III} = biL' = bin_s'a = bLS_T/aN_a \quad (2.26)$$

where $L' = n_s'a$ is an "effective" substrate length; n_s' is the mean number of stems laid down in the niche adjacent to the newly nucleated stem. The quantity n_s' is generally taken to be between 2 and 4 and independent of the overall substrate length L . Substituting the flux into Equation (2.25) gives

$$G_{III} = G_{O,III} \exp[-U^*/R(T_c - T_\infty)] \exp[-4b\sigma\sigma_e/(\Delta f)kT] \quad (2.27)$$

where

$$G_{O,III} = b(kT/h)n_s'J_1 \exp(2ab\sigma_e\phi/kT) \quad (2.28)$$

The Regime I and Regime III overall growth rate equations differ only in their pre-exponential factors such that

$$G_{O,I}/G_{O,III} = n_s/n_s' \approx n_s/3 \quad (2.29)$$

2.3.8 Regime Test

A general form for the growth rate equation for the three regimes is given by

$$G = G_o \exp[-U^*/R(T_c - T_\infty)] \exp[-K_g/T\Delta T f] \quad (2.30)$$

where for Regimes I and III

$$K_{g(I)}, K_{g(III)} = 4b\sigma\sigma_e T_m^0 (\Delta h_f) k \quad (2.31)$$

A plot of $\log G + U^*/R(T_c - T_\infty)$ versus $1/T(\Delta T)f$ will have the same slopes for Regimes I and III, which is twice that of Regime II (see Figure 8).

Lauritzen [41] introduced the dimensionless parameter Z to estimate whether crystallization in a given polymer is in Regime I or Regime II. Z is given by

$$Z = iL^2/4g \quad (2.32)$$

If $Z < 0.01$, strict adherence to Regime I behavior is expected and $K_g = 4b\sigma\sigma_e T_m^0 / (\Delta h_f)k$. If $Z = 0.1$, Regime I behavior is approximated. When $Z > 1$, Regime II behavior is expected and $K_g = 2b\sigma\sigma_e T_m^0 / (\Delta h_f)k$. Overall growth rate data is used to evaluate K_g . Using the measured value of K_g , a range of values for L that are consistent with Regime I or Regime II behavior is estimated. The estimated values for L frequently are reasonable for one regime but completely unrealistic for the other. The value of L must be in accord with morphological information. A model for the physical origin of the substrate length L is proposed by Hoffman [42]. L is treated as the persistence length between defects which have a capacity to inhibit surface completion.

2.3.9 Limitations of Secondary Nucleation Theory

2.3.9.1 Adjacent Re-entry

Surface nucleation theories assume chain folding with adjacent re-entry in order to make the model tractable. The probability of adjacent re-entry is normally expected to be less than one, and a modified, predominantly adjacent re-entry model has been used by many authors. The probability of non-adjacent re-entry of Gaussian chains can reach a maximum of $1/3$ as shown by Guttman et al. [43] using the mathematical "Gambler's Ruin" method. In addition,

Lauritzen-Hoffman secondary nucleation theory assumes nucleation from a chain end only.

Since secondary nucleation theory assumes regular adjacent re-entry and a large number of folds (at least five), polymer crystallization with fully extended chains or very few folds cannot be well explained. Point and Kovacs [44] claimed that secondary nucleation theory breaks down for the case of extended chain crystals of low molecular weight poly(ethylene oxide) because it results in σ values that are chain length dependent.

2.3.9.2 Constant Fold Period

In secondary nucleation theory, a fold plane once nucleated will grow with a constant fold period. The length of the first stem, which is a function of ΔT and ϕ , determines this fold period. Direct observations of the lamellar thickness of polyethylene by electron microscopy have shown that constant lamellar thickness is questionable. Several authors have addressed this problem [34,45]. The theory of Lauritzen and Passaglia accounts for all possible fold periods but fails to eliminate the " δl catastrophe". The δl catastrophe in Lauritzen-Hoffman secondary nucleation theory is a direct result of the imposed integration limits. Recent work suggests that the fold period is constant prior to thickening in several polymers.

2.4 Melting of Polymer Crystals

The melting temperature of a lamellar polymer crystal is controlled by several factors, including the lamellar thickness, the surface free energies, lattice imperfections, internal stress field, etc. Lamellar thickness and surface free energies are dominant factors while lattice imperfections and internal stress fields are often neglected for simplicity. It is important to derive an expression for melting point in terms of lamellar thickness and surface free energies.

2.4.1 Thermodynamic Considerations

The free energy of formation of a single lamellar polymer crystal as shown in Figure 2.6 may be written as [46]

$$\Delta\phi = 2(a+b)l\sigma + 2ab\sigma_e - abl\Delta f \quad (2.33)$$

where a and b are the lateral dimensions, l the thickness, σ and σ_e are the lateral and fold surface free energies respectively, and Δf is the bulk free energy of fusion. Since $a \ll l$ and $b \ll l$, the first term in Equation (2.33) is much smaller than the second and third terms and may be neglected. At the crystal's melting temperature T_m , $\Delta\phi = 0$. Substituting $\Delta\phi = 0$ and $\Delta f = \Delta h_f \Delta T / T_m^0$ into Equation (2.33), one obtains

$$T_m = T_m^{\circ}(1 - 2\sigma_e/\Delta h_f l) \quad (2.34)$$

where Δh_f is the heat of fusion per unit volume of crystal. Thus the observed melting point for a thin crystal is depressed below that of an infinite crystal (T_m°) by the amount $2\sigma_e/\Delta h_f l$. A plot of T_m versus $1/l$ must be linear with intercept T_m° and σ_e determined from the slope.

2.4.2 Kinetic Considerations

Secondary nucleation theory predicts the initial lamellar thickness lg^* according to Equation (2.11). Due to isothermal thickening, the measured l is larger than lg^* . The average lamellar thickness at the end of crystallization can be expressed as [39]

$$l = \gamma lg^* \quad (2.35)$$

where γ , the thickening factor, has a value greater than one. Combining this with Equation (2.9) and substituting for Δf from Equation 2.18 leads to

$$l = \frac{2\sigma_e T_m^{\circ} \gamma}{\Delta h_f \Delta T} + \gamma \delta l \quad (2.36)$$

Equation (2.36) relates l to the supercooling, thus relating l to T_c . Substituting Equation 2.36 into Equation 2.34 gives

$$T_m = T_m^0 - (\Delta T/\gamma) (1 + K\Delta T)^{-1} \quad (2.37)$$

where $K = \Delta h_f \gamma l / 2\sigma_e T_m^0$. Hoffman et al. [51] assumed $2\sigma_e/\Delta f \gg \gamma l$, thus $K\Delta T \approx 0$ and then

$$T_m = T_m^0 - \Delta T/\gamma \quad (2.38)$$

This is a fairly good approximation for crystals formed at low supercoolings. Equation (2.38) may be written in terms of T_m and T_c to give

$$T_m' = T_m^0(1 - 1/\gamma) - T_c/\gamma \quad (2.39)$$

where T_m' is the melting temperature subject to the assumption $K\Delta T \approx 0$. Equation (2.39) suggests that the melting temperature of a polymer that has thickened by a factor γ during crystallization at T_c is a linear function of T_c .

However, $K\Delta T \approx 0$ is not always a good approximation, leading to curvature in a plot of the actual melting temperature T_m versus T_c . In some cases there is an upward curvature in T_m versus T_c data due to an increase in γ at higher temperatures. Since typically $K\Delta T \ll 1$, a binomial series expansion of Equation (2.37) gives

$$T_m = T_m^{\circ} - (\Delta T/\gamma) [1 - (K\Delta T) + (K\Delta T)^2] \quad (2.40)$$

Rearranging Equation (2.40) and combining with Equation 2.39 leads to

$$T_m' = T_m - (\Delta T/\gamma) [(K\Delta T) - (K\Delta T)^2] \quad (2.41)$$

The initial values of γ and T_m° are estimated from a T_m versus T_c plot and by an iterative method relatively accurate final values for γ and T_m° are obtained and thus values of T_m' obtained.

2.5 The Effects of Pressure

Hydrostatic pressure is known to affect the crystallization and physical properties of polymers. The glass transition temperature T_g and the melting temperature T_m are two important parameters for kinetics analysis at high pressures as well as at atmospheric pressure. Some experimental observations and theoretical treatments for morphology, crystallization, glass transition temperature, and melting temperature are briefly discussed in this section.

2.5.1 Morphology

The effects of pressure on the morphology of several polymers have been studied. For polyethylene at sufficiently

high pressures, extended chain lamellae of increasing thickness become dominant. Geil et al. [47] reported the morphology of polyethylene samples which were melt crystallized under pressure. These samples showed little or no folding. Wunderlich and Arakawa [48] reported that two different types of crystals form in high density polyethylene, depending on temperature and pressure. A new hexagonal liquid crystalline high pressure phase for polyethylene was reported by Bassett and Turner [49]. At high pressures polyethylene passes through a hexagonal intermediate phase [50] and this phase is responsible for chain extension occurring. Tseng and Phillips [51] reported banded spherulites for LPE below 350 MPa hydrostatic pressure and extended chain spherulites above 350 MPa.

For cis-polyisoprene at pressures up to 300 MPa, three morphologies existed. These were single crystals, spherulites, and oblate spheroids [52]. Chain-extended lamellae have not been observed in cis-polyisoprene.

The γ -form of isotactic polypropylene has been observed in samples isothermally crystallized and slow cooled from the melt at pressures above 32.4 MPa [53], but its morphology has not been characterized. As the pressure is increased, a larger proportion of the sample crystallizes in the γ -form until at 506.6 MPa only the γ -form is present.

2.5.2 Crystallization Kinetics

There have been relatively few studies of the effect of pressure on the crystallization kinetics of polymer systems. Phillips and Edwards [54] obtained linear growth rate data for cis-polyisoprene for pressures ranging from atmospheric to 400 MPa. The bell-shaped growth rate curves shift to higher temperatures with the application of pressure. An increase in the maximum growth rate is observed over the first 140 MPa of applied pressure. A large and sudden increase in fold surface free energy (σ_e) with increased pressure is attributed to a pressure-induced change in fold conformation.

Trans-polyisoprene exhibited a decrease in the maximum growth rate with an increase in pressure [55]. The decrease in maximum growth rate is attributed to a decrease with pressure of the temperature range ($T_m - T_\infty$) available for crystallization.

Tseng and Phillips investigated the pressure effects on the growth rate kinetics of linear polyethylene (LPE) and polyethylene terephthalate (PET). For PET, analysis of the growth rate data in terms of secondary nucleation theory yielded a possible Regime II-III transition. Fold surface free energy was found to increase dramatically with pressure. This is possibly due to the increase of non-adjacent re-entry and significant amount of loose folds. For LPE, the σ_e was

independent of pressure up to 200 MPa, implying that the structure of the fold surface does not change. The pressure dependence of the Regime I-II transition in LPE paralleled the pressure dependence of T_m^0 , indicating that the transition is thermodynamic.

2.5.3 Melting Response

As the pressure increases, the melting temperature usually increases. The Clausius-Clapeyron equation gives a quantitative expression for (dT/dP) from thermodynamic considerations as the following:

$$(dT/dP)_{eq} = \Delta H/T\Delta V \quad (2.42)$$

where ΔH and ΔV are the changes in enthalpy and volume respectively. The Clausius-Clapeyron equation can be written as

$$(dT_m/dP) = T_m\Delta V/\Delta H \quad (2.43)$$

Baer and Kardos [56] have studied the effect of pressure on the melting response for various polymers. They noted that the melting temperature and range of melting increased with increasing pressure for all polymers studied. The effect of pressure on the melting temperature of several polyamides [57] and trans-polyisoprene [58] have been reported. A linear increase in melting temperature with applied pressure

is observed which is 16°C per 100 MPa for nylon-6 and 15°C per 100 MPa for trans-polyisoprene.

The Clausius-Clapeyron equation can be written to express the equilibrium melting temperature at pressure as a function of the equilibrium melting temperature at atmospheric pressure. This is given by

$$(T_m^0)_P = (T_m^0)_{1 \text{ atm}} \exp[\Delta V/\Delta h_f(P - 1)] \quad (2.44)$$

where $\Delta V = V_a - V_c$; V_a and V_c are the specific volumes of amorphous and crystalline material and P is the pressure in atmospheres. According to Equation 2.44, T_m^0 is a steep function of pressure. Dalal [59] obtained equilibrium melting temperatures at pressures up to 260 MPa for cis-polyisoprene. Melting temperature data at pressure was obtained with an optical turbidimetric technique. The plots of crystallization temperature versus melting temperature were linear and shifted to higher temperatures with increasing pressure.

2.5.4 Glass Transition Temperature

The glass transition temperature increases approximately linearly with pressure. Since Fox and Flory [60] proposed that the free volume remains constant in the glassy state, free volume theories predict the change of the glass transition temperature with pressure (dT_g/dP) to be given by

$$dT_g/dP = \beta_f/\alpha_f \approx \Delta\beta/\Delta\alpha \quad (2.45)$$

where β_f and α_f are the free volume compressibility and expansion coefficient, respectively, and $\Delta\beta$ and $\Delta\alpha$ are the differences between the liquid and glass compressibilities and expansion coefficients, respectively.

The glass transition is assumed to be a true second-order transition with equilibrium properties by thermodynamic theories [61]. Then the variation of a second-order transition is given by the Ehrenfest relation

$$dT_2/dP = \Delta\beta/\Delta\alpha = (TV\Delta\alpha)/\Delta C_p \quad (2.46)$$

where ΔC_p is the difference in heat capacities between the glass and the liquid at the transition.

O'Reilly [62] has tabulated the empirical values of dT_g/dP for several polymers, with most of the values around $20^\circ - 24^\circ$ per 100 MPa of pressure. Mizoguchi and Ishikawa [63] have derived an expression for dT_g/dP based on Eyring's modified hole theory. The calculated results from this theory are in better agreement with experimental data than those obtained from free volume theory $\Delta\beta/\Delta\alpha$.

2.6 Molecular Weight Effects

Molecular weight and molecular weight distribution affect the rate of polymer crystallization, degree of crystallinity, and the observed melting temperature. The effect of molecular weight on a number of polymer systems has been studied. Poly(phenyl-p-silphenylene)siloxane (TMPS) [64] growth kinetics were studied at different crystallization temperatures as a function of molecular weight. Linear growth rate increased with decreasing molecular weight. However, the crystallization temperature of the maximum in the growth rate curves did not change for the different molecular weight fractions. Magill reported that the pre-exponential term G_0 increased with decreasing molecular weight in the molecular weight range 8,000 - 430,000.

Mandelkern et al. [65] analyzed polyethylene fractions data and determined that the interfacial free energy σ_e increased with increasing molecular weight. They suggested the change in σ_e with molecular weight indicated a change in the interfacial structure. Fatou and Mandelkern [66] reported an asymptotic value of 138.5°C for the melting temperature in a study of the effect of molecular weight on melting for polyethylene fractions. Ergoz et al. [67] found that for polyethylene the crystallization rate at fixed supercooling goes through a maximum as a function of

molecular weight. They also showed that the maximum degree of crystallinity decreased as molecular weight increased. Hoffman et al. [68] observed two morphologies in polyethylene fractions. For fractions with molecular weight higher than 115,000, only spherulitic morphology was observed. For low molecular weight fractions (3,600 to 18,000) only axialitic growth was observed. For intermediate molecular weight fractions (18,000 to 115,000) spherulites were found at large supercooling ($\Delta T > 18^\circ$) but at low supercoolings, axialites were found. The transition occurred around 127°C ($\Delta T = 18^\circ$). The change in morphology is attributed to a change in growth mechanism, with the high supercoolings associated with Regime II and the low supercooling associated with Regime I. The Regime I-II transition temperature was found to be molecular weight dependent. The transition temperature increased as the molecular weight increased in the range 18,000 to 115,000.

Allen [69] observed a noticeable molecular weight effect on linear growth rate in isotactic polypropylene in the molecular weight range 52,000 to 520,000. Unlike polyethylene, a maximum in the growth rate as a function of molecular weight occurs at fairly high supercoolings. At high supercoolings, the growth rates are relatively invariant with molecular weight.

The reptation concept proposed by de Gennes [70] suggests that under appropriate conditions, the overall friction coefficient of a linear polymer chain in the liquid state is proportional to its length. Recently Hoffman [30] has tested the reptation concept for the case of crystallization of polyethylene from the melt. The inclusion of the reptation concept in the kinetic nucleation theory allows the molecular weight dependence of the growth rate to be obtained.

2.7 Polymerization

Isotactic polypropylene (iPP) was first made by Natta [71] in Italy using modified Ziegler-type initiators. This initiator system, referred to as Ziegler-Natta or coordination initiators, consists of an organometallic compound of a Group I-III metal with a halide or other derivative of a Group IV-VIII transition metal. The polymerizations are carried out in hydrocarbon solvents. A typical conventional coordination initiator system for the polymerization of propene to iPP is titanium trichloride (TiCl_3), the transition metal component, and diethylaluminum chloride [$(\text{C}_2\text{H}_5)_2\text{AlCl}$], the Group I-III metal component. The initiator system performs two functions. First, the system supplies the species which initiates the polymerization. Second, the initiator complex coordinates the propagating chain end and the incoming monomer so as to orient the

monomer with respect to the growing chain end to induce stereospecific addition. Recently process improvements and initiator system improvements have greatly improved the isotactic polypropylene produced. The new processes have broadened the applicability of iPP. The polymerization of iPP can be controlled to improve the properties for specific applications. The coordination initiator systems now yield as much as forty times the amount of polymer per unit of initiator than commercial systems of the early 1980's. The initiator systems are also more selective. The iPP has higher stereoregularity compared to the iPP produced by conventional systems. This improves the properties and eliminates a post-reactor step normally required to remove the atactic polypropylene.

2.8 Polymer Molecular Weights

Polymers are mixtures of various components. Linear polymers are mixtures of various chain lengths or molecular weights. Stereoregular polymers, such as polypropylene, are mixtures of lengths and numbers of d and l units as well as chain lengths. Branched polymers are polydisperse with respect to chain length and chain structure. Different experimental techniques to determine polymer molecular weights measure different kinds of average molecular weights. The most important kinds of molecular weight averages in

polymers are the number average, the weight average, the z and the $(z + 1)$ average, and the viscosity average.

The number average molecular weight, M_n , is usually measured with membrane osmometry or vapor-phase osmometry and is expressed by the following:

$$M_n = \frac{\sum_i n_i (M_i)}{\sum_i n_i} \quad (2.48)$$

where N_i is the number of molecules with weight M_i .

The weight average molecular weight, M_w , is measured with quasielastic light scattering and is expressed by the following:

$$M_w = \frac{\sum_i m_i (M_i)^2}{\sum_i m_i} \quad (2.49)$$

The z average average molecular weight is

$$M_z = \frac{\sum_i z_i (M_i)^3}{\sum_i z_i} \quad (2.50)$$

The z and $(z + 1)$ averages as well as the number and weight averages can be determined with a calibrated size exclusion chromatography system.

The viscosity average molecular weight, M_η , is

$$M_\eta = \left(\sum_i w_i M_i^{a_\eta} \right)^{1/a_\eta} \quad (2.51)$$

where a is the exponent of the molecular weight in the Mark-Houwink-Sakurada intrinsic viscosity $[\eta]$ versus molecular weight relation

$$[\eta] = KM^a \quad (2.52)$$

The weight average molecular weight is always greater than or equal to the number average molecular weight while the viscosity average molecular weight is between the number average and the weight average. The ratio M_w/M_n is often used as a measure of the polydispersity of a polymer sample. If a polymer is monodisperse, this ratio is unity. As the ratio increases, the polydispersity increases. At a fixed value of M_w/M_n there are an infinite number of different molecular weight distributions possible.

2.9 Tacticity Analysis

For polypropylene, the stereoregularity is dependent on the catalyst system that is used to synthesize the polymer. While changes in the catalyst systems have significantly increased the stereoregularity of iPP, the polymer still contains some syndiotactic placements. It is desirable to describe the monomer sequences or sequence distributions for each chain length. Average polymer structural information can be determined using either infrared (IR), ultraviolet (UV), or nuclear magnetic resonance (NMR) techniques.

However, presently only NMR is capable of determining average sequence distributions and number-average sequence lengths.

2.9.1 Tacticity from IR Spectroscopy

The IR spectra of iPP of different tacticities have been investigated by several authors . The conformational ordering has a strong influence on the mIR spectra as shown in Figure 2.9 . Polarized IR studies of uniaxially drawn PP have been essential to the analysis. Wave number assignments for the absorption maxima for iPP and sPP have been obtained by calculation and comparison with the spectra of deuterated PP samples. This information allows characterization of average polymer structure but not sequence distributions and sequence length, which require NMR.

2.9.2 Tacticity from NMR Spectroscopy

Both proton (^1H) and carbon 13 (^{13}C) NMR have been successfully used for tacticity analysis of polymers. An NMR spectrum represents directly the average polymer molecule. The characterization of tacticity from NMR involves three quantitative measurements [72]:

a) distributions of configurations of successive units such as dyads, triads, tetrads, etc.

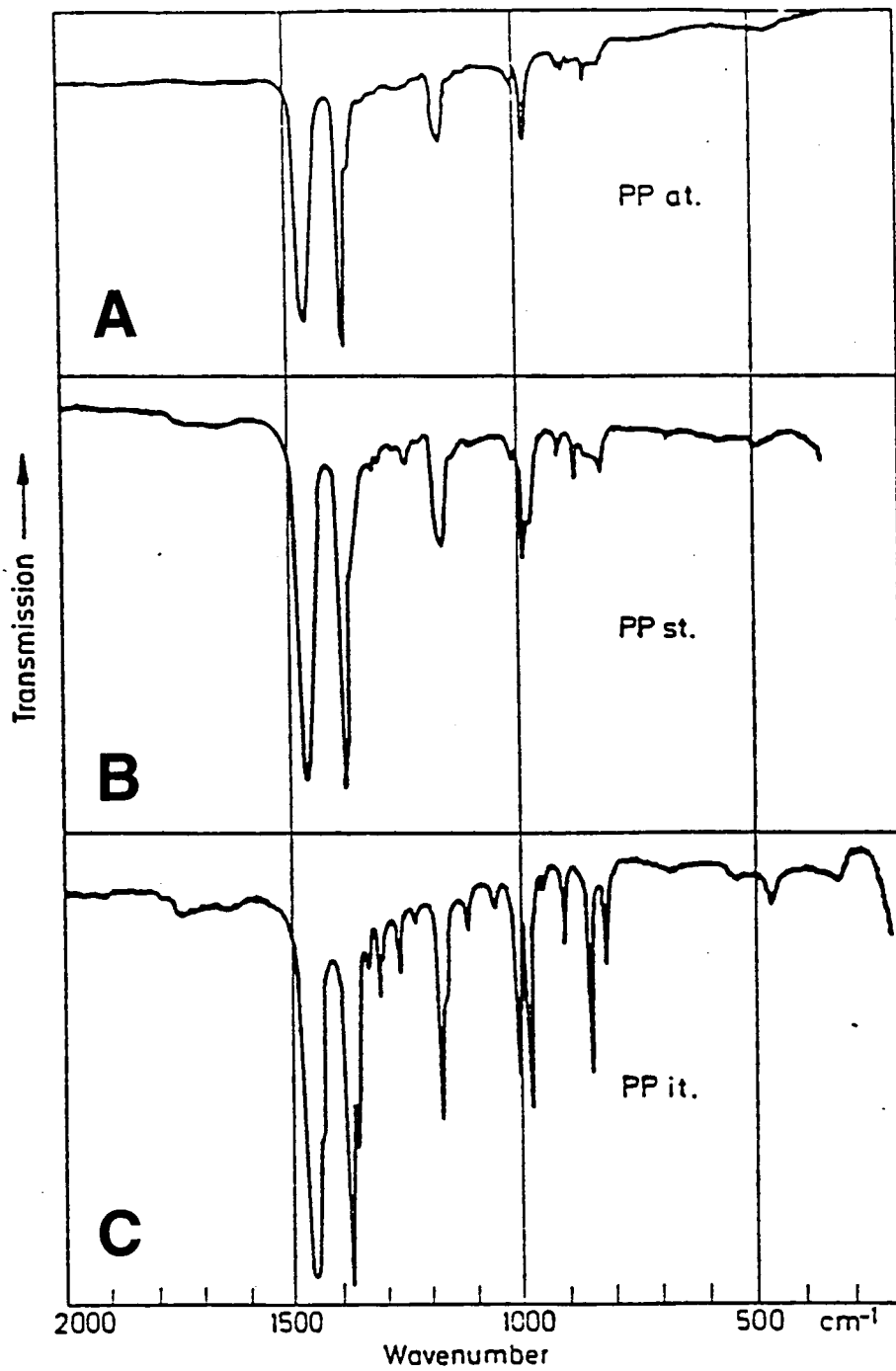


Figure 2.9 Infrared spectra of stereoregular forms of polypropylene: A. atactic, B. syndiotactic, C. isotactic.

b) number-average sequence length of like configurations.

c) number-average sequence lengths of meso and racemic dyads

where meso applies to adjacent monomer pairs with the same configuration while the opposite configuration is called racemic.

Chapter 3

Experimental and Analytical Techniques

3.1 Materials

Isotactic polypropylene was used in the experiments. Bulk isotactic polypropylenes having different molecular weights but similar molecular weight distributions was studied. Narrow molecular weight fractions of isotactic polypropylene obtained by temperature rising elution fractionation and fractional precipitation were studied. Table 3.1 lists the data for the various polypropylenes. The bulk samples were characterized in two forms: as received and extracted with hexane to remove atactic chains and any additives.

3.2 Bulk Crystallization

Equipment - Atmospheric Pressure

The bulk crystallization of iPP was followed by observation of the change in depolarized light intensity as a function of time. The experimental equipment consisted of either a Mettler FP52 or FP82 hot stage with Mettler FP5 or FP80 temperature control unit, Olympus BH-2 or Reichert Neovar-Pol transmission optical microscope, silicon diode photocell with photometric filter and cosine diffuser, United

Table 3.1. Characteristics of Polypropylene Materials

Sample	Resin Type	Melt Index	M _n	M _w	M _z	M _w /M _n
PP1	Homopolymer	35	58	150	287	2.58
PP4	Homopolymer	1400	27	82	159	3.00
PP5	Copolymer (0.5% ethylene)	34	58	148	266	2.55

Detector Technology Model 61 photometer, and a Houston Instruments OmniScribe chart recorder.

Equipment - Elevated Pressure

The crystallization of iPP at elevated pressures was carried out with the equipment shown in Figure 3.1. This equipment was divided into three sections: the pressure generating system, the temperature control system, and the detection/recording system.

The pressure generating system consists of a High Pressure Equipment Company screw driven hydraulic ram Model 37-5.75-60. The pressure was transmitted to the crystallization cell through high pressure tubing and measured on a Bourdon-type gauge. The system was filled with phosphate ester hydraulic fluid from the hydraulic reservoir under nitrogen gas pressure.

The temperature control system consisted of a Mettler FP5 control unit, an interfacing power amplifier, and a Haake D8L circulating temperature bath. The bath circulated silicon fluid through a heat exchanger on the high pressure cell by Fluran high temperature tubing. The flow rate was controlled with a valve on the bath.

The detection and recording system consisted of a Reichert Neovar-Pol polarized optical transmission microscope

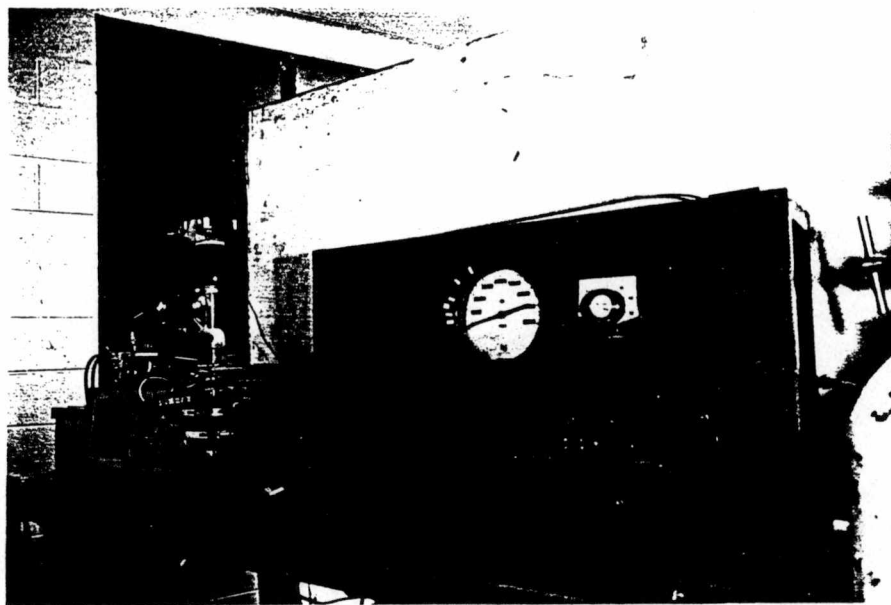
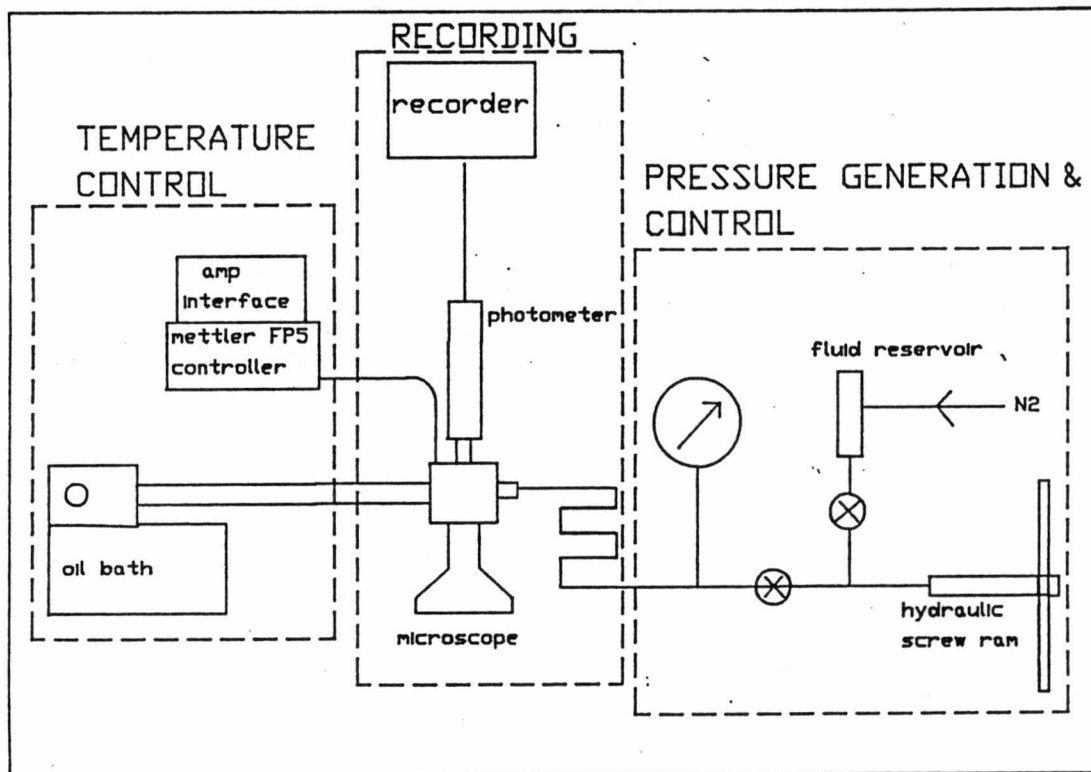


Figure 3.1 Elevated pressure system schematic and photograph.

modified to accept the high pressure cell, a Canon AE-1 35mm camera, and a filar micrometer eyepiece.

High Pressure Cell and Heat Exchanger

The high pressure cell is shown in Figure 3.2. The cell body and the upper and lower screw plugs was made of steel heat treated to a hardness of 55 Rockwell C.

The sample was held between two polished sapphire crystals which are then inserted into a machined brass tube. A third sapphire, sealing the other end of the cell, was held in place with a light helical spring to provide the low pressure seal. The screw plugs were sealed with o-rings backed by steel anti-extrusion rings and forced into place by brass spacers. A nonrotating washer on the lower screw plug prevented disturbing the anisotropic sapphire crystals. Four close-fitting grooves cut into the cell body mated with four tabs on the washer to prevent rotation. Hydraulic fluid was pumped into the cell through the inlet port.

A heat exchanger, Figure 3.3, surrounding the cell was used to heat and cool the cell. Insulation on the upper and lower surfaces and surrounding the sides of the heat exchanger reduced the heat loss from the heat exchanger. The heat exchanger consisted of two coaxial cylindrical pieces with the clearance between them sealed by o-rings. Silicone heating fluid circulated through the annular space. Three

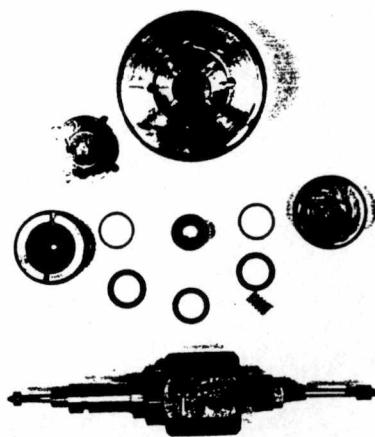
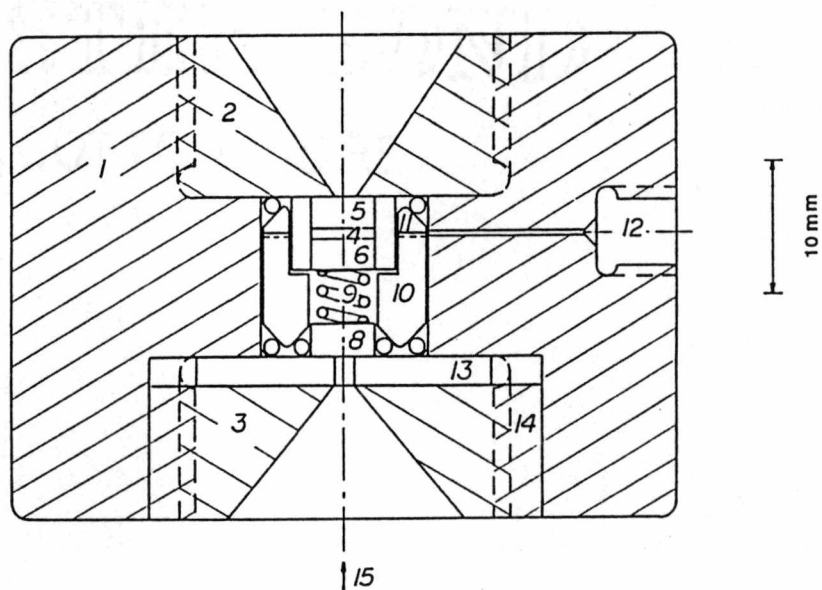


Figure 3.2 Elevated pressure cell schematic and photograph.

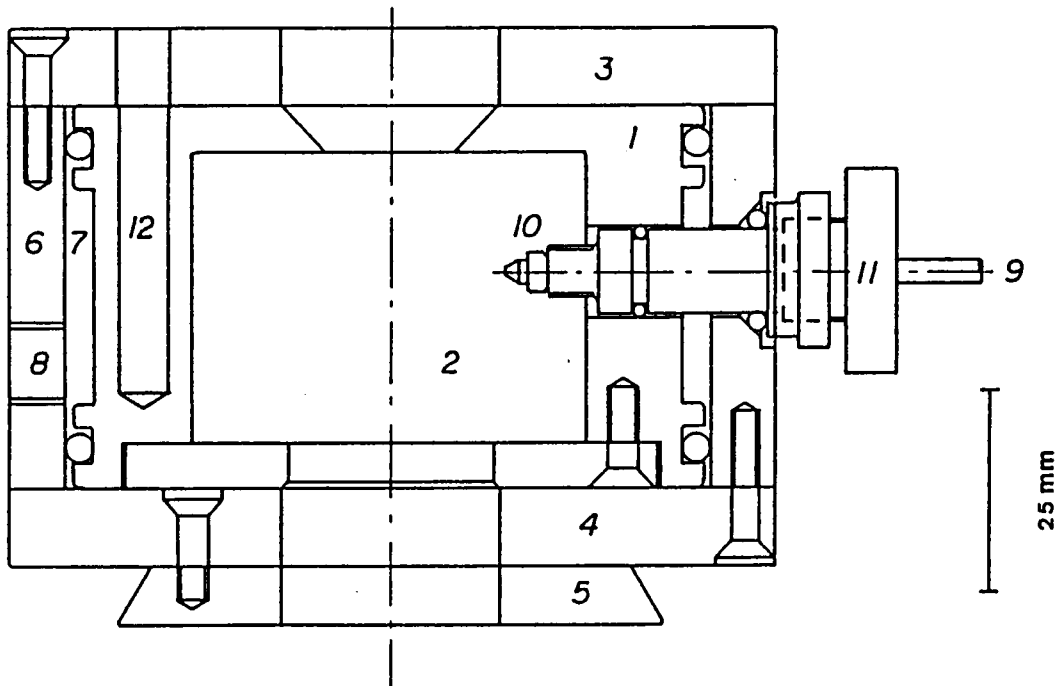


Figure 3.3 Elevated pressure system heat exchanger schematic.

100 W cartridge heaters heated the cell to the appropriate melting temperature while the circulating fluid, held at a temperature lower than the desired crystallization temperature, cooled the cell down to the crystallization temperature after melting the sample. An RTD probe, matched to the Mettler FP5, provided feedback for temperature control and a thermocouple provides a sample temperature readout.

Temperature Control

Isothermal crystallization requires a stable constant temperature over considerable lengths of time. Melting temperature determination requires a constant scanning rate. The Mettler FP5 control unit was chosen to satisfy the two temperature control requirements. The Mettler FP5 has a temperature range of -20°C to $+300^{\circ}\text{C}$ with a resolution of 0.1°C and an accuracy of 0.2°C . The Mettler FP5 was designed to control the temperature of a small microscope slide. This required much less power than the massive high pressure cell. An interfacing power amplifier, built by Dalal [59] was used to increase the power output sufficiently to heat the high pressure cell. The amplifier design allowed the Mettler FP5 to control the high pressure cell temperature.

Experimental Procedure

Atmospheric

Discs were punched from the iPP film approximately 200 μm thick. The iPP was placed between glass slide and cover slip and inserted into a Mettler hot stage for atmospheric experiments. The iPP was placed into the high pressure sample cell for elevated pressure experiments. After melting the sample at an appropriate temperature for 15 minutes, the photometer was zeroed, then the sample temperature was lowered to the desired crystallization temperature at a rate of approximately $40^{\circ}\text{C}/\text{min}$. The chart recorder was started when the light on the Mettler control unit indicated that the crystallization temperature had been reached. The recorder then traced the change in depolarized light intensity as a function of time.

Elevated Pressure

4.80 mm diameter discs were punched from the iPP films using steel punches to match the diameter of the sapphire crystals. The iPP was placed on a sapphire and the sapphire is placed into the machined brass tube. The second sapphire was then placed partially into the brass tube, then rotated relative to the first sapphire on a polarizing microscope to achieve minimum transmission of cross-polarized light. The brass tube was then placed into the high pressure cell, the

upper screw plug, and the third sapphire crystal were then placed into the cell. The third sapphire was then rotated relative to the sample assembly to again minimize transmission of cross-polarized light. The non-rotating washer was then positioned and the lower plug screwed into place. The cell was then connected to the high pressure tubing, filled with hydraulic fluid, and tested to ensure adequate pressure retention. The cell was then insulated and the heaters, RTD, and thermocouple connected to the heat exchanger. The cell was then mounted onto the microscope.

Sufficient pressure to adequately seat all the high pressure seals was applied prior to heating. The system was then heated above the melting temperature of the iPP for 10 to 15 minutes to erase any thermal history. The valve to the circulating fluid was opened and the Mettler FP5 reset to the desired crystallization temperature. After the high pressure cell reached steady state, the crystallization was followed optically and recorded as a function of time with the 35mm camera and the filar eyepiece.

Data Analysis

The crystallization isotherms, obtained from the depolarized light intensity measurements, were sigmoidal in shape. An initial, finite induction time τ elapsed during which no depolarization occurs. The intensity increased exponentially to a maximum rate with the onset of

crystallization and the rate decreased to a nearly constant value as a pseudo-equilibrium crystallinity was obtained. The crystallization curve then consisted of five regions with respect to the change in intensity as a function of time: 1) $dI/dt = 0$, the induction period; 2) $dI/dt > C$ where C is a constant, the exponentially increasing rate region; 3) $dI/dt = C$, a constant rate region; 4) $dI/dt < C$, a decreasing rate region and, 5) $dI/dt = C'$. In order to analyze the isotherms, one must know values for the intensity at time zero and at time infinity. The intensity at time zero can experimentally be set to zero. One must now define time infinity, t_{∞} , in order to obtain intensity at time infinity, I_{∞} . One can define t_{∞} as the time corresponding to the end of the fourth region, $dI/dt < C$ and the start of the fifth, $dI/dt = C'$. The normalized plots of $(I_{\infty} - I_t / I_{\infty} - I_0)$ versus t fit the Avrami equation[73]:

$$(I_{\infty} - I_t) / (I_{\infty} - I_0) = \exp(-Kt^n)$$

where I_t = intensity at time t

K = constant

n = constant

The constant n is characteristic of the type of nucleation and the constant K involves the nucleation density and linear growth rate.

The constants n and K were found analytically with a double logarithm technique. Taking the double logarithm of both sides of equation 3.1 (above) gives:

$$-\log \log[(I_{\infty} - I_t)/(I_{\infty} - I_0)] = n \log t + \log(K/2.303)$$

Plotting $-\log \log[(I_{\infty} - I_t)/(I_{\infty} - I_0)]$ versus $\log t$ yielded a line with slope $-n$ and intercept $\log(K/2.303)$.

3.3 Melting

The melting behavior of iPP was followed using several techniques: depolarized light intensity (DLI), optical micrography, and differential scanning calorimetry (DSC). The experimental equipment for DLI was the same as that used for atmospheric bulk crystallization. The experimental equipment for optical micrography of the melting behavior of iPP was the same as that used for spherulitic growth rate determination. The experimental equipment for DSC consisted of Haake D8L oil baths for isothermal crystallization of samples and a Perkin-Elmer DSC-7 for the differential scanning calorimetry of the isothermally crystallized samples.

Experimental Procedure

Depolarized Light Intensity

After performing an isothermal bulk crystallization experiment, the Mettler temperature control unit was set to a constant heating rate and either the depolarized light intensity or the transmitted light intensity recorded as a function of temperature through the melting transition. It was experimentally possible to simultaneously record the depolarized light intensity and the optical micrographic melting behavior using the Olympus BH-2 polarizing transmitted optical microscope equipped with the Olympus 35mm camera back and the automatic exposure control unit. This enabled the correlation of the observed melting behavior to the light intensity.

Differential Scanning Calorimetry

Isothermal crystallization for the DSC experiments was carried out in a Haake D8L temperature bath with silicone fluid (Dow 200) as the heating fluid. A sample 6mm in diameter was punched from 200 μm iPP films and placed into a DSC sample pan. The sample pan was sealed and placed into a glass vial purged with dry nitrogen gas. The glass vial was then submerged into a temperature bath at 190°C and kept at this temperature for about 20 minutes. The vial was then

transferred to another temperature bath at the crystallization temperature and kept at this temperature for sufficient time to ensure complete primary crystallization. This was ascertained from prior depolarized light intensity crystallization measurements. The sample was then transferred to the DSC and the corresponding DSC curve recorded. The DSC curve was then analyzed for melting onset, melting temperature, and heat of fusion.

Elevated Pressure

The melting behavior of iPP under elevated pressure was followed using transmitted light intensity (TLI) and depolarized light intensity. The experimental equipment at elevated pressure was the same as that used for elevated pressure bulk crystallization. Also, bulk samples crystallized at elevated pressure were run on the DSC at atmospheric pressure.

Experimental Procedure

After performing an isothermal crystallization experiment, the Mettler temperature control unit was set to a constant heating rate and the transmitted light intensity recorded as a function of temperature through the melting transition.

Data Analysis

The melting transition of iPP can be complicated by such factors as different crystallographic forms, differences in

crystalline perfection, and differences in crystallite size [74]. An acceptable definition of the melting temperature is required to evaluate the DSC curves. Isotactic polypropylene is known to exhibit multiple fusion endotherms that complicate the definition of the melting temperature as the peak temperature [75]. An end-of-fusion extrapolated return-to-baseline definition for the melting temperature might be more appropriate. Melting temperatures were then extrapolated in order to predict the equilibrium melting temperature. A plot of melting temperature versus crystallization temperature extrapolated to the line representing $T_m = T_c$ yields T_m^0 . This approach can have complications such as (a) accurate measurement of the melting temperature, (b) crystal thickening during crystallization, and (c) crystal thickening as the melting temperature is approached during the melting experiment. The thickening factor was calculated from the slope of the T_m versus T_c line [76].

3.4 Morphology

Equipment

The morphology of iPP isothermally crystallized at atmospheric and elevated pressures was studied using optical microscopy of thin films. Several microscopes were used including a Nikon Microphot, an Olympus BH-2, and a Reichert

Microstar IV. For thicker samples, the Nikon Microphot was employed in reflection mode to observe etch and fracture surfaces. Also samples sectioned from the bulk with a glass-knife microtome at liquid nitrogen temperatures were observed on the Olympus and the Reichert.

Sample Preparation

The iPP films used for linear growth rate studies were used for optical microscopy at atmospheric pressure as well as elevated pressure. For atmospheric pressure thick film bulk samples, isothermal crystallization were performed in a temperature bath. For elevated pressure thick film bulk samples, isothermal crystallization were performed in a custom piston-cylinder type high pressure apparatus. A schematic diagram of the high pressure cell is shown in Figure 3.4. A Carter hydraulic press with maximum 24000 lbs force was used in this experiment. The cell cylinder and the pistons were made of Vascomax 300 CVM maraging steel, which was heat-treated to a hardness of 55 Rockwell C. The diameter of the cell was 6.35 cm and the cylinder bore was 2 cm. A hole was bored at the center of the cell's wall to a depth of 1/2 of the cell depth for temperature measurement. The piston clearance was 30 μm . The cell was designed to take pressures up to 1000 MPa and temperatures beyond 300°C. A 3mm thick sample and a 300 μm thick sample separated by aluminum foil were placed into the cell. Tight fitting

teflon spacers were used to separate the samples and provide a low pressure seal. Brass delta rings on the pistons sealed the cell at high pressure.

A Thermolyne Fibrax heating tape was wrapped onto the outside of the cell and temperature was controlled with an Omega Model 49 proportional controller. An Omega J-type thermocouple mounted into the cell body was used to measure the temperature of the cell. Insulation surrounding the cell improved temperature stability.

After assembly, the cell was heated to an appropriate melting temperature for a time sufficient to ensure complete melting. Then the cell temperature was lowered to the desired crystallization temperature and the crystallization pressure was applied. After sufficient time to ensure complete crystallization of the sample, the temperature of the cell was lowered to room temperature and the pressure released.

An alternate procedure was employed above a certain pressure. This involved melting the sample at the desired crystallization temperature but at a pressure lower than the desired crystallization pressure. After sufficient melting, pressure was rapidly increased to the desired crystallization pressure.

Chapter 4

Results

4.1 Crystallization

4.1.1 Atmospheric Pressure Bulk Data

The isothermal bulk crystallization of a polymer follows a sigmoidal curve, as first reported by Bekkdahl [77] in his study of natural rubber. Figure 4.1 shows schematically a typical isothermal crystallization curve. The point A represents temperature equilibration of the sample. Point B represents initial detection of crystallinity. The location of point B is dependent on the method of measuring crystallinity thus, for instance, isothermal crystallization using DSC and DLI might show different times for point B. Point C represents the inflection of the crystallization curve, crystallinity (intensity) exponentially increasing up to that point. Beyond point C, the rate of increase of crystallinity is decreasing. Point D represents the end of primary crystallization. The half-time of crystallization, $t_{1/2}$, is defined as the time for development of 50% of the final crystallinity.

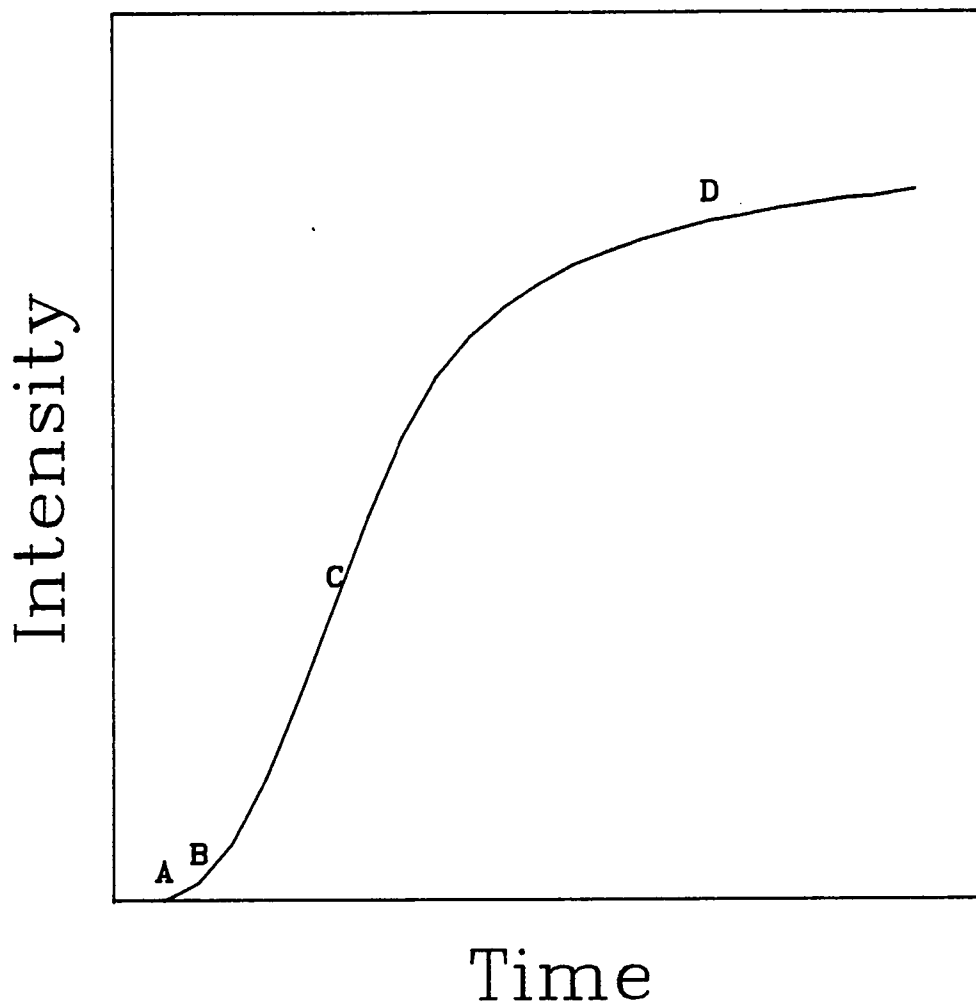


Figure 4.1 Schematic of intensity versus time relation typical of isothermal crystallization of polymers. Labeled points are defined in text.

The crystallization rate was a strong function of the crystallization temperature as well as the melting temperature, the melting temperature dependence being due to nucleation. For melting temperatures below the equilibrium melting temperature, nucleation density showed a strong temperature dependence, which was reflected in the crystallization curve. When the melting temperature was above T_m^0 , there was little temperature dependence of the nucleation density and the crystallization rate reflected the crystallization temperature dependence.

Crystallization can occur between the glass transition temperature T_g and the equilibrium melting temperature T_m^0 . The rate of crystallization exhibits a maximum between these two temperature limits. As the crystallization temperature approaches either limit, the rate of crystallization decreases. The experimental limits for observation of isothermal crystallization, however, are generally less than these theoretical limits. For iPP, isothermal crystallization can be measured from approximately 20° below T_m^0 to approximately 90° below T_m^0 .

Relative crystallinity plots of samples at various crystallization temperatures are shown in Figures 4.2 - 4.4, all isotherms showing the expected sigmoidal behavior. Figure 4.5 shows a comparison of the overall transformation kinetics at $T_c = 130^\circ\text{C}$ for iPP, $M_w = 151,000, 83,000$

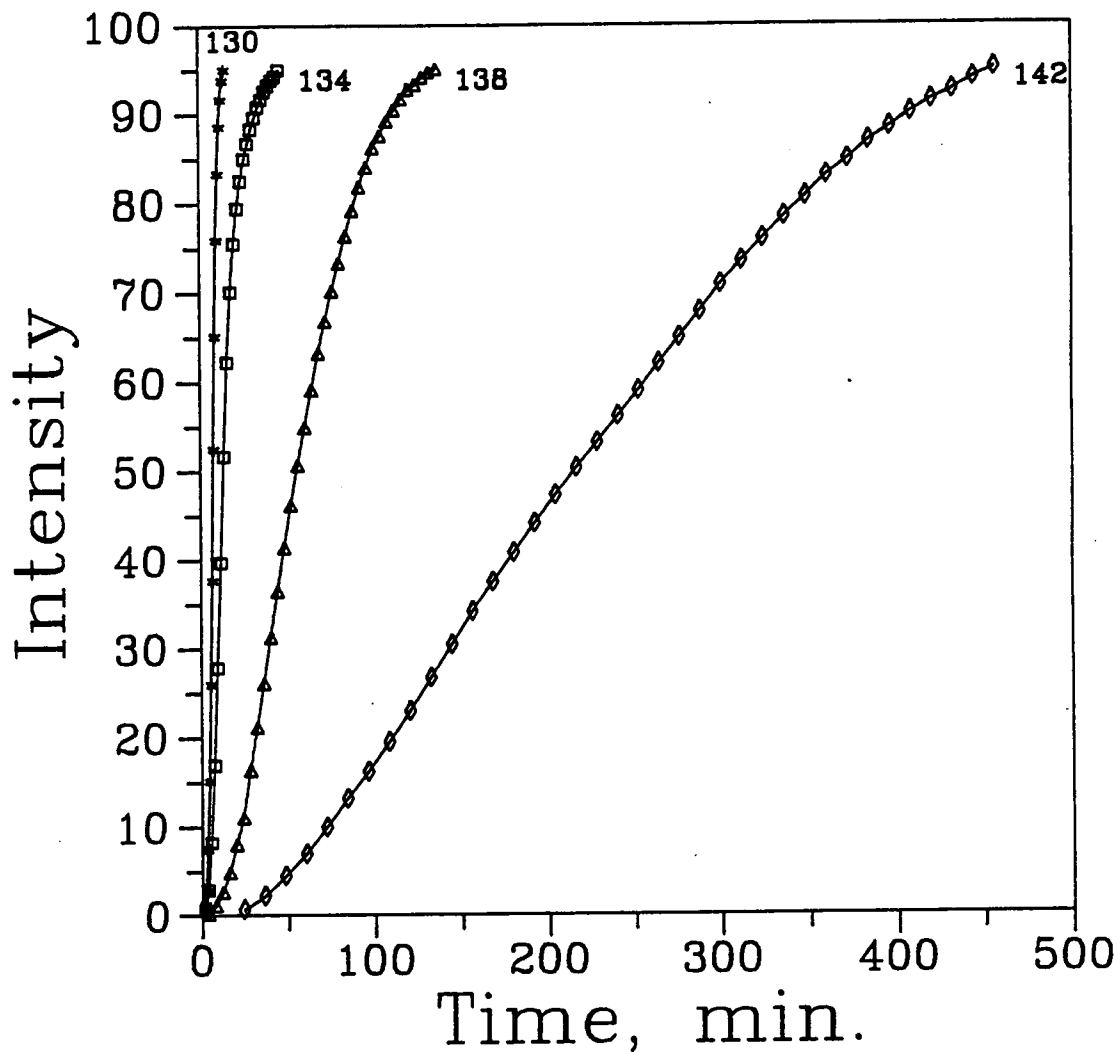


Figure 4.2 Light intensity versus time curves at various temperatures for isotactic polypropylene homopolymer $M_w = 151,000$.

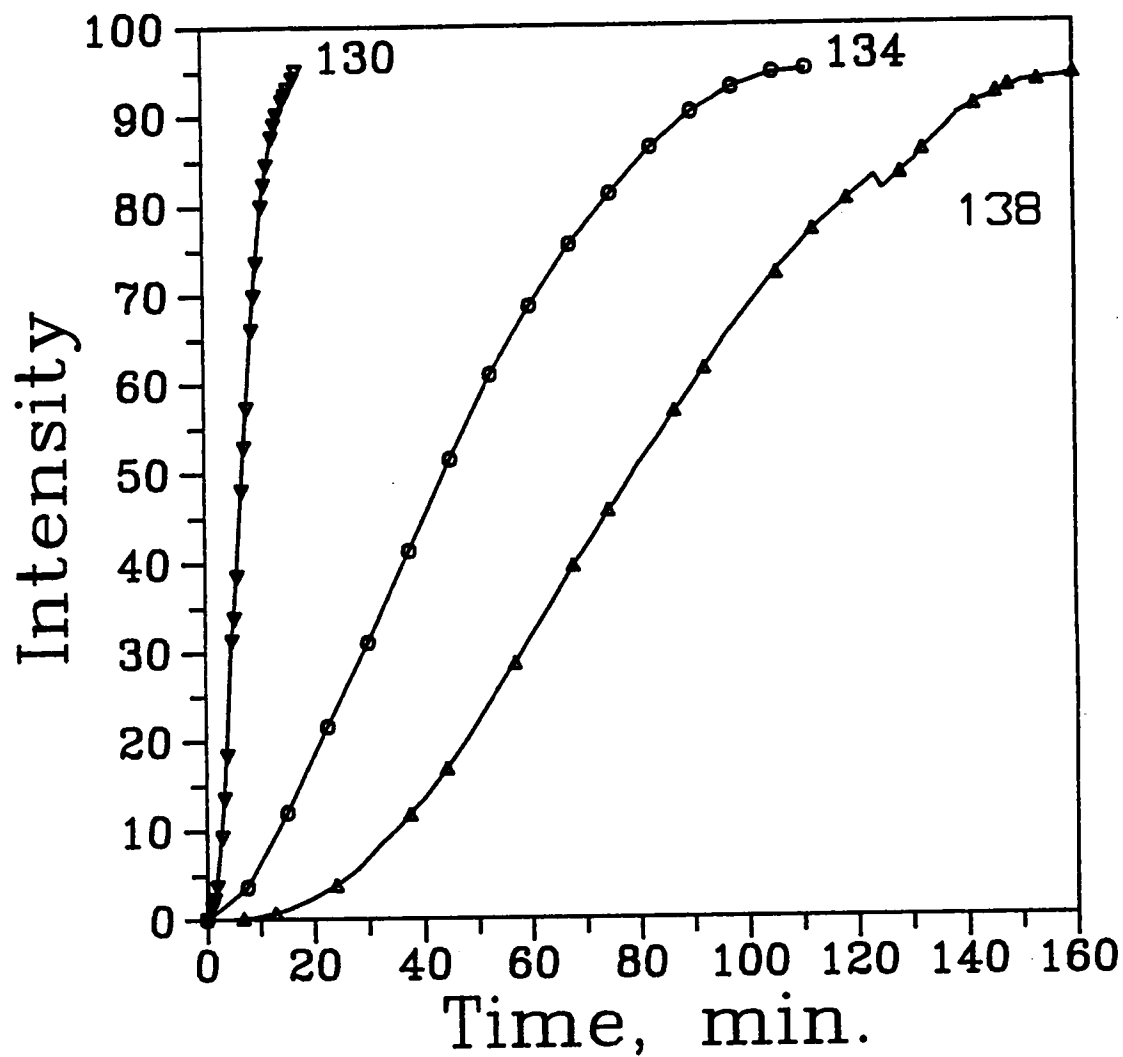


Figure 4.3 Light intensity versus time curves at various temperatures for isotactic polypropylene homopolymer $M_w = 83,000$.

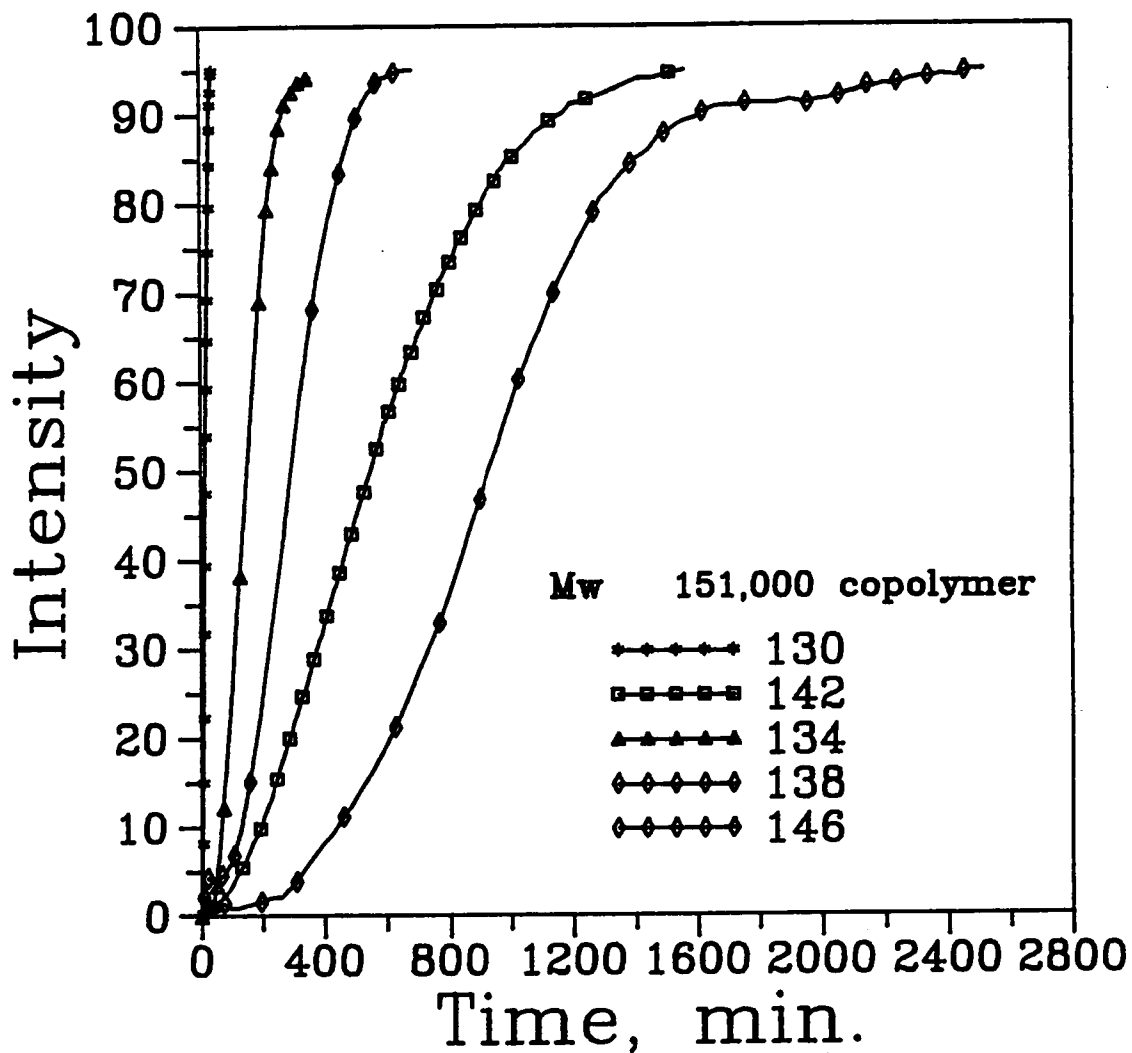


Figure 4.4 Light intensity versus time curves at various temperatures for isotactic polypropylene copolymer (0.5% ethylene) $M_w = 151,000$.

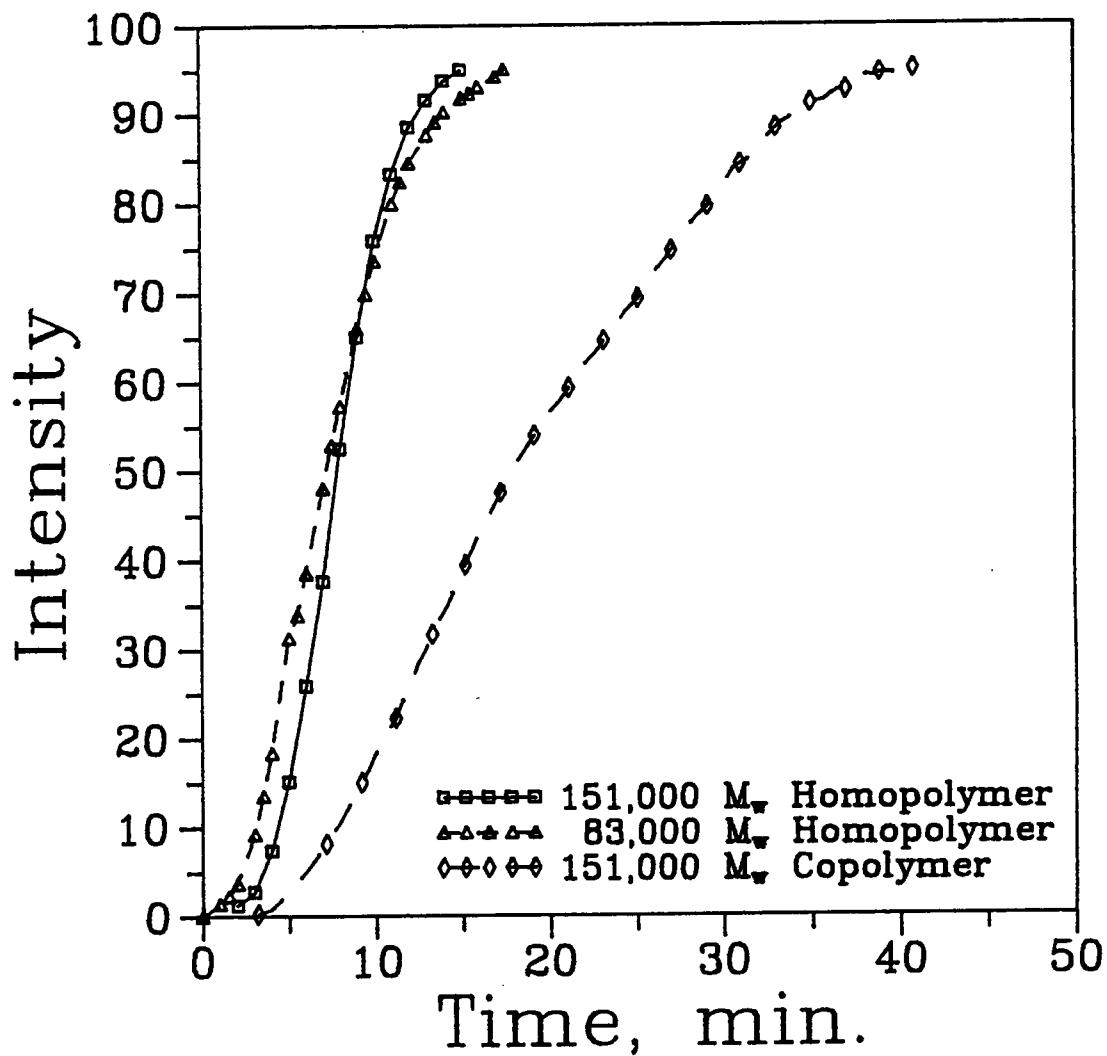


Figure 4.5 Comparison of the overall transformation kinetics at $T_c = 130^\circ\text{C}$ ($\Delta T = 57^\circ$) for isotactic polypropylene.

homopolymers and $M_w = 151,000$ copolymer (0.5% ethylene). Similar behavior was observed at other crystallization temperatures and for other samples.

The half-time of crystallization was used as a measure of the effect of crystallization temperature on overall transformation kinetics by plotting the reciprocal half-time versus the crystallization temperature. Figure 4.6 shows the crystallization behavior of the isotactic polypropylenes $M_w = 151,000$, $M_w = 83,000$ homopolymers and $M_w = 151,000$ copolymer. For all three samples, the rate of crystallization decreased rapidly with increasing crystallization temperature.

4.1.2 Elevated Pressure Bulk Data

The high pressure bulk data were obtained in a similar manner to the atmospheric pressure bulk kinetic data, except that the high pressure cell described in section 3.2 was used instead of the Mettler FP82 hot stage. Due to the light path through the high pressure cell, the experiment created more error in half-time estimation than that at atmospheric pressure.

Samples were melted at approximately 200°C at atmospheric pressure for sufficient time to ensure complete melting. Then a valve on the circulating oil bath was opened, allowing silicone oil at a temperature approximately 20°C below the desired crystallization temperature to rapidly cool the high pressure cell. At the same time, the Mettler

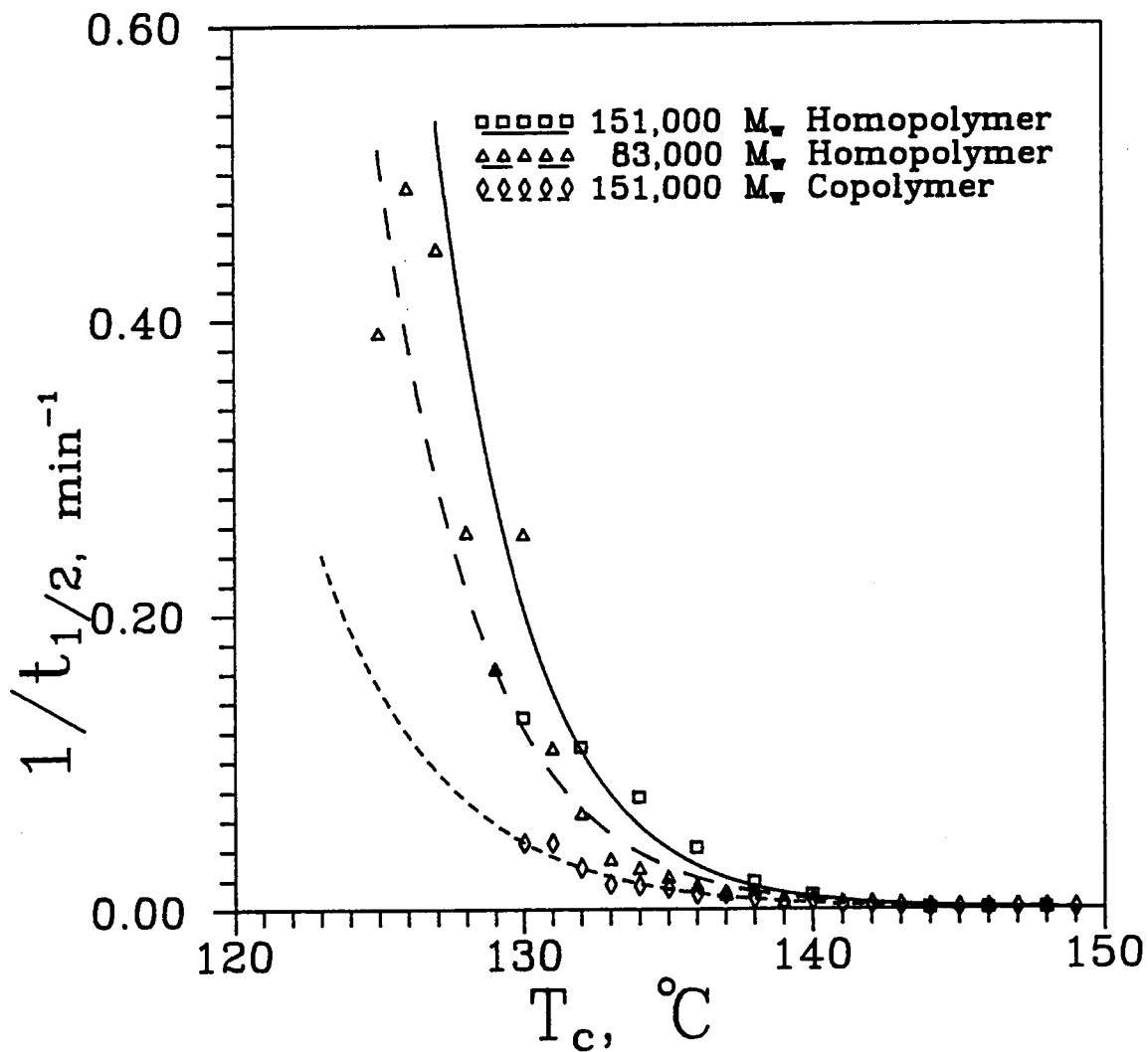


Figure 4.6 Reciprocal of crystallization half-times for isotactic polypropylenes as a function of crystallization temperature.

controller was reset to the desired crystallization temperature. The pressure was rapidly increased to the desired crystallization pressure while the cell cooled. This experimental procedure allowed for relatively rapid equilibration to the desired temperature (about two minutes for 50° supercooling). The lowest supercoolings obtained at atmospheric pressure on the Mettler FP82 hot stage were not practical on the high pressure system. Often low crystallization temperature runs on the pressure system were rejected because crystallization began before the cell equilibrated at the crystallization temperature. However, an acceptable experimental crystallization temperature range was achieved. Crystallization temperatures were initially chosen to duplicate the corresponding supercooling range achieved for the atmospheric pressure crystallization series.

Due to the nature of the high pressure cell, direct measurement of the sample temperature at pressure was not practical. Therefore, prior to pressure experiments, a calibration of the temperature of the sample in the high pressure cell relative to the high pressure heat exchanger was completed. This was done by placing a thermocouple through the high pressure port into the high pressure cell and recording the temperatures at atmospheric pressure. The sample temperature - exchanger temperature relation was then fit linearly, with a good (99.9%) correlation found. This

linear fit was assumed to be correct at elevated pressure. At elevated pressures the correlation will be at least as good as at atmospheric pressure since thermal conductivity increases with pressure. Thus the sample temperature at pressure was determined by the Mettler FP5 set temperature and checked by the heat exchanger temperature.

Relative crystallinity plots of samples at various crystallization temperatures are shown in Figures 4.7 - 4.10 for crystallization pressures 25, 50, 75, and 100 MPa, respectively. Generally the isotherms showed sigmoidal behavior. It was observed, especially at 75 MPa crystallization pressure, that the intensity produced by formation of spherulites to impingement was relatively low. However, the intensity continued to increase and then plateau as expected. In Figure 4.9 this behavior can be observed as a small plateau in intensity at shorter times, followed by a substantial increase in intensity and another plateau at longer times. Figure 4.11 shows the crystallization behavior at several pressures for a constant supercooling of 50° . It is seen that the behavior changes somewhat with pressure.

Reciprocal half-times versus crystallization temperature at 25, 50, 75, and 100 MPa are shown in Figures 4.12, 4.13, 4.14, and 4.15, respectively. As with atmospheric pressure, the rate of crystallization decreased rapidly with increasing crystallization temperature. Figure 4.16 shows a plot of

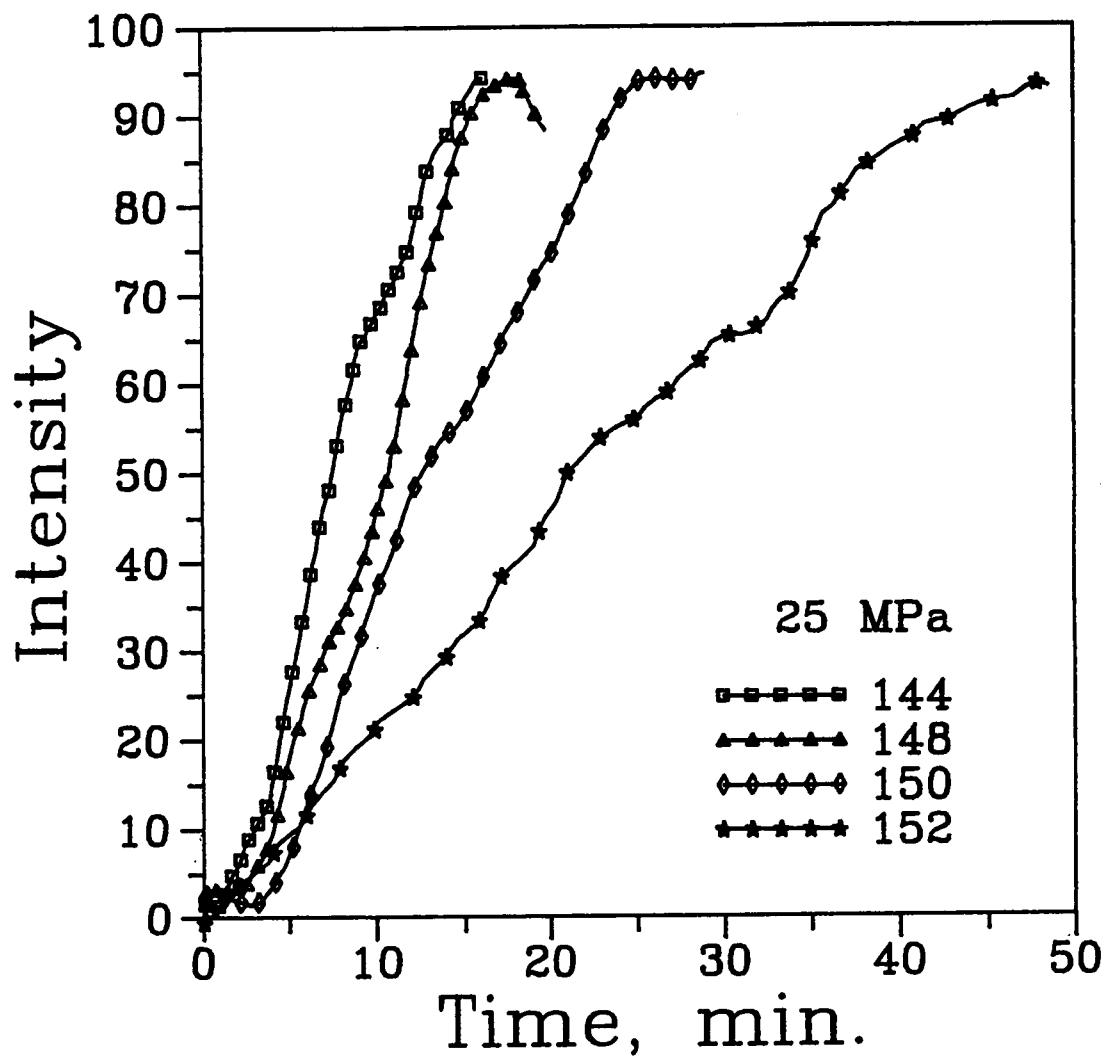


Figure 4.7 Light intensity versus time curves at various temperatures for isotactic polypropylene homopolymer $M_w = 83,000$. Crystallization pressure 25 MPa.

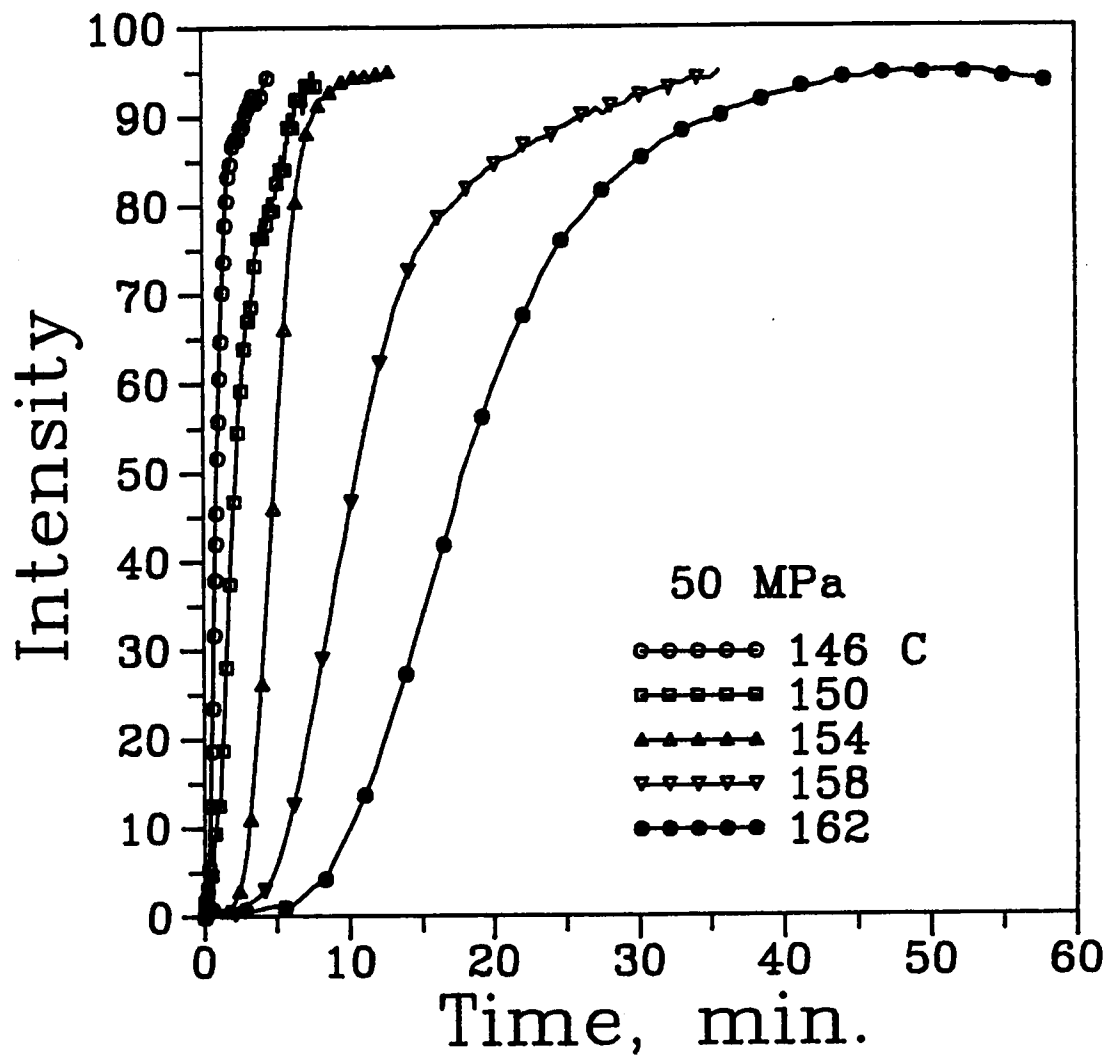


Figure 4.8 Light intensity versus time curves at various temperatures for isotactic polypropylene homopolymer $M_w = 83,000$. Crystallization pressure 50 MPa.

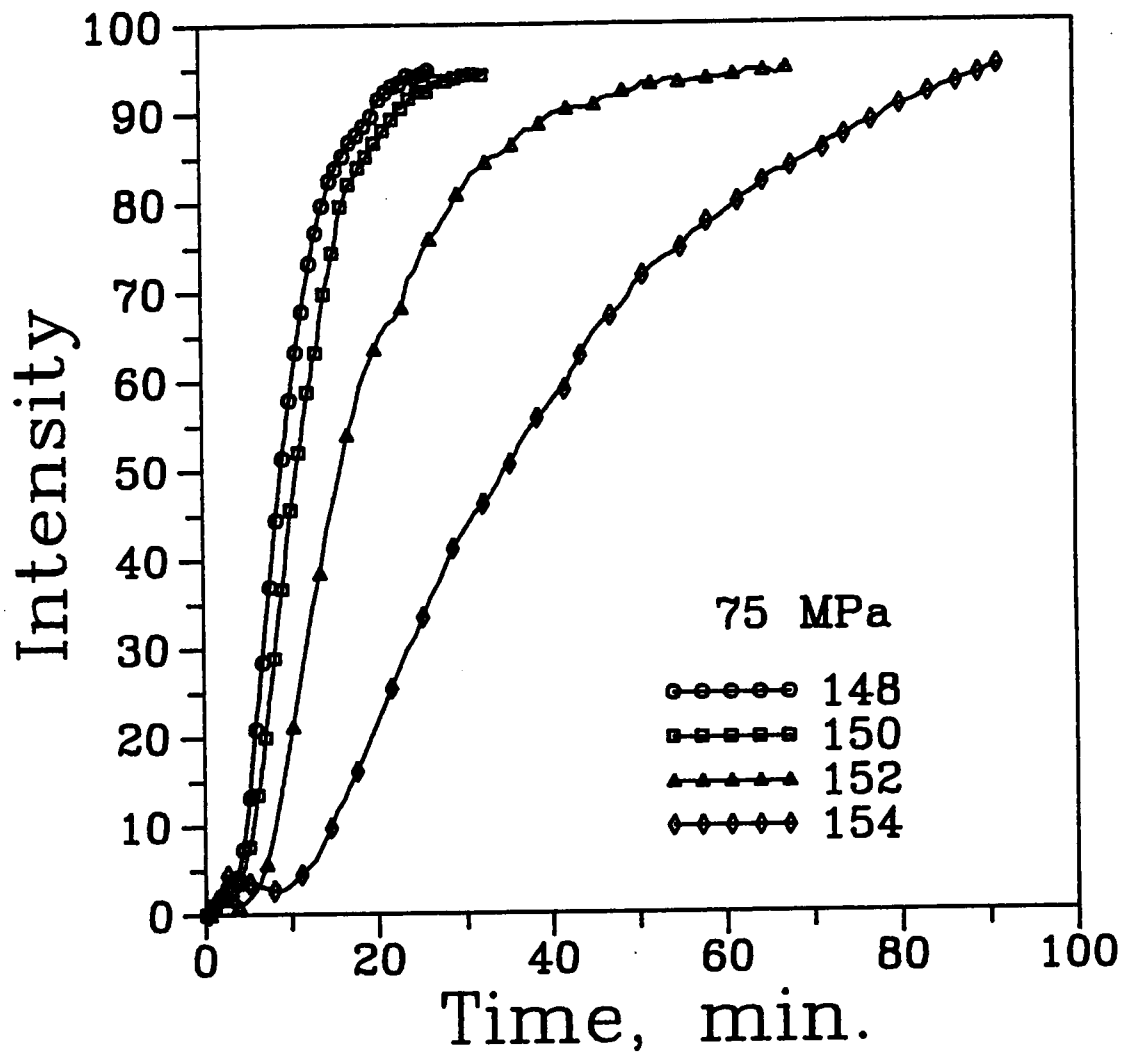


Figure 4.9 Light intensity versus time curves at various temperatures for isotactic polypropylene homopolymer $M_w = 83,000$. Crystallization pressure 75 MPa.

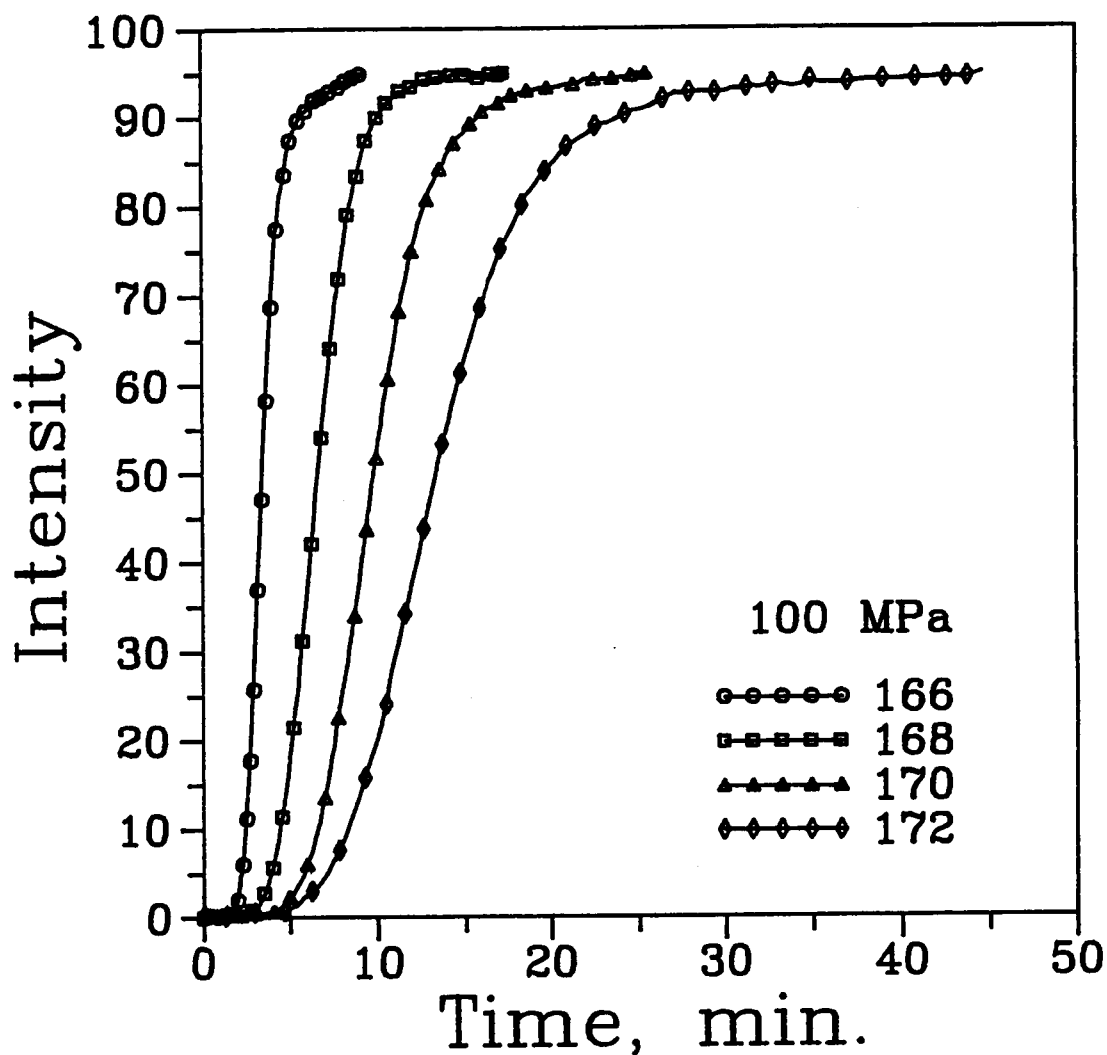


Figure 4.10 Light intensity versus time curves at various temperatures for isotactic polypropylene homopolymer $M_w = 83,000$. Crystallization pressure 100 MPa.

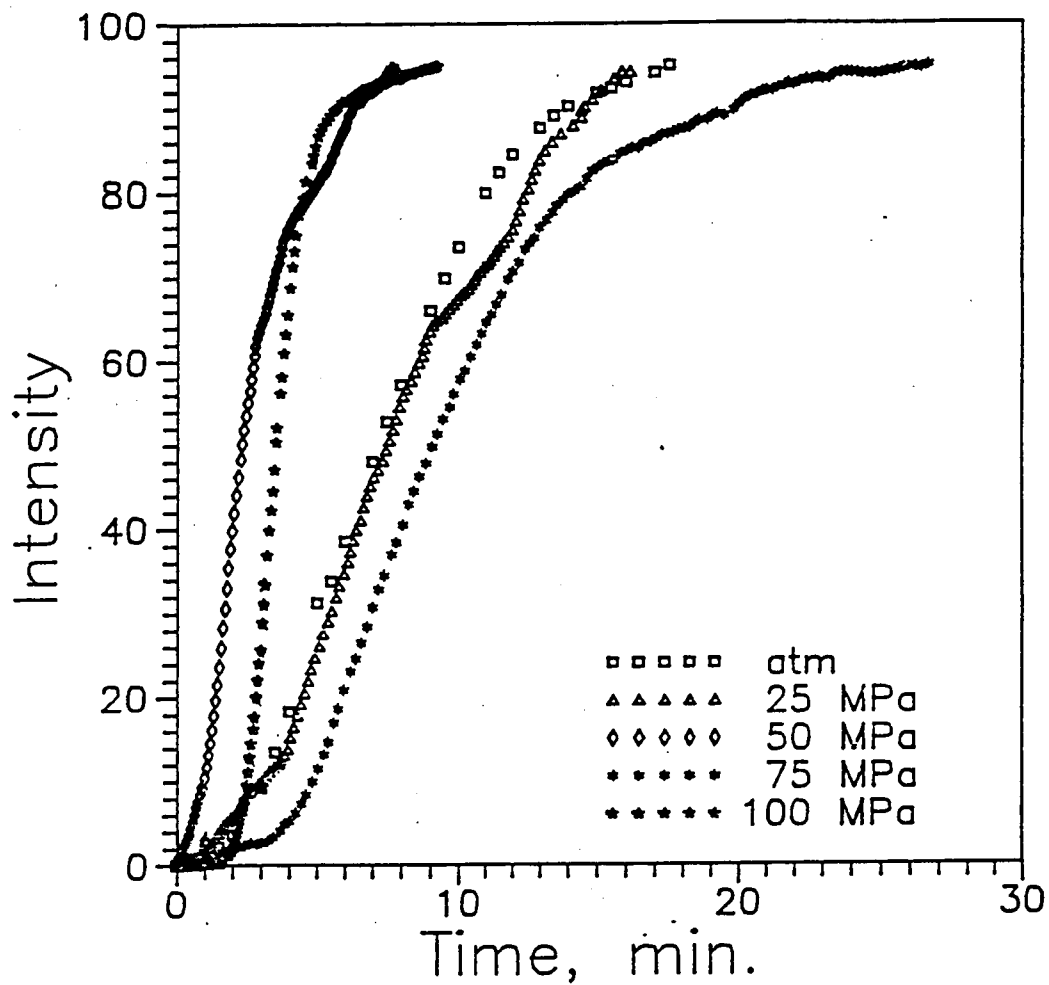


Figure 4.11 Light intensity versus time curves at $\Delta T = 50^\circ$ for isotactic polypropylene homopolymer $M_w = 83,000$ at several crystallization pressures.

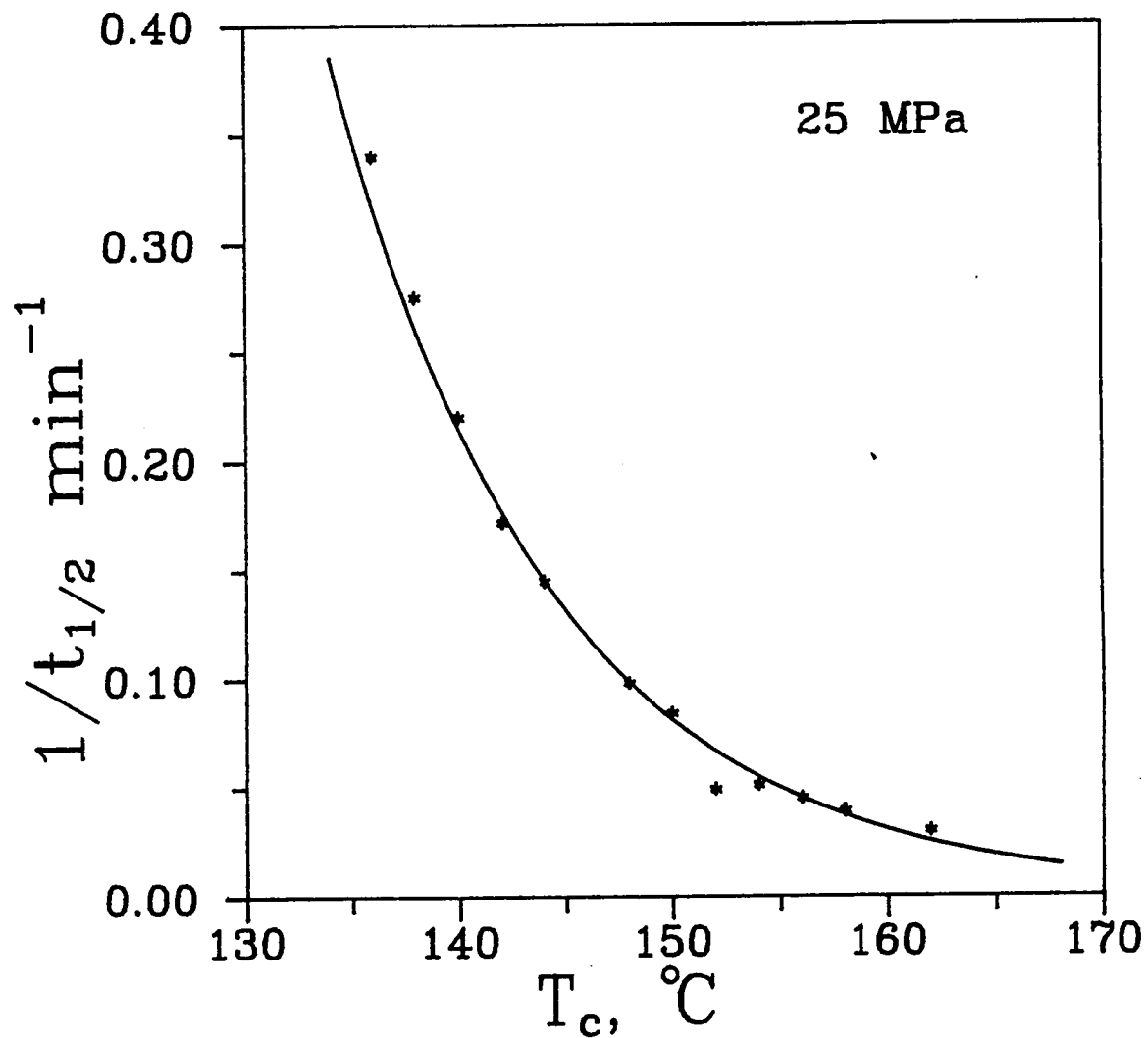


Figure 4.12 Reciprocal of crystallization half-times for isotactic polypropylene homopolymer $M_w = 83,000$ as a function of crystallization temperature. Crystallization pressure 25 MPa.

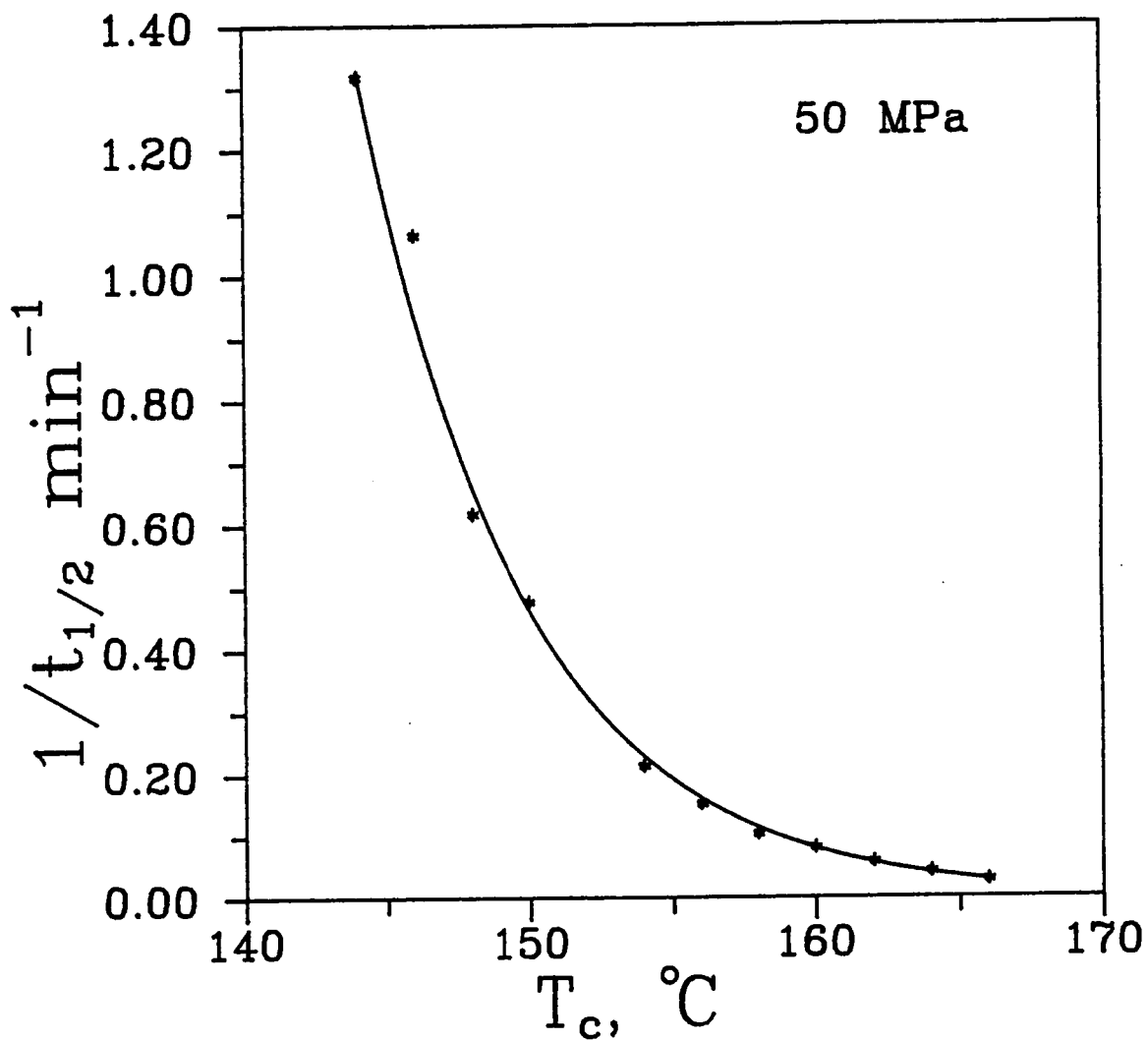


Figure 4.13 Reciprocal of crystallization half-times for isotactic polypropylene homopolymer $M_w = 83,000$ as a function of crystallization temperature. Crystallization pressure 50 MPa.

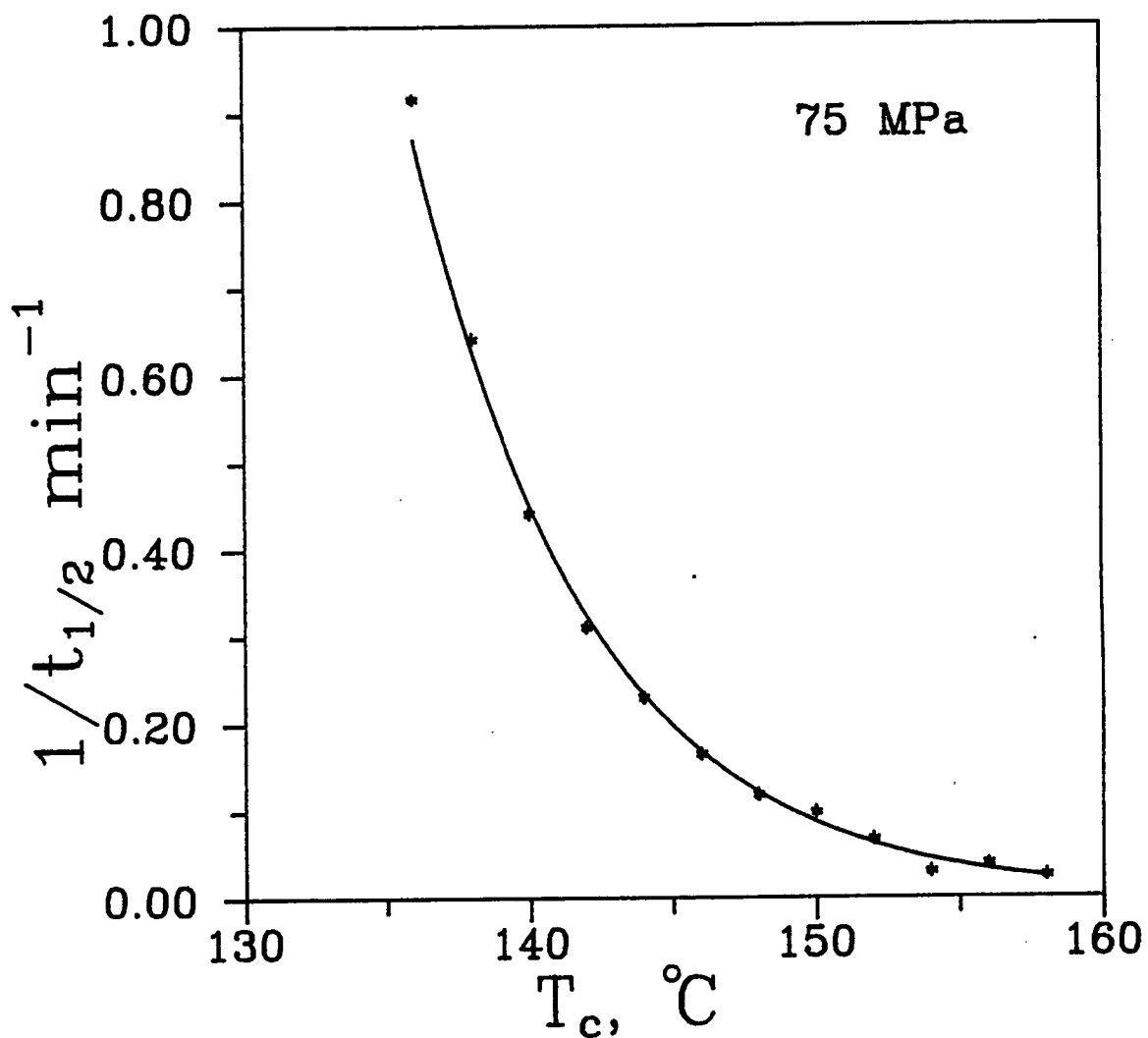


Figure 4.14 Reciprocal of crystallization half-times for isotactic polypropylene homopolymer $M_w = 83,000$ as a function of crystallization temperature. Crystallization pressure 75 MPa.

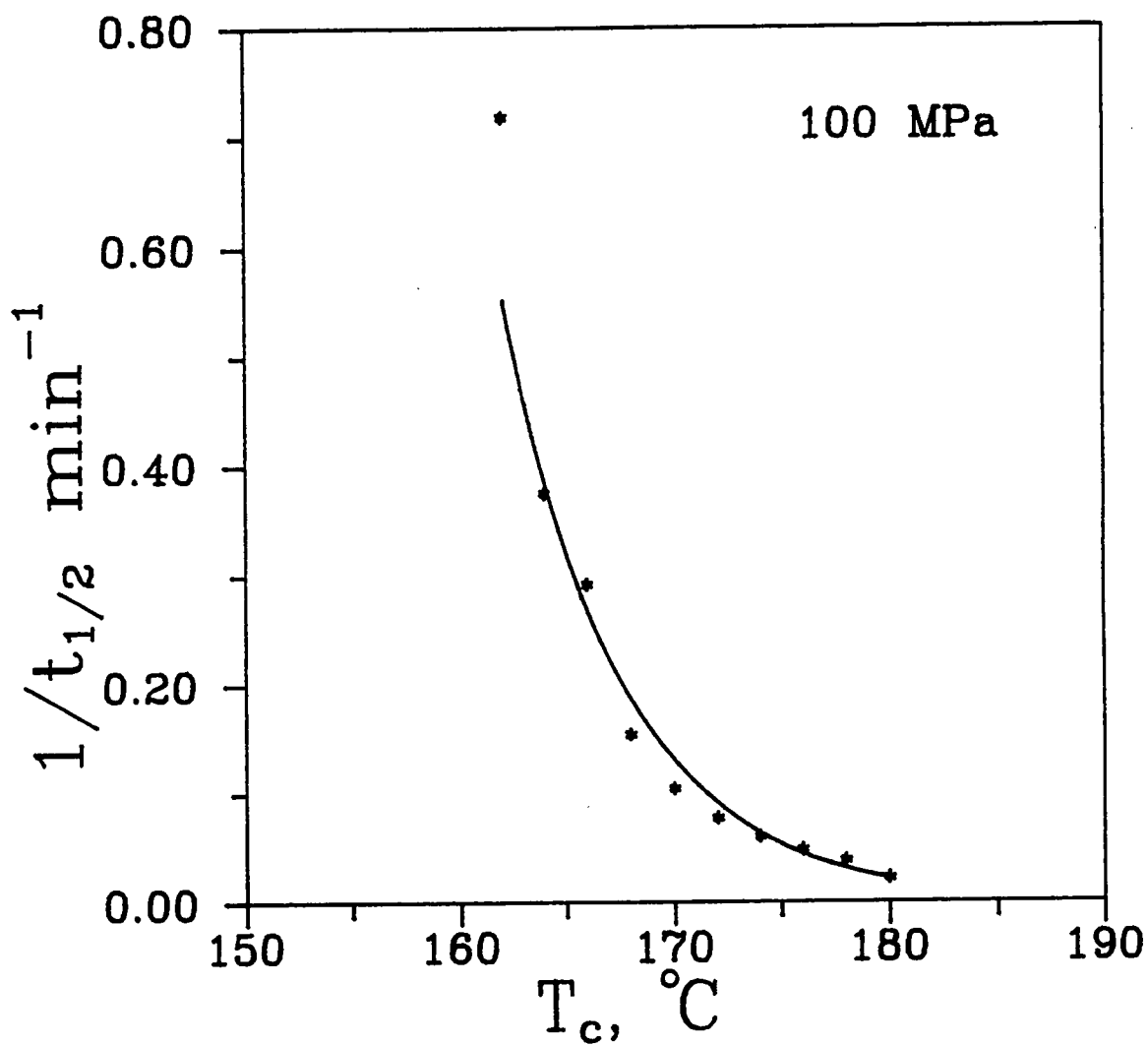


Figure 4.15 Reciprocal of crystallization half-times for isotactic polypropylene homopolymer $M_w = 83,000$ as a function of crystallization temperature. Crystallization pressure 100 MPa.

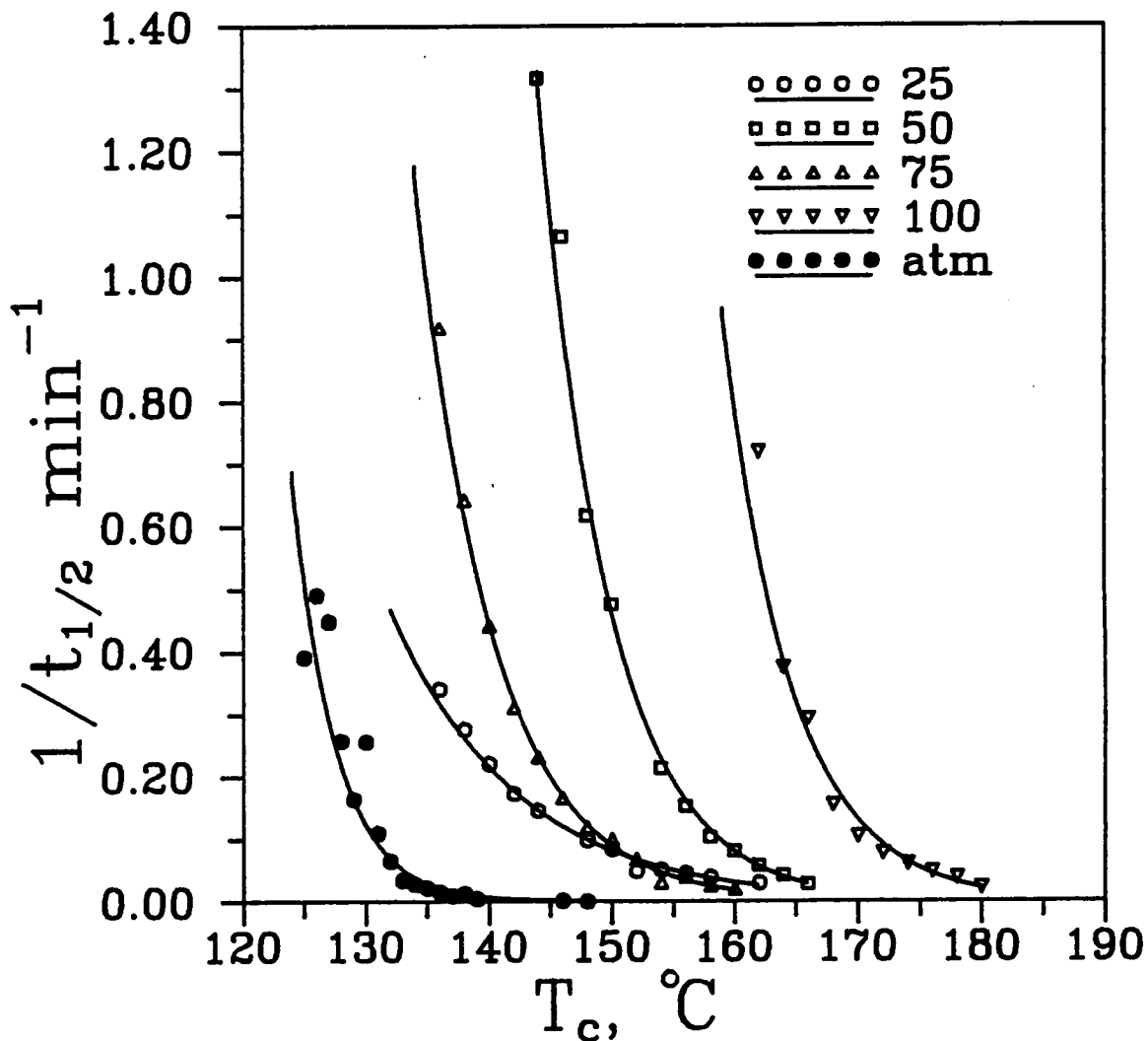


Figure 4.16 Comparison of reciprocal crystallization half-times for isotactic polypropylene homopolymer $M_w = 83,000$ at several crystallization pressures.

reciprocal half-time versus crystallization temperature at various pressures.

4.2 Thermal Analysis Results

The melting temperature of a polymer can be difficult to determine for several reasons:

- 1) Melting in polymers generally occurs over a range of temperatures,
- 2) Melting behavior depends upon the sample's thermal history, and
- 3) Melting behavior is dependent on heating rate.

Polymers form only metastable crystals at a given crystallization temperature [78]. These metastable crystals can undergo superheating, annealing, reorganization, and recrystallization. These phenomena affect the thermal analysis of polymers. Polymorphism can add to the difficulty of interpreting the thermal analysis traces. Polymorphism is the existence of more than one crystal structure under a given crystallization condition. iPP is such a polymer and can exhibit several distinctly different crystal structures: the α -form, which is monoclinic [79] and generally the most predominant; the β -form, which is hexagonal [80]; the γ -form, which has a proposed orthorhombic structure [81]; and a disorganized form often referred to as pseudo-smectic [82], .

Such polymorphism can lead to multiple peaks or a convoluted peak in differential scanning calorimetry.

4.2.1 Differential Scanning Calorimetry

Samples were isothermally crystallized for sufficient time to ensure complete primary crystallization, this time being determined by a *priori* bulk crystallization experiments. Melting behavior was studied for various samples at atmospheric pressure conditions over a crystallization temperature range from approximately 30° supercooling to approximately 60° supercooling. Melting was studied using differential scanning calorimetry, depolarized light intensity, and optical microscopy. At elevated pressure, melting was studied using depolarized light intensity. However, samples that were crystallized at elevated pressure were also studied at atmospheric pressure conditions using differential scanning calorimetry and depolarized light intensity combined with optical microscopy.

Differential Scanning Calorimetry

Atmospheric Pressure

Figure 4.17 shows the typical DSC melting behavior of the $M_w = 83,000$ homopolymer as a function of crystallization temperature. Single peak endotherm behavior was observed up to an isothermal crystallization temperature of 130°C. Convoluted peaks were observed for all other T_c 's. An

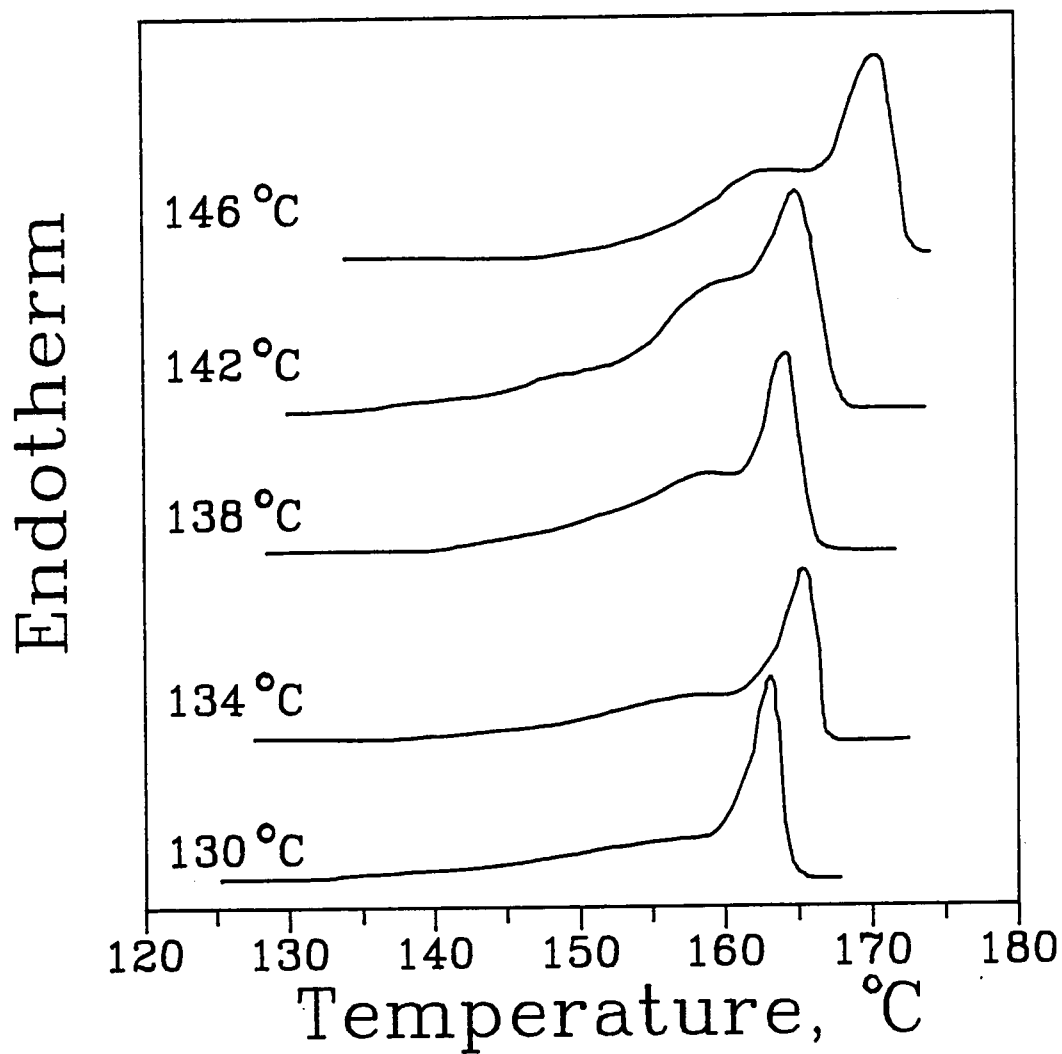


Figure 4.17 DSC melting behavior of isotactic polypropylene homopolymer $M_w = 83,000$ for various isothermal crystallization temperatures. Heating Rate = $10^\circ\text{C}/\text{min}$.

interpretation of the observed melting behavior from the literature proposes that for low T_c ($<130^\circ\text{C}$), the low T_m peak represents melting of crystals formed during isothermal crystallization while the high T_m peak is due to crystals formed due to recrystallization or reorganization. The DSC melting behaviors of the $M_w = 83,000$ homopolymer and $M_w = 151,000$ copolymer are similar to that of the $M_w = 151,000$ homopolymer. Figure 4.18 shows typical DSC behavior of the $M_w = 151,000$ homopolymer as a function of the same crystallization temperature used for the 83,000 homopolymer. Figure 4.19 shows typical DSC behavior of the $M_w = 151,000$ copolymer.

Figure 4.20 compares the DSC melting behavior of the $M_w = 151,000$, $M_w = 84\text{K}$ homopolymers, and the $M_w = 151,000$ copolymer (0.5% ethylene). The 151,000 homopolymer and the 151,000 copolymer showed similar thermal behavior at this particular crystallization temperature. The 83,000 homopolymer, however, did show a more distinct shoulder at the lower temperatures. Figure 4.21 compares the DSC behavior of the polypropylenes at a higher crystallization temperature. In all three samples there were two distinct peaks. Again the 151,000 homopolymer and 151,000 copolymer showed similar behavior while the 83,000 homopolymer was different at the lower temperatures.

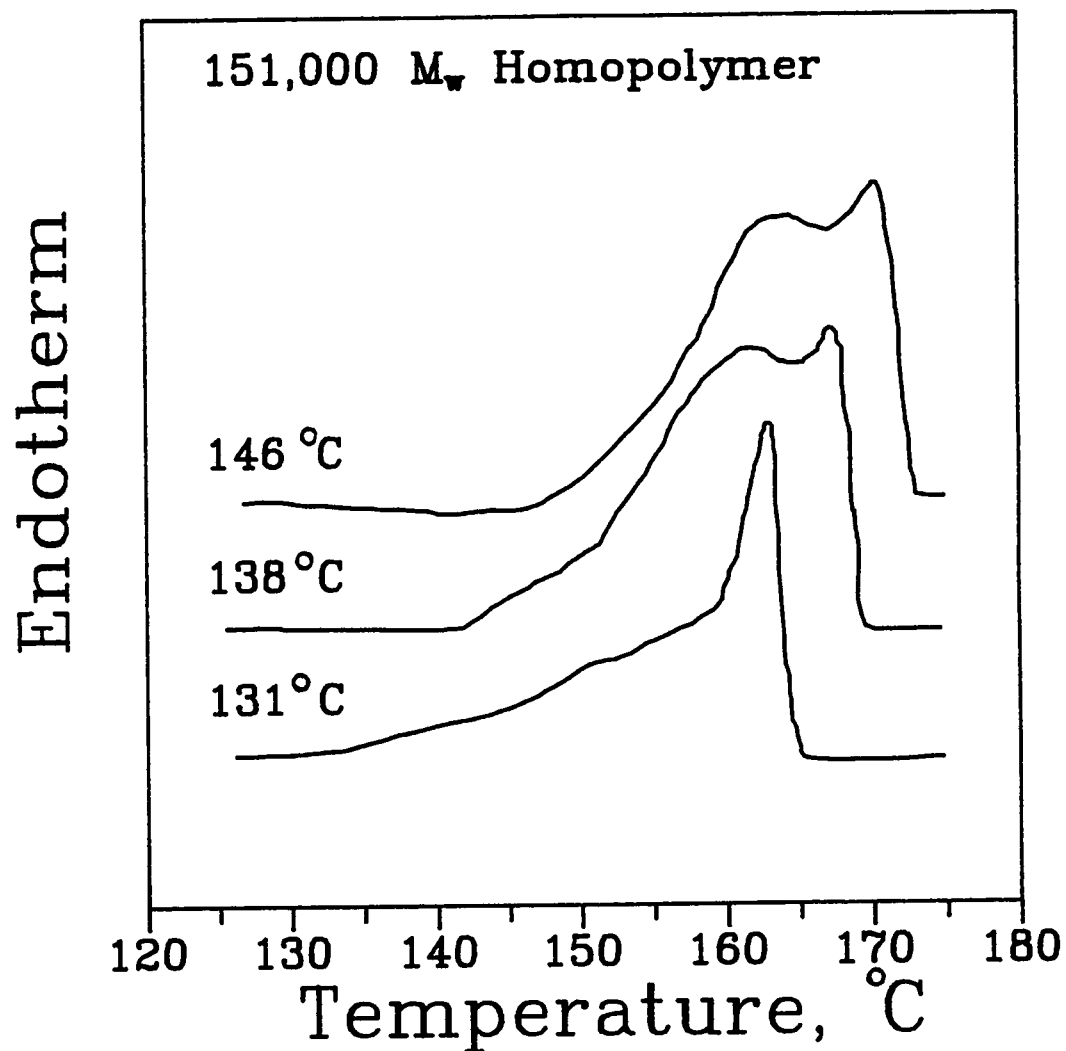


Figure 4.18 DSC melting behavior of isotactic polypropylene homopolymer $M_w = 151,000$ for various isothermal crystallization temperatures. Heating Rate = $10^\circ\text{C}/\text{min}$.

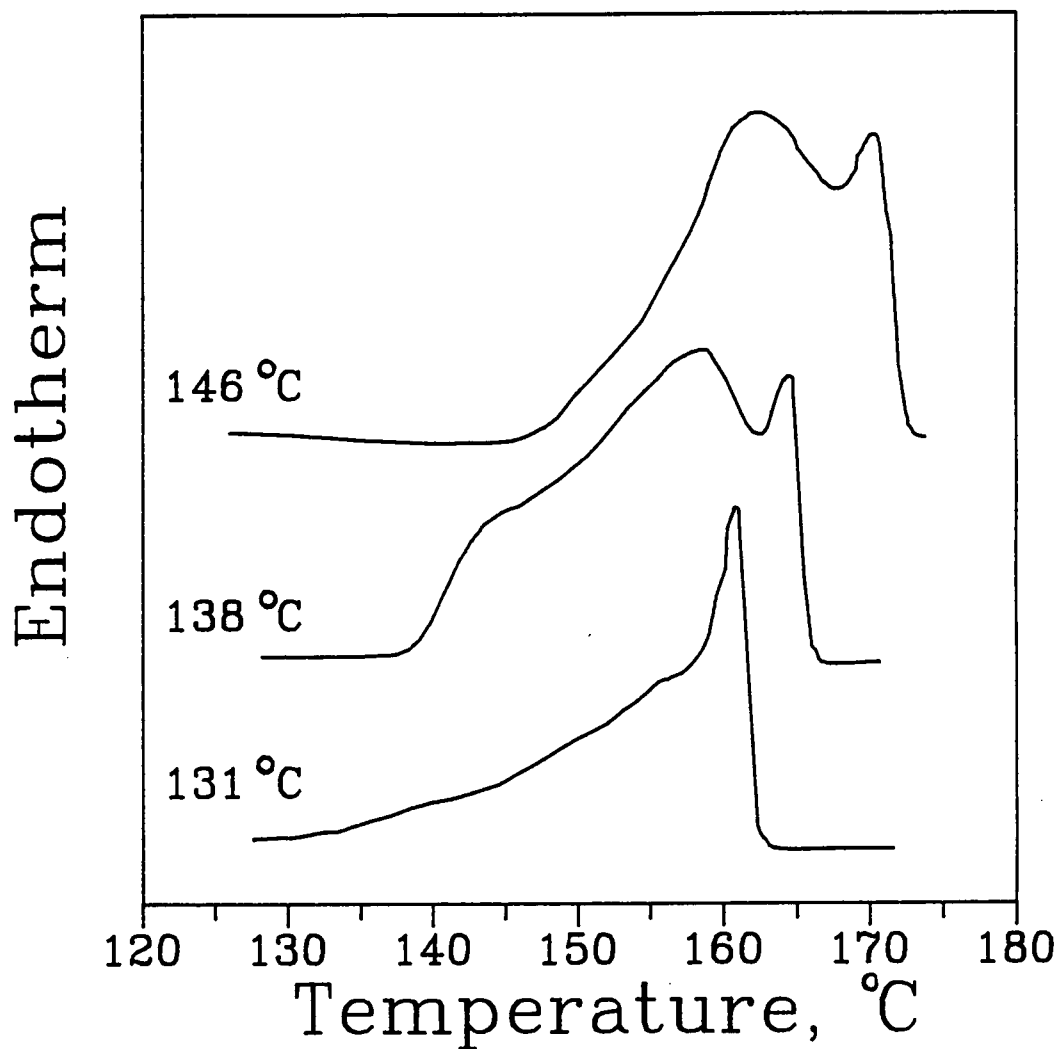


Figure 4.19 DSC melting behavior of isotactic polypropylene copolymer $M_w = 151,000$ for various isothermal crystallization temperatures. Heating Rate = $10^\circ\text{C}/\text{min}$.

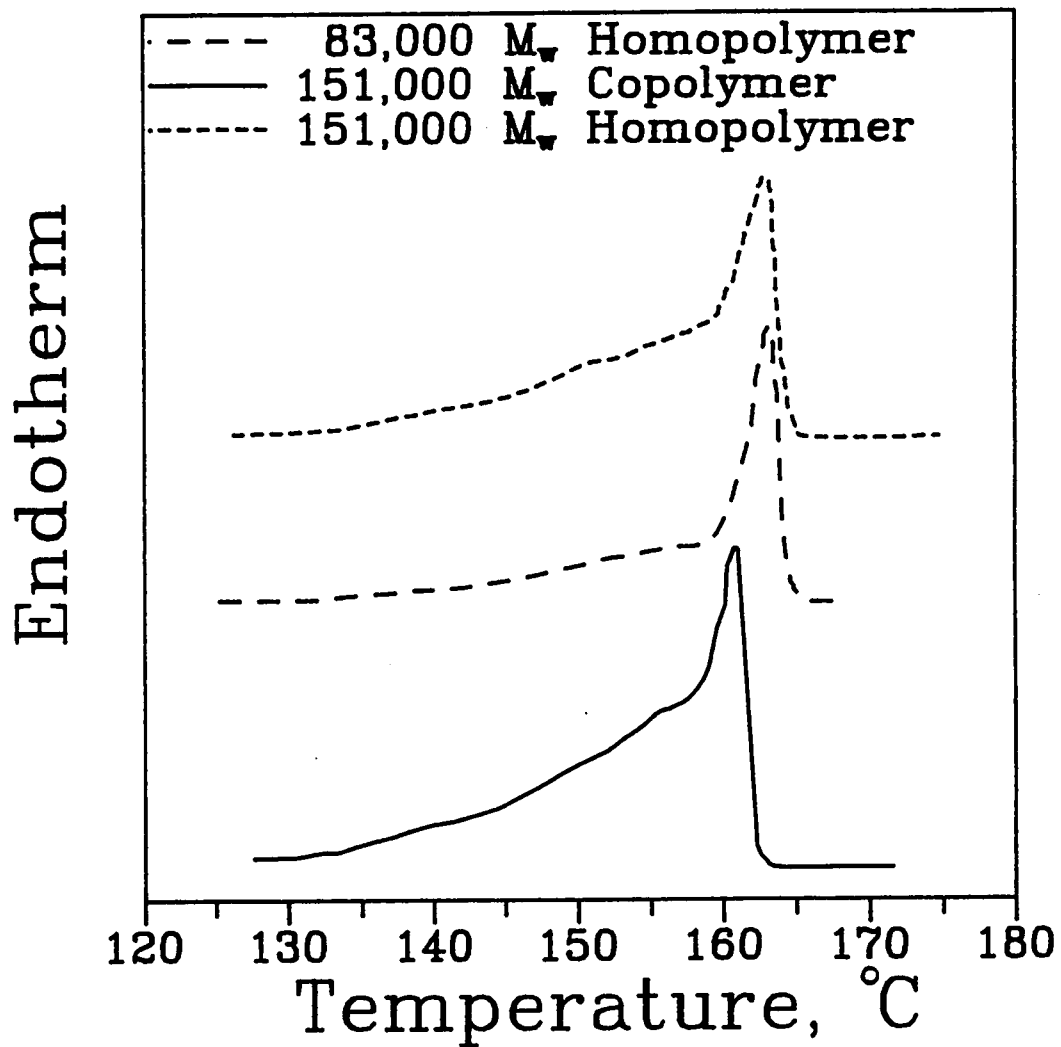


Figure 4.20 Comparison of DSC melting behavior at 10°C/min heating rate for isotactic polypropylenes isothermally crystallized at $T_c = 130^\circ\text{C}$.

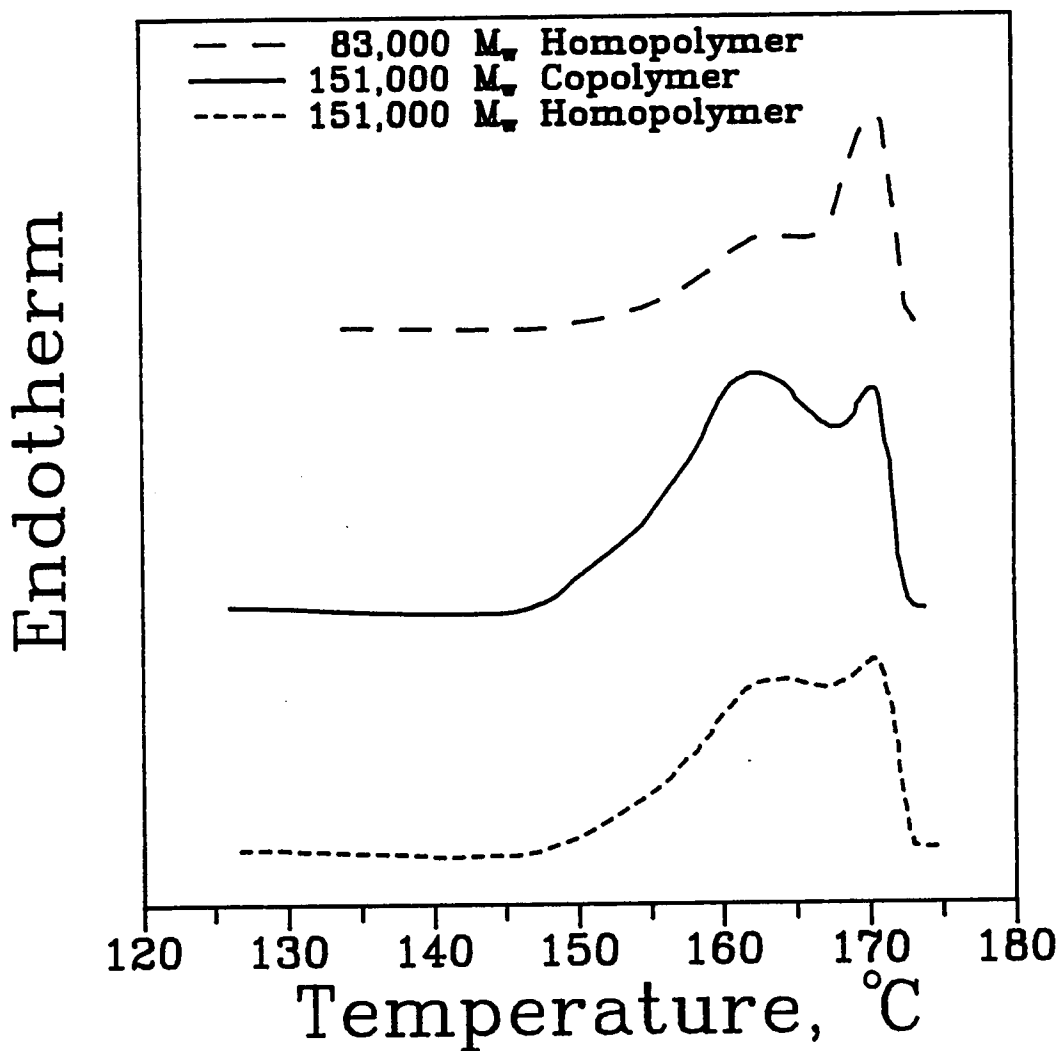


Figure 4.21 Comparison of DSC melting behavior at 10°C/min. heating rate for isotactic polypropylenes isothermally crystallized at $T_c = 146^\circ\text{C}$.

Heating rate has a significant effect on the observed DSC melting behavior for polypropylene. Figure 4.22 shows the effect of heating at three constant rates of 1°, 3°, and 10°C/min. on the DSC behavior of the $M_w = 83,000$ homopolymer crystallized at 130°C. At a 10°C/min. heating rate, the DSC exhibited a significant low temperature shoulder, with a relatively sharp peak at 163.2°C. At a heating rate of 3°C/min., a low temperature shoulder still existed but the sharp peak had shifted to lower temperatures and a high temperature shoulder now exists. The peak maximum occurred at 159.3°C, a shift of approximately 4°C for the 10°C/min. scan. At a heating rate of 1°C/min., the DSC exhibited a distinct low temperature shoulder and two distinct peaks, the low temperature peak maximum at 160.0°C and the high temperature peak maximum at 165.0°C. The low temperature peak maximum was close to that of the 3°C/min. scan. However, the high temperature peak maximum was higher than that of the 10°C/min. scan.

Elevated Pressure

Differential scanning calorimetry at atmospheric pressure was performed on a series of elevated pressure crystallized samples. The samples were prepared at a fixed supercooling of 50° with the crystallization temperature at a given pressure determined by the equilibrium melting temperature at that pressure. The equilibrium melting

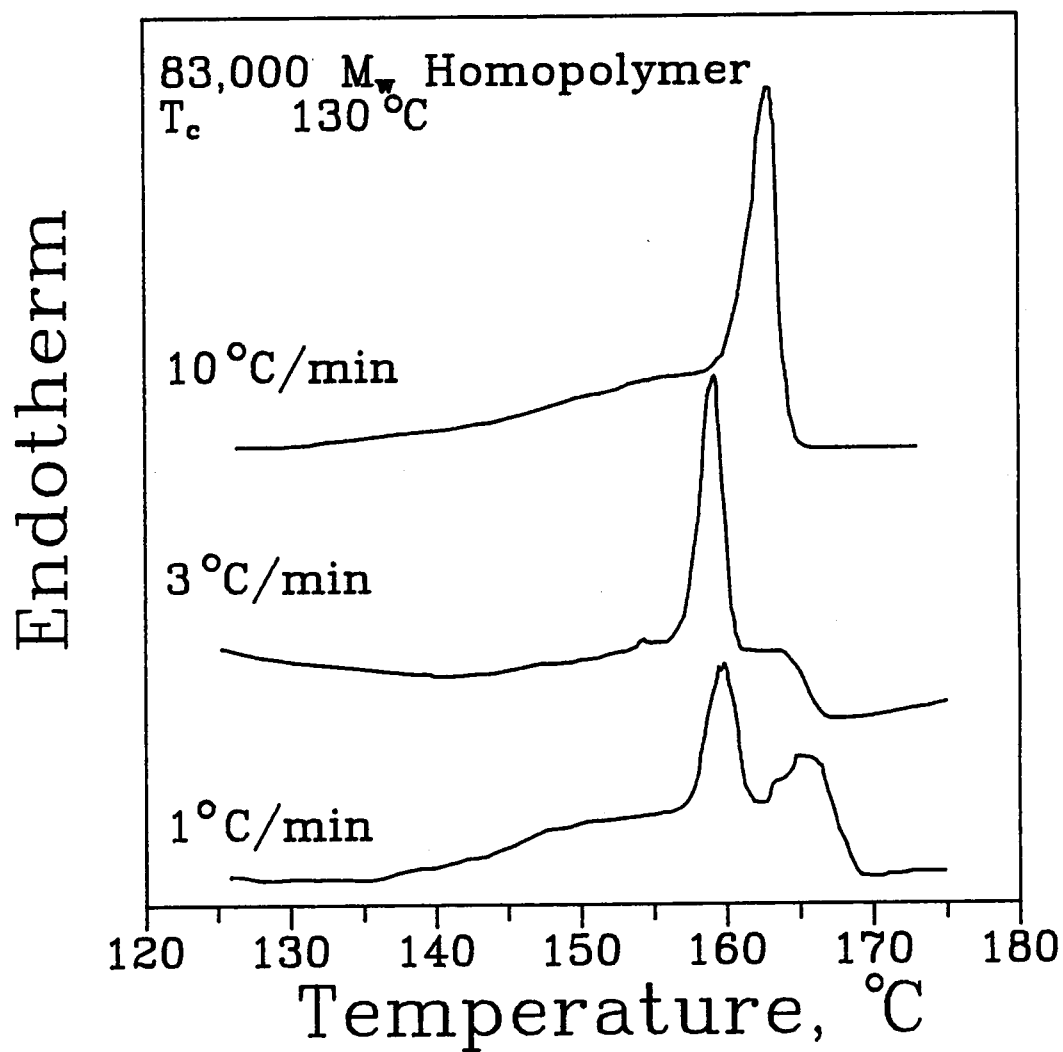


Figure 4.22 Heating rate effect on DSC melting behavior for isotactic polypropylene homopolymer $M_w = 83,000$ isothermally crystallized at $T_c = 130^\circ\text{C}$.

temperature at each pressure was determined *a priori* using T_m versus T_c data obtained from DLI bulk crystallization/melting experiments. Figure 4.23 shows the DSC behavior at a heating rate of $10^\circ\text{C}/\text{min}$. for samples crystallized at several pressures. It was seen that, as the crystallization pressure increases, the endotherm changed shape. The region below the peak melting temperature for atmospheric became an increasingly distinct shoulder with increasing pressure. By 150 MPa, this shoulder became the dominant peak. The high temperature peak did not completely disappear. This behavior was similar to that reported in the literature for polypropylene [53,83]. Kardos et al. attributed the low temperature peak in DTA experiments to the γ modification of polypropylene. They showed that with increasing heat rate, the peak associated with the γ form increased. At low heating rates ($<10^\circ\text{C}/\text{min}$.), two peaks were observed for a sample slow-cooled at 500 MPa. This sample showed only one peak at a heat rate of $40^\circ\text{C}/\text{min}$.

Figure 4.24 shows the DSC behavior of pressure crystallized polypropylene, $M_w = 83,000$, at a heating rate of $40^\circ\text{C}/\text{min}$. For pressures below 100 MPa, the DSC endotherms for heating rates of $10^\circ\text{C}/\text{min}$. and $40^\circ\text{C}/\text{min}$. were qualitatively similar. For pressures of 100 MPa and above, the heating rate had a more significant effect on the shape of the endotherm.

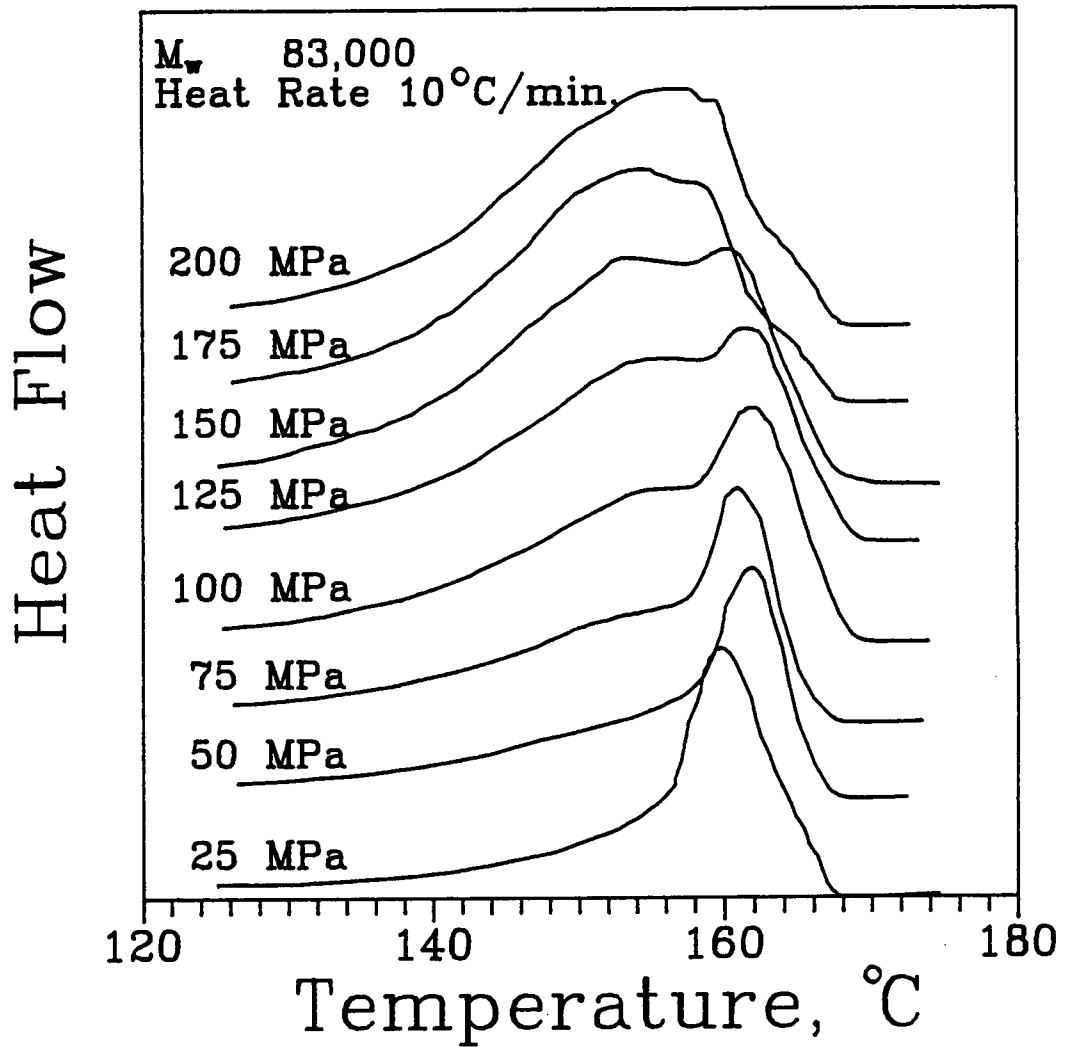


Figure 4.23 DSC melting behavior of isotactic polypropylene homopolymer $M_w = 83,000$ crystallized at fixed supercooling $\Delta T = 50^\circ$ at several crystallization pressures. Heating Rate = $10^\circ\text{C}/\text{min}$.

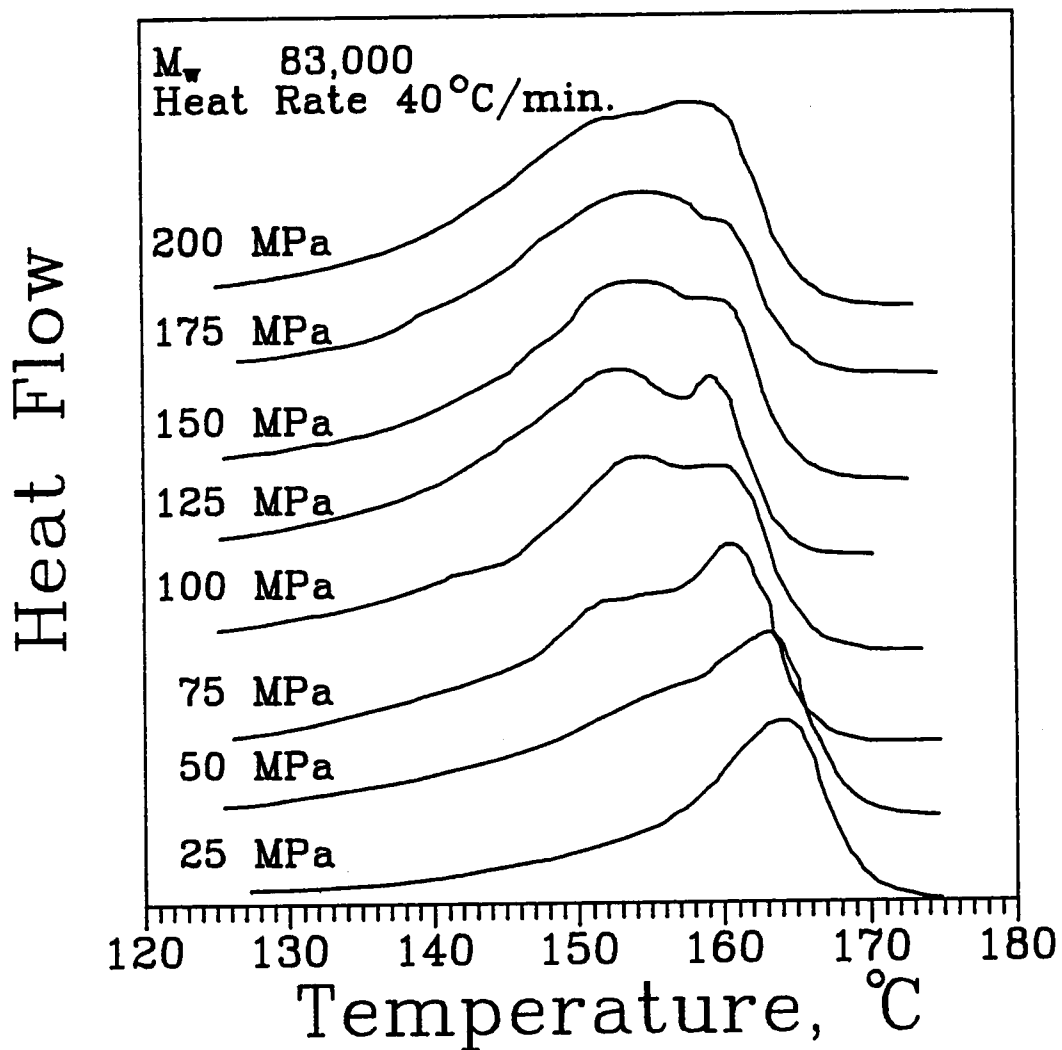


Figure 4.24 DSC melting behavior of isotactic polypropylene homopolymer $M_w = 83,000$ crystallized at fixed supercooling $\Delta T = 50^\circ$ at several crystallization pressures. Heating Rate = 40°C/min.

4.2.2 Depolarized Light Intensity

Atmospheric Pressure

The depolarized light intensity technique can be used to study the melting behavior of polymers [84]. An advantage of the DLI technique is that it allows simultaneous recording of depolarized light intensity and optical micrographs during crystallization and melting. This allows one to correlate the morphological changes that occur during crystallization or melting with the thermal transitions.

The DLI melting experiments were performed following the DLI bulk crystallization experiments. Thus after following the isothermal crystallization to the end of the primary crystallization, the sample was then heated at a given constant heating rate and the light intensity recorded as a function of temperature through melting of the sample. A series of simultaneous DLI and optical microscopy was also performed in order to directly compare DSC and DLI with the observed morphology and to correlate the DSC and DLI thermal behaviors.

Figure 4.25 displays typically observed DLI melting behavior for iPP isothermally crystallized at various temperatures. On initial heating from the crystallization temperature, there was an increase in the observed light intensity. This increase was partially attributed to a change in sample thickness due to thermal expansion.

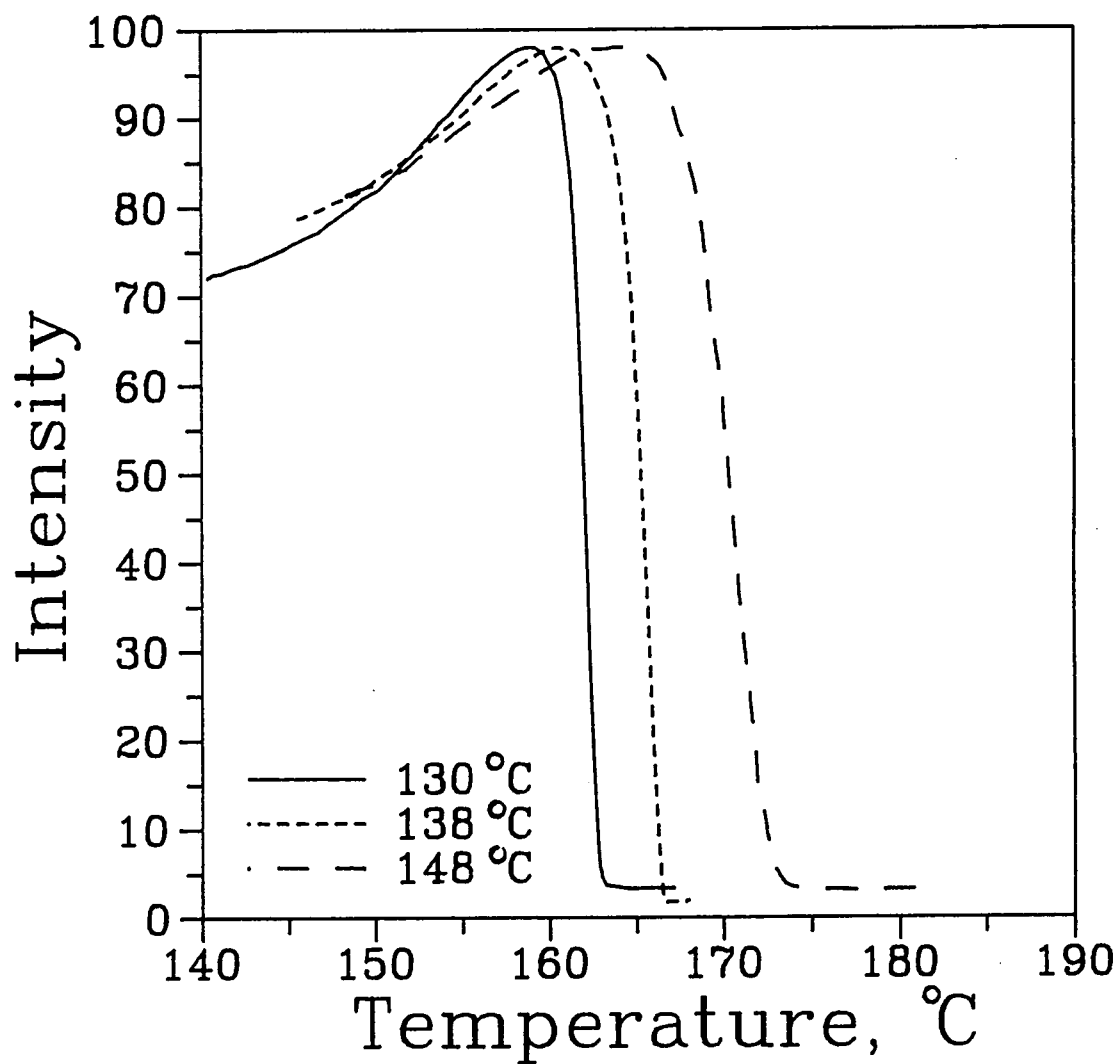


Figure 4.25 DLI melting behavior of isotactic polypropylene homopolymer $M_w = 83,000$ isothermally crystallized at various temperatures. Heating Rate = $10^\circ\text{C}/\text{min}$.

However, this increase was also a result in the change in the internal structure of the spherulites [85]. After reaching the maximum, the light intensity dropped sharply. Occasionally, the intensity exhibited a plateau before the final baseline. Visual observations indicated that this initial plateau was not associated with the final melting.

Figure 4.26 shows the effect of heating rate on the observed DLI melting behavior for isotactic polypropylene $M_w = 83,000$ isothermally crystallized at $T_c = 130^\circ\text{C}$. It is seen that increasing the heating rate shifts the observed melting temperature to lower temperatures. Also, the $1^\circ\text{C}/\text{min}$. heating rate scan exhibits a small plateau region prior to the final melting that is not observed at the other heating rates.

Figure 4.27 compares the DLI melting behavior of the $M_w = 83,000$ homopolymer and the $M_w = 151,000$ copolymer. The observed melting behavior for an isothermal crystallization temperature of 130°C is similar for the two samples, with the intensity maximum occurring at near the same temperature and the return-to-baseline melting at essentially the same temperature. The DSC peak melting temperatures for the two samples, while different than the return-to-baseline melting determined from DLI, are also essentially the same temperature.

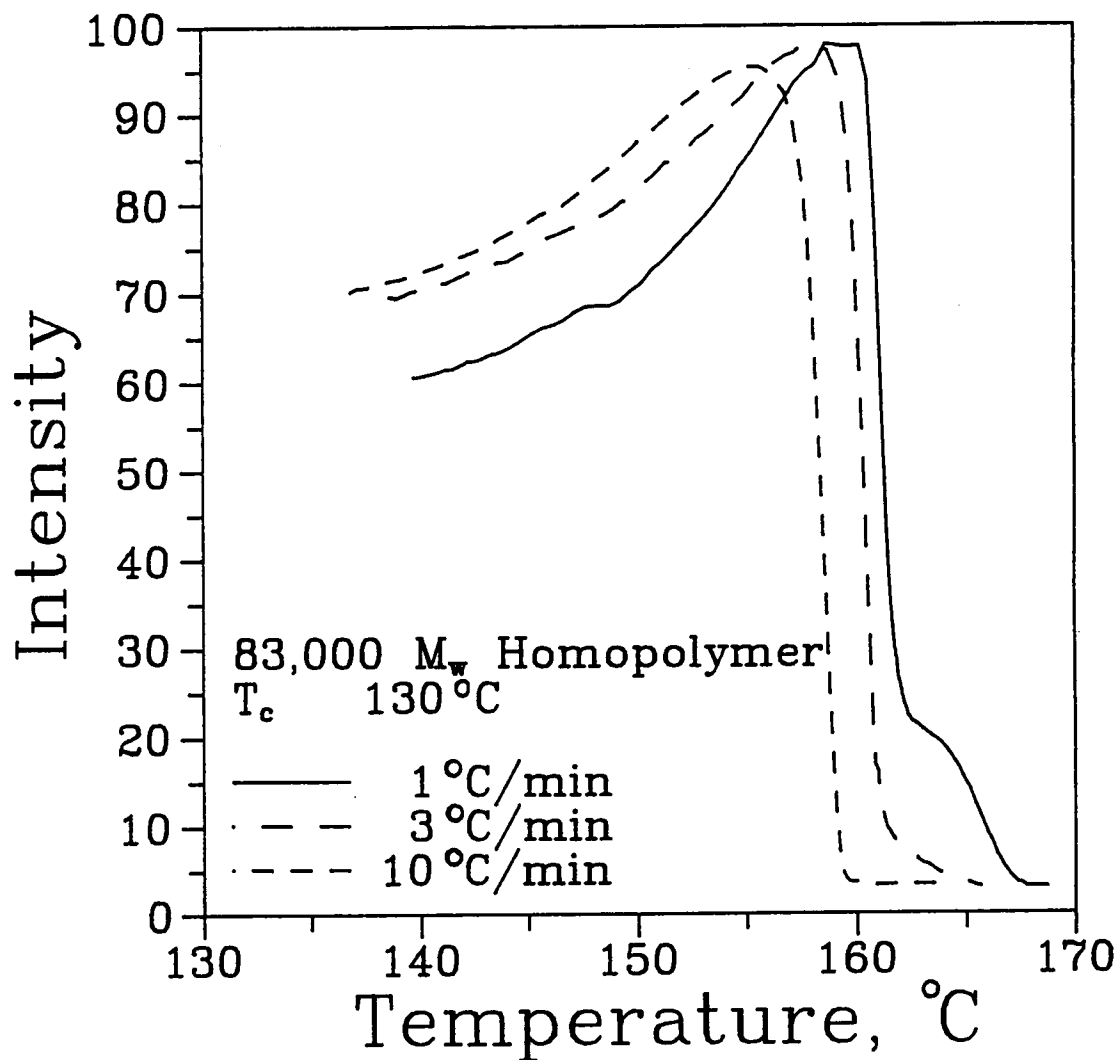


Figure 4.26 DLI melting behavior as a function of heating rate for isotactic polypropylene homopolymer $M_w = 83,000$ isothermally crystallized at $T_c = 130^\circ\text{C}$.

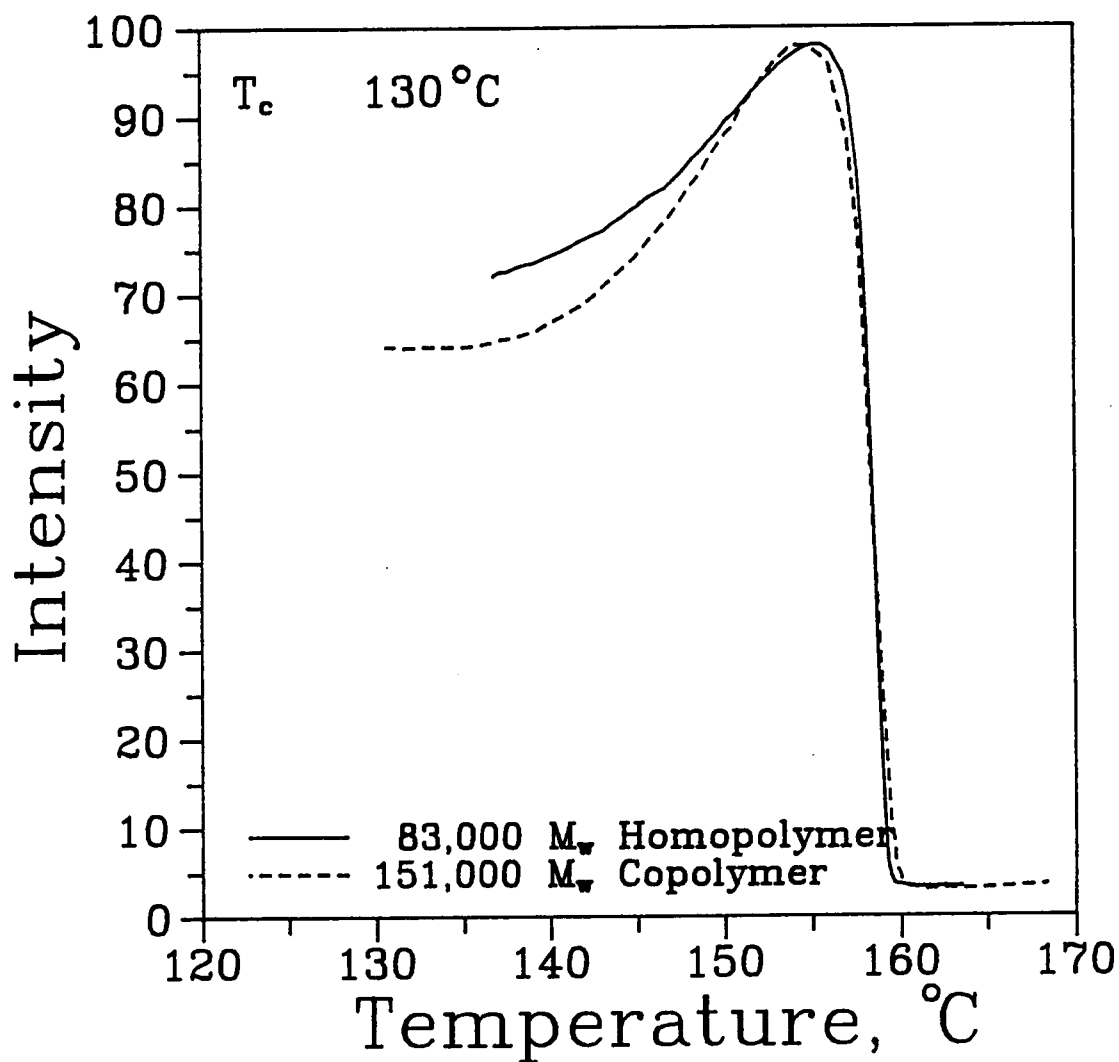


Figure 4.27 DLI melting behavior for isotactic polypropylenes isothermally crystallized at $T_c = 130^\circ\text{C}$. Heating Rate $10^\circ\text{C}/\text{min}$.

Elevated Pressure

Two sets of DLI experiments were performed on pressure crystallized samples. One set consisted of melting the samples at the crystallization pressure after isothermal crystallization. This allowed quantification of the equilibrium melting temperature as a function of pressure. The second set of DLI experiments consisted of melting the elevated pressure crystallized samples at atmospheric pressure. Depolarized light intensity was recorded on heating at a fixed rate at atmospheric pressure for pressure crystallized samples to correlate with the differential scanning calorimetry. After the initial melt, the sample was recrystallized either by cooling from the melt at a fixed rate or by isothermal crystallization to evaluate the effect of elevated pressure on the sample's behavior. Figure 4.28 shows the DLI behavior of samples isothermally crystallized at various pressures at fixed supercooling $\Delta T = 50^\circ$. As seen in Figure 4.28, the 25 MPa crystallized sample behaved qualitatively similar to the atmospheric pressure crystallized sample. Both exhibited an intensity decrease to a plateau, followed by an increase in intensity to a maximum and then a rapid decrease through the return-to-baseline. The 50 MPa crystallized sample showed a slight shoulder on the decreasing intensity portion of the curve in a temperature region similar to the 25 MPa sample. The 100 MPa

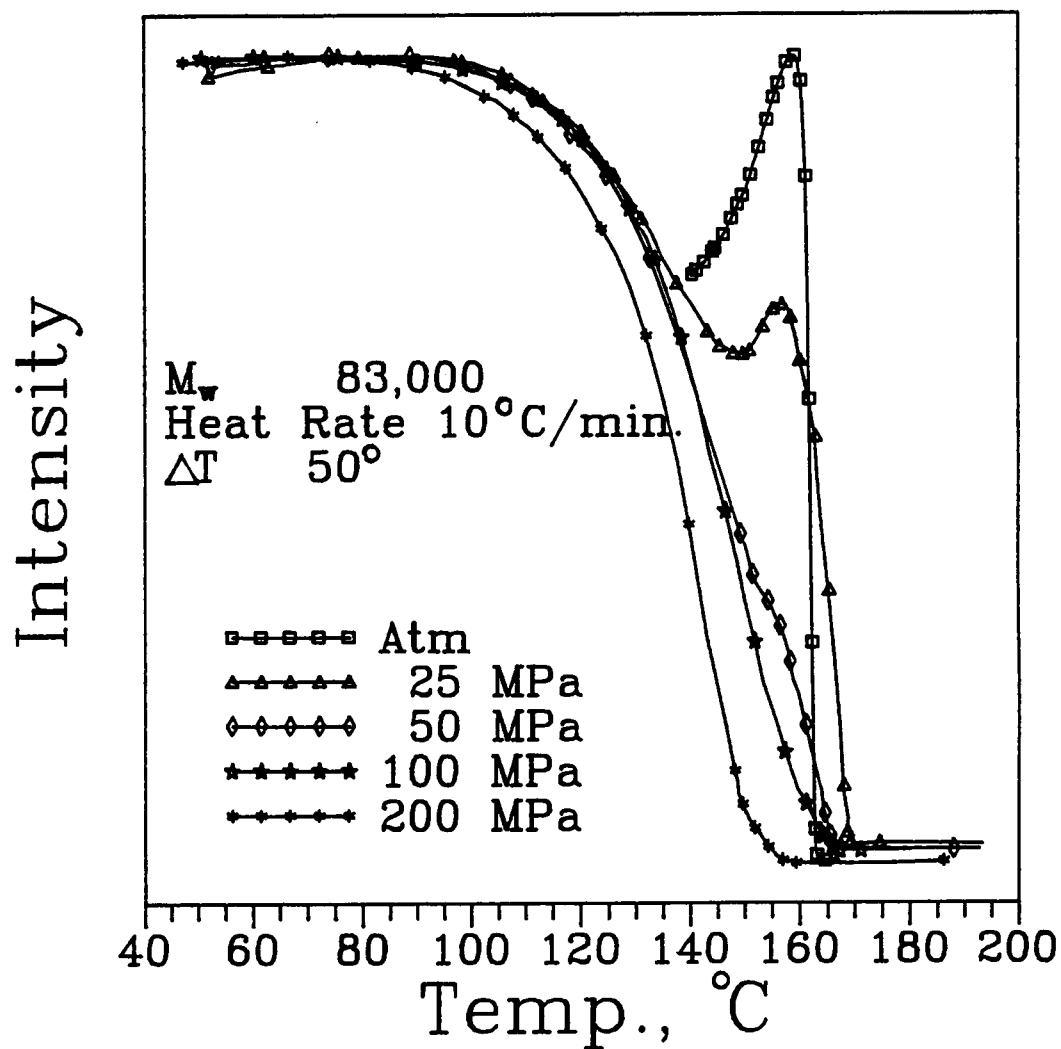


Figure 4.28 DLI melting behavior of isotactic polypropylene crystallized at fixed supercooling $\Delta T = 50^\circ$ for several crystallization pressures. Heating Rate = $10^\circ\text{C}/\text{min.}$ Melting performed at atmospheric pressure.

and 200 MPa crystallized samples showed only a continuous decrease to the return-to-baseline after the intensity maximum.

Figure 4.29 shows the DLI behavior at atmospheric pressure of the initial melt of a 200 MPa pressure crystallized sample and the remelt of the sample after isothermal crystallization at $T_c = 130^\circ\text{C}$. The remelt behavior was distinctly different than that of the initial melt of the pressure crystallized sample and from that observed for an atmospheric pressure crystallized sample. The remelt exhibited a more complex light intensity trace than an atmospheric melt in that it had a shoulder region and plateau region on the initial intensity decrease region. This was followed by an intensity increase in the temperature region similar to that of the atmospheric melt. On the final decreasing intensity region, there was a slight shoulder atypical of an atmospheric melt. In observing the morphology of the recrystallized pressure crystallized samples, a larger amount of the material crystallized in the β form in comparison to the material crystallized only at atmospheric pressure. Figure 4.30 shows the morphology of the 200 MPa crystallized sample, the recrystallized (at atmospheric pressure) sample, and the atmospheric pressure crystallized sample.

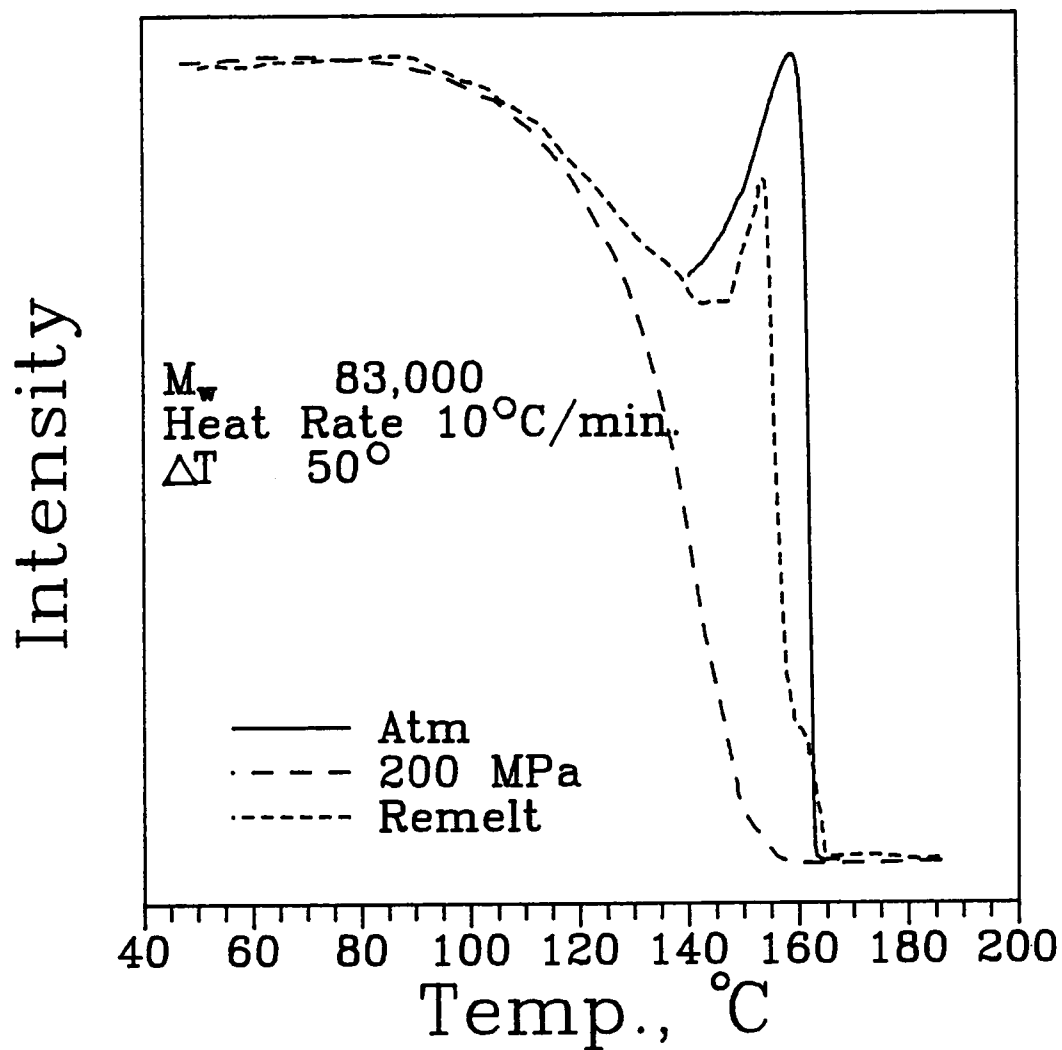


Figure 4.29 DLI melting behavior of isotactic polypropylene crystallized at fixed supercooling $\Delta T = 50^\circ$ at 200 MPa. Heating rate = $10^\circ\text{C}/\text{min.}$ Melting performed at atmospheric pressure.

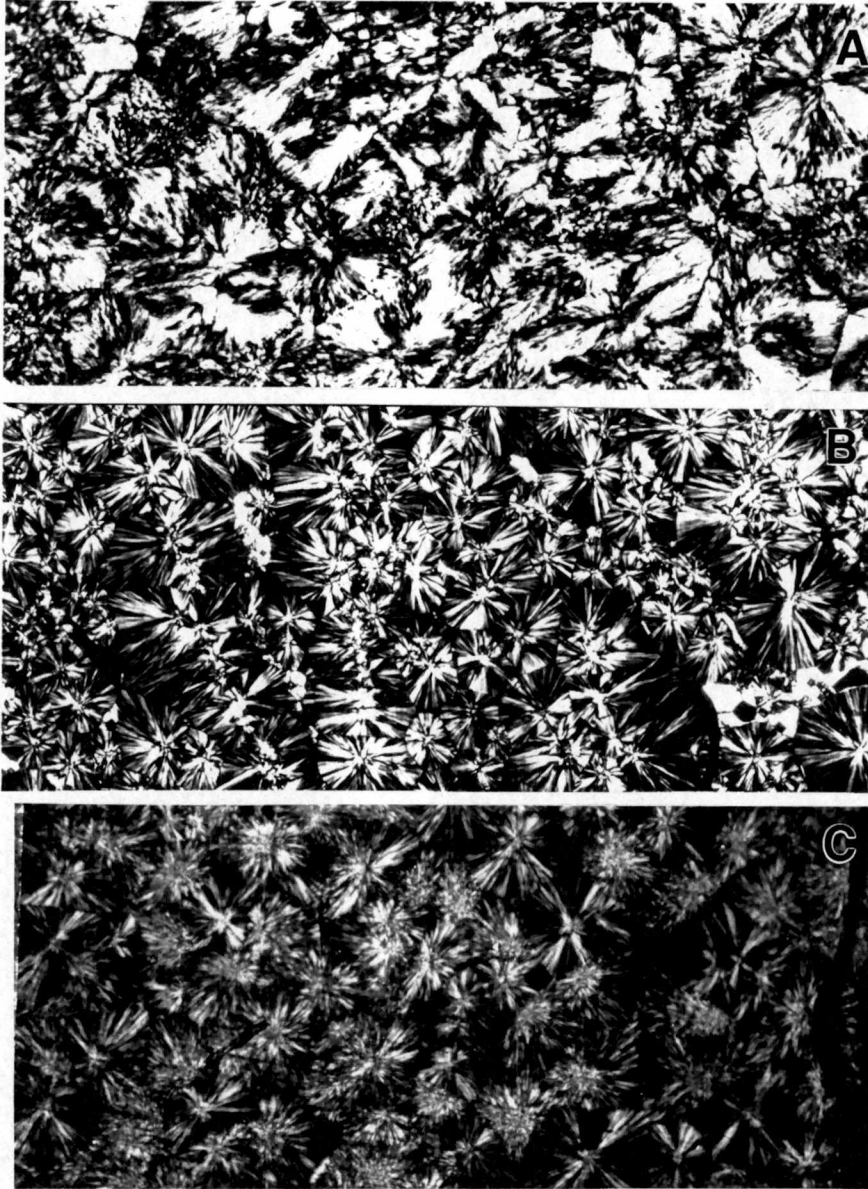


Figure 4.30 Optical morphology of A. 200 MPa crystallized sample ($\Delta T = 50^\circ$); B. recrystallization of (A.) at atmospheric pressure, ($\Delta T = 50^\circ$); C. atmospheric pressure crystallized ($\Delta T = 50^\circ$)

The light intensity versus temperature curves for samples isothermally crystallized and melted at elevated pressures are shown in Figures 4.31, 4.32, 4.33 and 4.34 for crystallization pressures of 25, 50, 75, and 100 MPa, respectively. All heating rates were 3°C/min. The nature of the elevated pressure DLI melting behavior of the 25 MPa crystallized samples was more complex than that of the other elevated pressures in that it exhibited more maxima and minima in intensity. The elevated pressure melting behavior of the 50 MPa and 100 MPa pressure crystallized samples was qualitatively similar. The 50 MPa data did show some evidence of an intensity plateau prior to the final melting that was not observed in the 100 MPa data. The 100 MPa data showed little intensity increase on heating before the rapid intensity decrease on melting. The 75 MPa data exhibited a more significant intensity increase on heating than that of the 50 MPa or 100 MPa data. However, the 75 MPa data was similar to the 100 MPa data since it did not exhibit any intensity plateau.

In comparing the observed DSC melting behavior at atmospheric pressure for the pressure crystallized samples to the observed DLI melting behavior at elevated pressure for these samples, it is seen that the DLI behavior in general show a sharp melting transition with no plateau in intensity prior to the final melting. The DSC shows an increase in a

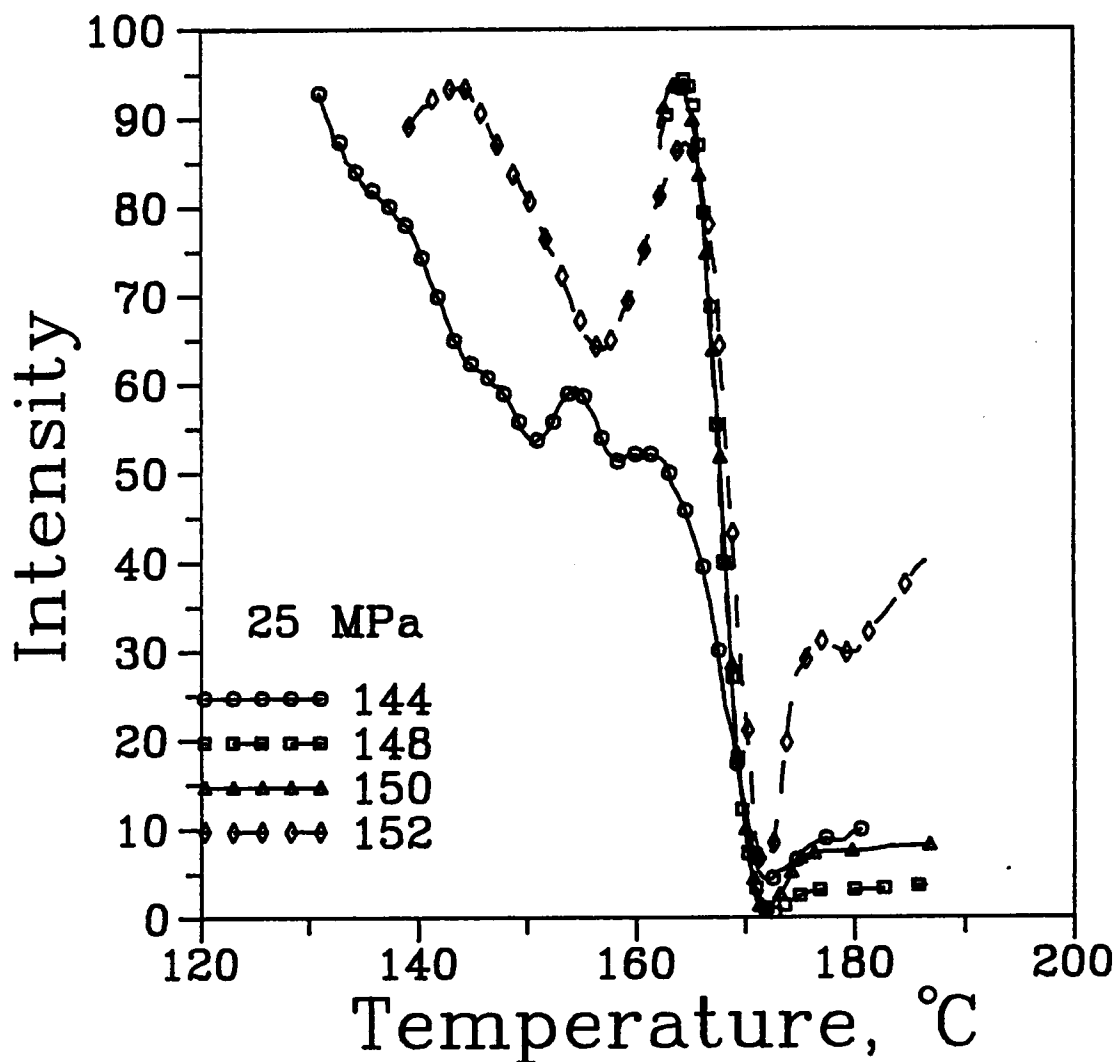


Figure 4.31 DLI melting behavior of isotactic polypropylene homopolymer $M_w = 83,000$ isothermally crystallized at 25 MPa crystallization pressure; various temperatures. Heating rate $3^\circ\text{C}/\text{min}$. Melted at 25 MPa.

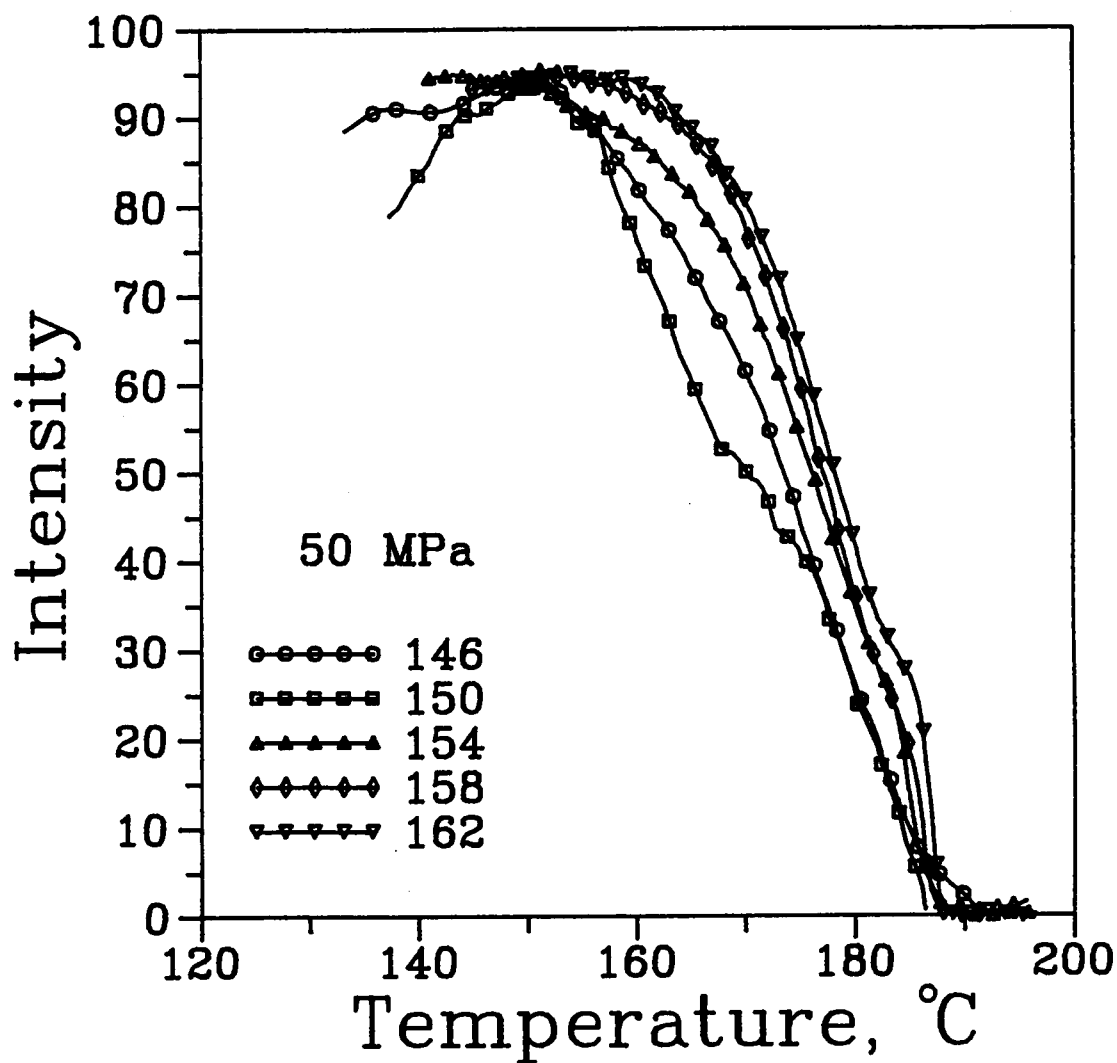


Figure 4.32 DLI melting behavior of isotactic polypropylene homopolymer $M_w = 83,000$ isothermally crystallized at 50 MPa crystallization pressure; various temperatures. Heating rate $3^\circ\text{C}/\text{min}$. Melted at 50 MPa.

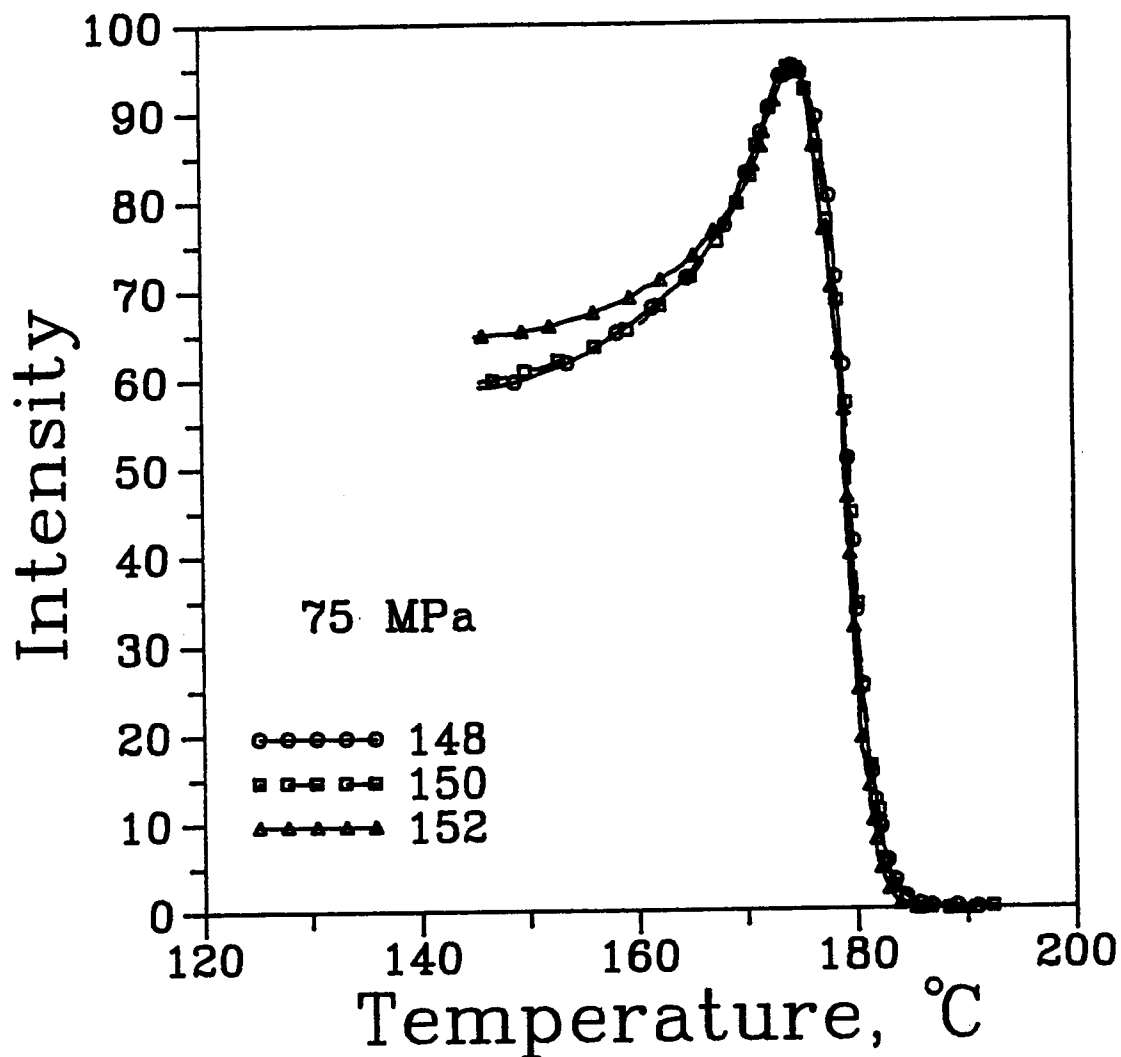


Figure 4.33 DLI melting behavior of isotactic polypropylene homopolymer $M_w = 83,000$ isothermally crystallized at 75 MPa crystallization pressure; various temperatures. Heating rate $3^\circ\text{C}/\text{min}$. Melted at 75 MPa.

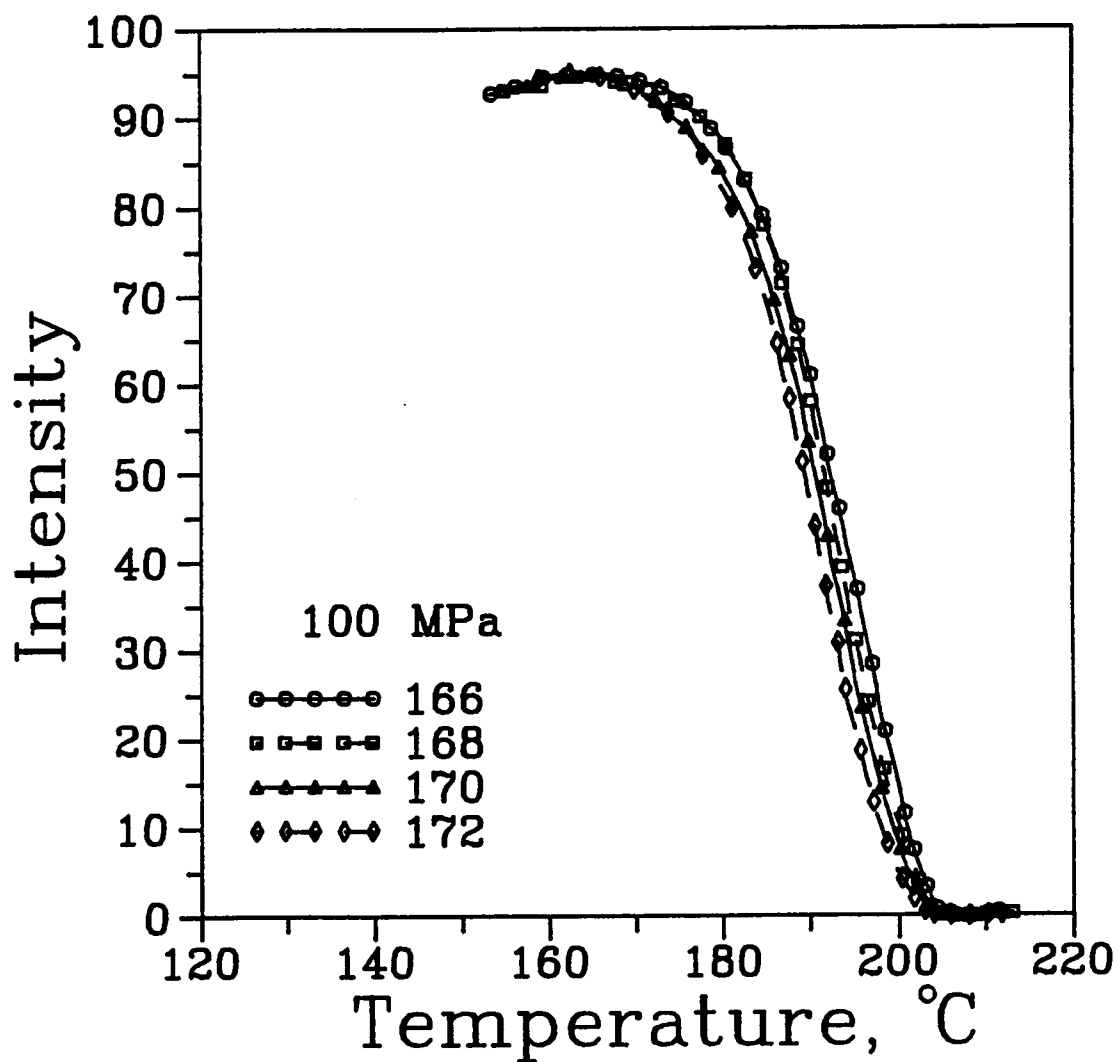


Figure 4.34 DLI melting behavior of isotactic polypropylene homopolymer $M_w = 83,000$ isothermally crystallized at 100 MPa crystallization pressure; various temperatures. Heating rate $3^\circ\text{C}/\text{min}$. Melted at 100 MPa.

flower temperature peak with increasing pressure. The 25 MPa data and to some extent the 50 MPa data show some evidence of multiple melting behavior in the elevated pressure DLI melting. The 75 MPa and the 100 MPa data do not show any evidence of this, but show rather sharp melting transitions.

4.3 Morphology

4.3.1 Atmospheric Pressure

Function of Crystallization Temperature

The morphology of the polypropylene samples observed with the optical microscope showed distinct differences as a function of crystallization temperature. The observed sign of the birefringence changed from positive at low crystallization temperatures, to negative at high temperatures with the change in sign occurring around 138°C. This agreed with literature data on the sign and magnitude of the birefringence of iPP [86] as a function of crystallization temperature which has been attributed to the lamellar composition [87]. At low crystallization temperatures, the ratio of radial lamellae to tangential lamellae is such that the birefringence is slightly positive. At high crystallization temperatures, the lamellar composition is such that the birefringence is negative. This lamellar composition effect has been correlated by electron

microscopy to the intrinsic birefringence of the polymer chain [88].

For the 151,000 M_w homopolymer, the birefringence at 130°C ($\Delta T = 55^\circ$) was mixed, with no distinct maltese cross under crossed polars (see Figure 4.35). Regions within a given spherulite varied in birefringence. This has been shown to correspond to a local variation in the compositions of radial and tangential lamellae [2]. At a crystallization temperature of 138°C ($\Delta T = 49^\circ$) the birefringence was somewhat less mixed but the maltese cross under crossed polars was still not distinct as shown in Figure 4.36. At 146°C ($\Delta T = 41^\circ$) the maltese cross was fully developed and the sign of the birefringence was negative (see Figure 4.37).

The 83,000 M_w homopolymer showed similar behavior to the 151,000 M_w homopolymer. Figure 4.38 shows the optical morphology of the low molecular weight homopolymer for several crystallization temperatures. At 130°C, the birefringence was mixed and the two homopolymers' morphological structures were qualitatively similar. At 138°C, the lower molecular weight homopolymer's birefringence appeared less mixed and the maltese cross was more distinct than the higher molecular weight homopolymer. The opposite statement could be made at $T_c = 146^\circ\text{C}$. However, the observed differences in the morphology between the bulk homopolymers was only slight. The density of the spherulites and

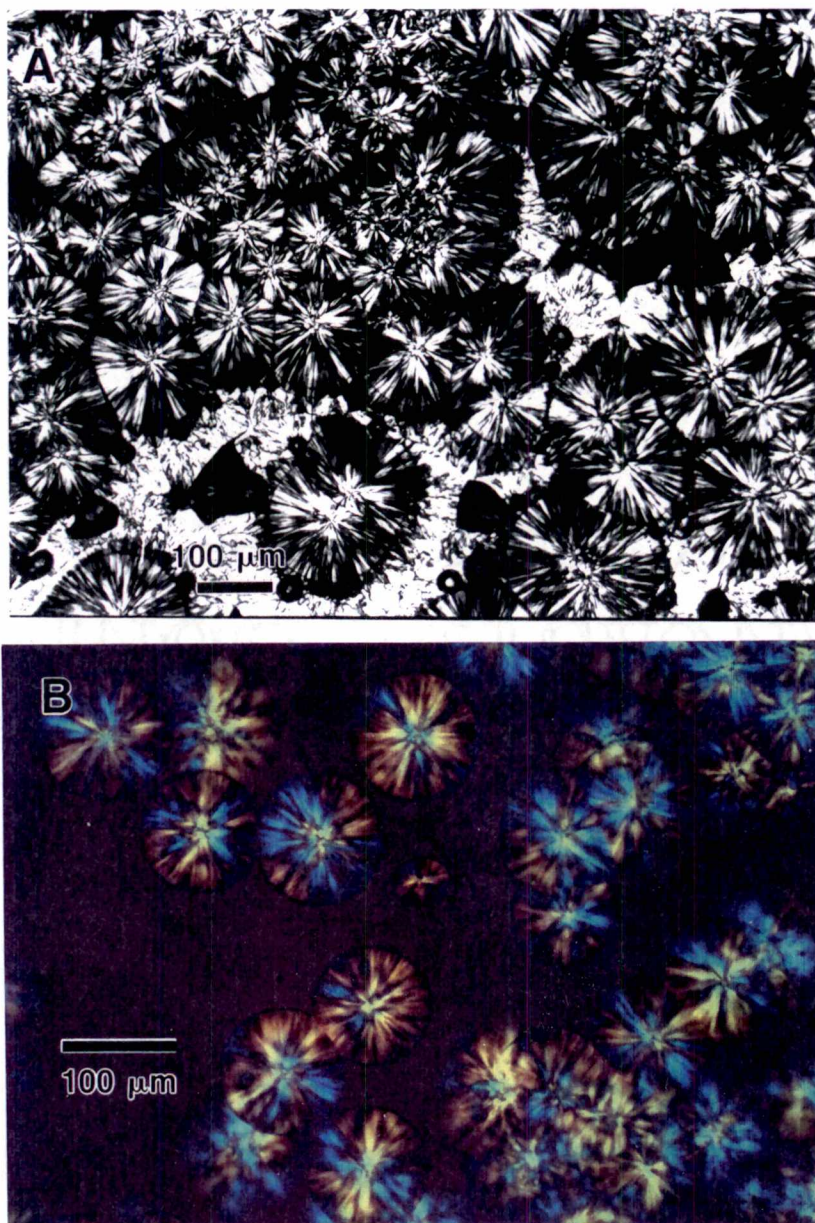


Figure 4.35 Optical micrographs of isotactic polypropylene homopolymer $M_w = 151,000$ isothermally crystallized at $T_c = 130^\circ\text{C}$ ($\Delta T = 57^\circ$): A. Crossed polars, B. Crossed polars, quarter wave plate.

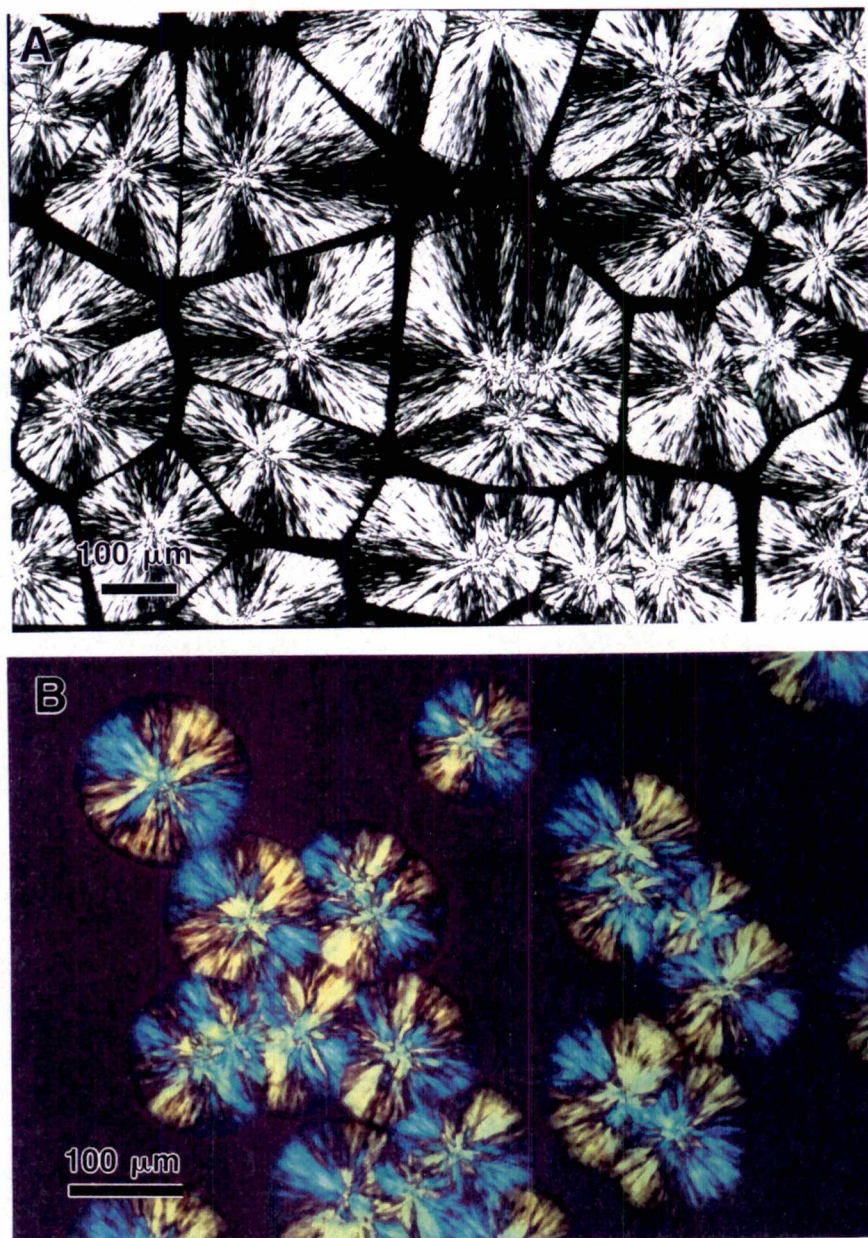


Figure 4.36 Optical micrographs of isotactic polypropylene homopolymer $M_w = 151,000$ isothermally crystallized at $T_c = 138^\circ\text{C}$ ($\Delta T = 49^\circ$): A. Crossed polars, B. Crossed polars, quarter wave plate.

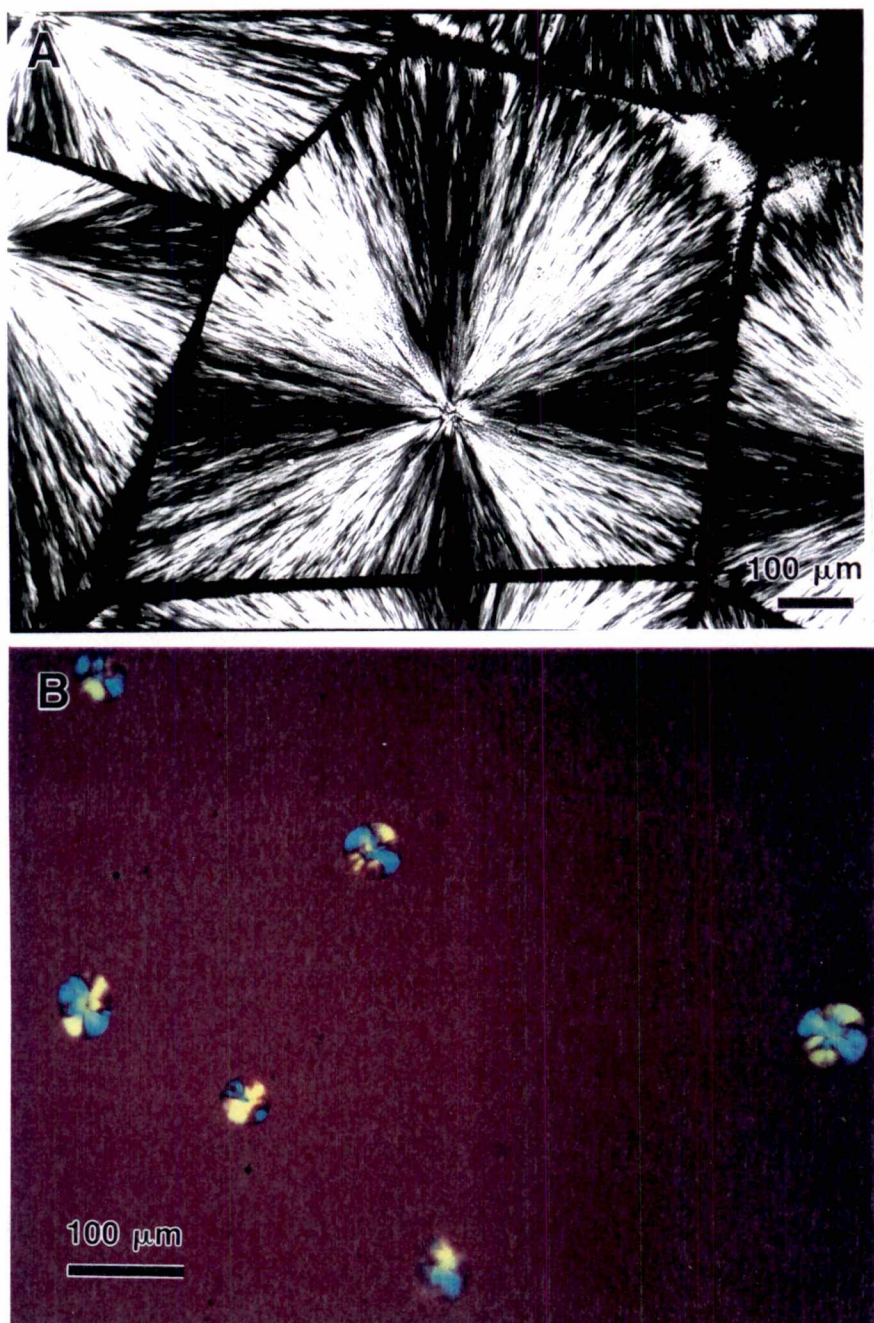


Figure 4.37 Optical micrographs of isotactic polypropylene homopolymer $M_w = 151,000$ isothermally crystallized at $T_c = 146^\circ\text{C}$ ($\Delta T = 41^\circ$): A. Crossed polars, B. Crossed polars, quarter wave plate.

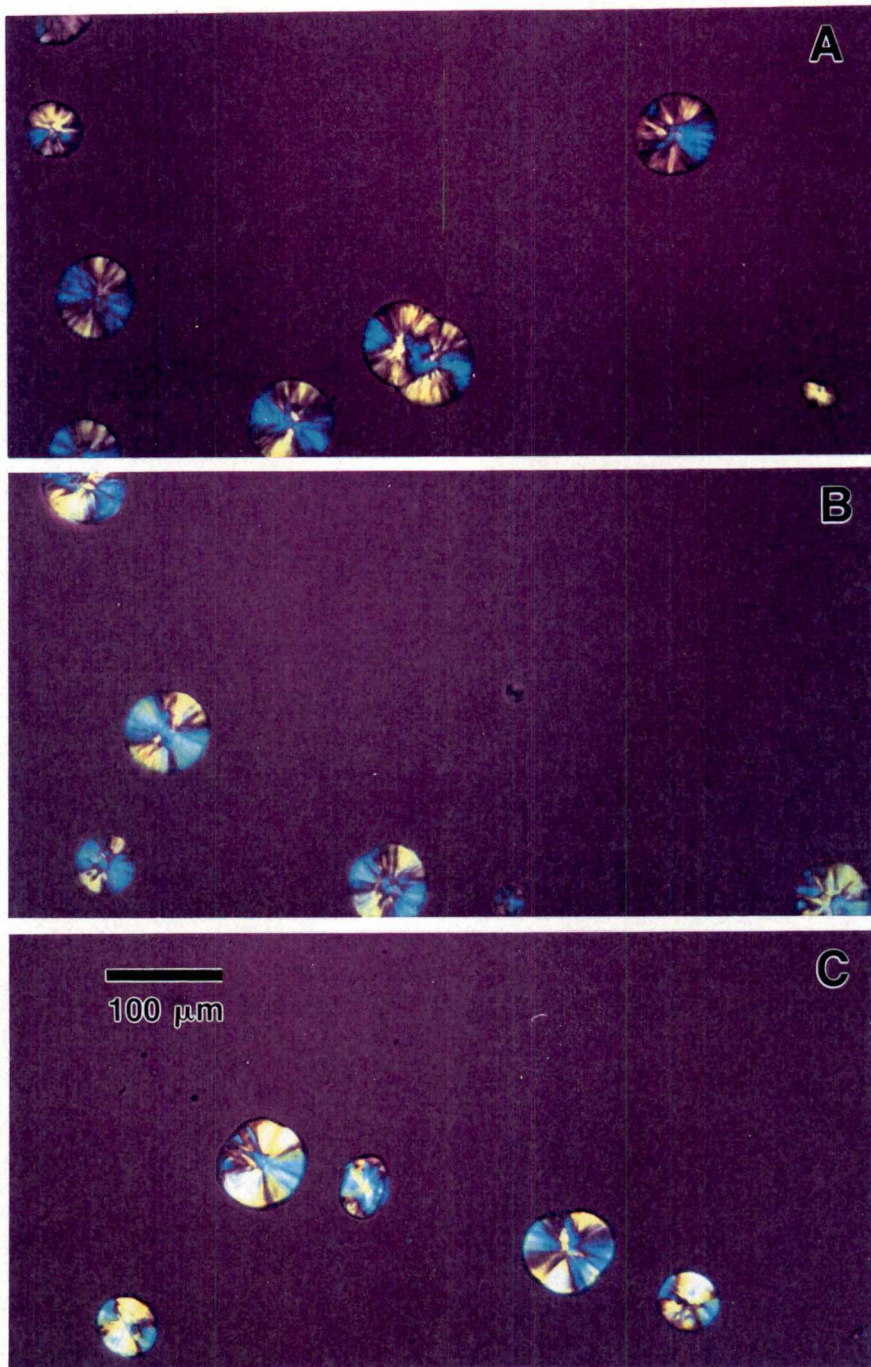


Figure 4.38 Optical micrographs of isotactic polypropylene homopolymer $M_w = 83,000$ as a function of crystallization temperature. A. $T_c = 130^\circ\text{C}$, B. $T_c = 138^\circ\text{C}$, C. $T_c = 146^\circ\text{C}$.

spherulitic diameters as a function of crystallization time were similar for the two homopolymers.

The copolymer's morphological trends were similar to those of the homopolymers. However, the spherulitic density and the spherulitic diameter as a function of crystallization time were both lower than the corresponding measurements for the homopolymers. Figure 4.39 shows the observed morphology of the copolymer for several crystallization temperatures. The copolymer exhibited a similar mixed birefringence to the homopolymers at $T_c = 130^\circ\text{C}$. The sign of the birefringence had changed by $T_c = 138^\circ\text{C}$ for the copolymer and a distinct maltese cross was observed under crossed polars. At 146°C , the observed morphologies of copolymer and homopolymers were similar. The sign of the birefringence was positive. The maltese cross was distinct in the three samples.

Morphology Development during Crystallization

A series of experiments was performed to study the spherulitic morphology development as a function of time at a given crystallization temperature. This experiment involved the simultaneous recording of the light intensity and the optical micrographs during crystallization. This then allowed the correlation of the development of morphology with the development of relative crystallinity in the system. Figure 4.40A shows the morphology observed under crossed polars and a full wave plate at a time just after initial

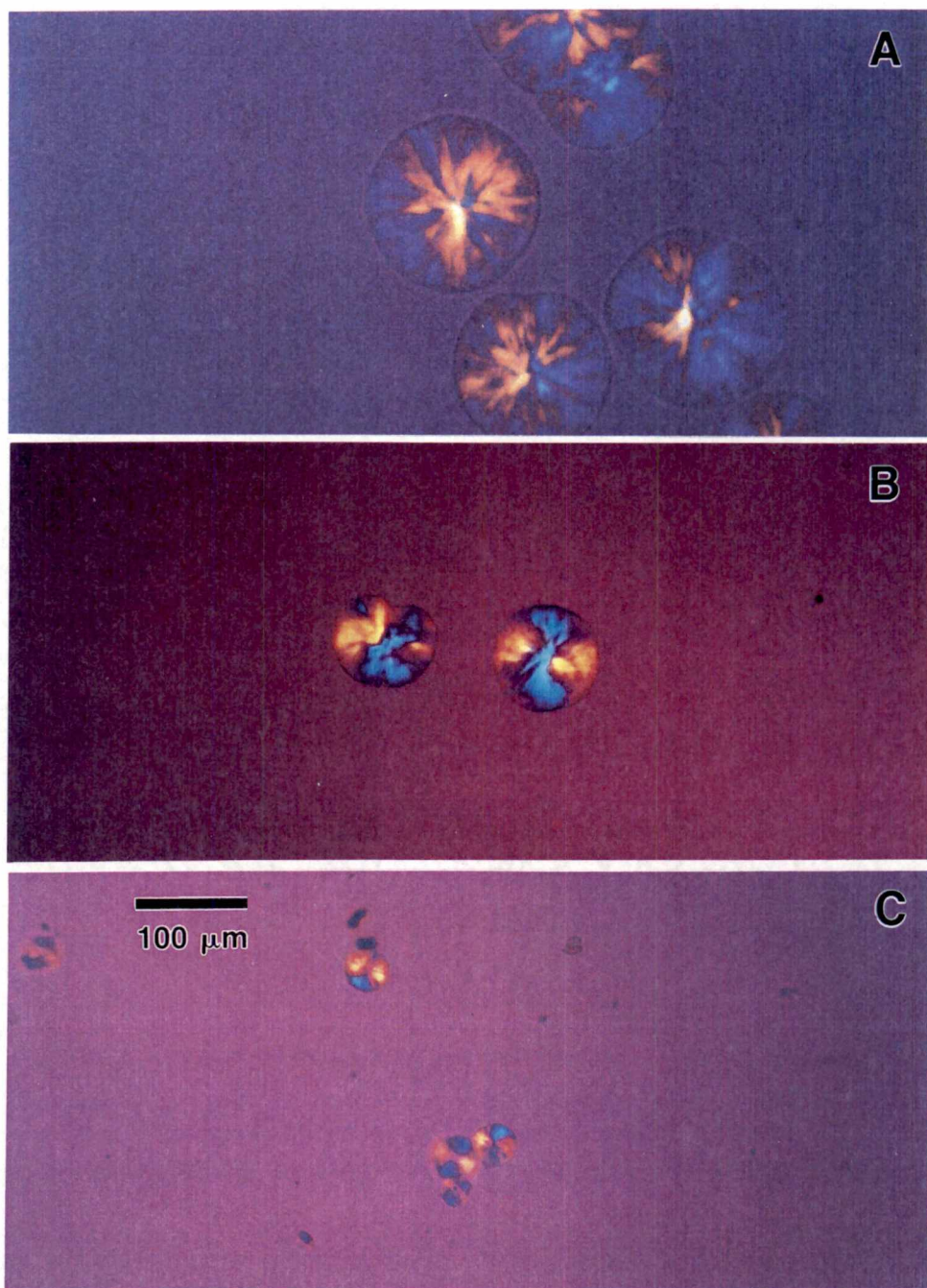


Figure 4.39 Optical micrographs of isotactic polypropylene copolymer $M_w = 151,000$ as a function of crystallization temperature A. $T_c = 130^\circ\text{C}$, B. $T_c = 138^\circ\text{C}$, C. $T_c = 146^\circ\text{C}$.

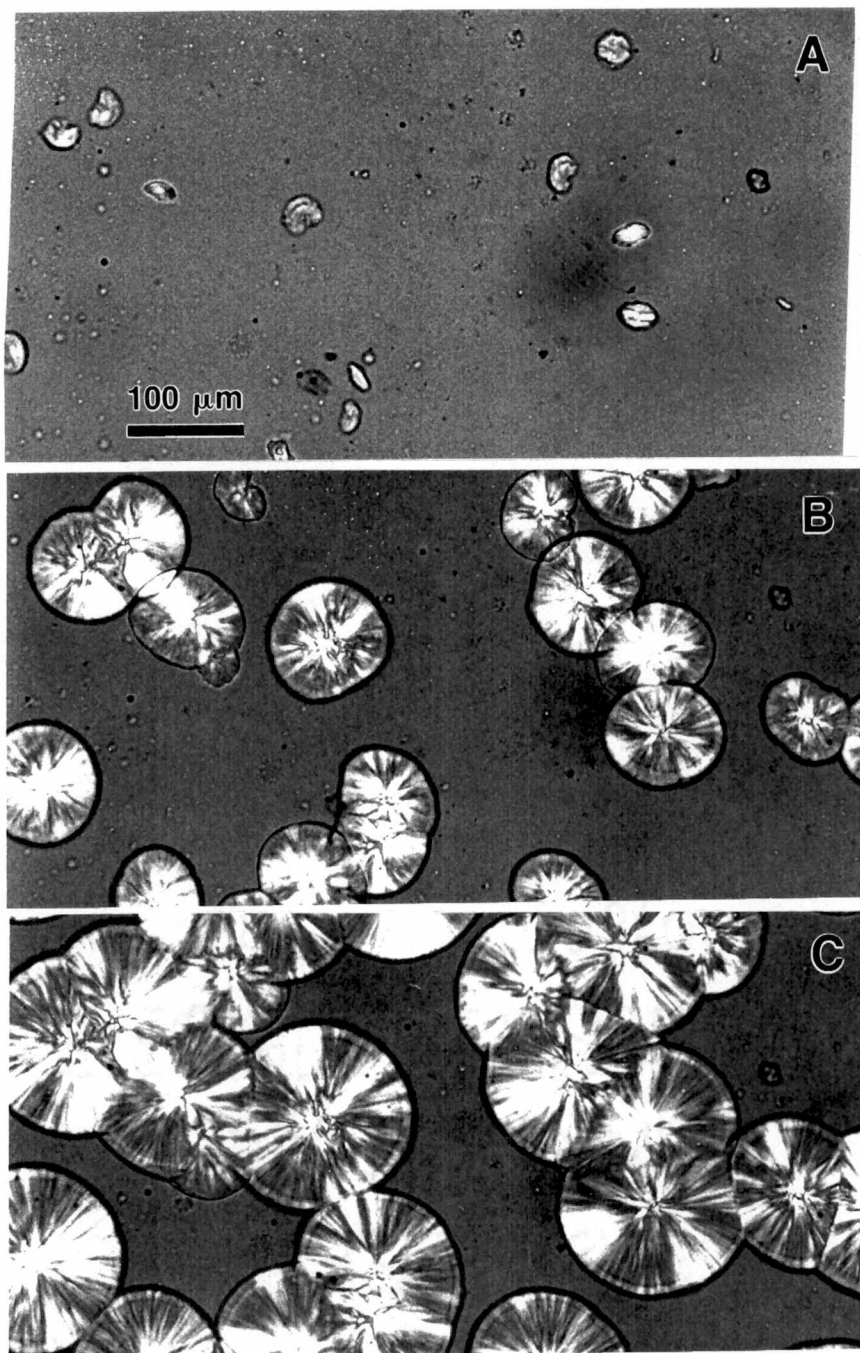


Figure 4.40 Optical micrographs of isotactic polypropylene homopolymer $M_w = 83,000$ as a function of crystallization time at $T_c = 130^\circ\text{C}$. A. $t_c = 0.8$ min., B. $t_c = 2.4$ min., C. $t_c = 4.5$ min.

fdetection of crystallinity by transmitted light intensity. At 130°C for the 83,000 M_w homopolymer, this time was about one minute. In the figure, it is seen that the entities are randomly distributed through the melt. Some appear approximately spherical, while others are ellipsoidal and still others exhibit an irregular geometry. At a relative crystallinity of 0.22, most of the entities from Figure 4.40A had assumed a nearly spherical shape (see figure 4.40B). The birefringence was mixed and impingement of spherulites was significant even at this level of crystallinity development. The interface between two impinged spherulites grew in a linear fashion, indicating that the growth rates of the two spherulites were approximately the same. As shown in Figure 4.40C, by the time the relative crystallinity had reached 0.59, all the growing spherulites were impinged with several other spherulites. This resulted in polyhedral shaped entities rather than true spherical shaped entities and had an effect on the rate of volume transformation of material. The severe impingement should have an effect on the bulk crystallization analysis, since interpreting the results of the analysis requires a known growth geometry. The behavior at other crystallization temperatures was similar, with changes in nucleation density and birefringence that have been discussed previously.

Morphology changes during Heating

The optical morphology was studied during melting experiments conducted at fixed heating rates. This allowed correlation of the morphological changes on heating with the observed DSC and DLI behaviors. The observed light intensity showed an initial increase on heating for all heating rates. This increase in intensity on heating has been partly attributed to the gradual melting of low molecular weight polymer at spherulite boundaries, melting within the spherulites, recrystallization, and changes in spherulite size [10]. At a heating rate of 10°C/min., it was seen that in comparing Figure 4.41B at 152°C to Figure 4.41A at the crystallization temperature 130°C, there was a subtle change in the structure of the spherulites. 152°C corresponds to a position below the maximum in the DLI trace, but below the onset temperature of the maximum melting peak in the DSC. Figure 4.41C shows the morphology at a temperature above the maximum in the DLI but below the maximum in the DSC. This shows more significant spherulite structural changes. Most changes appear to be internal rather than at spherulite boundaries. By 159°C, near the DLI return-to-baseline, interspherulitic changes are occurring as well as rapid internal structural changes with the spherulites (see Figure 4.41C). This temperature is still below the peak temperature in the DSC. The nature of the observed morphology on heating

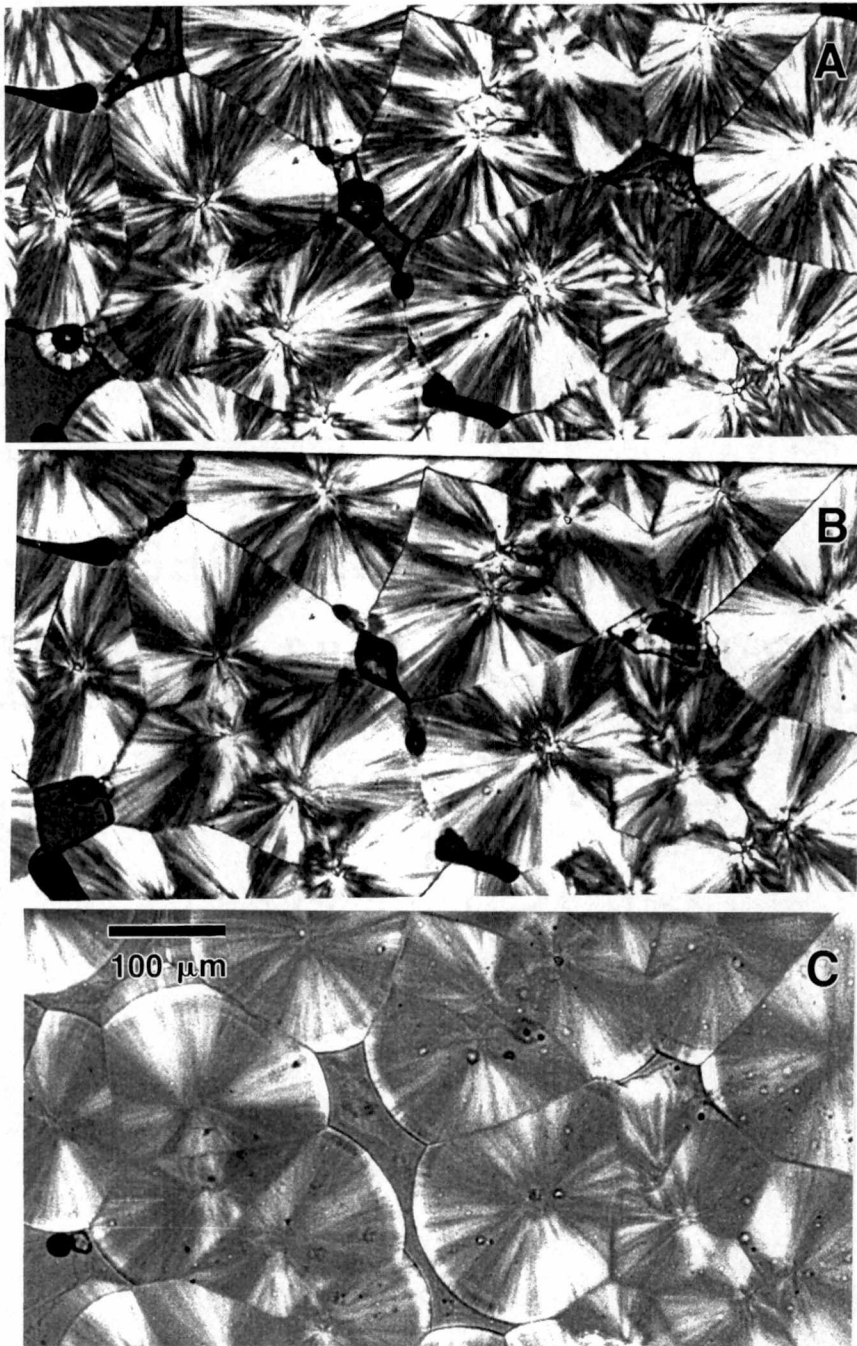


Figure 4.41 Optical micrographs of isotactic polypropylene homopolymer $M_w = 83,000$ morphology observed on heating from $T_c = 130^\circ\text{C}$ at $10^\circ\text{C}/\text{min}$. A. 130°C , B. 152°C , C. 159°C .

may indicate the melting of tangential branches in the sample prior to the melting of the dominant radial lamellae. It has been reported that the tangential lamellae are thinner than the radial lamellae and would thus melt at lower temperatures.

The relation between morphological changes and DSC and DLI behavior changed with heating rate. For a sample crystallized at 130°C and heated at 1°C/min., the observed morphology exhibits changes below the DLI peak. The DLI peak corresponded closely to the first peak melting temperature in the DSC. As with the 10°C/min. heating rate, the structure of the spherulites changed. More rapid changes occurred near the first plateau region of the DLI. This corresponded to the onset of the second melting peak in the DSC. Qualitatively, it appeared that the DLI return-to-baseline can be related to the onset of final melting in the DSC. This also appeared to be a temperature region where rapid morphological changes occurred, in intra- and interspherulitic structure. For a sample crystallized at 138°C, the spherulites showed changes on heating below the maximum in the light intensity. However, the more rapid morphological changes occurred after the DLI maximum but before the DSC peak temperature. For the large spherulites formed at 138°C, it was seen that on heating to the melting temperature, the spherulites 'skeletalize'; the spherulitic

boundaries remained distinct while the interior became increasingly faint. At present, it is not known whether this is a result of the variation in heat transfer across the spherulite or whether it is a result of variations within the spherulite resulting during crystallization.

4.3.2 Elevated Pressure

Function of Pressure

The morphology of the elevated pressure crystallized polypropylene samples showed obvious differences when compared to that of atmospheric pressure crystallized samples. Glass-knife microtomed sections of samples crystallized at a fixed supercooling of 50° were observed on the optical microscope under crossed polars. Figure 4.42 shows the optical micrographs of atmospheric crystallized and 25 MPa crystallized samples at a supercooling of 50° . Spherulite size and density were about the same and both show the mixed birefringence common to low T_c crystallized polypropylene. At 25 MPa, only a small portion of polypropylene has crystallized in the γ form (<10%). No distinct maltese cross is observed in either sample. This implied that the lamellar organization was similar for the two samples. For the 50 MPa and 75 MPa pressure crystallized samples, while no distinct maltese cross was formed, the quadrants exhibited qualitatively less mixed birefringence

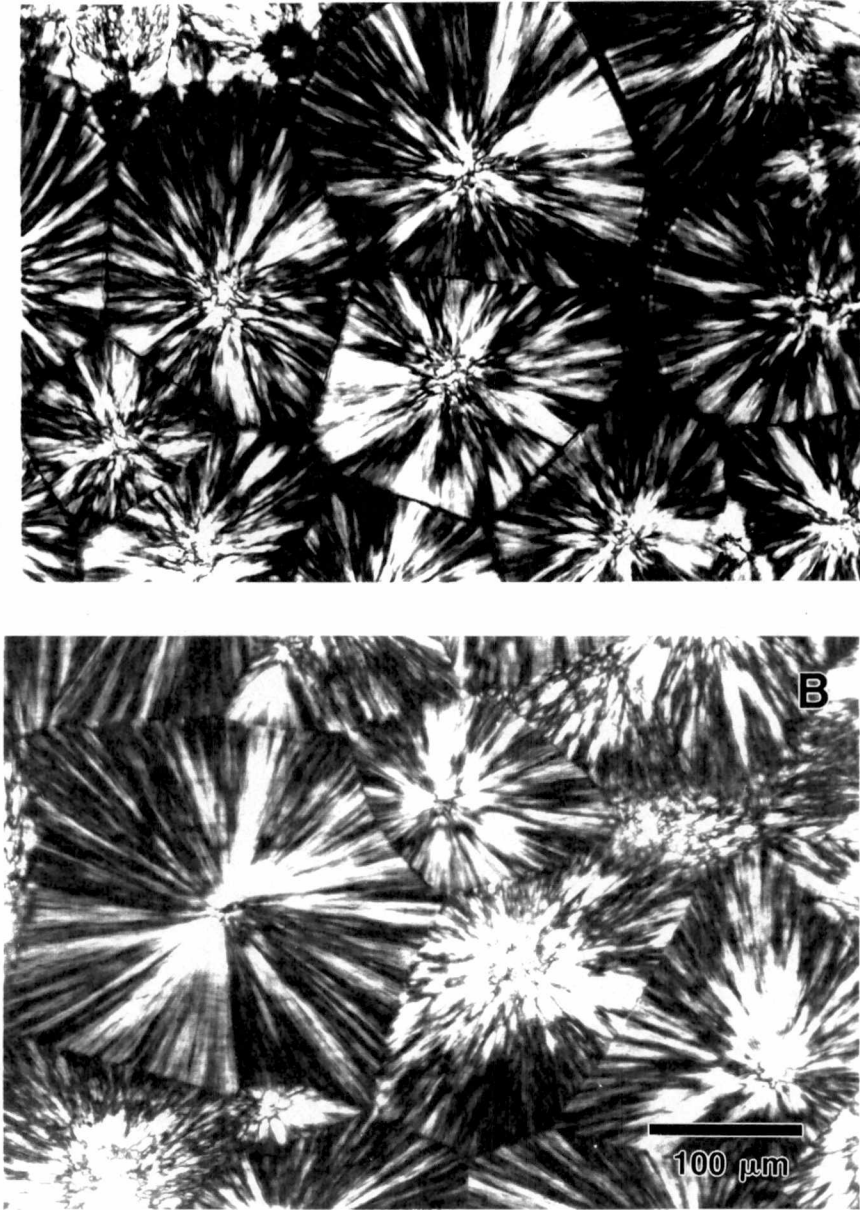


Figure 4.42 Optical micrographs of isotactic polypropylene homopolymer $M_w = 83,000$ at fixed supercooling $\Delta T = 50^\circ\text{C}$. A. atmospheric pressure crystallized, B. 25 MPa crystallized.

(see figure 4.43). By 100 MPa, a distinct maltese cross was observed. Approximately 60% of the material was in the γ form. However, there do not appear to be two different spherulite types - one for α form and one for γ form. At 200 MPa, the morphology was distinctly different from the lower crystallization pressure samples (see figure 4.44). No maltese cross was observed and the spherulites appeared less distinct. Over 90% of the material was in the γ form.

Function of Temperature.

At a given crystallization pressure, the morphology showed behavior as a function of isothermal crystallization temperature similar to that of the atmospheric samples. However, for 100 MPa crystallization, much of the birefringence that was observed at lower pressures was lost. Figure 4.45A shows the optical micrograph of the morphology for polypropylene $M_w = 83,000$ at $P_c = 50$ MPa, $T_c = 152^\circ\text{C}$ ($\Delta T = 53^\circ$). Spherulites showed mixed birefringence similar to that observed for atmospheric crystallization at similar supercooling ($T_c \approx 134^\circ\text{C}$ at atmospheric conditions). At this time of crystallization, most of the entities were spherulitic. The variation in spherulitic sizes indicated a time dependence of nucleation. By $T_c = 154^\circ\text{C}$, the birefringence was less mixed. It was seen that some of the entities exhibited an irregular shape (shown in Figure 4.45B by an arrow), while others showed typical spherulitic

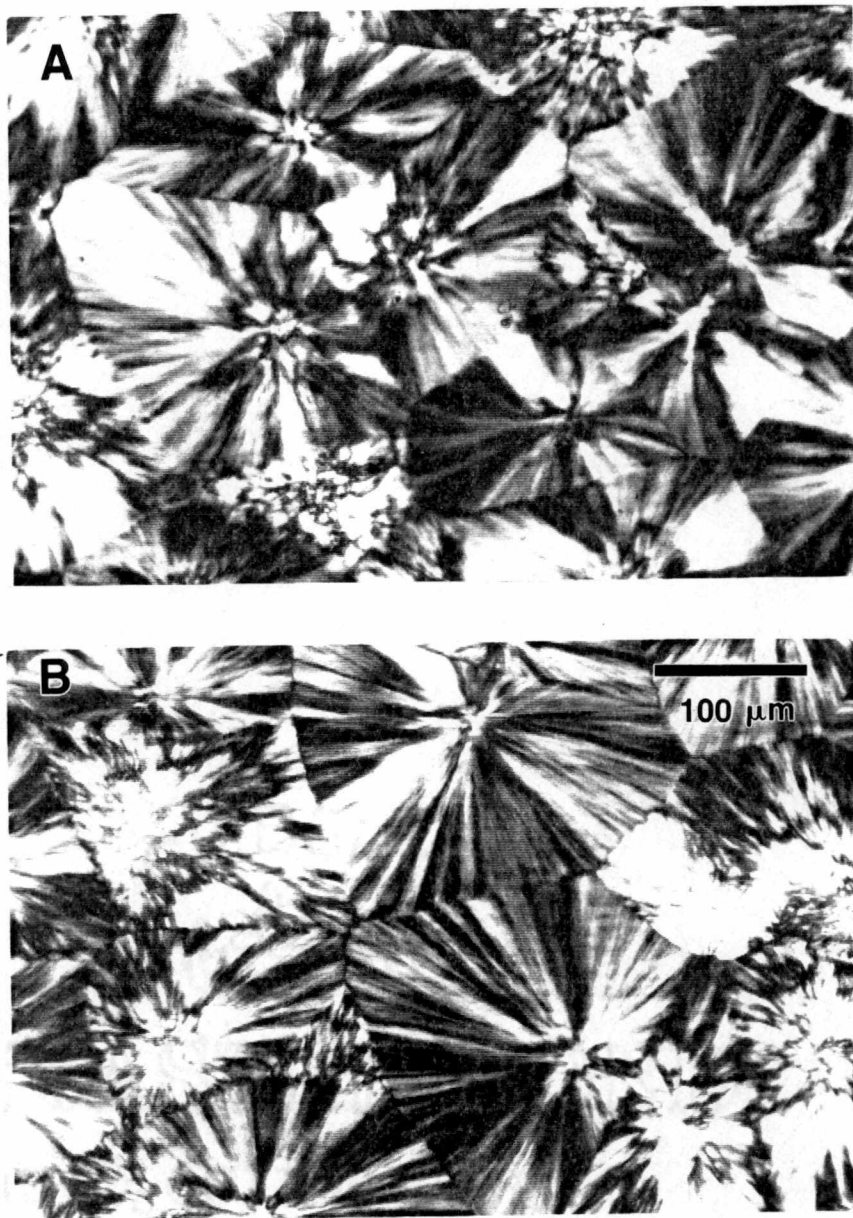


Figure 4.43 Optical micrographs of isotactic polypropylene homopolymer $M_w = 83,000$ at fixed supercooling $\Delta T = 50^\circ\text{C}$. A. 50 MPa crystallized, B. 75 MPa crystallized.

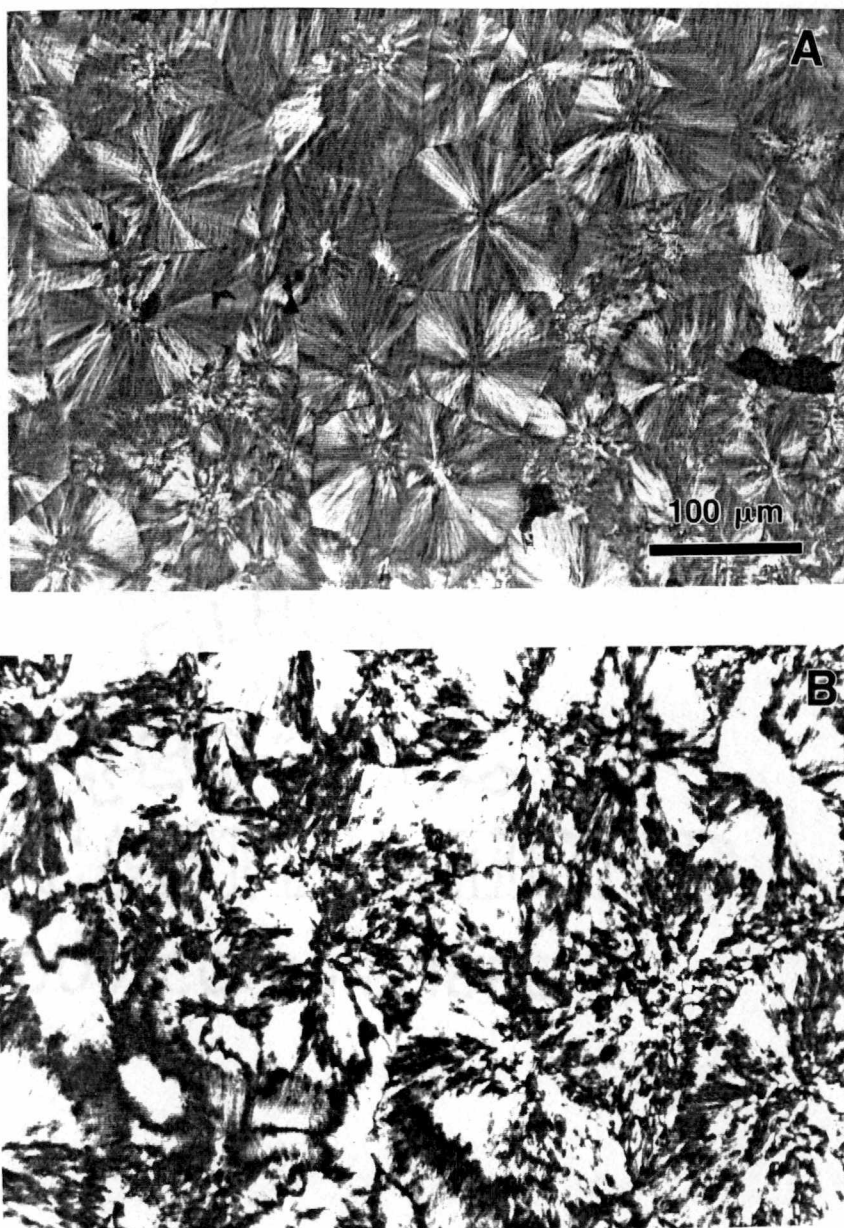


Figure 4.44 Optical micrographs of isotactic polypropylene homopolymer $M_w = 83,000$ at fixed supercooling $\Delta T = 50^\circ\text{C}$. A. 100 MPa crystallized, B. 200 MPa crystallized.

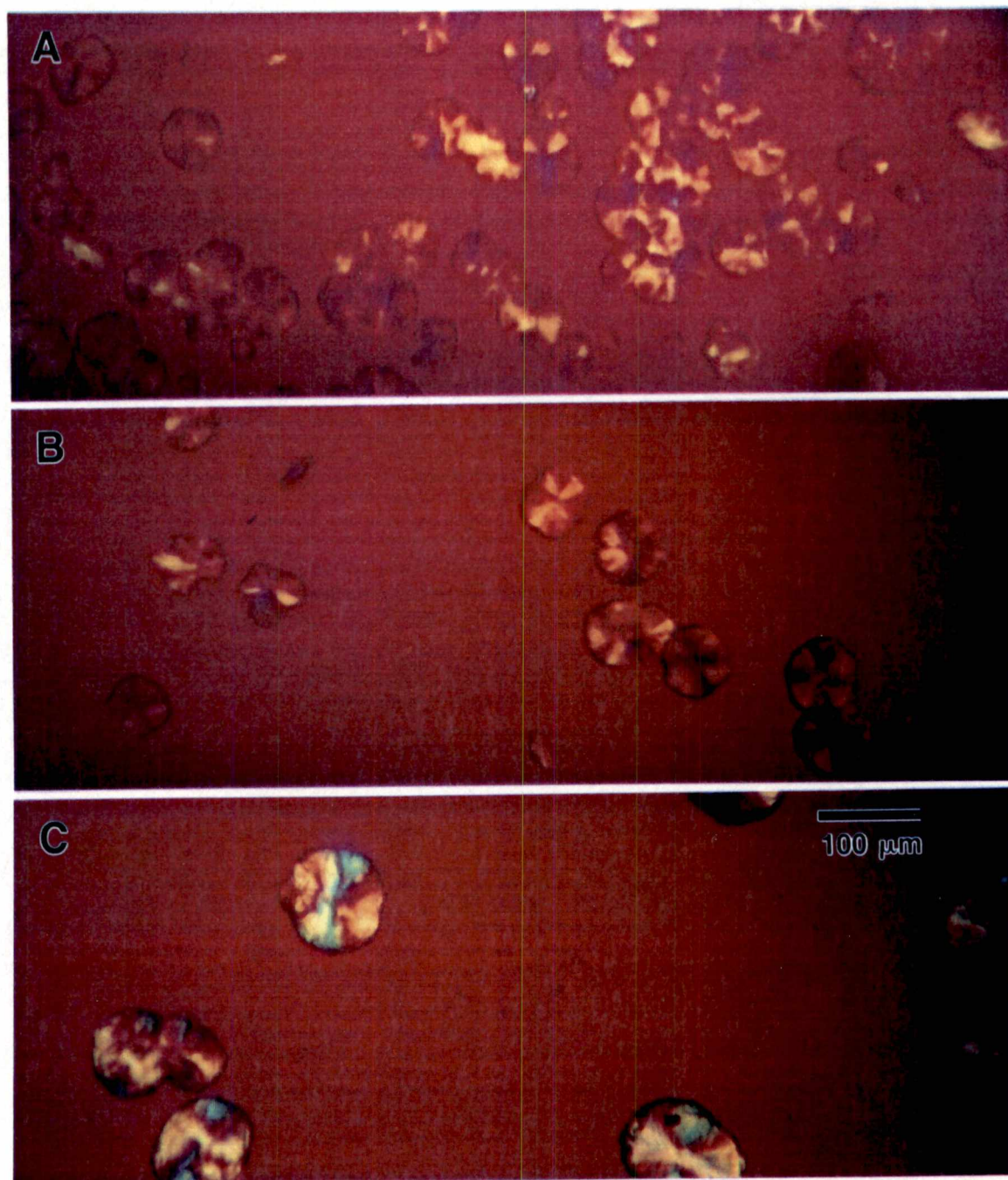


Figure 4.45 Optical micrographs of isotactic polypropylene homopolymer $M_w = 83,000$ isothermally crystallized at $P_c = 50$ MPa. A. 152°C , B. 154°C , C. 156°C .

behavior. By $T_c = 156^\circ\text{C}$ (see Figure 4.45C), the spherulites appeared more regular and the birefringence exhibited a distinct maltese cross under crossed polars.

At 75 MPa, the maltese cross became distinct at a higher supercooling (see Figure 4.46A). At $T_c = 156^\circ\text{C}$ ($\Delta T = 58^\circ$) a distinct maltese cross was observed under crossed polars. The sign of the birefringence was negative indicating a change in the lamellar habit with respect to an equivalent supercooling at atmospheric pressure.

At 100 MPa, the spherulites were pale. The shape was irregular, varying from spherical to ellipsoidal, to quadritic. In Figure 4.46B, an arrow indicates a quadritic entity. It exhibited a negative birefringence, as do the spherulites. No distinct quadrites were observed at a comparable supercooling at atmospheric conditions. However, quadrites were observed under atmospheric conditions at relatively low supercoolings ($<30^\circ$) as indicated in Figure 4.47. The angle between the major axes of the quadrites observed under elevated pressure crystallization was the same as that observed at atmospheric conditions.

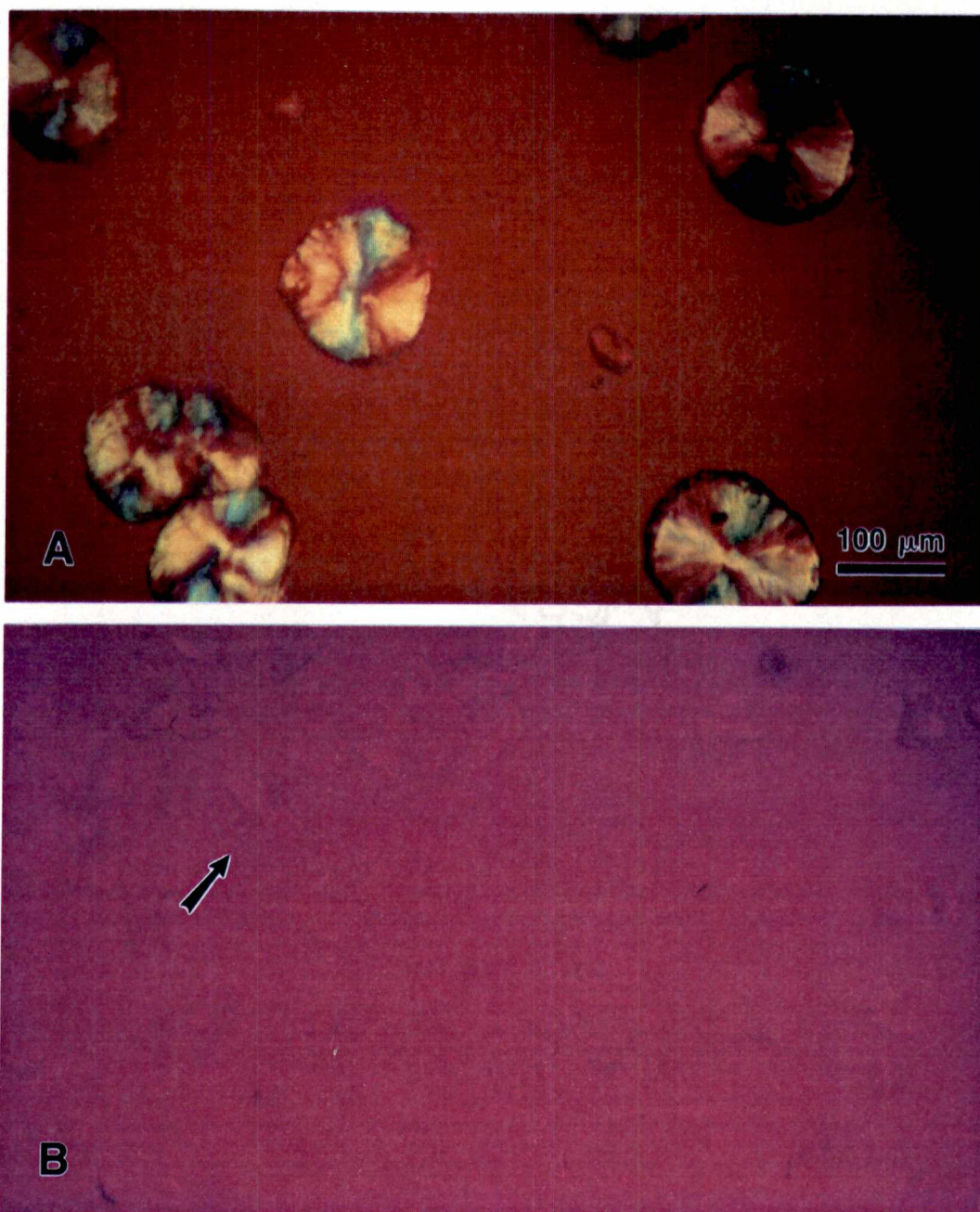


Figure 4.46 Optical micrographs of isotactic polypropylene homopolymer $M_w = 83,000$ isothermally crystallized. A. $P_c = 75$ MPa, $T_c = 156^\circ\text{C}$, B. $P_c = 100$ MPa, $T_c = 166^\circ\text{C}$.

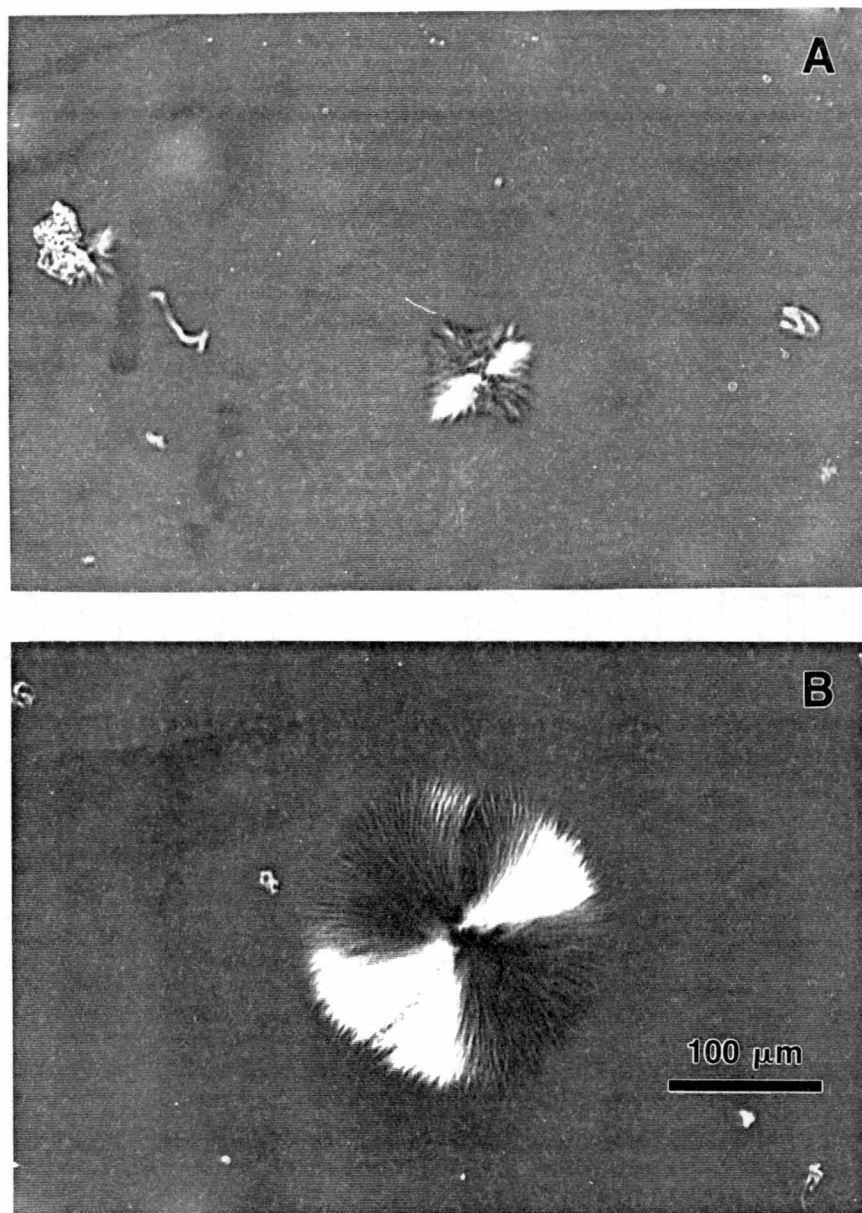


Figure 4.47 Optical morphology of isotactic polypropylene $M_w = 83,000$ isothermally crystallized at atmospheric pressure and $T_c = 156^\circ\text{C}$

Chapter 5

Discussion

5.1 Thermal Analysis

5.1.1 Equilibrium Melting Temperature

The equilibrium melting temperature T_m° is important in describing the relationship of polymer properties to structure and in the analysis of crystallization kinetics and nucleation processes. For the analysis of crystallization growth rate data, T_m° is needed to determine the degree of supercooling $\Delta T = T_m^{\circ} - T_c$. Despite the importance of the equilibrium melting temperature, the experimental determination of T_m° is often difficult and there is disagreement over the value of T_m° even for widely studied polymers such as polyethylene and polypropylene.

Several methods, theoretical and experimental, exist for the determination of T_m° for polymers. The methods are as follows:

- 1) Extrapolation of T_m for low molecular weight homologs to infinite molecular weight,
- 2) Extrapolation of T_m versus T_c data to the $T_m = T_c$ line,
- 3) Extrapolation of T_m versus $1/l$ data to $1/l = 0$.

The first method is a theoretical method developed by Flory and Vrij [89] where from an analysis of the equilibrium melting temperatures of monomeric homologs which form molecular crystals, the equilibrium melting temperature for the infinite chain can be calculated. By utilizing the data for n-paraffins, the T_m° for infinitely long linear polyethylene was concluded to be 145.5°C [68].

The idea that T_m° , T_m , and T_c might be simply related to one another was first mentioned by Lauritzen and Hoffman. The first systematic study showing an increase of T_m with increasing T_c was that of Wood and Bekkedahl on natural rubber [78]. In this method, the observed melting temperature T_m is plotted against the crystallization temperature T_c and the data extrapolated linearly to the line representing the relation $T_m = T_c$. The point of intersection is then taken to represent the T_m° of the sample. This procedure is based on Flory's statistical thermodynamic considerations of the fusion of polymers [90].

From a consideration of the thermodynamics of melting of a lamellar crystal, the relation of the T_m and l , lamellar thickness, is established. This relation is expressed as:

$$T_m = T_m^{\circ} \left[1 - \frac{2\sigma_e}{\Delta h_f l} \right] \quad 2.36$$

where σ_e = fold surface free energy and Δh_f = heat of fusion of the crystal. By plotting the observed melting temperature against the reciprocal of lamellar thickness, the equilibrium melting temperature is determined from the intercept of the linear extrapolation of the data to $1/l = 0$ (infinite thickness). This method also evaluates σ_e if Δh_f is known.

Atmospheric Pressure T_m^0

Figure 5.1 shows a plot of T_m versus T_c from DSC for iPP $M_w = 151k$ with the extrapolation of the line through the experimental data to the $T_m = T_c$ line to a value of $T_m^0 = 187^\circ\text{C}$. the definition of the melting temperature chosen for this figure was the modified return-to-baseline, which is a measure of the melting of the most perfect crystals in the material. The equilibrium melting temperature extrapolation does change depending on the chosen melting temperature. The value determined compared favorably with values in the literature for highly stereoregular iPP of 187.5°C [91]. The thickening factor determined from the slope was 2.2 for this material. This is a measure of the increase of the lamellar thickness over that predicted as the critical thickness l_g^* . The T_m^0 and γ values obtained for the other iPP samples were similar to those of the 151,000 homopolymer. Table 5.1 reports the values of T_m^0 and γ for the samples at atmospheric pressure .

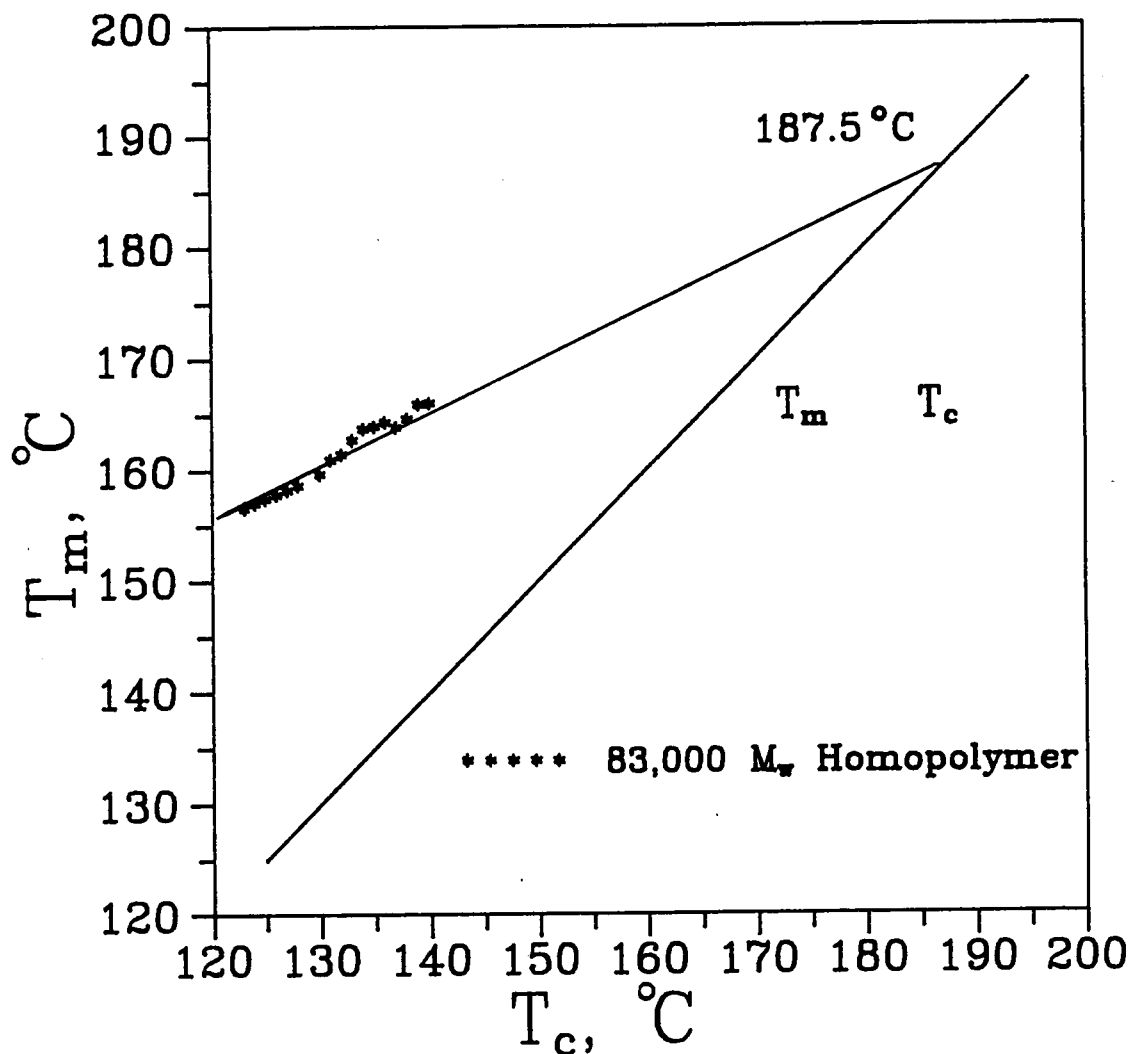


Figure 5.1 Melting temperature versus crystallization temperature for isotactic polypropylenes. DSC heating rate 10°C/min. Modified return-to-baseline melting definition.

Table 5.1 Values of the Equilibrium Melting Temperature, T_m^0 , and the Thickening Factor, γ , for isotactic polypropylenes crystallized at atmospheric pressure.

Sample	T_m^0 (°C)	γ
83,000 M_w	187.8	2.44
151,000 M_w	188.5	1.83
151,000 M_w copolymer	188.7	1.60

In general, two values of the equilibrium melting temperature for iPP have been reported in the literature, one approximately 187°C [92] and the other approximately 210°C [93]. Both values have supporting data from DSC and SAXS. It is sometimes possible to obtain both values from a single set of data, depending on the crystallization temperature range chosen for the linear extrapolation. Several explanations can be given for the large discrepancies in the T_m^0 values for iPP. These include sample heterogeneity (molecular weight and/or microstructure), thermal history, experimental technique, polymorphism, recrystallization, and reorganization. It has been shown that the melting behavior of iPP is dependent on the microstructure [94]. As the stereoregularity of iPP increases, the melting temperature increases. The monoclinic form of iPP shows an order limiting structure and a disorder limiting structure [95]; the crystallization temperature strongly affects which structure is obtained. The disorder limiting structure has a random distribution of up and down chains in each site of the unit cell of space group C2/c. The order limiting structure has well-defined up and down helices in group P2₁/c. the ratio of order limiting to disorder limiting structure can be related to the DSC behavior [96].

For nonisothermal crystallization and for isothermal crystallization below $\approx 130^\circ\text{C}$, a portion of the material can

crystallize in the β -form. The β -form melts approximately 10 - 15° below the α -form [] and this material can then recrystallize, complicating the observed DSC melting behavior.

Elevated Pressure T_m^0

Following the crystallization of polypropylene at elevated pressure, the determination of melting temperatures was performed in the same equipment using the DLI technique previously described in section 3.3. The heating rate employed was 3°C/min. This was found to be the fastest rate that could be controlled for the high pressure system.

Depolarized light intensity melting data obtained at atmospheric pressure using the Mettler hot stage and the high pressure cell were compared and found to be in good agreement. Similar comparisons made by Dalal [59] using cis-polyisoprene and Tseng [97] using linear polyethylene also showed good agreement. The DLI melting results were also correlated with DSC melting results, again with good agreement.

The melting temperatures of samples that were crystallized and melted at pressures ranging from atmospheric pressure to 100 MPa are presented in Figure 5.2. All determinations were made at 3°C/min. and the modified return-to-baseline melting definition described above was used

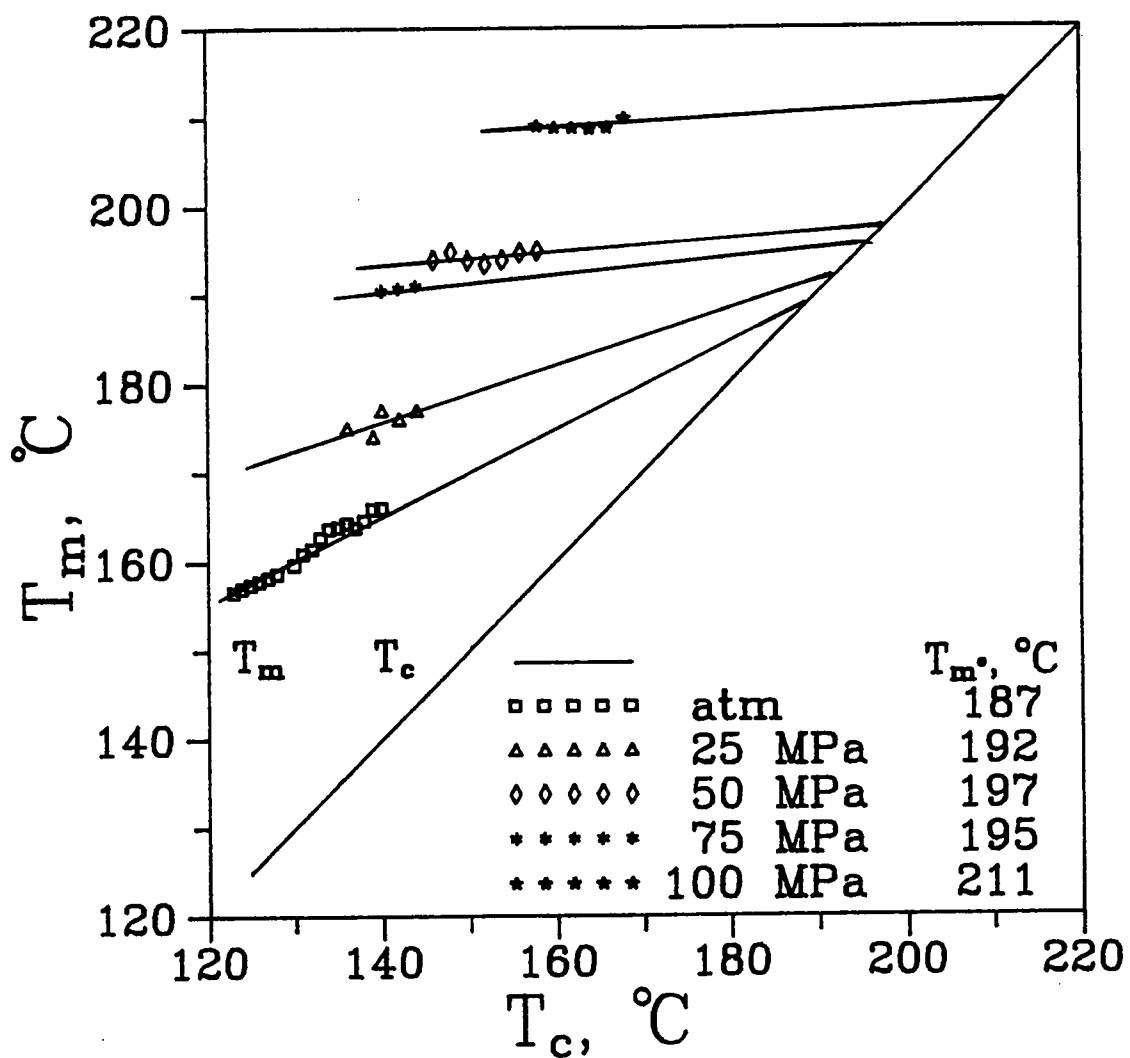


Figure 5.2 Melting temperature versus crystallization temperature for isotactic polypropylene crystallized at elevated pressure DLI heating rate 3°C/min. Modified return-to-baseline melting definition.

throughout. Extrapolations of the data to the $T_m = T_c$ line yielded values of T_m^0 according to equation 2.39. The data generally fit well to a linear relationship. The thickening factor, γ , at each pressure was obtained from the slope of the line. The values of T_m^0 and γ at each pressure are presented in Table 5.2. With increasing pressure, the thickening factor increased. This has also been shown to occur with linear polyethylene [98]. This indicated that the thickening process was more effective with increasing pressure.

One can evaluate the change in T_m^0 with pressure, dT_m^0/dP , from the pressure melting data. Figure 5.3 shows the extrapolated equilibrium melting temperatures, T_m^0 , as a function of crystallization pressure. Also shown is a prediction of T_m^0 using the Clapyron equation. While there was some deviation from linearity, particularly with the 75 MPa data, a linear fit to the data yielded a dT_m^0/dP of 24 K/100 MPa. This was in good agreement with the prediction from the Clapyron equation of 23 K/100 MPa. This also agreed well with the dT_m^0/dP of other polymers. Table 5.3 shows the results of dT_m^0/dP from this work and the literature for several polymer systems. It is possible that the deviation at 75 MPa of T_m^0 to a value that is lower than that at 50 MPa is partly a result in the changing composition of the crystallizing system. It is possible that the 75 MPa T_m^0 simply reflects the melting of the γ form of polypropylene,

Table 5.2 Values of the Equilibrium melting temperature, T_m° , and the Thickening factor, γ , for isotactic polypropylene crystallized at elevated pressure.

Pressure MPa	T_m° ($^\circ\text{C}$)	γ
atm	187	2.44
25	192	3.61
50	197	19.23
75	195	6.67
100	211	15.87

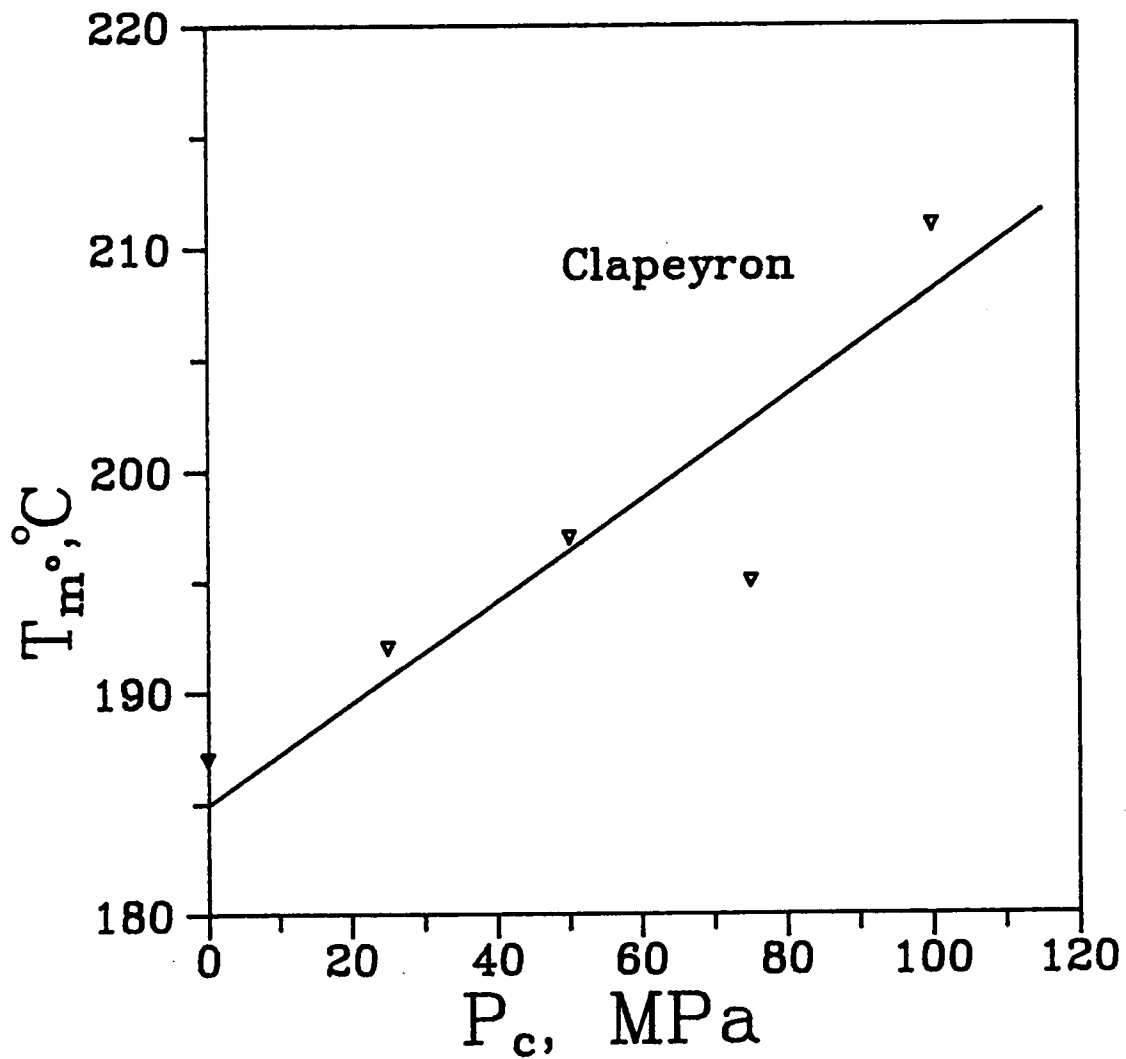


Figure 5.3 Change in equilibrium melting temperature T_m° with crystallization pressure P_c .

Table 5.3 Change in Melting Temperature with Pressure for isotactic polypropylene and other polymers.

Polymer	dT_m/dP ($^{\circ}\text{C}/100 \text{ MPa}$)	Source
iPP	23	This work
	24.3	V. Karl et al [99]
	37.7	Reinshagen [100]
	36.6	Nakafuku [101]
PE	35.2	Davidson [102]
	23.0	Tseng [97]
PET	54.7	Siegmann [103]
	50.6	Hiramatsu [104]
cis-IP	23.3	Dalal (T _m vs T _c) [59]
	27.0	Dalal (T _m vs 1/1)
PVF2	41.0	Nakafuku105
	34.0	Nakafuku
PEO	21.0	Fortune [106]

which is known to melt 10 - 15° below the α form. Nakafuku [107] has shown that the dT_m/dP of the α and γ forms of polypropylene are similar, with that of the γ form being slightly higher. It is interesting to observe that the dT/dP values obtained for PE (Tseng) and cis-IP (Dalal) using essentially the same experimental technique are equivalent. Also, the range of values for iPP can partly be attributed to different experimental conditions - experimental technique and materials. Up to 75 MPa, the melting could be α dominated. While in the literature it has been stated that the γ triclinic converts to the α monoclinic through a solid-solid transition on heating near the γ melting temperature at atmospheric pressure [108], it is not clear exactly what occurs at elevated pressure. Recently this statement of a solid-solid transition for the γ to α has been challenged [109] due to the nature of the proposed γ orthorhombic cell's nonparallel chain stem arrangement. It has been shown [110] that the α and γ forms can coexist on the lamellar level. At present, it is not known whether there is a significant difference in lamellar thickness between the two species that would result in different melting temperatures.

5.1.2 Comparison of DSC and DLI

The relation of the DSC heating curves to the DLI heating curves is generally complex. Figure 5.4 shows a

comparison of the DLI heating curve to the DSC heating curve for iPP $M_w = 151,000$ isothermally crystallized at 130°C , heated at a rate of $10/\text{min}$. The relation between the DLI heating scans and the DSC thermograms changed as a function of heating rate and crystallization temperature. Table 5.4 gives results of the DSC/DLI comparison for peak and return-to-baseline melting temperatures. The optically determined melting temperatures, observed during the DLI heating scans, correlated with the DSC peak temperature for DSC scans exhibiting only a single fusion peak.

5.2 Kinetics Analysis

5.2.1 Avrami Analysis

Bulk crystallization kinetics were initially analyzed using the Avrami approach. The depolarized light intensity versus time plots were transformed using the relation:

$$I_\infty - I_t / I_\infty - I_0 = \theta(t) \quad 5.1$$

where θ is the relative crystallinity and I_0 , I_t , and I_∞ are the light intensities at the start, intermediate, and end of primary crystallization. The relative crystallinity was then analyzed using the Avrami equation:

$$\theta(t) = \exp(-kt^n) \quad 5.2$$

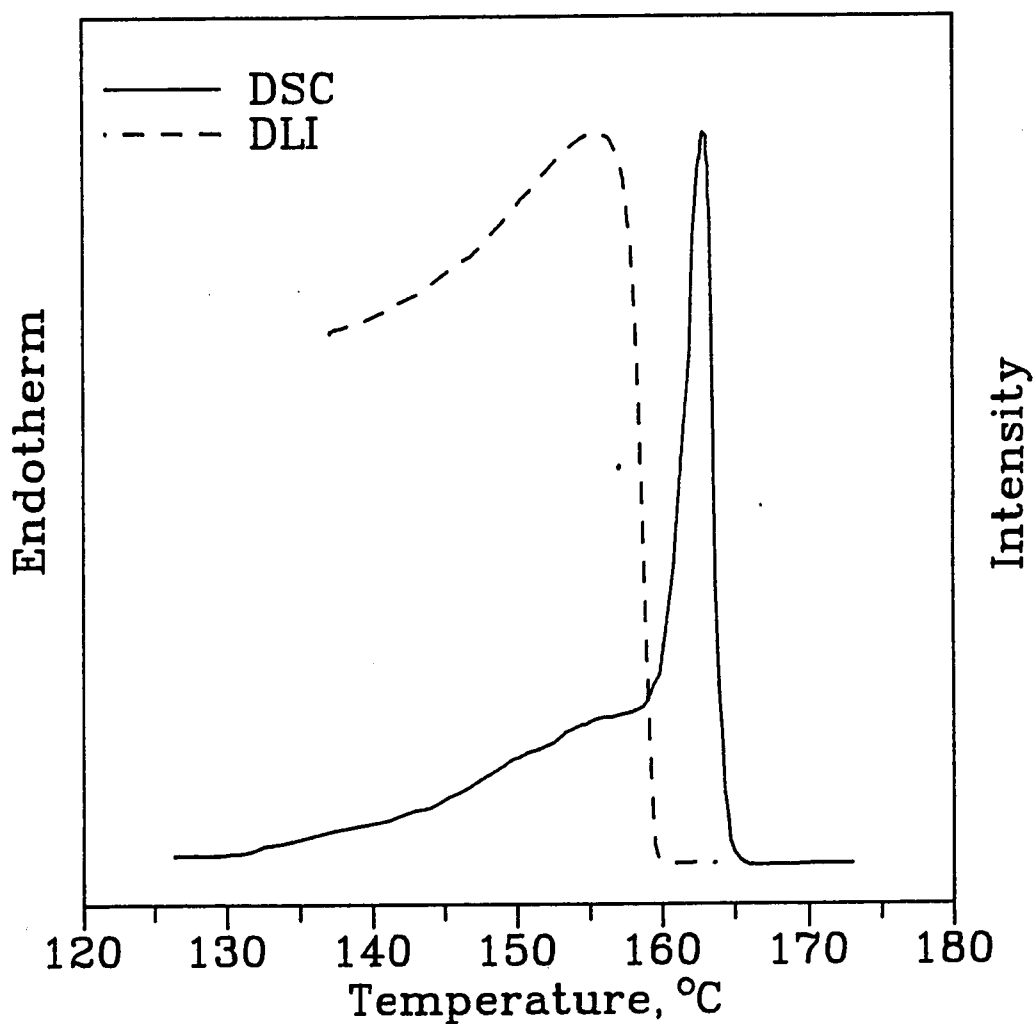


Figure 5.4 Comparison of DSC and DLI melting behavior for isotactic polypropylene homopolymer $M_w = 83,000$ isothermally crystallized at atmospheric pressure, $T_c = 130^\circ\text{C}$. Heating rate $10^\circ\text{C}/\text{min}$.

Table 5.4 Values for DSC and DLI melting analysis for isotactic polypropylenes crystallized at atmospheric pressure

T _c (°C)	M _w = 151,000 Homopolymer				M _w = 151,000 Copolymer			
	DSC		DLI		DSC		DLI	
	Peak (°C)	RTB (°C)	Onset (°C)	RTB (°C)	Peak (°C)	RTB (°C)	Onset (°C)	RTB (°C)
125				164.5	157.2			
126				164.3	157.8			
127	161.5	165.4		164.6	158.2	165.6		
128				165.1	158.6			
129	162.0	164.3		166.7				
130	163.3	164.7	162.9	167.2	159.6		160.0	163.9
131	163.0	164.6	163.0	167.5	160.9	162.2	160.5	164.1
132	164.2	165.5	163.2	166.5	161.4	162.8	158.0	165.1
133	163.4	165.2	161.9	168.1	162.7	164.1	162.0	167.5
134	165.3	166.6	162.2	168.6	163.7	165.1	161.0	166.3
135	165.4	167.4	162.3	167.9	163.9	165.2	161.5	167.2
136	164.6	166.7	162.6	168.1	164.3	165.8	162.0	169.0
137					163.8	165.2	160.0	167.7
138		167.4			164.6	166.0	160.4	168.1
139					165.9	167.1		
140	167.1	169.4			166.0	167.3		
141							160.0	170.0
142	168.3	171.1						
143	169.1	171.5						172.3
144	169.2	172.0					161.2	
145	170.2	172.8					162.0	173.4

where k and n describe the rate and mechanism of crystallization, respectively.

Atmospheric Pressure

The data was plotted as $-\log(\log \theta)$ versus $\log t$ and the Avrami n and K were evaluated from the slope and intercept of the linear best fit of the data. Figure 5.5 shows Avrami plots for iPP $M_w = 151,000$ where $-\log(\log \theta)$ was plotted against \log time for several crystallization temperatures. At most of the crystallization temperatures, straight lines are obtained over a substantial portion of the crystallization process. It is also noted that the curves remain linear after impingement of the growing spherulites. Figure 5.6 shows Avrami plot for iPP $M_w = 83,000$ and Figure 5.7 show Avrami plots for the polypropylene copolymer $M_w = 151,000$ for several crystallization temperatures. Values of Avrami K and n parameters are summarized in Table 5.5 for polypropylene homopolymers $M_w = 151,000$ and $M_w = 83,000$ and copolymer (0.5% ethylene) $M_w = 151,000$ as a function of crystallization temperature. The Avrami n varied between about 2.3 and 3.6 for the three samples while the variation for a given sample was less. The homopolymers exhibited nearly identical values of n as a function of temperature, while the K values varied. The copolymer exhibited the lowest n values overall; this is partly due to the higher

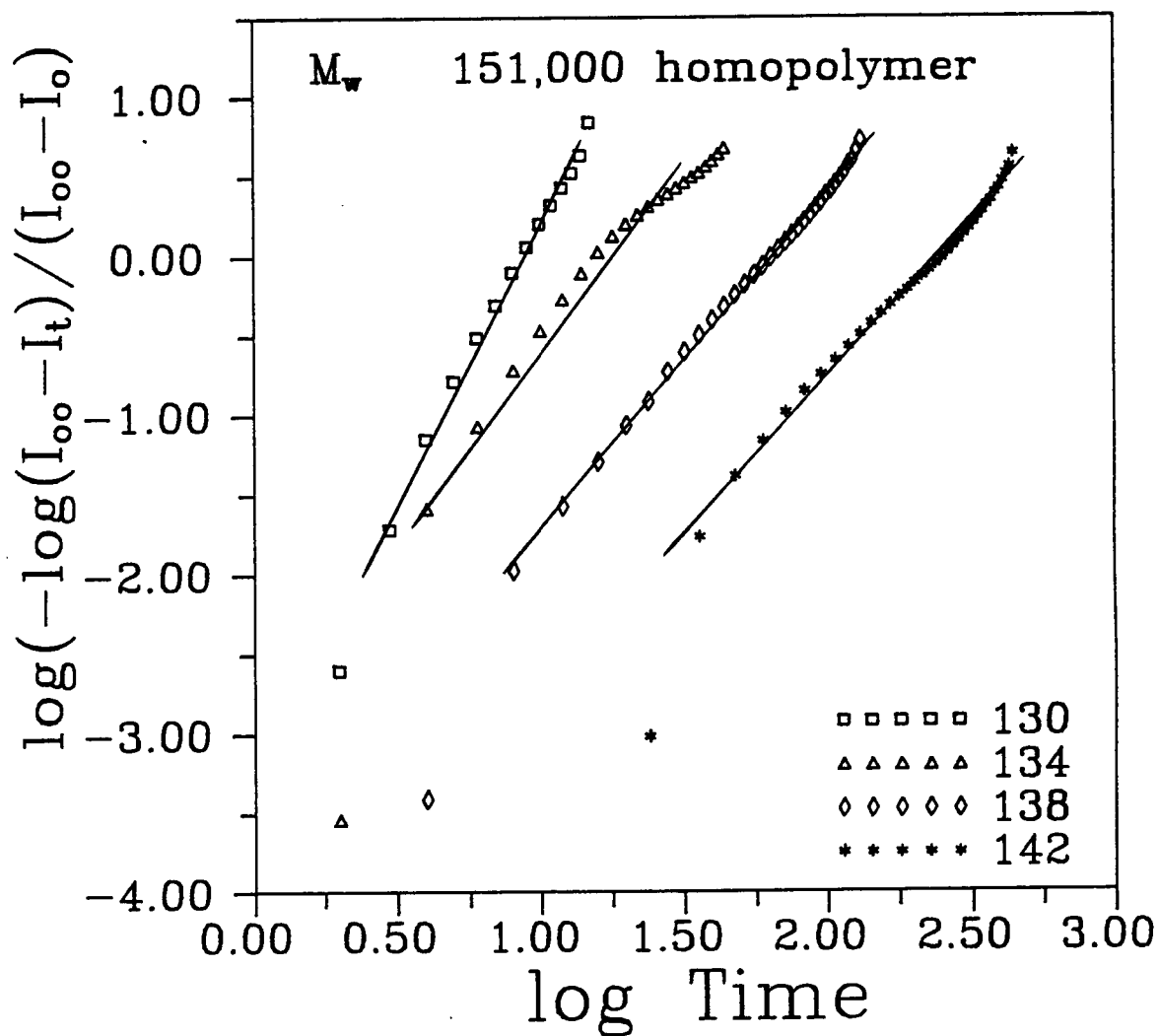


Figure 5.5 Avrami plots for isotactic polypropylene homopolymer $M_w = 151,000$ at various crystallization temperatures and atmospheric pressure.

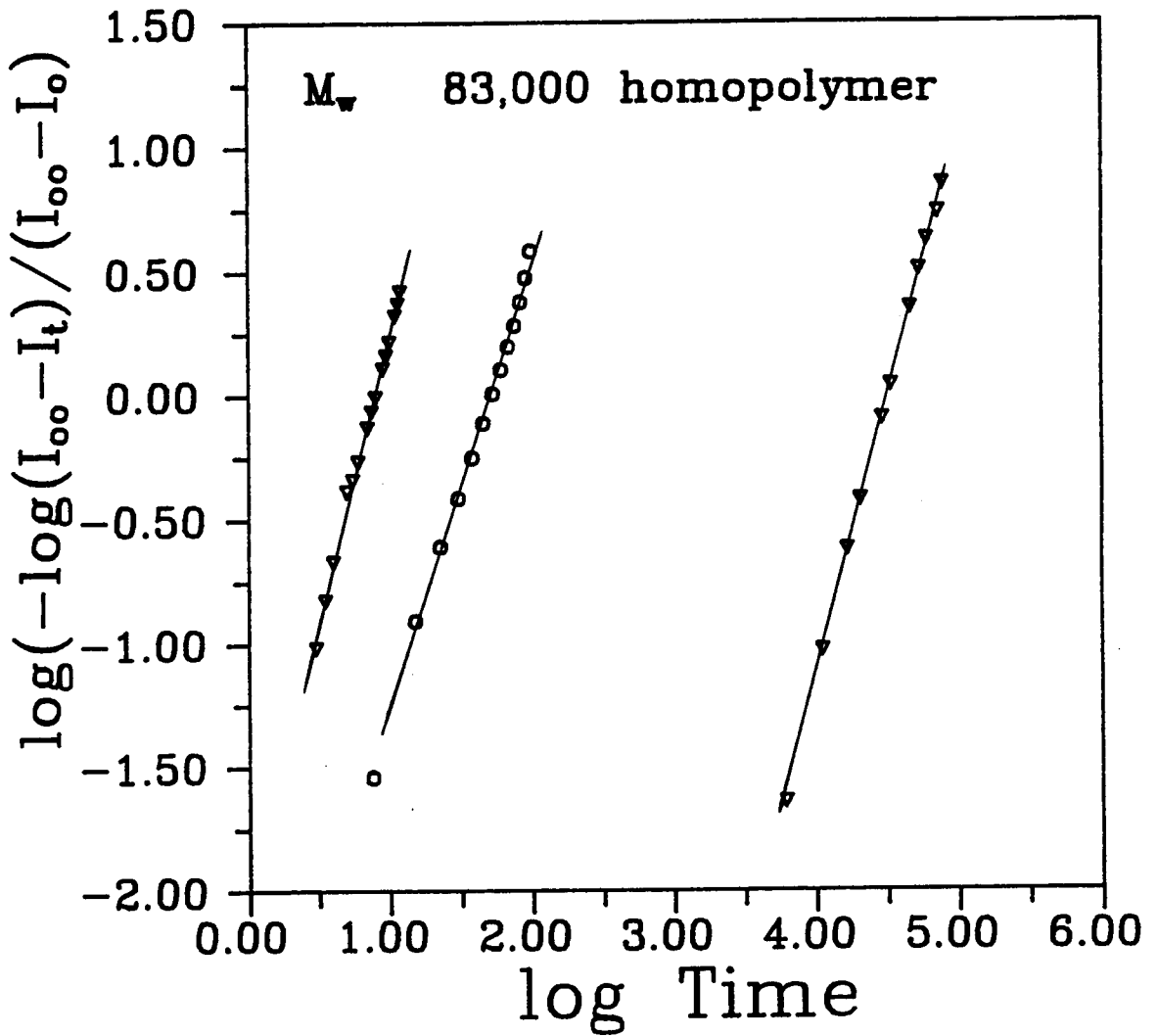


Figure 5.6 Avrami plots for isotactic polypropylene homopolymer $M_w = 83,000$ at various crystallization temperatures and atmospheric pressure.

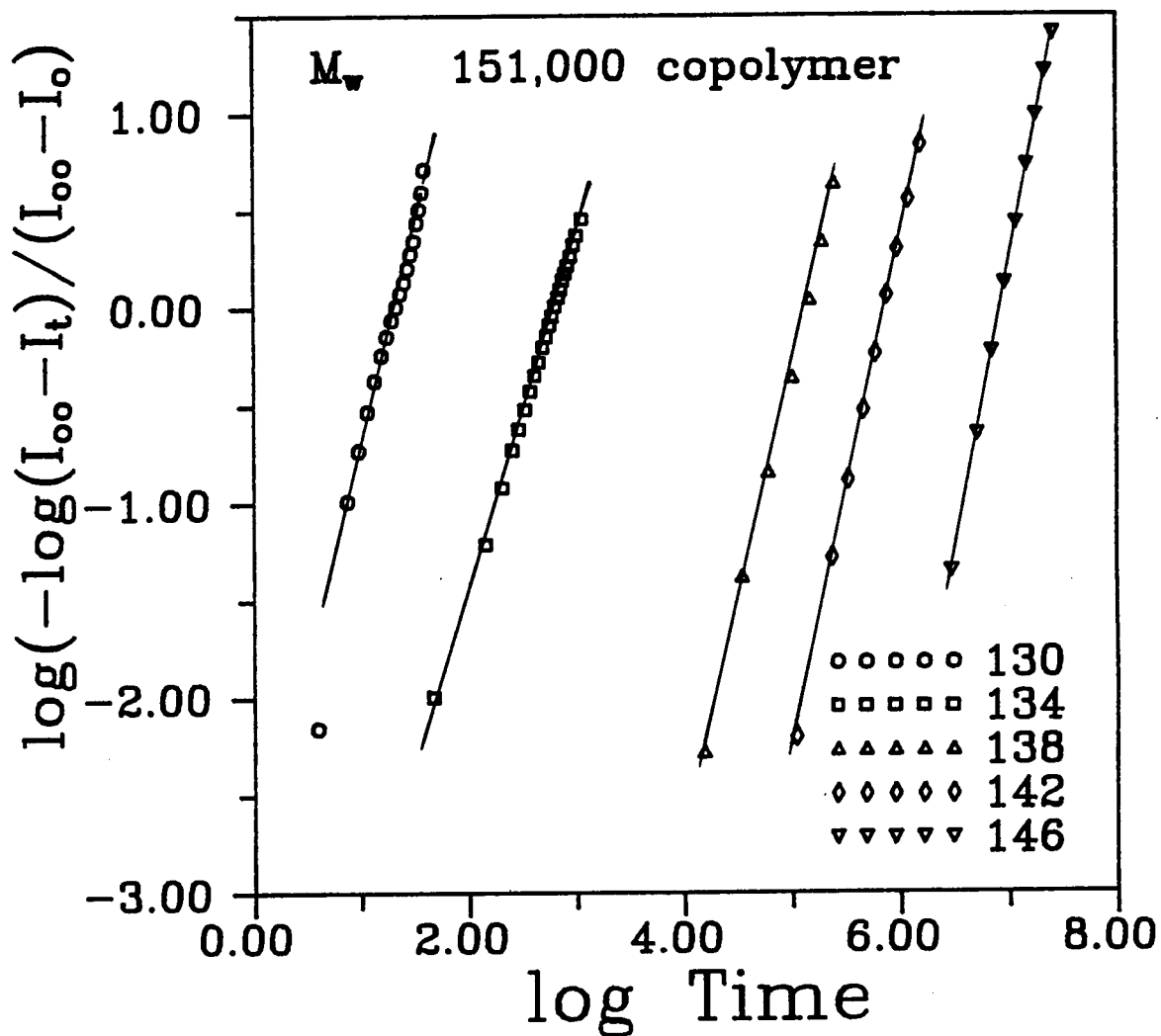


Figure 5.7 Avrami plots for isotactic polypropylene copolymer $M_w = 151,000$ at various crystallization temperatures and atmospheric pressure.

Table 5.5 Avrami Coefficients as a function of crystallization temperatures for isotactic polypropylene at atmospheric pressure (DLI).

T_c (°C)	$M_w = 83,000$ Homopolymer		$M_w = 151,000$ Homopolymer		$M_w = 151,000$ Copolymer	
	n	log K	n	log K	n	log K
125	3.38	0.88	3.38			
126	3.45	1.24	3.45			
127	3.22	1.25	3.22			
128	2.85	1.62	2.85			
129	2.56	2.61	3.56			
130	3.11	2.30	3.11	2.89	3.32	3.07
131	3.03	2.49	3.03		2.91	3.00
132	2.61	2.59	2.61	3.12	2.96	3.62
133	3.12	3.61	3.12		2.41	1.33
134	2.77	3.36	2.77	3.38	2.84	5.16
135	2.84	3.58	2.84		2.51	11.07
136	3.21	4.25	3.21	3.85	1.97	9.58
137					2.06	10.01
138					2.35	12.07
139					2.31	12.68
140					2.60	13.77
141					2.50	15.10
142			2.91	4.94	2.60	15.25
143					2.17	13.83
144			3.03	6.45		

crystallization temperatures that were studied for the copolymer since the samples exhibited some decrease in the n value with increasing temperature. Figure 5.8 shows crystallization isotherms for isotactic polypropylene $M_w = 151,000$, $T_c = 136^\circ\text{C}$, fit by the Avrami equation with $n = 3$ and $n = 2$ and the corresponding K calculated from the half time of crystallization. Here the better fit is $n = 3$. The value of the Avrami exponent n often differs from the integral values required by theory. Part of the discrepancy is possibly accounted for by the assumptions made in deriving the Avrami equation.

Elevated Pressure

The Avrami plots of bulk crystallization kinetic data for polypropylene $M_w = 83,000$ at 25, 50, 75, and 100 MPa are shown in Figures 5.9, 5.10, 5.11, and 5.12, respectively. The results of the evaluation of the Avrami exponent n are summarized in Table 5.6 as a function of crystallization temperature and pressure. As with the atmospheric pressure crystallized data, straight lines are obtained over a substantial portion of the crystallization process. The Avrami n values for the elevated pressure crystallization range from about 2.2 to 6.2. This range is significantly larger than that of the atmospheric pressure crystallized data. There does not seem to be a general trend of

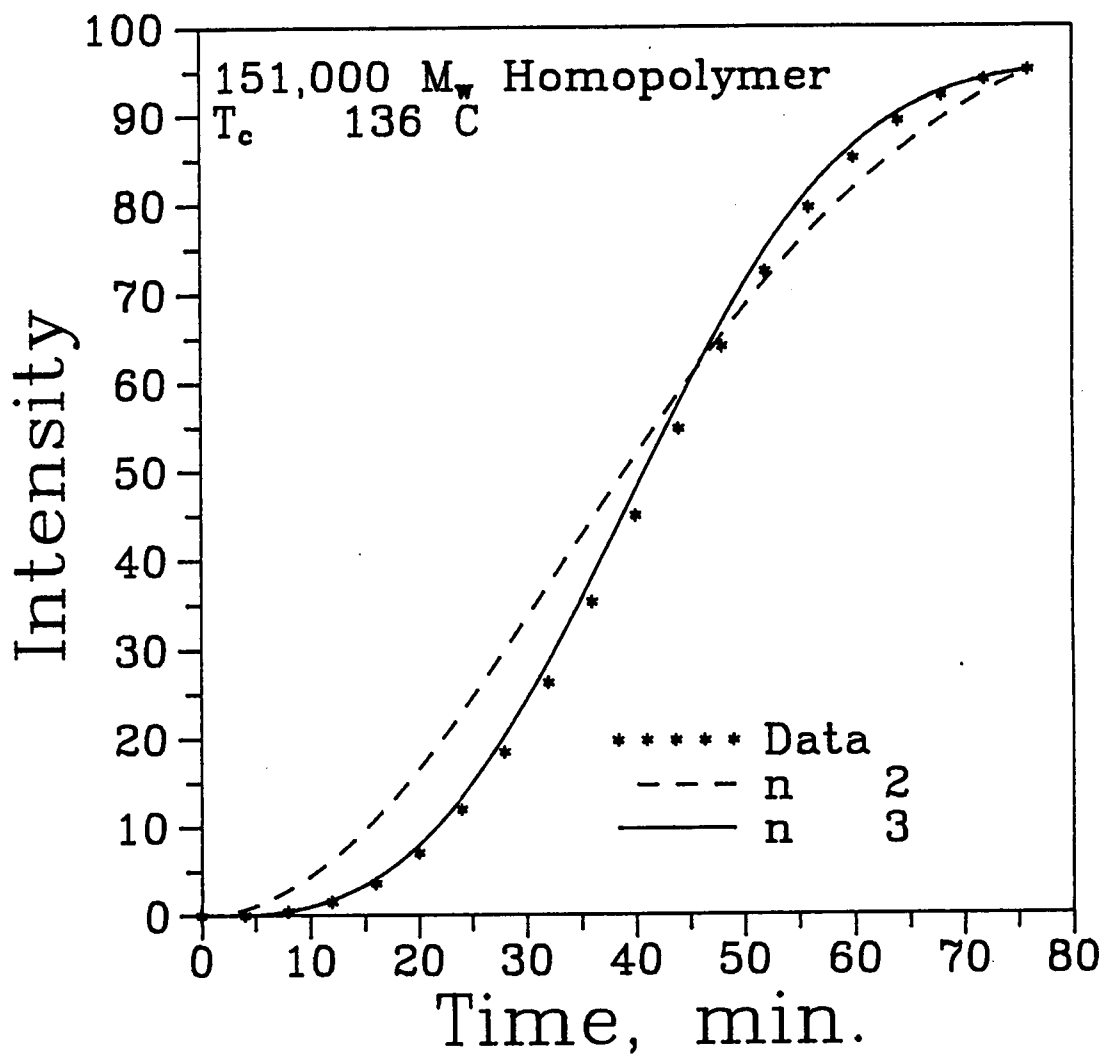


Figure 5.8 Comparison of experimental and theoretical I versus t data for isotactic polypropylene $M_w = 151,000$.

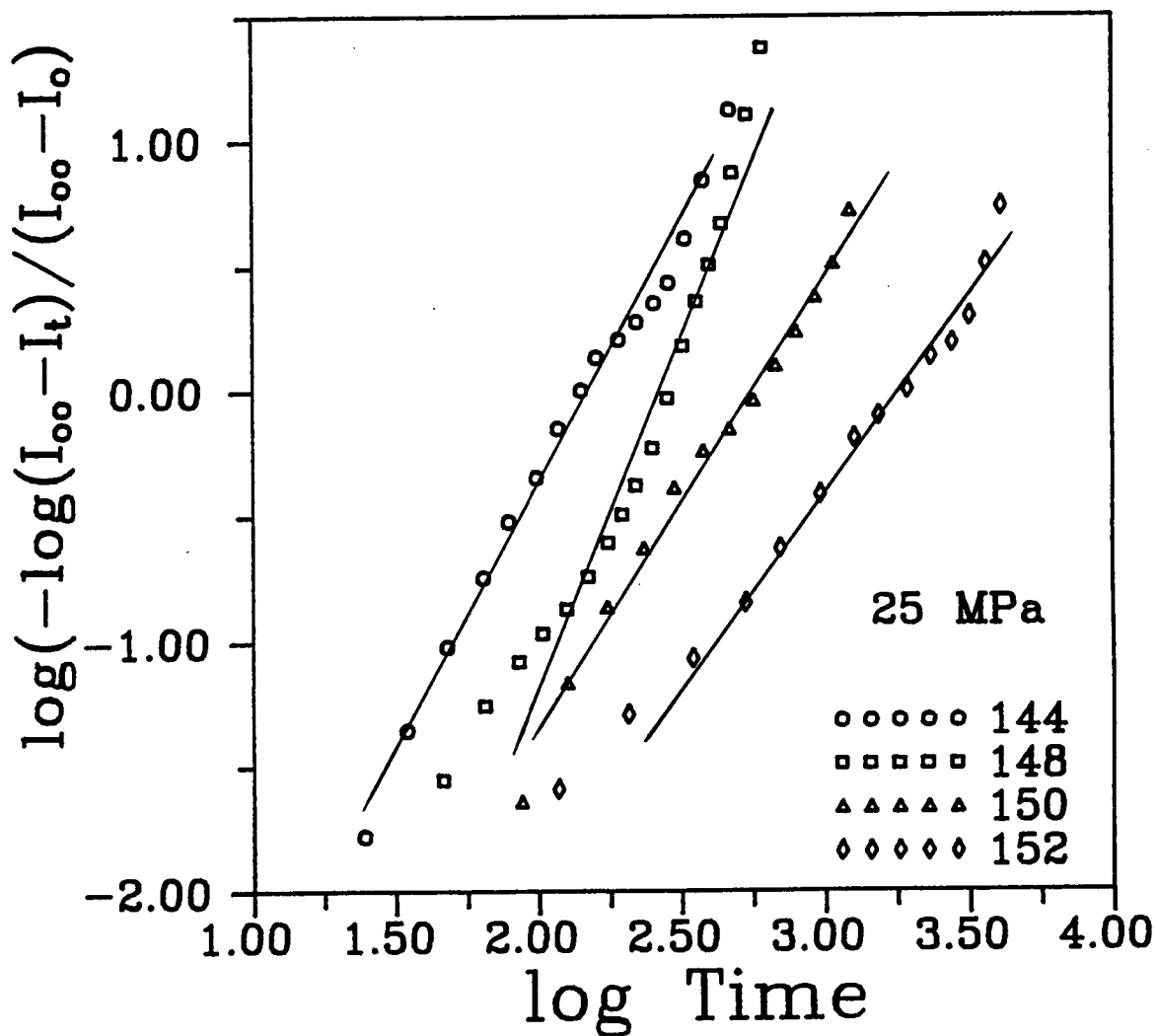


Figure 5.9 Avrami plots for isotactic polypropylene homopolymer $M_w = 83,000$ crystallized at 25 MPa pressure, various temperatures.

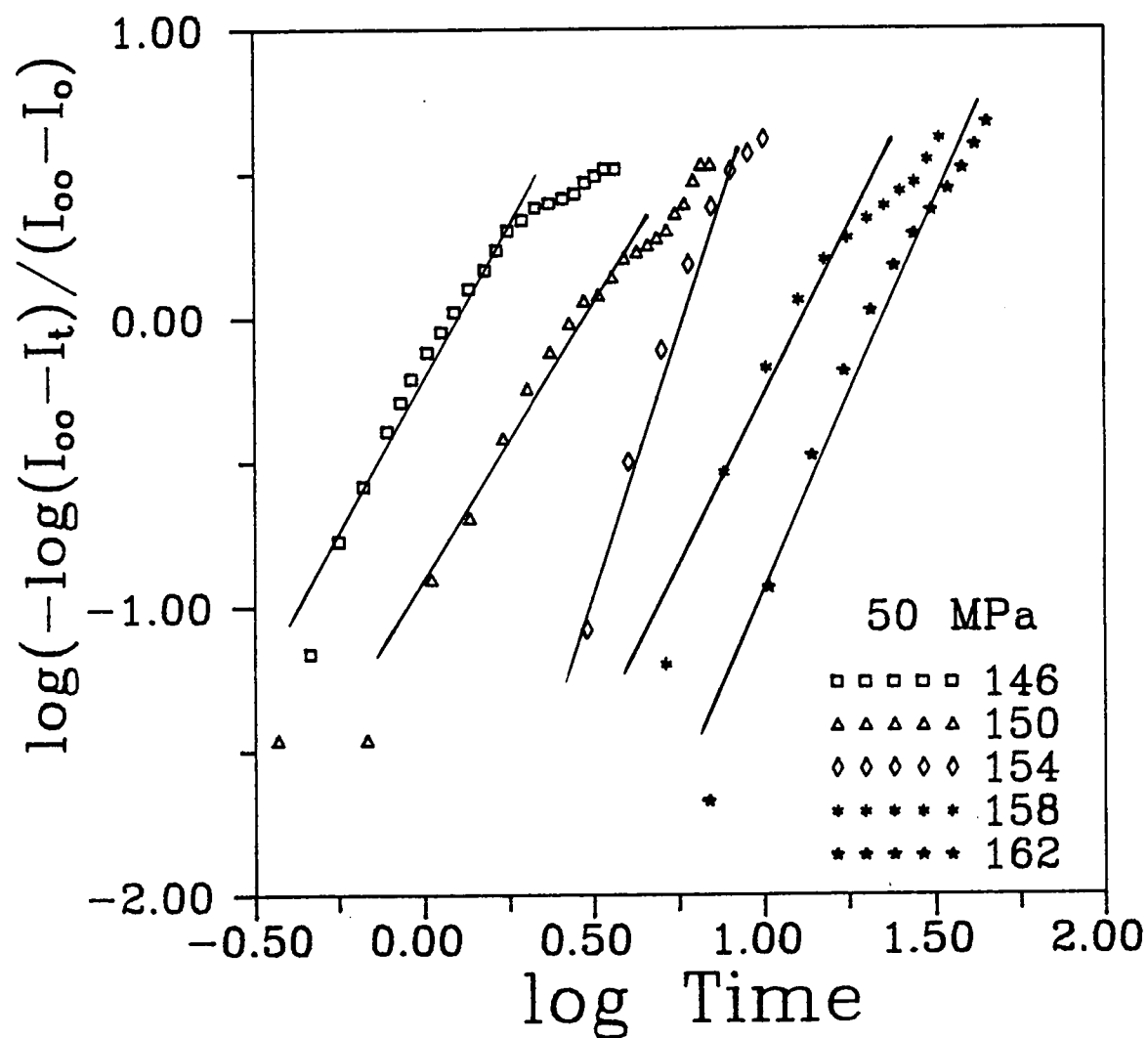


Figure 5.10 Avrami plots for isotactic polypropylene homopolymer $M_w = 83,000$ crystallized at 50 MPa pressure, various temperatures.

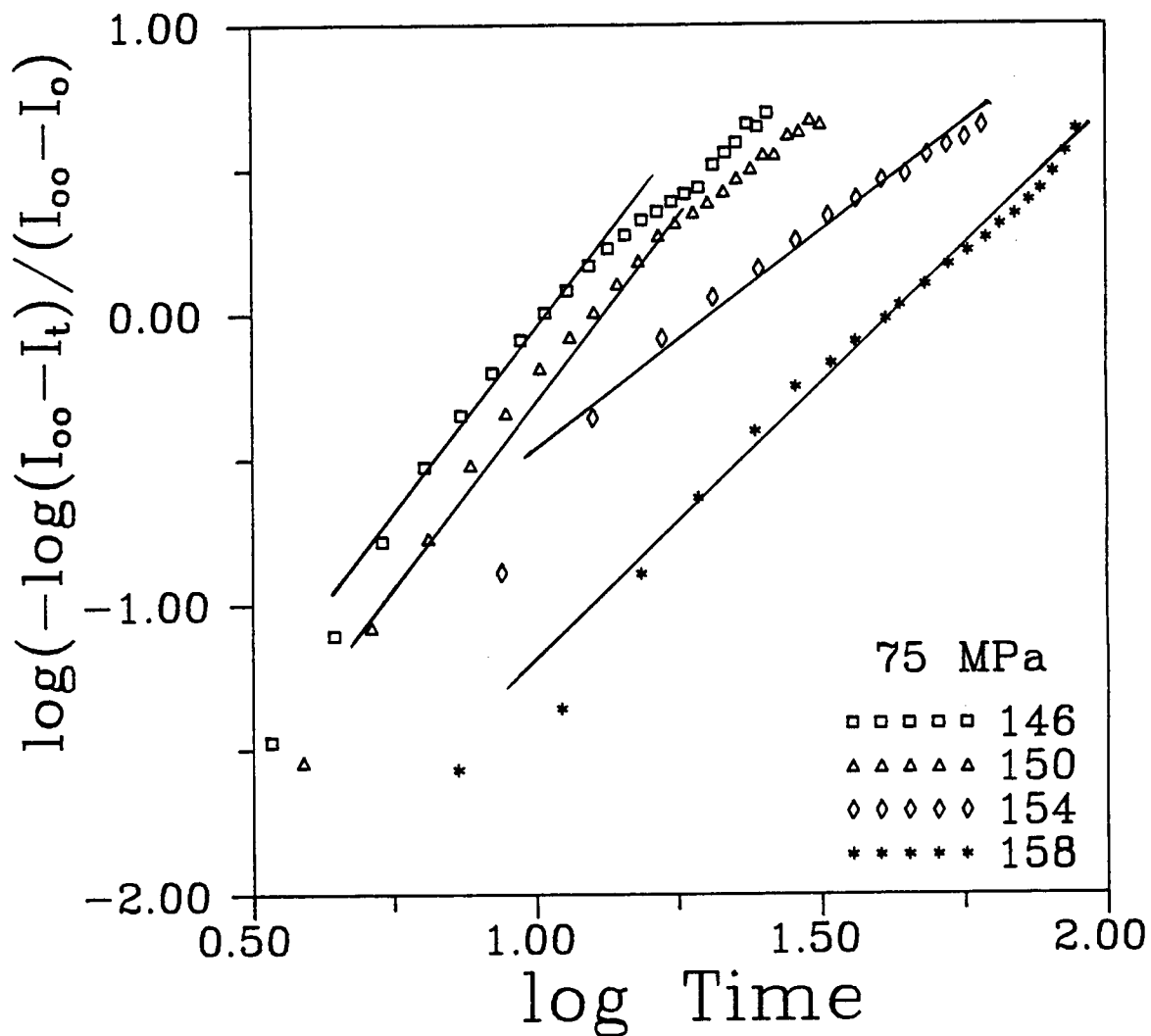


Figure 5.11 Avrami plots for isotactic polypropylene homopolymer $M_w = 83,000$ crystallized at 75 MPa pressure, various temperatures.

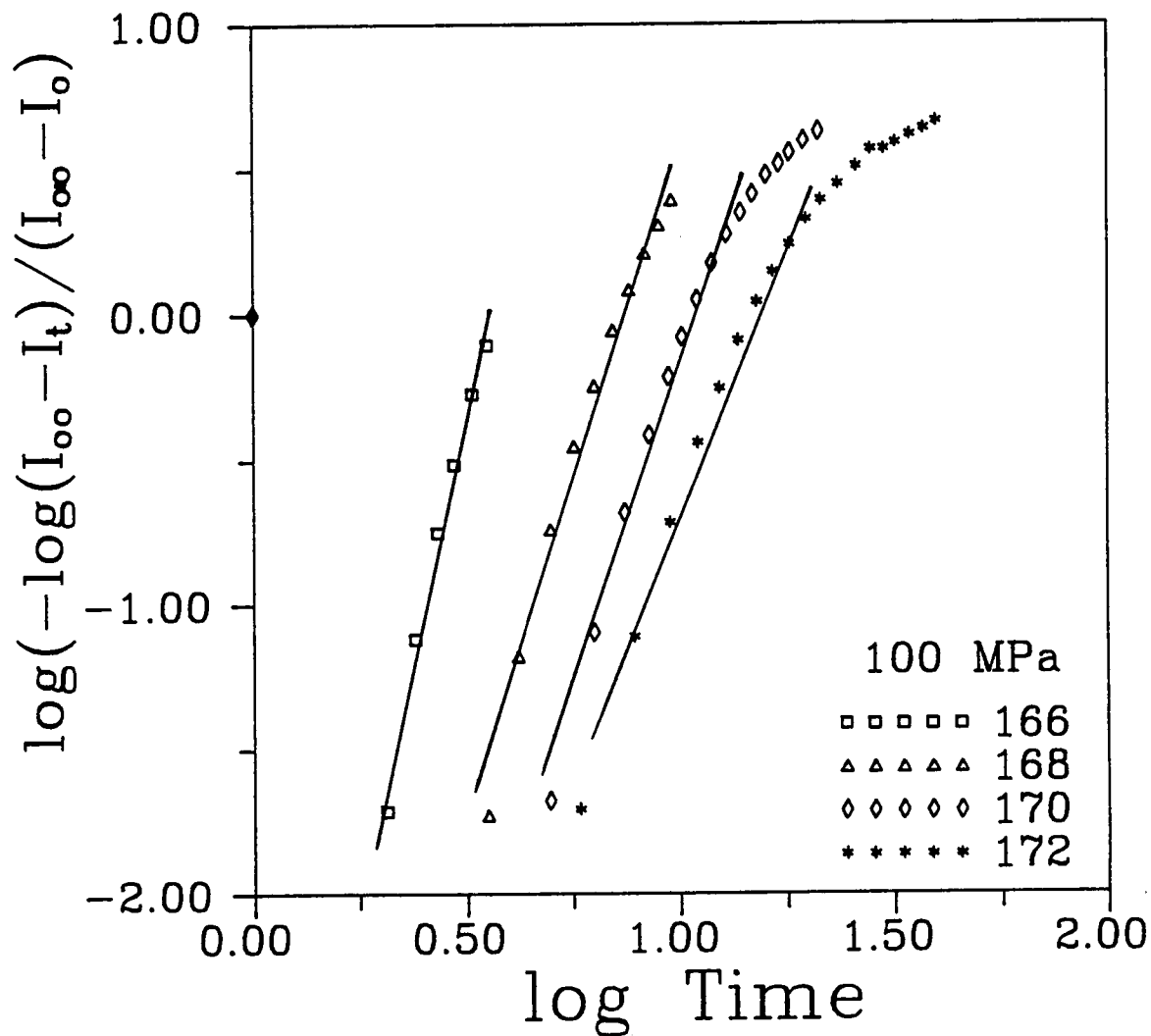


Figure 5.12 Avrami plots for isotactic polypropylene homopolymer $M_w = 83,000$ crystallized at 100 MPa pressure, various temperatures.

Table 5.6 Avrami Coefficients as a Function of Supercooling for iPP $M_w = 83,000$ at various elevated pressures (DLI).

ΔT	25 MPa		50 MPa		75 MPa		100 MPa	
	n	log K	n	log K	n	log K	n	log K
51			3.11	0.10				
47	2.13	4.63	2.20	0.95	2.67	2.75		
45					2.65	2.94	6.25	3.51
43	2.63	6.26	4.74	3.46			4.65	4.04
41	1.93	5.30			5.87	6.51	5.87	5.97
39	1.29	4.21	3.65	3.91			4.97	5.74
37					2.68	4.11		
35			3.77	4.82				

increasing n with increasing pressure. However, each pressure does exhibit a value greater than the maximum value of 4 predicted by theory and it is not known why the values are this high.

5.2.2 Half-time Analysis

Atmospheric Pressure

It has been shown [111] that using the reciprocal of crystallization half-times as a measure of crystallization rate and analyzing the data using secondary nucleation theory can give useful information. Before one can apply secondary nucleation theory to half-time data, the data must be analyzed for nucleation type. Because bulk crystallization includes both nucleation and growth effects, the bulk crystallization kinetics data must be analyzed to determine whether the nucleation is homogeneous or heterogeneous. While heterogeneous nucleation has only a temperature dependence, homogeneous nucleation has a temperature and a time dependence. If the bulk crystallization occurred with homogeneous nucleation, the analysis of half-time data using secondary nucleation theory would be inappropriate. Ross and Frolen's analysis of nucleation in polyethylene [112] suggests that a straight line will exist in the plot of $\log I + U^*/R(T_c - T_\infty)$ versus $1/T(\Delta T)^2 f^2$ in the same crystallization regime for homogeneous nucleation, where I is the nucleation

rate. If one can substitute the reciprocal half-time, $1/t_{1/2}$, for I , then the analysis for nucleation can be performed. Figure 5.13 shows the plot of $\log(1/t_{1/2}) + U^*/R(T_c - T_\infty)$ versus $1/T(\Delta T)^2 f^2$. It is seen that the data for all three samples is nonlinear. Therefore, the reciprocal half-time data can be substituted for G in secondary nucleation kinetics analysis. Figures 5.14, 5.15, and 5.16 show the kinetics analysis of the $M_w = 83,000$ homopolymer, $M_w = 151,000$ homopolymer, and the $M_w = 151,000$ copolymer, respectively. Figure 5.17 shows the kinetics results of the three bulk samples together. Linear relationships existed for the reciprocal half-time kinetics data. However, for the high molecular weight homopolymer and the copolymer, no clear regime transition were evident over the experimental crystallization temperature range. In the kinetics analysis, the values of U^* of 1500 cal/mole [46] and T_∞ of -42°C ($T_g - 30^\circ\text{C}$) [113] were taken from the literature. For the bulk polypropylene of $M_w = 83,000$, two distinct lines can be seen in the figure. The transition temperature corresponding to the intersection of these two lines was approximately 136°C . This is about $1-2^\circ$ lower than that reported for polypropylene using linear growth rate kinetics [114]. Analysis of the slopes of the lines using secondary nucleation theory gave values of $\sigma\sigma_e$ for Regimes II and III of 1000 and 1230 erg^2/cm^4 , respectively. Values of 746 and 786 erg^2/cm^4 from

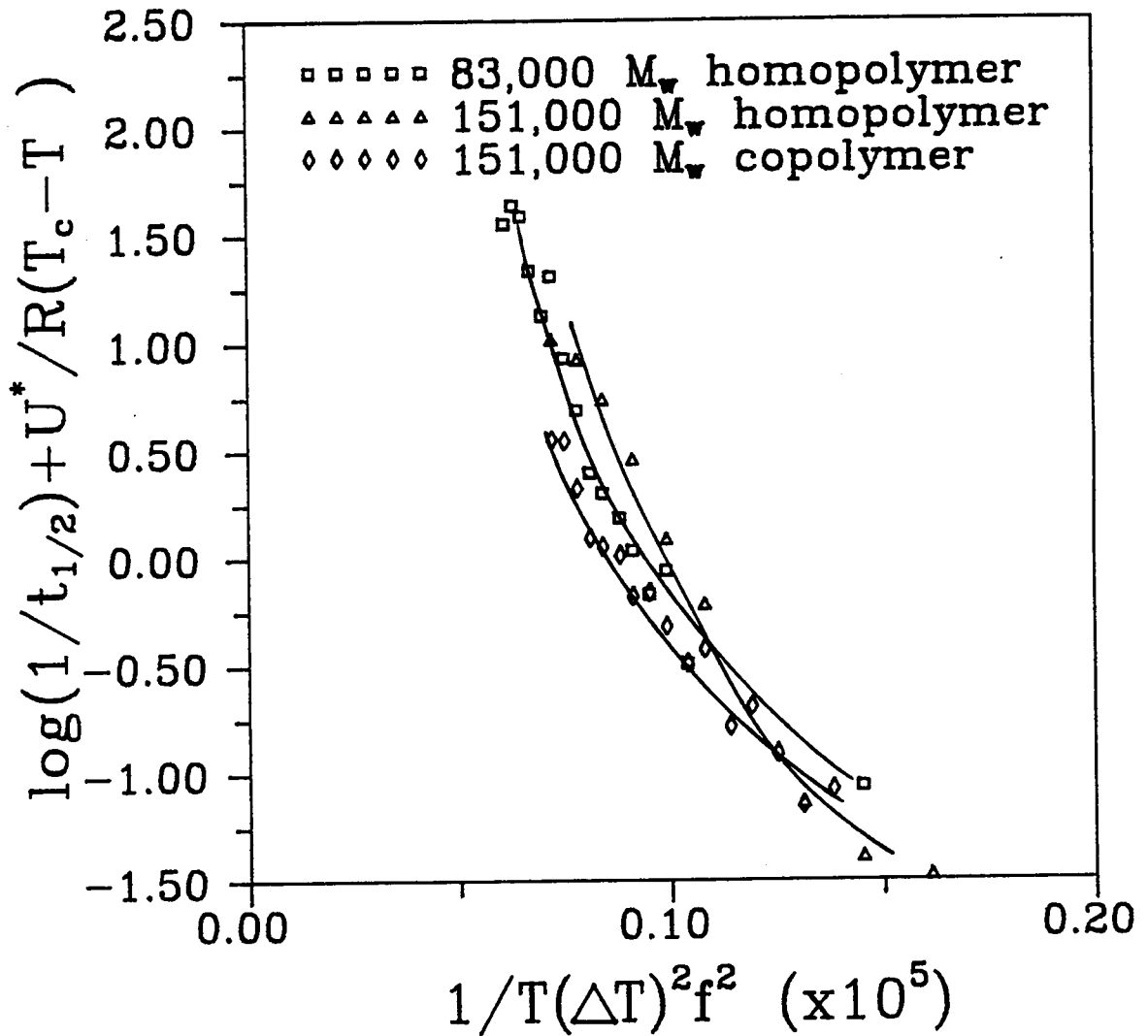


Figure 5.13 Homogeneous nucleation analysis for isotactic polypropylene crystallized at atmospheric pressure.

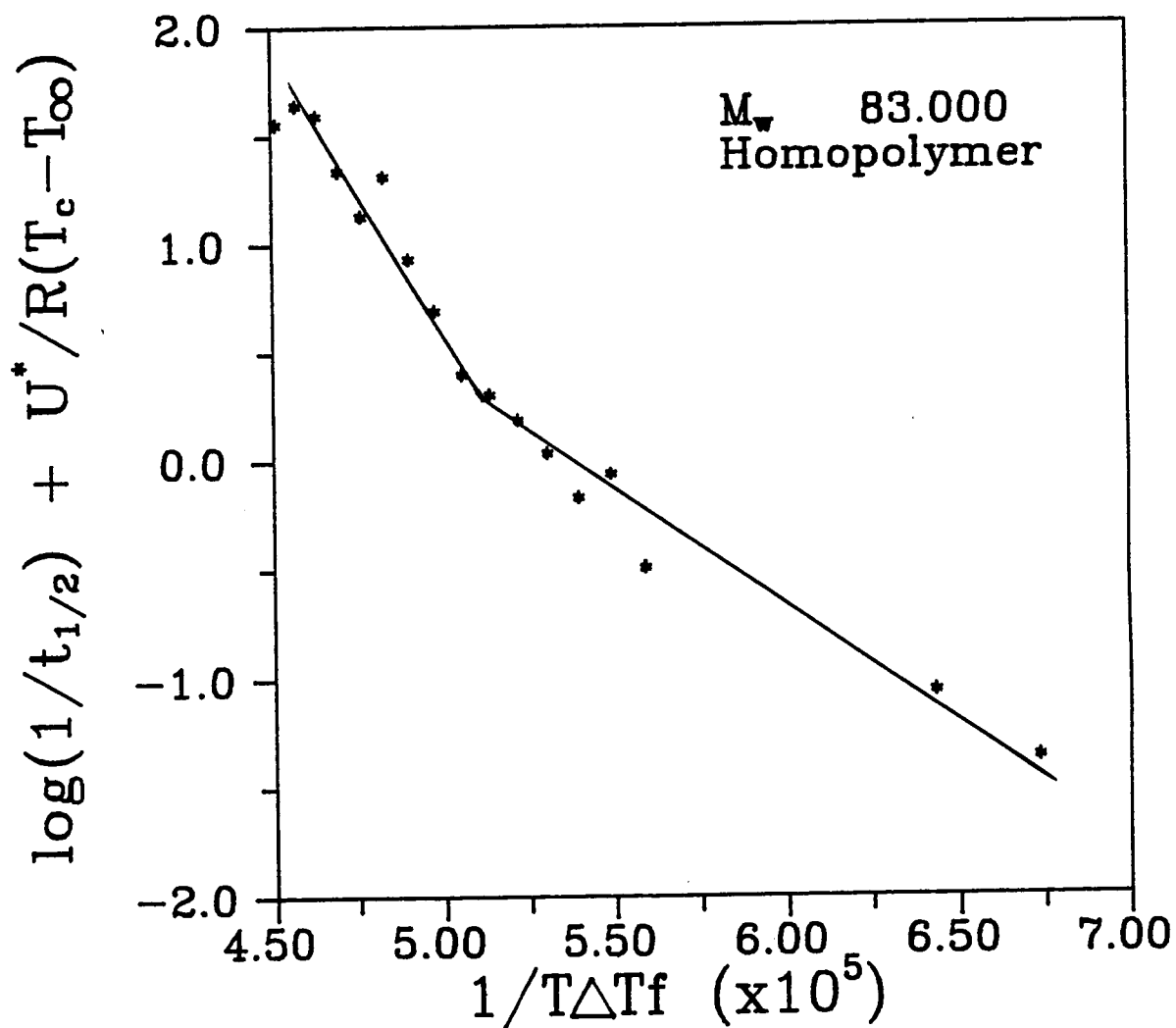


Figure 5.14 Kinetics analysis plot for isotactic polypropylene homopolymer $M_w = 83,000$ using reciprocal half-time data.

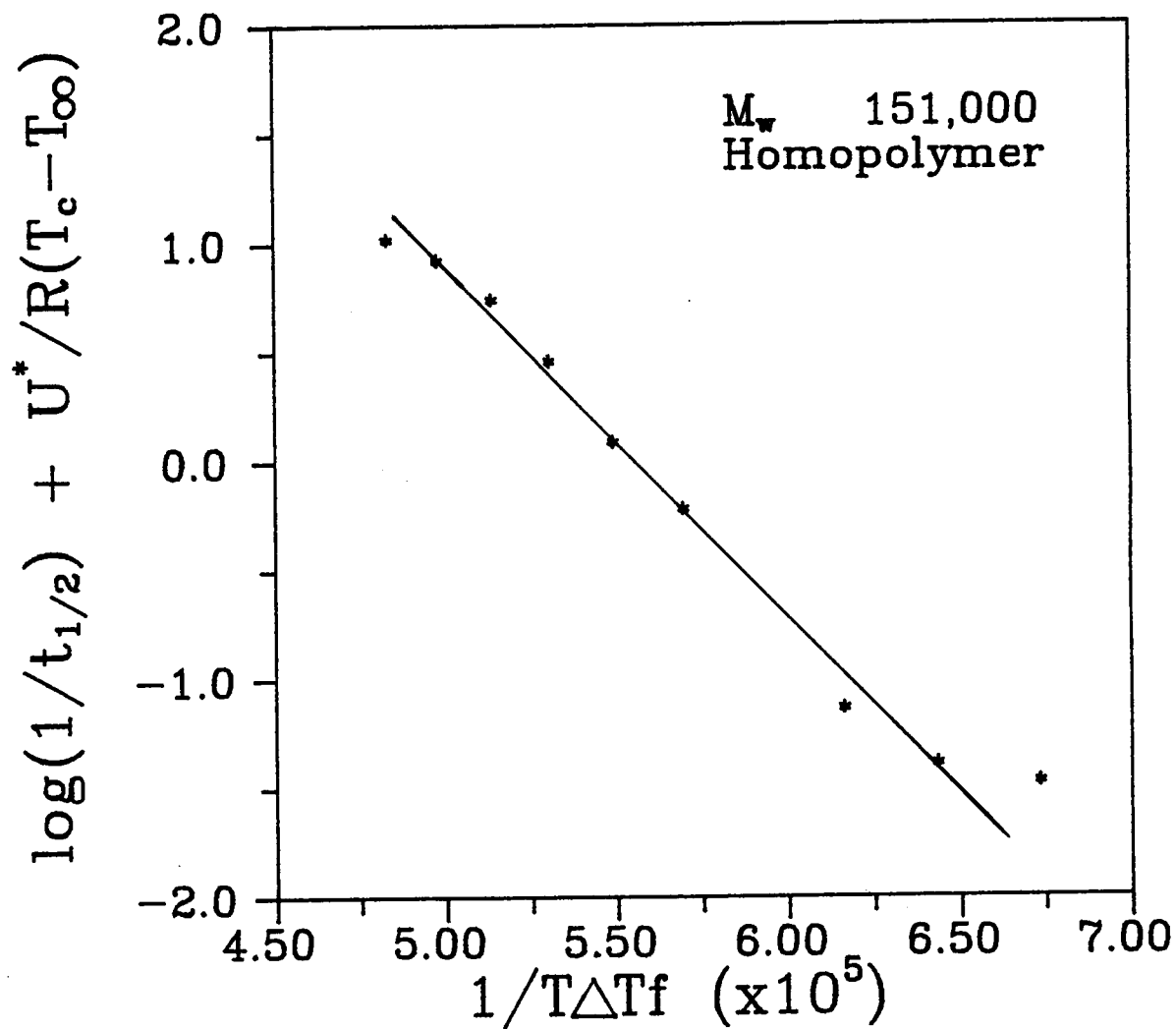


Figure 5.15 Kinetics analysis plot for isotactic polypropylene homopolymer $M_w = 151,000$ using reciprocal half-time data.

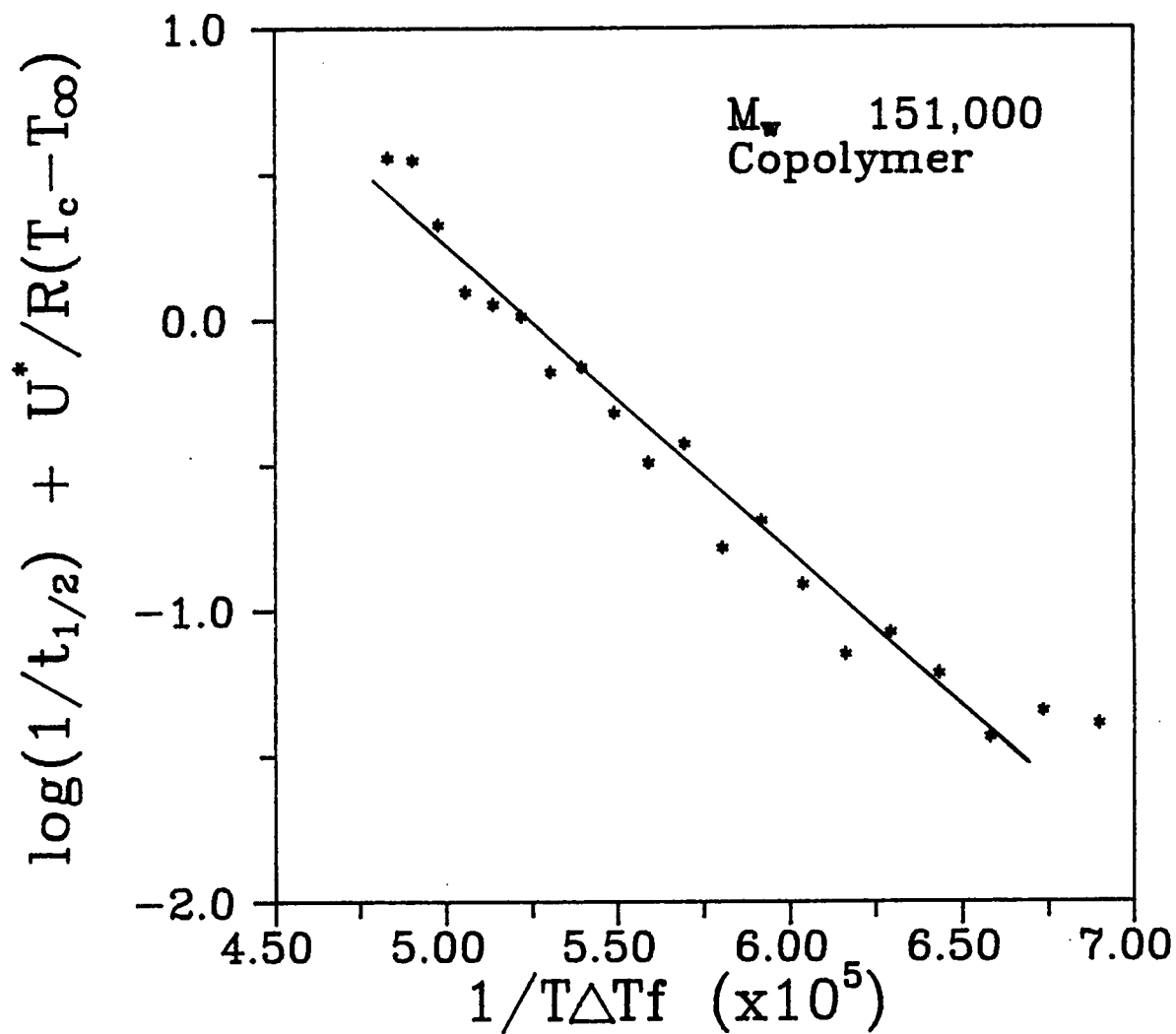


Figure 5.16 Kinetics analysis plot for isotactic polypropylene copolymer $M_w = 151,000$ using reciprocal half-time data.

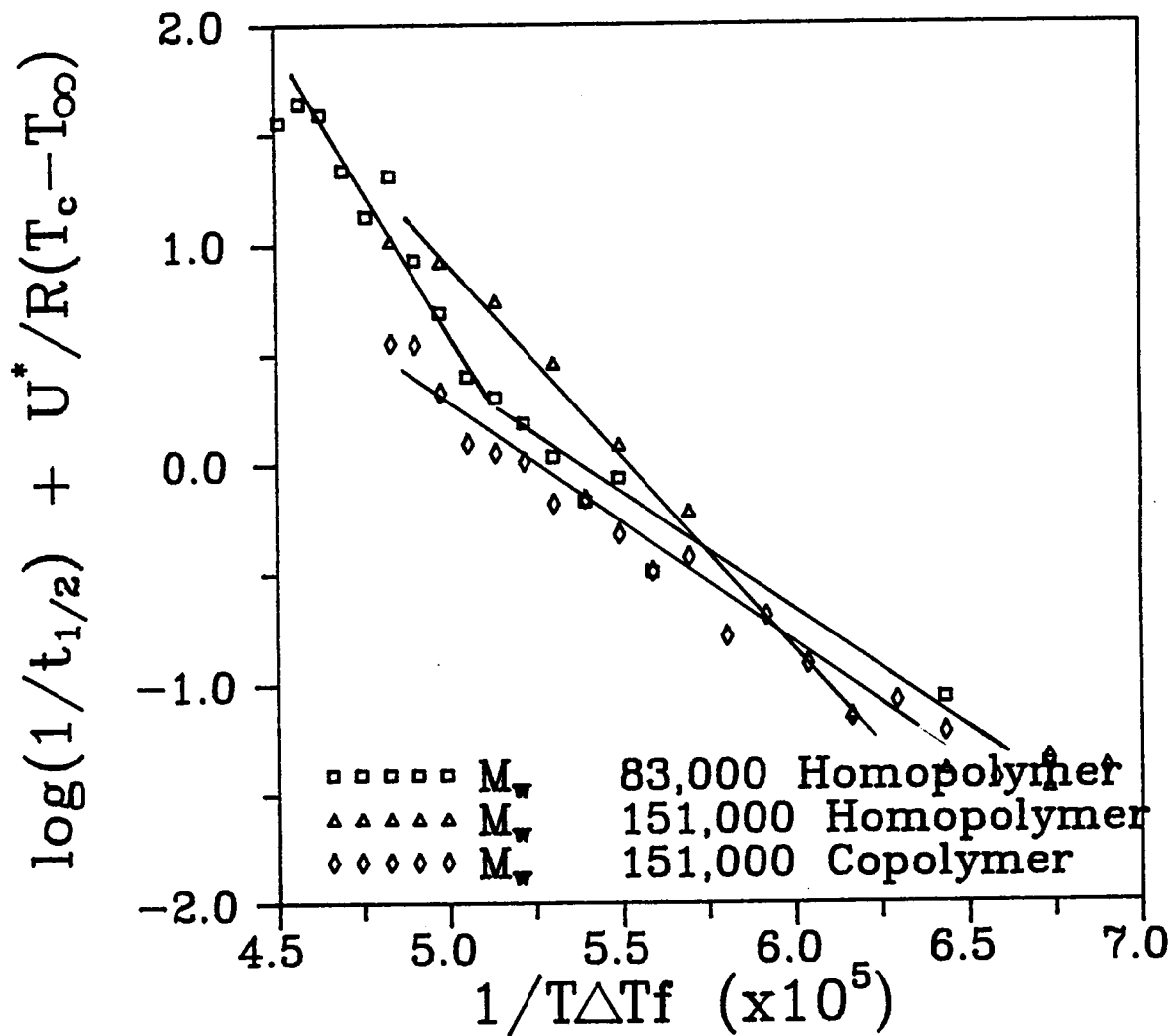


Figure 5.17 Kinetics analysis comparison using reciprocal half-time data for isotactic polypropylenes.

the literature [115] using linear growth rate data are somewhat lower. The slope ratio of Regime III to Regime II was 2.46. This is higher than the 2.0 predicted by theory and somewhat higher than that reported in the literature for an average of several polypropylene linear growth kinetics data sets of 2.09. Recently, Hammami [116] correlated results for polypropylene using half-time kinetics and linear growth kinetics. He showed that for his data, the two results were also different. It has been reported that the differences between half-time kinetics analysis and linear growth rate kinetics analysis may be due to nucleation effects being incorporated into the half-time analysis. However, Hammami accounted for this by rewriting the half-time analysis equation to include nucleation effects. His results then showed good agreement between half-time kinetics analysis and linear growth rate kinetics analysis.

It is unclear why the high molecular weight homopolymer and the copolymer do not show a transition. It is known that high molecular weight and broad molecular weight distribution can obscure a transition in linear growth data [4]. The results of half-time kinetics analysis are summarized in Table 5.7.

Table 5.7 Results of Half-Time Kinetics Analysis of iPP at Atmospheric Pressure

Sampl	Regim	K_g	$\log (\sigma\sigma_e)$ (erg)	σ_e (erg)	q (Kcal)	K_g/K_g	T_{tran} (°C)	ΔT
$M_w=83$	III	5.20	11.94	1228	106.8	10.6	137	48
	II	2.12	4.83	1000	87.0	8.6		
$M_w=15$		3.41	8.24	804	70.0	6.9		
$M_w=15$		2.30	5.21	543	47.2	4.7		

Elevated Pressure

To determine whether secondary nucleation theory could be applied to the half-time data, the data were first analyzed using a nucleation analysis of Ross and Frolen [117]. Figure 5.18 shows the plot of $\log(1/t_{1/2}) + U^*/R(T_c - T_\infty)$ versus $1/T(\Delta T)^2 f^2$ where $1/t_{1/2}$ has been substituted for I , the homogeneous nucleation rate, in the Ross-Frolen analysis. It is seen that, for all pressures, the data are nonlinear over the entire temperature range. This allows the reciprocal half-time data to be substituted for the linear growth rate G in secondary nucleation theory kinetics analysis.

The elevated pressure bulk crystallization data was analyzed using the half-time procedure described in the previous section. Plots of the kinetics analysis for 25, 50, 75, and 100 MPa are shown in Figures 5.19, 5.20, 5.21, and 5.22, respectively. Figure 5.23 shows the kinetics analysis results as a function of pressure, including atmospheric pressure. It is clear from the plots that the data for a given pressure cannot be fitted to one line. Rather, the data appeared to fit well to two lines, indicating a regime transition. The transition for all the pressure kinetics was assumed to be a Regime II - Regime III transition. In performing the kinetics analysis at each pressure, a value of $U^* = 1500$ cal/mole was used. The T_m^0 for a given pressure

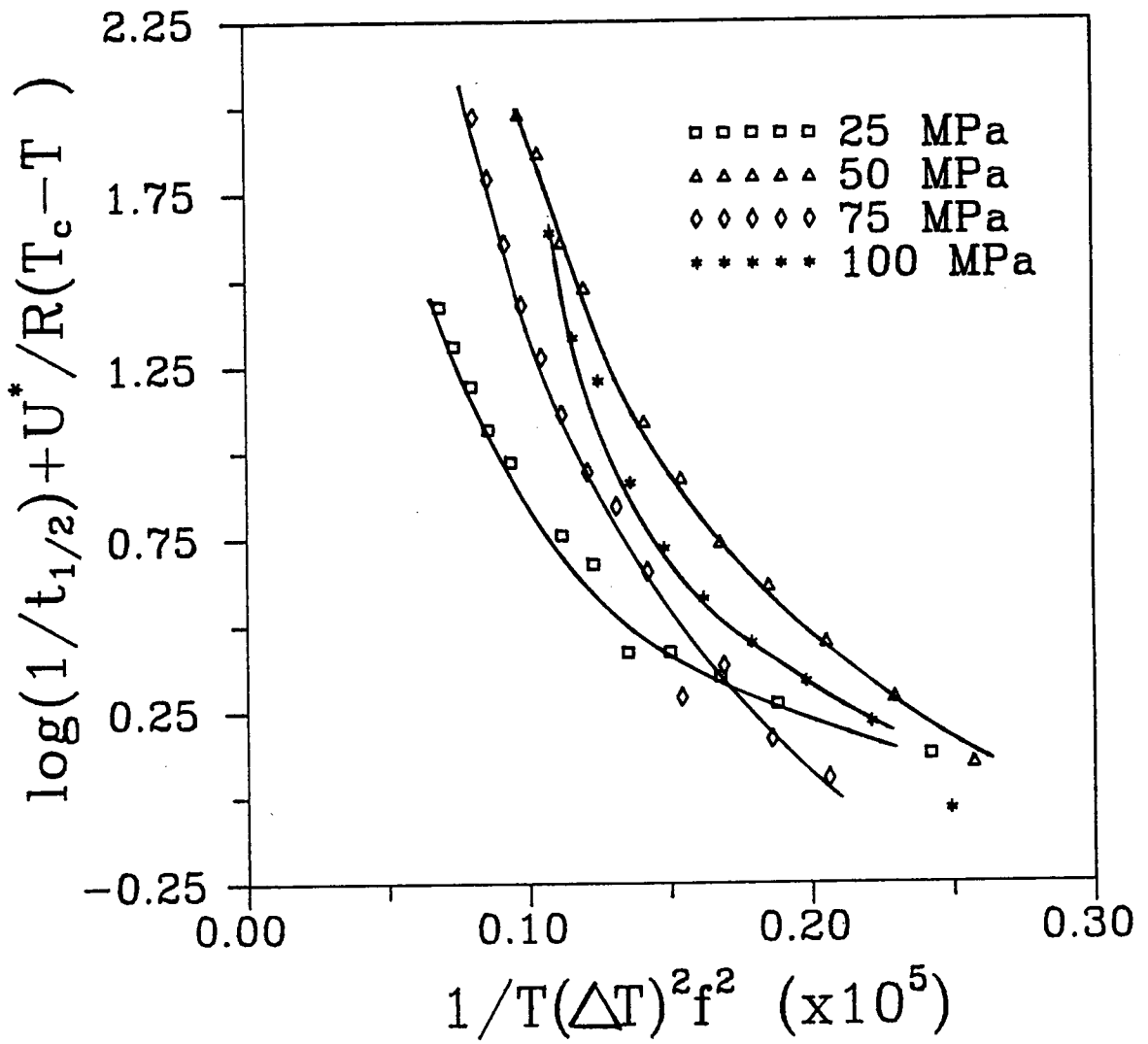


Figure 5.18 Homogeneous nucleation analysis for isotactic polypropylene $M_w = 83,000$ crystallized at elevated pressure.

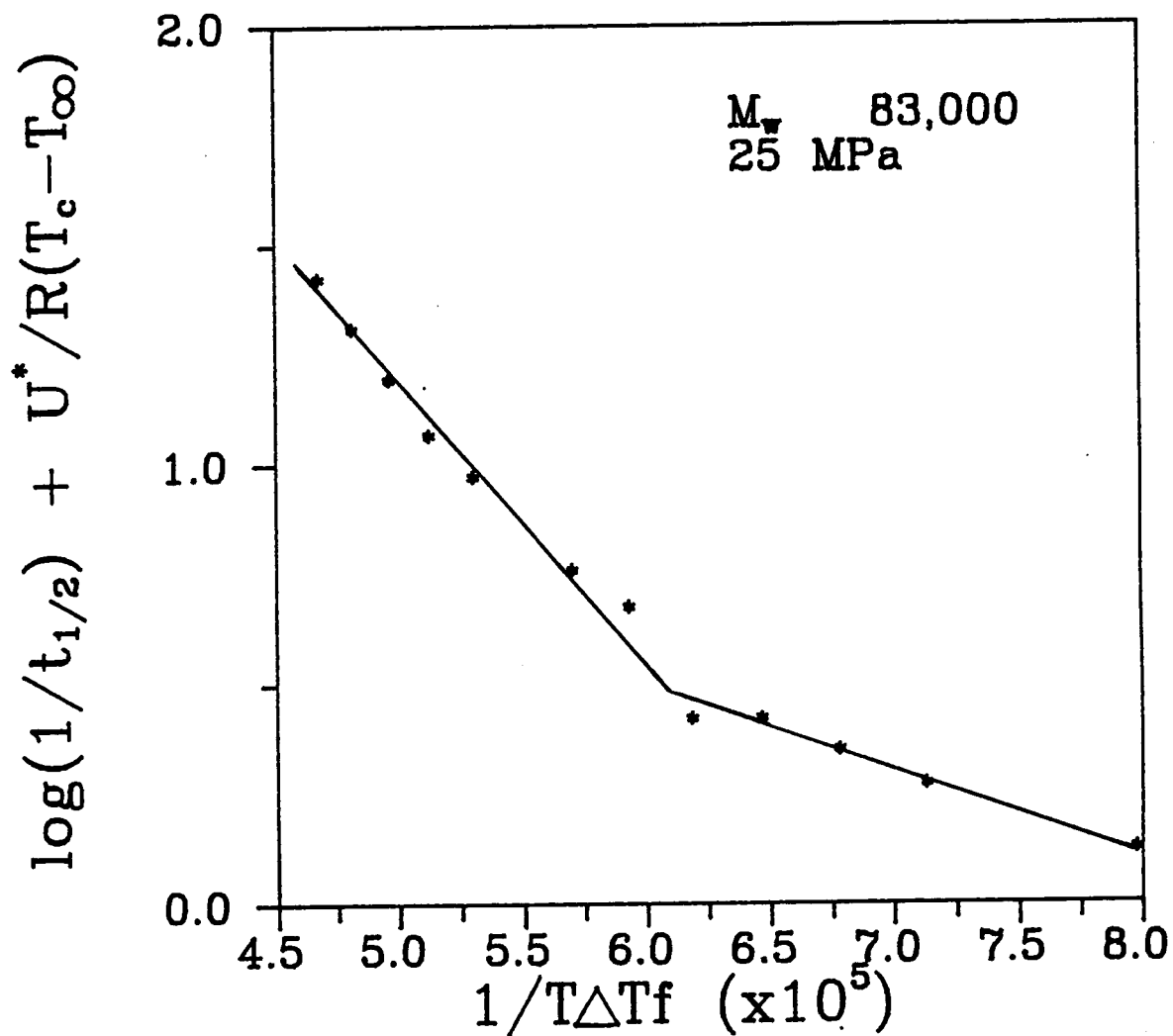


Figure 5.19 Reciprocal half-time kinetics analysis plot for isotactic polypropylene $M_w = 83,000$ crystallized at 25 MPa pressure.

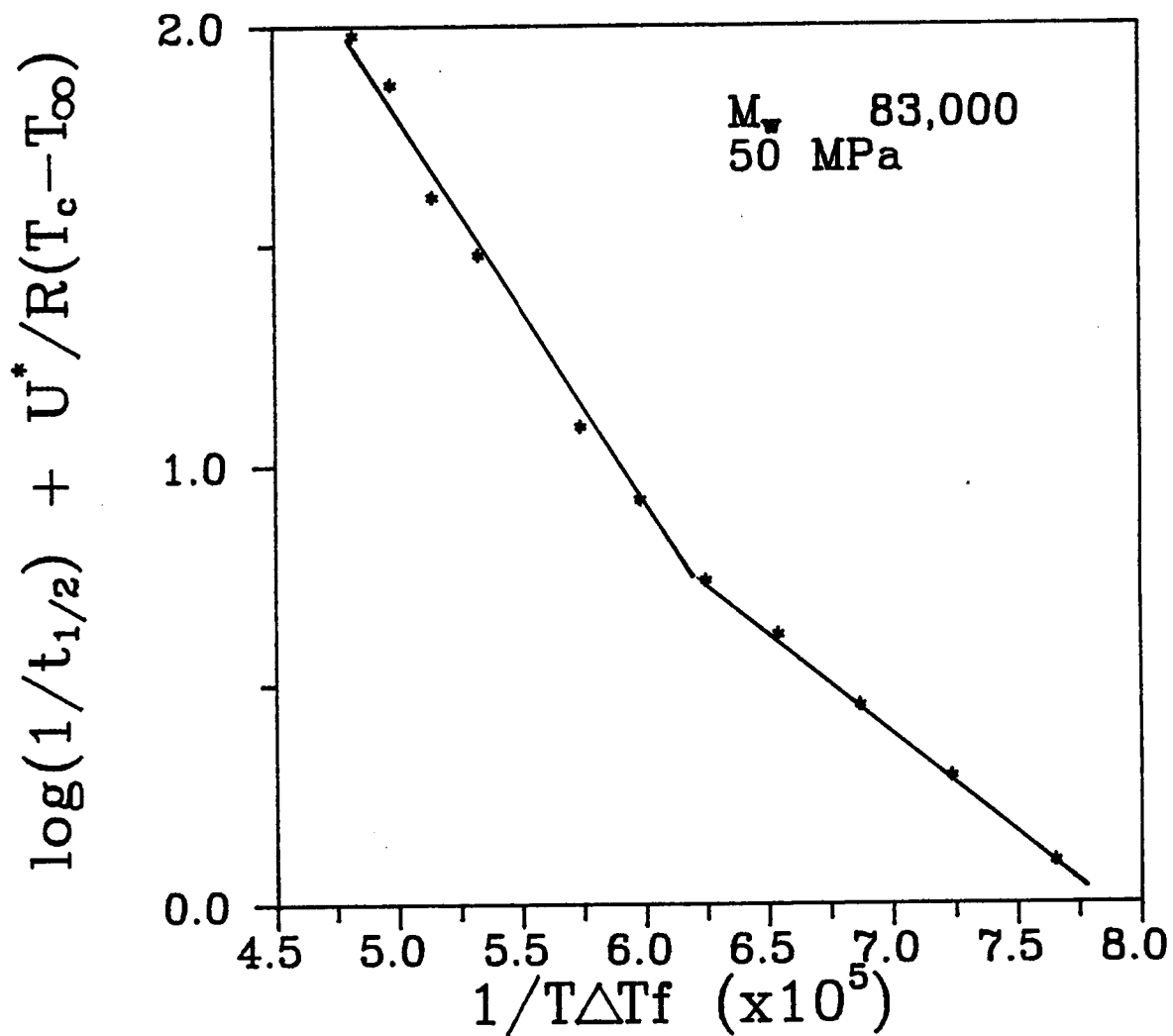


Figure 5.20 Reciprocal half-time kinetics analysis plot for isotactic polypropylene $M_w = 83,000$ crystallized at 50 MPa pressure.

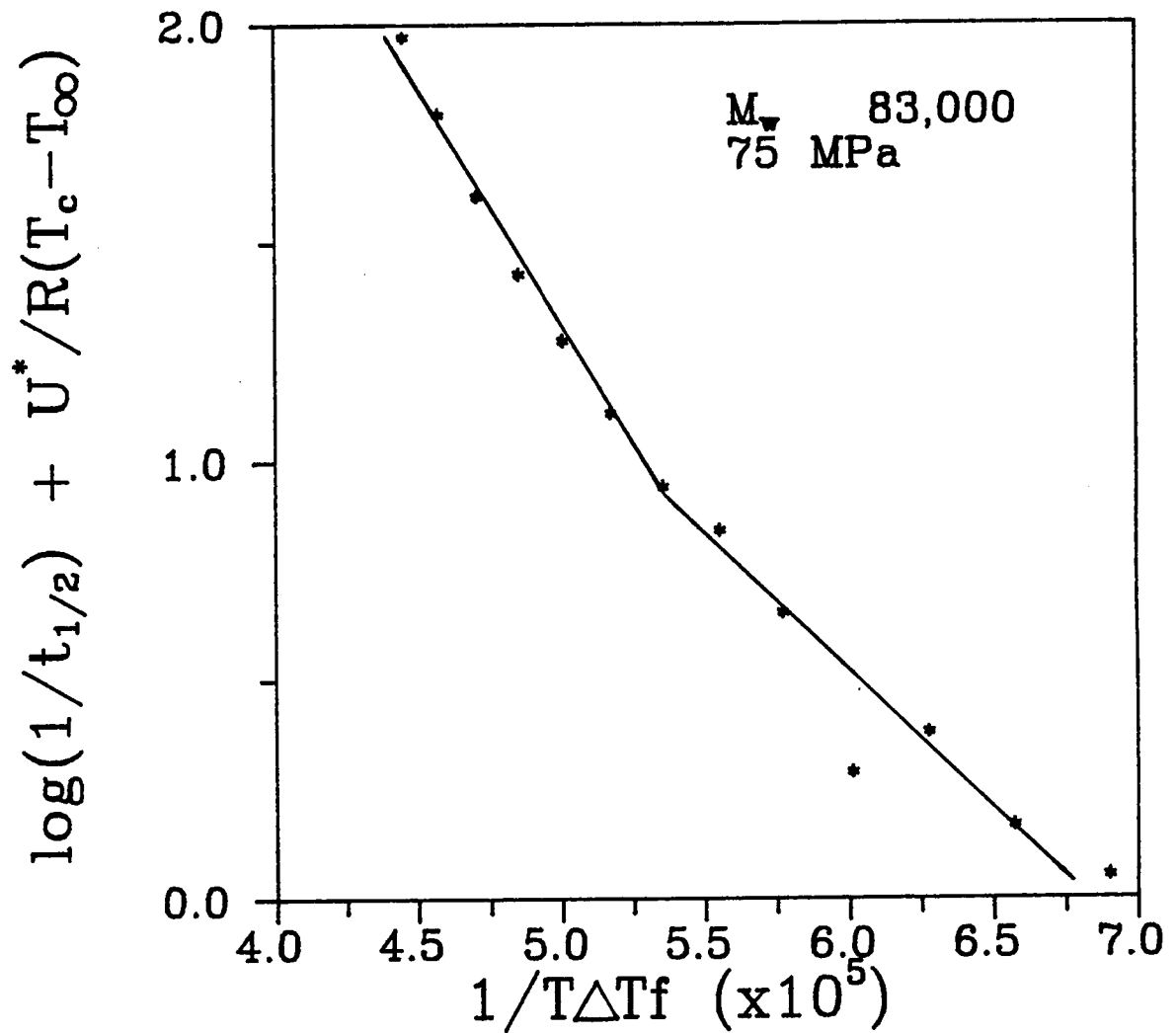


Figure 5.21 Reciprocal half-time kinetics analysis plot for isotactic polypropylene $M_w = 83,000$ crystallized at 75 MPa pressure.

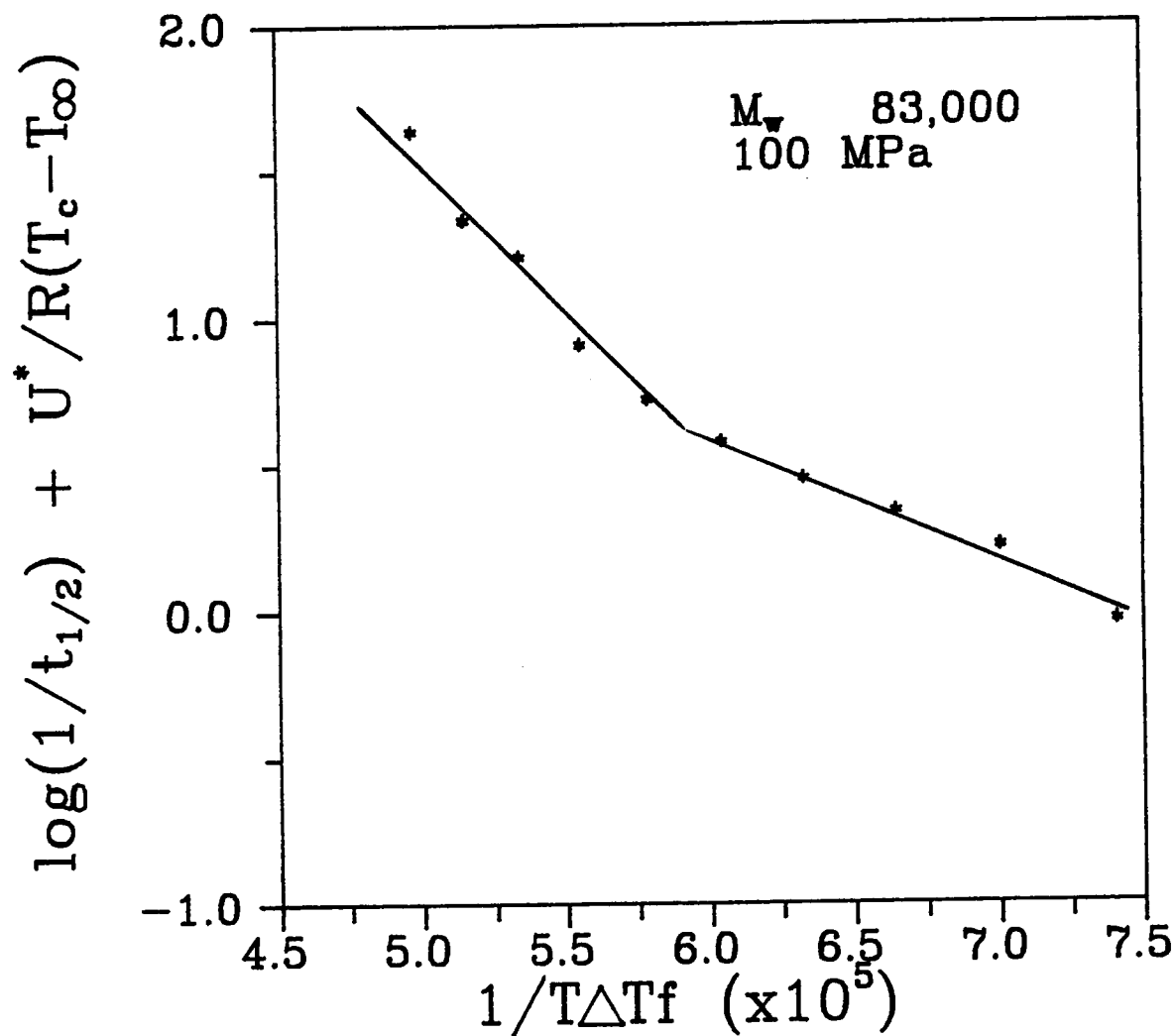


Figure 5.22 Reciprocal half-time kinetics analysis plot for isotactic polypropylene $M_w = 83,000$ crystallized at 100 MPa pressure.

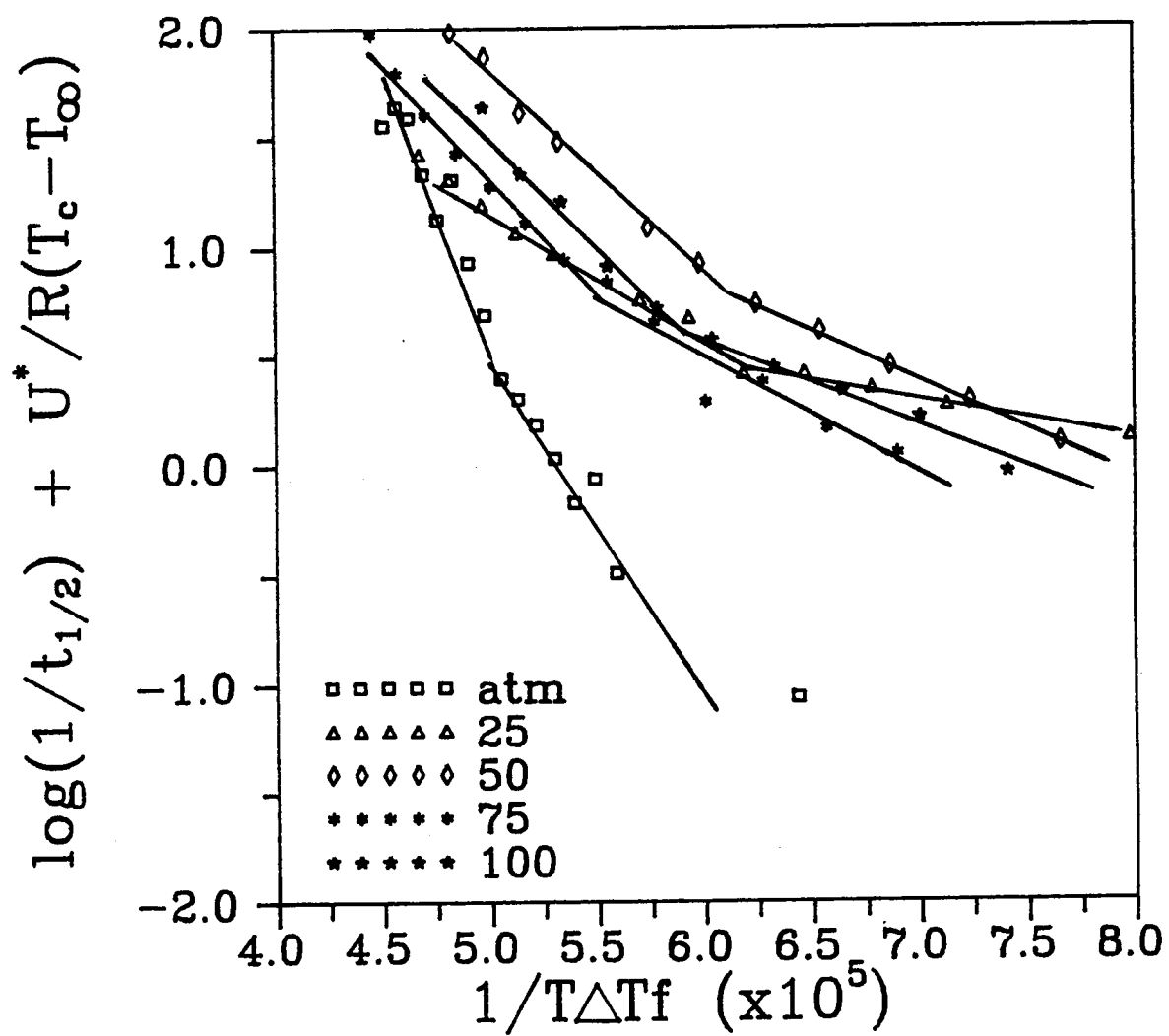


Figure 5.23 Reciprocal half-time kinetics analysis plot for isotactic polypropylene $M_w = 83,000$ crystallized at elevated pressure.

was determined from the DLI pressure melting data, and a change in the glass transition temperature T_g with pressure (dT_g/dP) of $20^\circ/100$ MPa was assumed [118]. The $\sigma\sigma_e$ product was determined using a_0 and b_0 for the monoclinic crystal structure. Table 5.8 gives the results of the half-time kinetics analysis. It is seen that at all elevated pressures, the slopes of the Regime II and Regime III data are smaller than those for the atmospheric pressure data. The ratio $K_g(\text{III})/K_g(\text{II})$ for the elevated pressure data, with the exception of the 25 MPa data, are reasonably close to the theoretical prediction of 2. Figure 5.24 shows the behavior of the Regime II - Regime III transition temperature as a function of pressure. While the transition temperatures were higher than the atmospheric pressure transition temperature, the transition does not shift with pressure in a regular fashion. The data qualitatively change in a fashion similar to that of the equilibrium melting temperature change with pressure.

Table 5.8 Results of Half-Time Kinetics Analysis of iPP at Various Pressures

Press (MPa)	Regime	Kg	log ($\sigma\sigma_e$ (erg	σ_e (erg	q (kcal	Kg/Kg	T _{tran} (°C)	ΔT																																																												
atm	III	5.20	11.94	1228	106.8	10.6	2.45	137	48																																																												
	II	2.12	4.83	1000	87.0	8.6				25	III	1.70	4.85	396			4.14	155	37	II	0.41	1.55	193			50	III	2.14	6.46	493	43.0	4.2	2.02	157	40	II	1.06	3.59	487	42.6	4.2	75	III	2.60	6.97	600	52.5	5.2	1.92	149	46	II	1.36	4.04	627	54.9	5.4	100	III	2.28	6.47	509	44.3	4.4	2.30	171	40	II	0.99
25	III	1.70	4.85	396			4.14	155	37																																																												
	II	0.41	1.55	193						50	III	2.14	6.46	493	43.0	4.2	2.02	157	40	II	1.06	3.59	487	42.6	4.2	75	III	2.60	6.97	600	52.5	5.2	1.92	149	46	II	1.36	4.04	627	54.9	5.4	100	III	2.28	6.47	509	44.3	4.4	2.30	171	40	II	0.99	3.18	442	38.5	3.8												
50	III	2.14	6.46	493	43.0	4.2	2.02	157	40																																																												
	II	1.06	3.59	487	42.6	4.2				75	III	2.60	6.97	600	52.5	5.2	1.92	149	46	II	1.36	4.04	627	54.9	5.4	100	III	2.28	6.47	509	44.3	4.4	2.30	171	40	II	0.99	3.18	442	38.5	3.8																												
75	III	2.60	6.97	600	52.5	5.2	1.92	149	46																																																												
	II	1.36	4.04	627	54.9	5.4				100	III	2.28	6.47	509	44.3	4.4	2.30	171	40	II	0.99	3.18	442	38.5	3.8																																												
100	III	2.28	6.47	509	44.3	4.4	2.30	171	40																																																												
	II	0.99	3.18	442	38.5	3.8																																																															

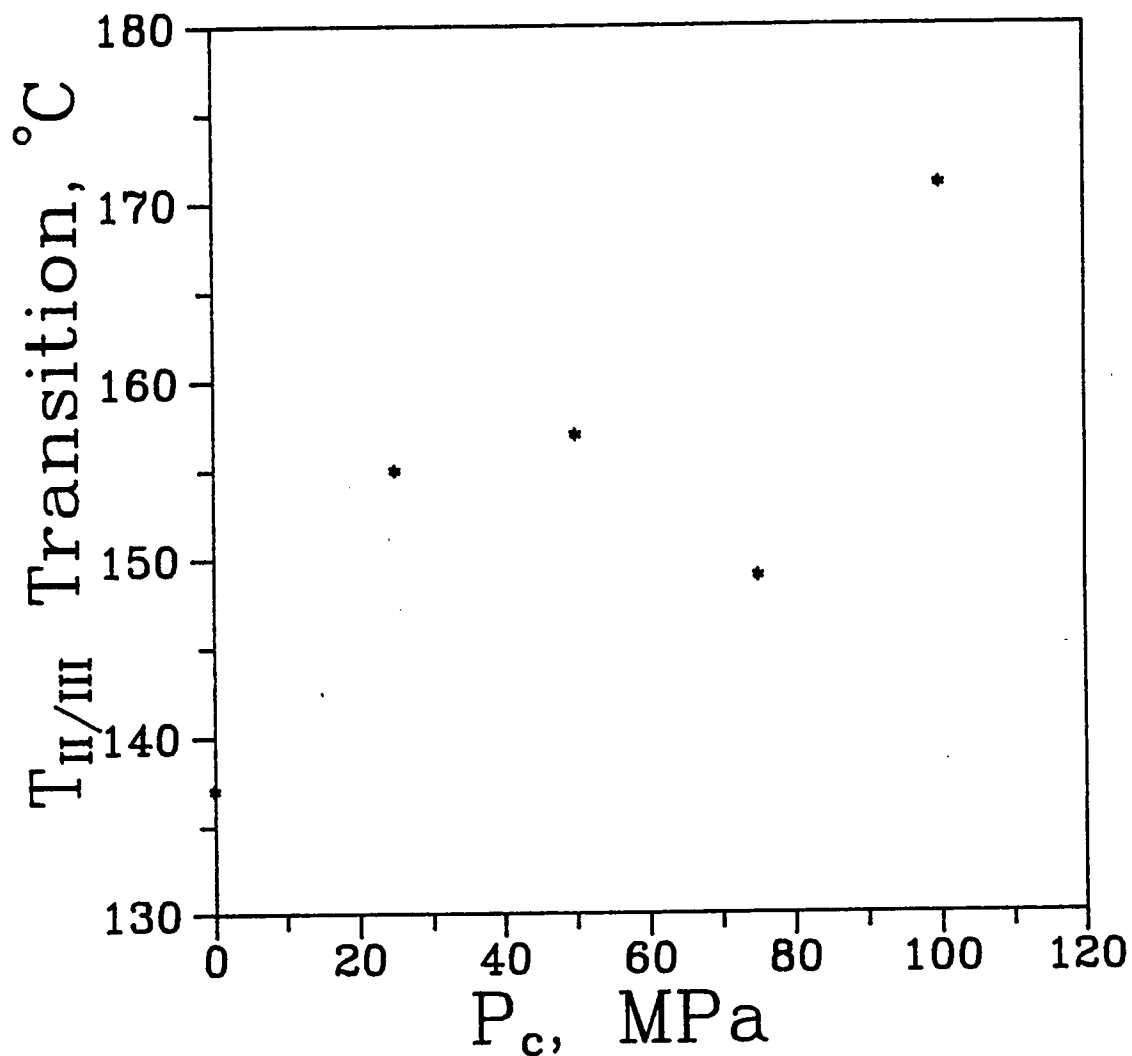


Figure 5.24 Regime transition temperature for isotactic polypropylene $M_w = 83,000$ as a function of crystallization pressure.

Chapter 6

Conclusions

A study of the morphology, thermal behavior, and crystallization behavior of isotactic polypropylene at atmospheric pressure and elevated pressure has been studied. At atmospheric pressure, two homopolymers of similar MWD but different molecular weights and a copolymer with a weight average molecular weight equal to that of one of the homopolymers were studied. At elevated pressure, the lower molecular weight homopolymer was studied at pressures up to 200 MPa. Several interesting results have been seen.

6.1 Morphology

At atmospheric pressure, the morphology observed in the optical microscope shows little difference between the two homopolymers. However, the copolymer does exhibit different behavior than the homopolymers.

At elevated pressures, the observed morphology is spherulitic at all pressures and temperatures studied. Some quadritic morphologies are present under certain conditions but only in combination with spherulites and only infrequently. The internal structure of the spherulites must change as evidenced by the observed changes in birefringence with pressure.

6.2 Thermal Behavior

It is interesting that the homopolymer and copolymer of equal Mw show more similar DSC behavior than the low molecular weight homopolymer. All samples exhibited complex melting behavior common to isotactic polypropylene. In addition, the melting behavior as measured with depolarized light intensity (DLI) was determined and compared to the DSC behavior. The morphology observed with the optical microscope on heating was correlated with the DSC and DLI behaviors.

The melting behavior of elevated pressure crystallized samples showed significant changes with crystallization pressure, both at elevated pressure melting and atmospheric pressure melting. The observed melting temperatures at elevated pressure allowed a determination of the change in melting temperature with change in pressure, dT_m/dP .

6.3 Crystallization Behavior

The Avrami analysis of the bulk crystallization data indicate that, for the homopolymers and the copolymer crystallized at atmospheric pressure, the values of the Avrami exponent n range from about 2 to about 3.5, with most of the values around 3. This value is indicative of heterogeneous nucleation with spherulitic growth. The n values are in agreement with the literature. For the

elevated pressure crystallization data, the values of the Avrami exponent range from below 2 to above 6.

The kinetics analysis of the bulk crystallization half-time data indicate at least a regime II - regime III transition for the lower molecular weight homopolymer, which is expected for isotactic polypropylene. The other samples did not exhibit a clear transition, possible due to molecular weight and molecular weight distribution effects.

The kinetics analysis of the elevated pressure data also exhibited Regime II - Regime III transitions. These transitions were observed at all pressures studied. The values of $\sigma\sigma_e$, σ_e and q determined from the kinetics seem to decrease with increasing pressure. The values are lower than those at atmospheric pressure. The regime transition temperature increased with increasing pressure.

Chapter 7

Recommendation for Further Work

7.1 Linear Growth Rate Kinetics

Additional information can be obtained using linear growth rates. This would allow evaluation of the fold surface free energy which can reveal changes in the nature of the fold surface.

7.2 Stereoregularity

A complete study of crystallization behavior of isotactic polypropylene requires information on the stereoregularity. The effect of stereoregularity on crystallization has not been isolated from the effects of molecular weight and molecular weight distribution on crystallization. Recent advances in catalyst systems allow better control of stereoregularity such that a proper study could be conducted.

7.3 Copolymers

A further study of additional copolymers would include several comonomer ratios of ethylene - propylene as well as other comonomers such as butylene. This study could provide information on the effect of copolymerization on crystallization behavior as well as morphological development.

7.4 Additional Morphological Studies

Additional morphological studies would include characterization with wide angle X-ray diffraction of crystal structure as a function of crystallization pressure and crystal perfection as a function of crystallization temperature. Lamellar structure as a function of crystallization temperature and pressure would be studied with small angle X-ray scattering and electron microscopy.

References

References

1. J.H. Reinshagen and R.W. Dunlap, *J. Appl. Polym. Sci.*, 17, 3619 (1973).
2. J.L. Kardos, A.W. Christiansen, and E. Baer, *J. Polym. Sci.*, A2, 4, 777 (1966).
3. C. Nakafuku, *Polymer* 22, 1673 (1981).
4. J.D. Hoffman, *Polymer* 24, 3 (1983) .
5. E.N. Dalal and P.J. Phillips, *Macrom.* 17, 248 (1984).
6. H.T. Tseng and P.J. Phillips, *Macrom.* 18, 18 (1985).
7. A. Keller, *Phil. Mag.*, 2, 1171 (1957).
8. E.W. Fischer and G.F. Schmidt, *Angew. Chem.* 74, 551 (1962) .
9. P.H. Till, Jr., *J. Polym. Sci.*, 24, 301 (1957) .
10. F.J. Padden and H.D. Keith, *J. Appl. Phys.* 30, 1479 (1959) .
11. D.R. Norton, Ph.D. dissertation, Univ. of Bristol, 1984.
12. D.R. Norton and A. Keller, *Polymer* 26, 704 (1985) .
13. H.D. Keith and F.J. Padden, Jr.
14. A.J. Lovinger, J.O. Chua, and C.C. Gryte, *J. Polym. Sci. Polym. Phys. Ed.* 15, 641 (1977) .
15. J. Henson, M.S. thesis, Univ. of Tenn. Knoxville, 1979.
16. J.W.S. Hearle, "Polymers and Their Properties.", vol. 1, John Wiley and Sons, New York, 1982.
17. A. Keller, *Phil. Mag.*, 2, 1171 (1957).
18. P.J. Flory, *J. Am. Chem. Soc.*, 84, 2857 (1962).

-
19. K. Hermann, O. Gerngross, and W. Abitz, *Z. Phys. Chem.*, 10, 371 (1930).
 20. P.H. Till, Jr., *J. Polym. Sci.*, 24, 1273 (1957).
 21. E.W. Fischer, *Z. Naturforsch.*, 12A, 1171 (1957).
 22. M.I. Bank and S. Krimm, *J. Polym. Sci., Polym. Symp.* 53, 347 (1975) .
 23. J.D. Hoffman, *Faraday Discuss. Chem. Soc.*, 68, 378 (1979) .
 24. C.M. Guttman and E.A. DiMarzio, *Macro.* 15, 525(1982).
 25. E.W. Fischer, H. Goddar, and G.F. Schmidt, *Proc. Conf. on Polymer Struct. and Mech. Prop.*, April 19-21 (1967).
 26. L. Mandelkern, *Proc. Sagamore Army Material Res. Conf.*, 20th, Syracuse Univ. Press, Syracuse, New York (1975).
 27. P.J. Flory and D.Y. Yoon, *Nature* 272, 226 (1978).
 28. J.D. Hoffman and R.L. Miller, *Macro.* 21, 3038 (1988).
 29. E.A. DiMarzio, C.M. Guttman, and J.D. Hoffman, *Faraday Discuss. Chem. Soc.* 68, 210 (1979).
 30. J.I. Lauritzen, Jr., and J.D. Hoffman, *J. Res. Nat. Bur. Stand.* 64A, 73 (1960).
 31. F.P. Price, *J. Polym. Sci.* 42, 49 (1960).
 32. F.C. Frank and M. Tosi, *Proc. Roy. Soc.* A265, 323 (1961).
 33. D.M. Sadler, *Polymer* 24, 1401 (1983).
 34. J.I. Lauritzen and J.D. Hoffman, *J. Appl. Phys.* 44, 4430 (1973).
 35. P.J. Phillips, *Polymer Preprints* 20, 483 (1979).
 36. J.D. Hoffman and J.J. Weeks, *J. Res. Nat. Bur. Stand.* A66, 13 (1962).
 37. T. Suzuki and A.J. Kovacs, *Polymer J.* 1, 82 (1970).

-
38. J.D. Hoffman and J.J. Weeks, *J. Chem. Phys.* 37, 1723 (1962).
 39. J.I. Lauritzen, Jr., *J. Appl. Phys.*, 44, 4353 (1973).
 40. I.C. Sanchez and E.A. DiMarzio, *J. Res. Nat. Bur. Stand.* A76, 213 (1972).
 41. J.I. Lauritzen, Jr., *J. Appl. Phys.* 44, 4353 (1973)
 42. J.D. Hoffman, *Polymer* 26, 1763 (1985).
 43. C.M. Guttman, E.A. DiMarzio, and J.D. Hoffman, *Polymer* 22, 1466 (1981).
 44. J.J. Point and A.J. Kovacs *Macro.* 13, 399 (1979).
 45. J.I. Lauritzen, Jr., and Passaglia, *J. Res. Nat. Bur. Stand.* A71, 261 (1967).
 46. J.D. Hoffman, G.T. Davis, and J.I. Lauritzen, Jr., "Treatise on Solid State Chemistry," N.B. Hannay, Ed., Plenum Press, New York (1976) Vol. 3.
 47. P.H. Geil, F.R. Anderson, B. Wunderlich, and T. Arakawa, *J. Polym. Sci.* A2, 3707 (1962).
 48. B. Wunderlich and T. Arakawa, *J. Polym. Sci.* A2, 3697 (1964).
 49. D.C. Bassett and B. Turner, *Nature* 240, 146 (1972).
 50. D.C. Bassett and B. Turner, *Phil. Mag.* 29, 925 (1974).
 51. H.T. Tseng and P.J. Phillips, *Macro.* 18, 1565 (1984).
 52. B.C. Edwards and P.J. Phillips, *J. Polym. Sci., Polym. Phys. Ed.* 13, 2117 (1975).
 53. J.L. Kardos, A.W. Christiansen, and E. Baer, *J. Poly. Sci.* A2, 4, 777 (1966).
 54. P.J. Phillips. and B.C. Edwards, *J. Polym. Sci., Polym. Physics Ed.* 14, 377 (1976).
 55. C.K.L Davies and M.C.M. Cucarella, *J. Mat. Sci.* 15, 1557 (1980).
 56. E. Baer and J.L. Kardos, *J. Polym. Sci.* A3, 2827 (1965).

-
57. S. Gogolewski and A.J. Pennings, *Polymer* 18, 654 (1977).
 58. C.K.L. Davies and M.C.M. Cucarella, *J. Mat. Sci.* 15, 1557 (1980).
 59. E.N. Dalal, Ph.D. dissertation, Univ. of Utah 1983.
 60. T.G. Fox and P.J. Flory, *J. Appl. Phys.* 28, 581 (1950).
 61. J.H. Gibbs and E.A. Dimarzio, *J. Chem. Phys.* 28, 373 (1958).
 62. J.M. O'Reilly, *J. Polym. Sci.*, 57, 429 (1962).
 63. Mizoguchi and Ishikawa (1975).
 64. J.H. Magill, *J. Appl. Phys.* 35, 3249 (1964).
 65. M. Gopalan and L. Mandelkern, *J. Phys. Chem.* 71, 3833 (1967).
 66. J.G. Fatou and L. Mandelkern, *J. Phys. Chem.* 69, 417 (1965).
 67. E. Ergoz, J.G. Fatou, and L. Mandelkern, *Macro.* 5, 142 (1972).
 68. J.D. Hoffman, L.J. Frolen, G.S. Ross, and J.I. Lauritzen, Jr., *J. Res. Nat. Bur. Stand.* A79, 671 (1975).
 69. R.C. Allen, Ph.D. dissertation, Virginia Polytechnic Institute 1984.
 70. P.G. de Gennes, *J. Chem. Phys.*, 55, 572 (1971).
 71. G. Natta, *J. Polym. Sci.* 16, 143 (1955).
 72. J.C. Randall, *Polymer Sequence Determination: Carbon 13 NMR Method* (1977).
 73. M. Avrami, *J. Chem. Phys.* 7, 1103 (1939).
 74. Y.S. Yadav and P.C. Jain, *Polymer* 27, 721 (1986).
 75. V. Petraccone et al., *Makrom. Chem., Rapid Comm.*, 5, 631 (1984).

-
76. J.D. Hoffman and J.J. Weeks, *J. Res. Natl. Bur. Stand. A66*, 13 (1962).
 77. N. Bekkedahl, *Trans. Faraday Soc.* 35, 483 (1939).
 78. B. Wunderlich, *Macro. Physics*.
 79. G.Natta and P. Corradini, *Nuovo Cimento, Suppl.* 15, 68 (1960).
 80. H.D. Keith et al., *J. Appl. Phys.* 30, 1485 (1959).
 81. S. Bruckner and S. Meille, *Nature* 340, 455 (1989).
 82. P. Corradini et al. *Polymer Comm.* 30, 281 (1989).
 83. J.A. Sauer and K.D. Pae, *J. Appl. Phys.* 39, 4959 (1968).
 84. E. Dalal and P.J. Phillips, *Macro.* 16, 1754 (1983).
 85. E.M. Barrall, J.F. Johnson, and R. S. Porter, *Applied Polymer Symposia* 8, 191 (1969).
 86. F.J. Padden, Jr. and H.D. Keith, *J. Appl. Phys.* 30, 1479 (1959).
 87. D.R. Norton and A. Keller, *Polymer* 26, 704 (1985).
 88. M. Hikosaka and T. Seto, *Polymer J.* 5, 111 (1973).
 89. P.J. Flory and A. Vrij, *J. Am. Chem. Soc.* 84, 3548 (1963).
 90. P.J. Flory, *Statistical Mechanics of Chain Molecules*, Interscience (1969).
 91. S.Z.D. Cheng et al, *Macro.* 23, 298 (1990).
 92. H.S. Bu, S.Z.D. Cheng, and B. Wunderlich, *Macrom. Chem.* 9, 76 (1988).
 93. B. Monnasse and J.M. Haudin, *Colloid and polym. Sci.* 263, 822 (1985).
 94. J.J. Janimak, PhD dissertation, Univ. of Akron (1990).
 95. G. Guerra et al., *J. Polym. Sci.: Phys.* 22, 1029 (1984).

-
96. R. Napilitano, B. Pirozzi, and V. Varriale, *J. Polym. Sci.: Phys.* 28, 139 (1990).
 97. H.T. Tseng, PhD dissertation, Univ. of Utah (1984).
 98. H.T. Tseng and P.J. Phillips, *Macro.* 18, 1565 (1985).
 99. V. Karl, F. Asmussen, K. Ueberreiter, *Makrom. Chem.* 178, 2037 (1977).
 100. J. H. Reinshagen and R.W. Dunlap, *J. Appl. Polym. Sci.* 17, 3619 (1973).
 101. C. Nakafuku, *Polymer* 22, 1673 (1981).
 102. T. Davidson and B. Wunderlich, *J. Polym. Sci. A2*, 7, 377 (1969).
 103. A. Siegmann and P.J. Harget, *J. Polym. Sci., Polym. Phys.* 18, 2181 (1980).
 104. N. Hiromatsu and M. Yasuniwa, *Polym. J.* 12, 105 (1980).
 105. C. Nakafuku and M. Yasuniwa, *Polym. J.*, 19, 845 (1987).
 106. L.R. Fortune and G.N. Malcolm, *J. Phys. Chem* 64, 934 (1960).
 107. C. Nakafuku, *Polymer* 22, 1673 (1981).
 108. A. Turner-Jones et al., *Makrom. Chem* 75, 134 (1964).
 109. S. Meille et al., *Macro.* 23, 4114 (1990).
 110. B. Lotz et al., *J. Polym. Sci.: Polym. Phys.* 24, 2017 (1986).
 111. W.S. Lambert, MS thesis, Univ. of Tenn., Knoxville (1988).
 112. G. Ross and Frolen, *J. Res. Nat. Bur. Stand.* 79A, 701 (1975).
 113. D.R. Burfiueled and Y. Doi, *Macro.* 16, 702 (1983).
 114. S.Z.D. Cheng et al, *Macro.* 23, 298 (1990).
 115. E.J. Clark and J.D. Hoffman, *Macro.* 17, 878 (1984).
 116. A. Hammami, MS thesis, Univ. of Tenn, Knoxville (1990).

-
117. G.S. Ross and L.J. Frolen, J. Res. Natl. Bur. Stand.
79A, 701 (1975).
118. J.A. Sauer and K. D. Pae, Proceedings of the 4th
International Conf.on High Pressure, Kyoto, 17 (1974).

Vita

Richard A. Campbell was born in Clarksdale, Mississippi on May 29, 1960. He entered Mississippi State University in August of 1978, and received a Bachelor of Science degree in Chemical Engineering in May of 1982. He then attended the University of Southern Mississippi, studying polymer science. In August of 1986, he entered the University of Tennessee, Knoxville to study polymer engineering in the Department of Materials Science and Engineering. He earned his Master of Science degree in Polymer Engineering in May 1991.